

**A MULTI-REGION MULTI-TIMESCALE BURNING PLASMA DYNAMICS  
MODEL FOR TOKAMAKS**

A Dissertation  
Presented to  
The Academic Faculty

By

Zefang Liu

In Partial Fulfillment  
of the Requirements for the Degree  
Doctor of Philosophy in the  
Nuclear Engineering Program

Georgia Institute of Technology

August 2022

Copyright © Zefang Liu 2022

**A MULTI-REGION MULTI-TIMESCALE BURNING PLASMA DYNAMICS  
MODEL FOR TOKAMAKS**

Approved by:

Dr. Weston Stacey, Advisor  
Nuclear and Radiological Engineer-  
ing Program  
*Georgia Institute of Technology*

Dr. Steven Biegalski, Co-Advisor  
Nuclear and Radiological Engineer-  
ing Program  
*Georgia Institute of Technology*

Dr. Bojan Petrovic  
Nuclear and Radiological Engineer-  
ing Program  
*Georgia Institute of Technology*

Dr. Dan Kotlyar  
Nuclear and Radiological Engineer-  
ing Program  
*Georgia Institute of Technology*

Dr. Yajun Mei  
School of Industrial and Systems  
Engineering  
*Georgia Institute of Technology*

Dr. Craig Petty  
DIII-D National Fusion Facility  
*General Atomics*

Date Approved: July 7, 2022

## ACKNOWLEDGEMENTS

I would like to thank my advisor, Dr. Weston Stacey, for his guidance and encouragement in my Ph.D. education and research. I would like to thank my co-advisor, Dr. Steven Biegalski, for his help in the Nuclear Engineering Ph.D. program. I would like to thank the rest of my thesis committee: Dr. Bojan Petrovic, Dr. Dan Kotlyar, Dr. Yajun Mei, and Dr. Craig Petty, for their help with my proposal and defense presentations. I would like to thank Dr. Theresa Wilks and Dr. Donald Spong for their comments and feedback on my research during the 2021 U.S. Transport Taskforce Workshop. I would like to thank Dr. Richard Groebner and Dr. Orso Meneghini from General Atomics for their assistance. I would like to thank William DeShazer and Jonathan Roveto from the Georgia Tech Fusion Research Center for their technical help. Finally, I would like to thank my parents for their support in my study and life.

Experiment data are from the DIII-D National Fusion Facility, which is supported by US DOE under DE-FC02-04ER54698.

## TABLE OF CONTENTS

<b>Acknowledgments</b> . . . . .	iii
<b>List of Tables</b> . . . . .	ix
<b>List of Figures</b> . . . . .	xi
<b>Summary</b> . . . . .	xvii
<b>Chapter 1: Introduction</b> . . . . .	1
1.1 Nuclear Fusion and Tokamaks . . . . .	1
1.2 Literature Survey . . . . .	3
1.3 Research Purposes . . . . .	4
<b>Chapter 2: A Multinodal Burning Plasma Dynamics Model</b> . . . . .	7
2.1 Geometry . . . . .	7
2.2 Balance Equations and Transport Terms . . . . .	8
2.2.1 Particle Balance Equation and Particle Transport . . . . .	9
2.2.2 Energy Balance Equation and Energy Transport . . . . .	13
2.2.3 Particle and Thermal Diffusivities . . . . .	17
2.3 Sources and Sinks . . . . .	18
2.3.1 External Particle Sources . . . . .	18

2.3.2	Ohmic and Auxiliary Heating . . . . .	20
2.3.3	Fusion and Alpha Heating . . . . .	23
2.3.4	Radiations . . . . .	26
2.3.5	Collisional Energy Transfer . . . . .	33
2.3.6	Ion Orbit Loss . . . . .	34
2.3.7	Atomic and Molecular Processes . . . . .	37
2.4	Multinodal Model Framework . . . . .	40
2.4.1	Core Region . . . . .	42
2.4.2	Edge Region . . . . .	44
2.4.3	Scrape-Off Layer Region . . . . .	45
2.4.4	Divertor Region . . . . .	47
2.5	Summary . . . . .	49
<b>Chapter 3: Computational Methods . . . . .</b>		<b>50</b>
3.1	Limitations of Previous Works . . . . .	50
3.2	Multinodal Model Formulas . . . . .	52
3.2.1	Parametric Diffusivity Model . . . . .	53
3.2.2	Dynamical System . . . . .	55
3.3	Optimization Algorithms . . . . .	57
3.3.1	Mean Squared Error Loss . . . . .	57
3.3.2	Back Propagation Algorithm . . . . .	58
3.3.3	Vanishing and Exploding Gradient Problem . . . . .	59
3.4	GTBURN Package . . . . .	60

3.5	Summary . . . . .	62
<b>Chapter 4:</b>	<b>Multinodal Model Simulations for DIII-D Plasmas . . . . .</b>	<b>64</b>
4.1	Assumptions for Modeling DIII-D Plasmas . . . . .	64
4.2	Particle and Energy Balance Equations . . . . .	65
4.3	Diffusivity and Transport Time Models . . . . .	70
4.4	Experiment Data and Simulation Settings . . . . .	72
4.5	Computation Results . . . . .	77
4.5.1	Shot 131190 . . . . .	78
4.5.2	Shot 140418 . . . . .	83
4.5.3	Shot 140420 . . . . .	87
4.5.4	Shot 140427 . . . . .	92
4.5.5	Shot 140535 . . . . .	96
4.6	Summary . . . . .	101
<b>Chapter 5:</b>	<b>Multinodal Model Simulations for ITER Plasmas . . . . .</b>	<b>104</b>
5.1	Assumptions for Modeling ITER Plasmas . . . . .	104
5.2	Particle and Energy Balance Equations . . . . .	107
5.3	Computation Results of Inductive Operation Scenarios . . . . .	111
5.3.1	Inductive Operation Scenario 2 . . . . .	112
5.3.2	Inductive Operation Scenario 1 . . . . .	118
5.3.3	Hybrid Operation Scenario 3 . . . . .	119
5.4	Computation Results of Non-Inductive Operation Scenarios . . . . .	121
5.4.1	Non-Inductive Operation Scenario 4 . . . . .	123

5.4.2	Non-Inductive Operation Scenario 6 and 7 . . . . .	126
5.5	Sensitivity Analyses . . . . .	126
5.5.1	Sensitivity Analysis of Diffusivities . . . . .	128
5.5.2	Sensitivity Analysis of Electron Cyclotron Radiation Parameters . .	130
5.5.3	Sensitivity Analysis of Impurity Fractions . . . . .	131
5.5.4	Sensitivity Analysis of Ion Orbit Loss Timescales . . . . .	132
5.6	Summary . . . . .	134
<b>Chapter 6: Conclusion . . . . .</b>		<b>136</b>
6.1	Research Conclusions . . . . .	136
6.2	Future Research . . . . .	138
6.2.1	Improvement Directions of the Multinodal Model . . . . .	139
6.2.2	Burning Plasma Control . . . . .	142
<b>Appendix A: One-Nodal Burning Plasma Dynamics Model . . . . .</b>		<b>145</b>
A.1	Global Dynamics Equations . . . . .	145
A.2	Volume-Averaged Quantities . . . . .	147
A.3	Particle and Energy Diffusion . . . . .	147
A.4	Confinement Time Models . . . . .	148
A.5	Computation Results . . . . .	150
A.6	Summary . . . . .	153
<b>Appendix B: A General Multinodal Model for Plasma Transport . . . . .</b>		<b>157</b>
B.1	Geometry . . . . .	157

B.2	Particle Balance Equations . . . . .	158
B.3	Energy Balance Equations . . . . .	160
<b>Appendix C: Radial Electric Field and Electrostatic Potential Profiles . . . . .</b>		<b>163</b>
C.1	Radial Electric Field Profile for DIII-D . . . . .	163
C.2	Radial Electric Field Profile for ITER . . . . .	164
<b>References . . . . .</b>		<b>164</b>



## LIST OF TABLES

4.1	Experiment shots [10] from DIII-D used in this study, where densities and temperatures are volume-averaged over the whole plasma. . . . .	73
4.2	DIII-D experimental signals from OMFIT [80] used in the multinodal model.	74
4.3	Hyperparameters in the solver and optimizer. . . . .	76
4.4	Parameters in the nodal particle and thermal diffusivities for the DIII-D plasma. . . . .	77
4.5	Mean squared errors for shots in the testing set. . . . .	78
5.1	Typical parameters of ITER inductive and hybrid operation scenarios. Reproduced with permission from the ITER Technical Basis [31]. . . . .	113
5.2	Optimized parameters in the nodal particle and thermal diffusivities for the ITER inductive scenarios. . . . .	115
5.3	Parameters of ITER non-inductive operation scenarios, where WNS is for weak negative shear, SNS is for strong negative shear, and WPS is for weak positive shear. Reproduced with permission from the ITER Technical Basis [31]. . . . .	123
5.4	Optimized parameters in the nodal particle and thermal diffusivities for the ITER non-inductive scenarios. . . . .	124
5.5	Sensitivities of the diffusivity parameters for the ITER design scenario 2. . .	129
5.6	Summary of sensitivity analyses for the ITER design scenario 2. . . . .	130
5.7	Sensitivities of the ECR parameters for the ITER design scenario 2. . . . .	131
5.8	Sensitivities of the impurity fractions for the ITER design scenario 2. . . . .	132

5.9	Sensitivities of the IOL parameters for the ITER design scenario 2. . . . .	134
A.1	Hyperparameters in the solver and optimizer. . . . .	151
A.2	Tuned coefficients in the density and energy confinement time scaling laws as the Equation A.14. . . . .	151
A.3	Mean square errors for shots in the testing set. . . . .	152

## LIST OF FIGURES

1.1	The reactivities computed from the Bosch-Hale model [4] for several important fusion reactions as functions of the ion temperature. . . . .	2
2.1	The geometry of the multinodal model, where each node is a toroidal shell and each interface is a torus surface. . . . .	8
2.2	Several important deposition profiles in the tokamak plasma, where neutral beam injection and cyclotron heating power deposition profiles are fitted from Kessel et al. [30], and gas puffing profile is fitted from Baylor et al. [29]. . . . .	20
2.3	Fusion alpha heating without radiation and transport losses for a typical inductive operation scenario of ITER. . . . .	24
2.4	Electron temperature and density profiles fitted for the electron cyclotron radiation (ECR) calculation, where $T_e$ and $n_e$ are the typical electron temperatures and densities in the ITER inductive operation [31, 7]. . . . .	30
2.5	Electron temperature and density profiles fitted for the electron cyclotron radiation (ECR) calculation, where $T_e$ and $n_e$ are the typical electron temperatures and densities in the ITER non-inductive operation [7]. . . . .	31
2.6	Ion particle and energy cumulative loss fractions for DIII-D, where $I_P = 1.5$ MA, $R_0 = 1.75$ m, $a = 0.885$ m, $T_i = 1$ keV, $B_{\phi 0} = 1.98$ T, and the electrostatic potential is from the Appendix C.1. . . . .	36
2.7	Ion particle and energy cumulative loss fractions for ITER, where $I_P = 9.731$ MA, $R_0 = 6.2$ m, $a = 2$ m, $T_i = 6$ keV, $B_{\phi 0} = 5.3$ T, and the electrostatic potential is from the Appendix C.2. . . . .	37
2.8	The cross section of the DIII-D plasma with the core, edge, and SOL regions in the multinodal model. The divertor region is omitted here. . . . .	41

3.1	Workflow chart for the GTBURN, where solid lines are for the forward flow to solve the problem and dash lines are for back propagation to optimize the parameters in the diffusivity model. . . . .	62
4.1	Signals of the shot 131190 from the DIII-D tokamak, where the plasma current, toroidal magnetic field, safety factor, gas puffing, ohmic heating, neutral beam injection (NBI), electron cyclotron heating (ECH), and ion cyclotron heating (ICH) are included. . . . .	79
4.2	Simulation results of the shot 131190 for the core node, where $\hat{n}_{\sigma}^{\text{node}}$ and $\hat{T}_{\sigma}^{\text{node}}$ are from the multinodal model, while $n_{\sigma}^{\text{node}}$ and $T_{\sigma}^{\text{node}}$ are from the experimental measurement. . . . .	81
4.3	Diffusivities and transport times from the core to the edge for the shot 131190 with the optimized diffusivity model. . . . .	81
4.4	Simulation results of the shot 131190 for the edge node, where $\hat{n}_{\sigma}^{\text{node}}$ and $\hat{T}_{\sigma}^{\text{node}}$ are from the multinodal model, while $n_{\sigma}^{\text{node}}$ and $T_{\sigma}^{\text{node}}$ are from the experimental measurement. . . . .	82
4.5	Diffusivities and transport times from the edge to the SOL for the shot 131190 with the optimized diffusivity model. . . . .	82
4.6	Simulation results of the shot 131190 for the SOL node, where $\hat{n}_{\sigma}^{\text{node}}$ and $\hat{T}_{\sigma}^{\text{node}}$ are from the multinodal model, while $n_{\sigma}^{\text{node}}$ and $T_{\sigma}^{\text{node}}$ are from the experimental measurement. . . . .	83
4.7	Diffusivities and transport times from the SOL to the divertor for the shot 131190 with the optimized diffusivity model. . . . .	84
4.8	Signals of the shot 140418 from the DIII-D tokamak, where the plasma current, toroidal magnetic field, safety factor, gas puffing, ohmic heating, neutral beam injection (NBI), electron cyclotron heating (ECH), and ion cyclotron heating (ICH) are included. . . . .	84
4.9	Simulation results of the shot 140418 for the core node, where $\hat{n}_{\sigma}^{\text{node}}$ and $\hat{T}_{\sigma}^{\text{node}}$ are from the multinodal model, while $n_{\sigma}^{\text{node}}$ and $T_{\sigma}^{\text{node}}$ are from the experimental measurement. . . . .	85
4.10	Diffusivities and transport times from the core to the edge for the shot 140418 with the optimized diffusivity model. . . . .	86

4.11	Simulation results of the shot 140418 for the edge node, where $\hat{n}_\sigma^{\text{node}}$ and $\hat{T}_\sigma^{\text{node}}$ are from the multinodal model, while $n_\sigma^{\text{node}}$ and $T_\sigma^{\text{node}}$ are from the experimental measurement. . . . .	87
4.12	Diffusivities and transport times from the edge to the SOL for the shot 140418 with the optimized diffusivity model. . . . .	87
4.13	Simulation results of the shot 140418 for the SOL node, where $\hat{n}_\sigma^{\text{node}}$ and $\hat{T}_\sigma^{\text{node}}$ are from the multinodal model, while $n_\sigma^{\text{node}}$ and $T_\sigma^{\text{node}}$ are from the experimental measurement. . . . .	88
4.14	Diffusivities and transport times from the SOL to the divertor for the shot 140418 with the optimized diffusivity model. . . . .	88
4.15	Signals of the shot 140420 from the DIII-D tokamak, where the plasma current, toroidal magnetic field, safety factor, gas puffing, ohmic heating, neutral beam injection (NBI), electron cyclotron heating (ECH), and ion cyclotron heating (ICH) are included. . . . .	89
4.16	Simulation results of the shot 140420 for the core node, where $\hat{n}_\sigma^{\text{node}}$ and $\hat{T}_\sigma^{\text{node}}$ are from the multinodal model, while $n_\sigma^{\text{node}}$ and $T_\sigma^{\text{node}}$ are from the experimental measurement. . . . .	90
4.17	Diffusivities and transport times from the core to the edge for the shot 140420 with the optimized diffusivity model. . . . .	90
4.18	Simulation results of the shot 140420 for the edge node, where $\hat{n}_\sigma^{\text{node}}$ and $\hat{T}_\sigma^{\text{node}}$ are from the multinodal model, while $n_\sigma^{\text{node}}$ and $T_\sigma^{\text{node}}$ are from the experimental measurement. . . . .	91
4.19	Diffusivities and transport times from the edge to the SOL for the shot 140420 with the optimized diffusivity model. . . . .	91
4.20	Simulation results of the shot 140420 for the SOL node, where $\hat{n}_\sigma^{\text{node}}$ and $\hat{T}_\sigma^{\text{node}}$ are from the multinodal model, while $n_\sigma^{\text{node}}$ and $T_\sigma^{\text{node}}$ are from the experimental measurement. . . . .	92
4.21	Diffusivities and transport times from the SOL to the divertor for the shot 140420 with the optimized diffusivity model. . . . .	93
4.22	Signals of the shot 140427 from the DIII-D tokamak, where the plasma current, toroidal magnetic field, safety factor, gas puffing, ohmic heating, neutral beam injection (NBI), electron cyclotron heating (ECH), and ion cyclotron heating (ICH) are included. . . . .	93

4.23	Simulation results of the shot 140427 for the core node, where $\hat{n}_\sigma^{\text{node}}$ and $\hat{T}_\sigma^{\text{node}}$ are from the multinodal model, while $n_\sigma^{\text{node}}$ and $T_\sigma^{\text{node}}$ are from the experimental measurement. . . . .	94
4.24	Diffusivities and transport times from the core to the edge for the shot 140427 with the optimized diffusivity model. . . . .	95
4.25	Simulation results of the shot 140427 for the edge node, where $\hat{n}_\sigma^{\text{node}}$ and $\hat{T}_\sigma^{\text{node}}$ are from the multinodal model, while $n_\sigma^{\text{node}}$ and $T_\sigma^{\text{node}}$ are from the experimental measurement. . . . .	95
4.26	Diffusivities and transport times from the edge to the SOL for the shot 140427 with the optimized diffusivity model. . . . .	96
4.27	Simulation results of the shot 140427 for the SOL node, where $\hat{n}_\sigma^{\text{node}}$ and $\hat{T}_\sigma^{\text{node}}$ are from the multinodal model, while $n_\sigma^{\text{node}}$ and $T_\sigma^{\text{node}}$ are from the experimental measurement. . . . .	97
4.28	Diffusivities and transport times from the SOL to the divertor for the shot 140427 with the optimized diffusivity model. . . . .	97
4.29	Signals of the shot 140535 from the DIII-D tokamak, where the plasma current, toroidal magnetic field, safety factor, gas puffing, ohmic heating, neutral beam injection (NBI), electron cyclotron heating (ECH), and ion cyclotron heating (ICH) are included. . . . .	98
4.30	Simulation results of the shot 140535 for the core node, where $\hat{n}_\sigma^{\text{node}}$ and $\hat{T}_\sigma^{\text{node}}$ are from the multinodal model, while $n_\sigma^{\text{node}}$ and $T_\sigma^{\text{node}}$ are from the experimental measurement. . . . .	99
4.31	Diffusivities and transport times from the core to the edge for the shot 140535 with the optimized diffusivity model. . . . .	99
4.32	Simulation results of the shot 140535 for the edge node, where $\hat{n}_\sigma^{\text{node}}$ and $\hat{T}_\sigma^{\text{node}}$ are from the multinodal model, while $n_\sigma^{\text{node}}$ and $T_\sigma^{\text{node}}$ are from the experimental measurement. . . . .	100
4.33	Diffusivities and transport times from the edge to the SOL for the shot 140535 with the optimized diffusivity model. . . . .	100
4.34	Simulation results of the shot 140535 for the SOL node, where $\hat{n}_\sigma^{\text{node}}$ and $\hat{T}_\sigma^{\text{node}}$ are from the multinodal model, while $n_\sigma^{\text{node}}$ and $T_\sigma^{\text{node}}$ are from the experimental measurement. . . . .	101

4.35	Diffusivities and transport times from the SOL to the divertor for the shot 140535 with the optimized diffusivity model. . . . .	101
5.1	The cross section of the ITER plasma with the core and edge regions in the multinodal model. . . . .	105
5.2	Plasma temperature and density profiles at the current flat-top phase for the inductive operational scenario. Reproduced with permission from the ITER Technical Basis [31]. . . . .	112
5.3	Densities and temperatures of the ITER design scenario 2. . . . .	116
5.4	Powers of the ITER design scenario 2. . . . .	117
5.5	Energy flows for the ITER inductive scenario 2 simulated by the multinodal model at 15 s. . . . .	118
5.6	Densities and temperatures of the ITER design scenario 1. . . . .	119
5.7	Densities and temperatures of the ITER design scenario 3. . . . .	120
5.8	Powers of the ITER design scenario 3. . . . .	120
5.9	Energy flows for the ITER hybrid scenario 3 simulated by the multinodal model at 15 s. . . . .	121
5.10	Plasma temperature and density profiles at the current flat-top phase for the steady state weak negative shear (WNS) operational scenario. Reproduced with permission from the ITER Technical Basis [31]. . . . .	124
5.11	Densities and temperatures of the ITER design scenario 4. . . . .	125
5.12	Powers of the ITER design scenario 4. . . . .	126
5.13	Energy flows for the ITER non-inductive scenario 4 simulated by the multinodal model at 15 s. . . . .	127
5.14	Densities and temperatures of the ITER design scenario 6. . . . .	127
5.15	Densities and temperatures of the ITER design scenario 7. . . . .	128
5.16	Sensitivity of the thermal diffusivity between the core and edge for the ITER design scenario 2. . . . .	130

5.17	Sensitivity of the wall reflection coefficient in the electron cyclotron radiation for the ITER design scenario 2. . . . .	132
5.18	Sensitivity of the beryllium impurity fraction for the ITER design scenario 2.	133
5.19	Sensitivity of the argon impurity fraction for the ITER design scenario 2. . .	133
6.1	Workflow chart for the GTBURN for determining particle and energy sources, where solid lines are for the forward flow to solve the problem and dash lines are for back propagation to update undetermined particle and energy sources. . . . .	143
A.1	Simulation results of the shot 131190, where $\hat{n}_\sigma$ and $\hat{T}_\sigma$ are from the one-nodal model, while $n_\sigma$ and $T_\sigma$ are from the experimental measurement. . . .	154
A.2	Simulation results of the shot 140418, where $\hat{n}_\sigma$ and $\hat{T}_\sigma$ are from the one-nodal model, while $n_\sigma$ and $T_\sigma$ are from the experimental measurement. . . .	154
A.3	Simulation results of the shot 140420, where $\hat{n}_\sigma$ and $\hat{T}_\sigma$ are from the one-nodal model, while $n_\sigma$ and $T_\sigma$ are from the experimental measurement. . . .	155
A.4	Simulation results of the shot 140427, where $\hat{n}_\sigma$ and $\hat{T}_\sigma$ are from the one-nodal model, while $n_\sigma$ and $T_\sigma$ are from the experimental measurement. . . .	155
A.5	Simulation results of the shot 140535, where $\hat{n}_\sigma$ and $\hat{T}_\sigma$ are from the one-nodal model, while $n_\sigma$ and $T_\sigma$ are from the experimental measurement. . . .	156
B.1	A diagram for the general multinodal model, where each node is a toroidal shell and each internodal surface is a torus surface. . . . .	157



## SUMMARY

Controlled thermonuclear fusion in tokamaks brings forth demands for burning plasma dynamics research. The deuterium-tritium fusion generates energetic alpha particles, which first transfer their energy to core electrons. The heated electrons and remaining fusion alpha particles then heat core ions through Coulomb collisions, which can increase the fusion reaction rate and may conceivably lead to a thermal runaway instability. Meanwhile, core electrons lose energy to the edge plasma and wall through electron cyclotron radiation, bremsstrahlung, impurity radiation, and transport; and core ions lose energy through transport to the edge and ion orbit loss. The various timescales of radiation and transport processes in different regions are vital to the determination of tokamak operation.

A multi-region multi-timescale transport model is developed to simulate burning plasma dynamics in tokamaks. Regions including the core, edge, scrape-off layer, and divertor are modeled as separate nodes. Fusion alpha heating with a time delay between heating electrons and ions is considered. Ohmic and auxiliary heating methods are included. Radiations such as electron cyclotron radiation, bremsstrahlung, line radiation, and recombination radiation are involved. Coulomb collisional energy transfer is utilized for energy redistribution among species. Ion orbit loss is included as one edge plasma effect. Transport times between nodes are derived theoretically from the fluid model, where diffusivity parameters are computed numerically from experiment data by machine learning. The transport model is validated by application to DIII-D non-fusion plasmas in various auxiliary heating conditions.

Both inductive and non-inductive ITER operation scenarios are simulated with the model. Simulation results with sensitivity analyses indicate the radiation and transport can promptly remove extra heat from the core plasma and thereby inhibit the thermal runaway instability from the fusion alpha heating. This model can be used for tokamak deuterium-tritium burn control studies in the future.

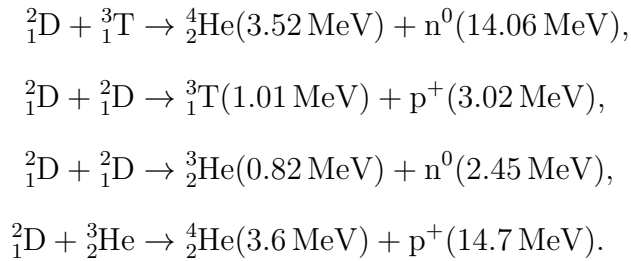
# CHAPTER 1

## INTRODUCTION

Fusion has a great potential to provide essentially inexhaustible energies for the later 21st century and future. In this research, a multi-region multi-timescale transport model is developed for fusion burning plasma simulations. This chapter introduces background knowledge about nuclear fusion and tokamaks first, where two primary magnetic confinement devices used in this research are presented. Then, several relevant previous works about burning plasmas are surveyed, and their conclusions with limitations are given. Lastly, energy transfer processes in tokamak burning plasmas are analyzed, and the research purposes of this thesis are put forward.

### 1.1 Nuclear Fusion and Tokamaks

Under proper conditions, light atomic nuclei can merge and convert mass deficit to energy via nuclear fusion. A significant amount of energy is released during this process. Fusion reactions with primary interests [1, 2, 3] are listed as follows:



One measure of the fusion reaction probability is the cross section  $\sigma$ . When reactants have a distribution of velocities, the reactivity  $\langle\sigma v\rangle$  can be introduced as an average of the cross-section and velocity product. The reaction rate is computed by  $n_1 n_2 \langle\sigma v\rangle$ , where  $n_1$  and  $n_2$  are particle densities of reactants. Several important fusion reactivities  $\langle\sigma v\rangle$

are computed from the Bosch-Hale model [4] and shown in the Figure 1.1 with the ion temperature  $T_i$  in a log-log scale. This figure indicates the strong temperature dependence of the fusion reactivity in roughly  $\langle\sigma v\rangle \propto T_i^2$ .

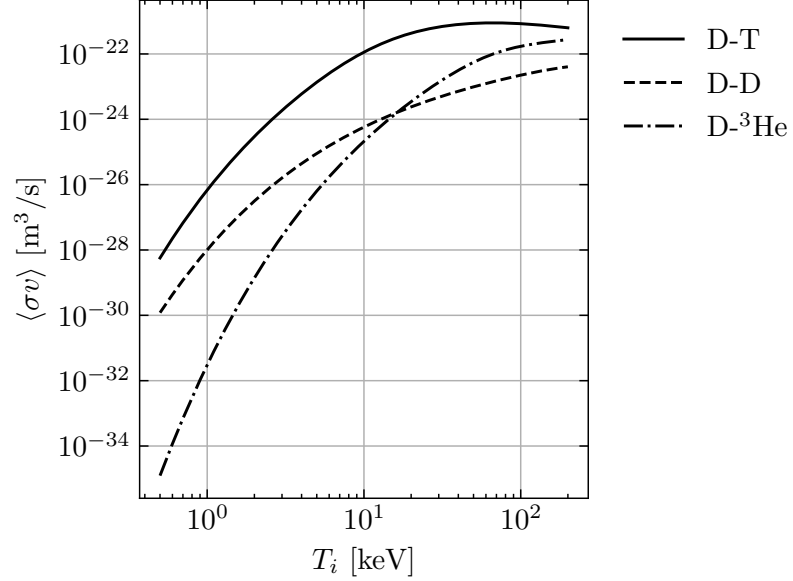


Figure 1.1: The reactivities computed from the Bosch-Hale model [4] for several important fusion reactions as functions of the ion temperature.

The Coulomb repulsion between two charged particles must be overcome when two nuclei fuse. One way to achieve this goal is to heat the fusion fuels to a high enough temperature, where ions and electrons are separated. This fourth fundamental state of matter is called plasma. However, the hot plasma is not allowed to contact the wall, where the charged particles will recombine and become neutral particles again. One way to confine the plasma is to use magnetic fields, and one such kind of magnetic device is the tokamak, a toroidal chamber with magnetic coils.

Tokamaks have been proven to be the most successful device in producing and maintaining plasmas with parameters of density, temperature, and energy confinement time closest to the fusion power reactor requirements. The world's largest magnetic confinement device is the International Thermonuclear Experimental Reactor (ITER) [5], which is being built in southern France. ITER is planned to generate the first plasma in 2025 and start the

deuterium-tritium operation in 2035. This research will also use the experiment data from the DIII-D tokamak, operated since the late 1980s by General Atomics (GA) in San Diego and built on the update of the earlier Doublet III.

## 1.2 Literature Survey

Much research has been performed on fusion-relevant plasmas. We focus on the work about burning plasma dynamics here.

Wang et al. [6] simulated the dynamics of burning plasmas in ITER with a 1.5-dimensional up-down asymmetry Tokamak Transport Simulation Code (TTSC). This work showed that a large excursion of fusion power could occur with a slight improvement of plasma confinement, which would give difficulties to feedback controls. The effect of plasma profiles on fusion power excursion, changes in pumping efficacy, and magnetohydrodynamic sawtooth activity were also studied.

Green et al. [7] introduced studies of fusion burning plasma physics and fusion reactor technologies in ITER. The areas of burning plasma physics were categorized into energetic particle effects, self-heating phenomena, and reactor-scale physics. In addition, the plasma physics of ITER was also assessed in inductive drive scenarios, hybrid scenarios, and non-inductive drive scenarios.

Cordey et al. [8] re-examined the condition of the ELMy H-mode database. They applied principal component regression, an error in variables technique, and the selection of fewer variables to address shortcomings in the previous ordinary least squares regression for the tokamak energy confinement time scaling law. This new scaling law improved the performances for ITER at higher  $\beta_n$ .

Stacey [9] surveyed the experimental observations of several abrupt transition phenomena in plasma operating conditions. In addition, the theoretical thermal instabilities driven by the temperature dependence of various radiative and atomic physics cooling mechanisms were studied and compared with experimental observations.

Hill [10] developed a tokamak- and configuration-specific confinement tuning model and applied it to the DIII-D experiments. The results showed the improvement of the tuned model in simulating the experimental temperatures compared with the model using the ITER-98 scaling law. However, this tuned dynamic model solved only the global ion and electron temperatures, limiting its application to a more complicated system with multiple regions and timescales.

Hill [11] also studied the active and passive control mechanisms limiting plasma power excursion in the ITER. Several potential burning control mechanisms, including electron cyclotron radiation (ECR), impurity radiation, ion-orbit loss (IOL), and multi-faceted asymmetric radiation from the edge (MARFE) instabilities, were investigated. The ECR was found to be the most critical passive burning control mechanism at high temperatures. A framework of the multinodal dynamics model was presented for future research.

Stacey [12] researched the temporal and spatial dependence of the various heating and cooling mechanisms involved in fusion burning plasmas. A spatially coarse nodal space-time dynamics model was introduced for burning plasmas. The core and edge plasma's particle and energy balance equations were presented. This previous work gives directions for our work, where we will build one practical multinodal model based on the previous two-nodal model framework. We will also derive internodal transport times from the fluid theory and solve them from DIII-D experiment data with machine learning algorithms.

### **1.3 Research Purposes**

Fusion burning plasmas with alpha heating bring forth demands for research in burning plasma dynamics. International Thermonuclear Experimental Reactor (ITER) will experiment with deuterium-tritium (D-T) fusion reactions. The D-T fusion generates 14.1 MeV neutrons, which leave the plasma immediately, and 3.5 MeV fusion alpha particles, which are confined by the magnetic field within the tokamak. The fusion alpha particles transfer their energy to electrons before ions in the core plasma. The heated electrons produce elec-

tron cyclotron radiation (ECR), bremsstrahlung, and impurity radiation, which then heat edge electrons and the first wall. Such radiation processes are viewed as instantaneous energy transport compared with diffusion transport.

The remaining fusion alpha particles and heated electrons in the core plasma energize core ions through Coulomb collisions, which will increase the fusion reaction rate by increasing the fusion reactivity in the core region. This process may conceivably lead to a thermal runaway instability in the reactor, where more fusion reactions produce more fusion alpha particles and more heating in positive feedback. However, in the meantime, energy is also transported and radiated from the plasma core to the edge and wall. Such energy losses may inhibit the thermal runaway instability. Therefore, multiple timescales of various processes in different tokamak regions are crucial to burning D-T plasma operations.

When both radiation and transport processes are included, the plasma core cannot be modeled independently with only one timescale, such as an energy confinement time, which has been studied in previous global burning plasma dynamics models [1, 10, 11]. For example, radiations from the heated core electrons can have much more rapid responses to heat the edge and the wall, while transport processes send energy in relatively long timescales. Such fast and slow phenomena will couple the plasma core with the edge and other tokamak regions in multiple timescales.

A multi-region multi-timescale transport model based on previous research [12, 11] is developed for simulating burning plasma dynamics in tokamaks. Regions including the core, where most fusion reactions and ECR are generated, edge, where transport from the core and impurity radiation happen, scrape-off layer (SOL), where the atomic and molecular precesses are important, and divertor, where most waste materials are removed from the plasma, are modeled as separate nodes. The radiation and transport processes are contained in different timescales. Transport times between different nodes are derived from the fluid theory and computed through a parametric diffusivity formula, where parameters are

optimized based on experimental data with machine learning algorithms. An edge plasma phenomenon, ion orbit loss (IOL), is also considered. This transport model is validated for DIII-D non-fusion plasmas with various auxiliary heating conditions and simulated for ITER fusion plasmas in both inductive and non-inductive scenarios. This transport model can also be used for burning D-T plasma control in the future.

## CHAPTER 2

### A MULTINODAL BURNING PLASMA DYNAMICS MODEL

The core goal of this research is to model the burning plasmas properly. In this chapter, a multinodal burning plasma dynamics model is proposed. The geometry of the multinodal model is introduced first, then the particle and energy balance equations with internodal transport terms are derived from the fluid model. Next, multiple mechanisms in burning plasmas are considered in the multinodal model as the source and sink terms. External particle source, ohmic and auxiliary heating, fusion alpha heating, radiation, Coulomb collisional energy transfer, ion orbit loss, and atomic and molecular processes are visited. Lastly, all source and sink terms are assembled into particle and energy balance equations, and a framework for the multinodal model is presented.

#### 2.1 Geometry

The first thing to be introduced is the geometry of the multinodal model. One conventional tokamak is viewed as one torus. The cross section of the torus is assumed to be circular in this research. Following the flux surfaces from the inner side to the outer side, the torus is divided into three regions: the core, edge, and scrape-off layer (SOL). The divertor region is ignored here and will join the model at the end of this chapter. Each region is viewed as one separate node in the multinodal model.

The geometry of the multinodal model is illustrated in the Figure 2.1, where each node is a toroidal shell and each interface is a torus surface. The  $r_{\text{core}}$ ,  $r_{\text{edge}}$ , and  $r_{\text{sol}}$  are the minor radii for the surface  $A_{\text{core}}$ ,  $A_{\text{edge}}$ , and  $A_{\text{sol}}$  respectively. The  $\Delta r_{\text{core-edge}}$  is the radial distance between core and edge nodes, the  $\Delta r_{\text{edge-sol}}$  is the radial distance between edge and SOL nodes, and the  $\Delta r_{\text{sol-div}}$  is the radial distance from the SOL node center to its outer surface.



These radial distances are calculated as

$$\Delta r_{\text{core-edge}} = r_{\text{edge}}/2, \quad \Delta r_{\text{edge-sol}} = (r_{\text{sol}} - r_{\text{core}})/2, \quad \Delta r_{\text{sol-div}} = (r_{\text{sol}} - r_{\text{edge}})/2. \quad (2.1)$$

Lastly, the normalized minor radius is defined as  $\rho = r/a$ , where  $a$  is the minor radius of the plasma.

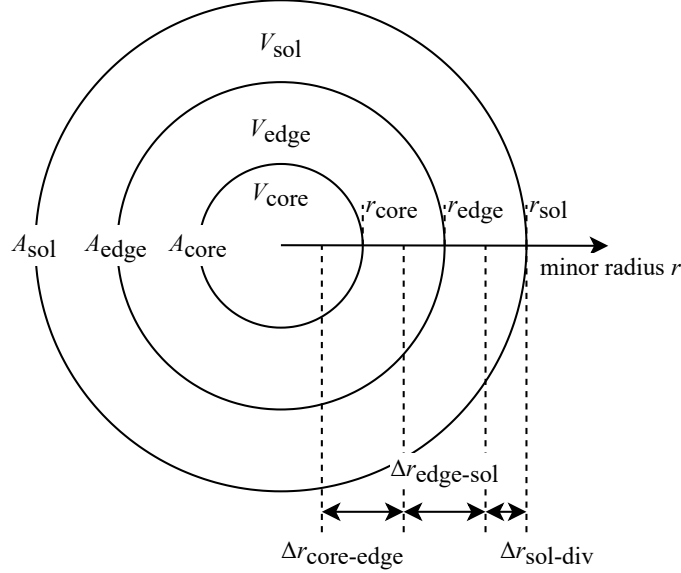


Figure 2.1: The geometry of the multinodal model, where each node is a toroidal shell and each interface is a torus surface.

Besides of the geometry, the set of ion species is defined as  $\mathcal{I} = \{D, T, \alpha, z_1, z_2, \dots\}$ , where D is for deuterons, T is for tritons,  $\alpha$  is for alpha particles, and  $z_1, z_2, \dots$  are for impurity particles. Also, the set of all species is defined as  $\mathcal{S} = \{e\} \cup \mathcal{I}$ , where  $e$  is for electrons.

## 2.2 Balance Equations and Transport Terms

After the geometry of the multinodal model is introduced, the particle and energy balance equations are derived from the fluid theory. The particle balance equation with the particle transport term is presented first, then the energy balance equation with the energy transport term is brought up next. Here, only three nodes in the multinodal model are considered:

the core, edge, and SOL nodes. A derivation for a general multinodal model is also given in the Appendix B, where any finite number of nodes is allowable.

### 2.2.1 Particle Balance Equation and Particle Transport

From the fluid theory, the continuity equation [1] for the species  $\sigma$  is

$$\frac{\partial n_\sigma}{\partial t} + \nabla \cdot \mathbf{\Gamma}_\sigma = S_\sigma, \quad \sigma \in \mathcal{S}, \quad (2.2)$$

where  $n_\sigma$  is the particle density,  $\mathbf{\Gamma}_\sigma = n_\sigma \mathbf{v}_\sigma$  is the particle flux, and  $S_\sigma$  is the net particle source.

#### *Core Particle Balance Equation*

By averaging the continuity equation in the core node, we have

$$\frac{1}{V_{\text{core}}} \int_{V_{\text{core}}} \frac{\partial n_\sigma}{\partial t} dV = \frac{1}{V_{\text{core}}} \int_{V_{\text{core}}} S_\sigma dV - \frac{1}{V_{\text{core}}} \int_{V_{\text{core}}} \nabla \cdot \mathbf{\Gamma}_\sigma dV. \quad (2.3)$$

where  $V_{\text{core}}$  is the volume of the core node. Let the volume-averaged particle density, net particle source, and particle transport term be

$$\bar{n}_\sigma^{\text{core}} = \frac{1}{V_{\text{core}}} \int_{V_{\text{core}}} n_\sigma dV, \quad (2.4)$$

$$\bar{S}_\sigma^{\text{core}} = \frac{1}{V_{\text{core}}} \int_{V_{\text{core}}} S_\sigma dV, \quad (2.5)$$

$$\bar{S}_{\sigma, \text{tran}}^{\text{core}} = -\frac{1}{V_{\text{core}}} \int_{V_{\text{core}}} \nabla \cdot \mathbf{\Gamma}_\sigma dV. \quad (2.6)$$

Then, the volume-averaged continuity equation or the particle balance equation for the core node is

$$\frac{d\bar{n}_\sigma^{\text{core}}}{dt} = \bar{S}_\sigma^{\text{core}} + \bar{S}_{\sigma, \text{tran}}^{\text{core}}. \quad (2.7)$$

By the divergence theorem, the particle transport term is transformed as

$$\bar{S}_{\sigma,\text{tran}}^{\text{core}} = -\frac{1}{V_{\text{core}}} \int_{V_{\text{core}}} \nabla \cdot \Gamma_{\sigma} dV = -\frac{1}{V_{\text{core}}} \int_{A_{\text{core}}} \Gamma_{\sigma} \cdot d\mathbf{S}. \quad (2.8)$$

From the Fick's law of diffusion,  $\Gamma_{\sigma} = -D_{\sigma} \nabla n_{\sigma}$ , where  $D_{\sigma}$  is the diffusion coefficient and  $\nabla n_{\sigma}$  is the density gradient. In toroidal coordinates, the density gradient [1] is written as

$$\nabla n_{\sigma} = \frac{\partial n_{\sigma}}{\partial r} \hat{\mathbf{r}} + \frac{1}{R_0 + r \cos \theta} \frac{\partial n_{\sigma}}{\partial \phi} \hat{\boldsymbol{\phi}} + \frac{1}{r} \frac{\partial n_{\sigma}}{\partial \theta} \hat{\boldsymbol{\theta}}. \quad (2.9)$$

We assume that the particle gradient has toroidal and poloidal symmetries on internodal surfaces, i.e.

$$\nabla n_{\sigma} = \frac{dn_{\sigma}}{dr} \hat{\mathbf{r}}. \quad (2.10)$$

Thus, the particle transport term becomes

$$\bar{S}_{\sigma,\text{tran}}^{\text{core}} = -\frac{1}{V_{\text{core}}} \int_{A_{\text{core}}} \Gamma_{\sigma} \cdot d\mathbf{S} = -\frac{1}{V_{\text{core}}} (\Gamma_{\sigma,r})_{A_{\text{core}}} A_{\text{core}}. \quad (2.11)$$

The radial flux at the core-edge interface  $A_{\text{core}}$  is approximated by

$$(\Gamma_{\sigma,r})_{A_{\text{core}}} = \left( -D_{\sigma} \frac{dn_{\sigma}}{dr} \right)_{A_{\text{core}}} \approx -D_{\sigma}^{\text{core}} \frac{\bar{n}_{\sigma}^{\text{edge}} - \bar{n}_{\sigma}^{\text{core}}}{\Delta r_{\text{core-edge}}}, \quad (2.12)$$

where  $D_{\sigma}^{\text{core}}$  is the diffusion coefficient at the surface  $A_{\text{core}}$  between the core and edge nodes, and  $\Delta r_{\text{core-edge}}$  is the radial distance between locations of average values, which is shown in the Figure 2.1. Then,

$$\bar{S}_{\sigma,\text{tran}}^{\text{core}} = -\frac{A_{\text{core}}}{V_{\text{core}}} (\Gamma_{\sigma,r})_{A_{\text{core}}} = -\frac{A_{\text{core}} D_{\sigma}^{\text{core}}}{V_{\text{core}} \Delta r_{\text{core-edge}}} (\bar{n}_{\sigma}^{\text{core}} - \bar{n}_{\sigma}^{\text{edge}}). \quad (2.13)$$

Let internodal particle transport times between core and edge nodes be

$$\tau_{P,\sigma}^{\text{core} \rightarrow \text{edge}} = \frac{V_{\text{core}} \Delta r_{\text{core-edge}}}{A_{\text{core}} D_{\sigma}^{\text{core}}} = \frac{r_{\text{core}}^2}{2r_{\text{core}}} \frac{\Delta r_{\text{core-edge}}}{D_{\sigma}^{\text{core}}}, \quad (2.14)$$

$$\tau_{P,\sigma}^{\text{edge} \rightarrow \text{core}} = \frac{V_{\text{edge}} \Delta r_{\text{core-edge}}}{A_{\text{core}} D_{\sigma}^{\text{core}}} = \frac{r_{\text{edge}}^2 - r_{\text{core}}^2}{2r_{\text{core}}} \frac{\Delta r_{\text{core-edge}}}{D_{\sigma}^{\text{core}}}, \quad (2.15)$$

where the torus shell volumes are  $V_{\text{core}} = 2\pi R_0 \cdot \pi r_{\text{core}}^2$  and  $V_{\text{edge}} = 2\pi R_0 \cdot \pi (r_{\text{edge}}^2 - r_{\text{core}}^2)$ , the torus surface areas are  $A_{\text{core}} = 2\pi R_0 \cdot 2\pi r_{\text{core}}$  and  $A_{\text{edge}} = 2\pi R_0 \cdot 2\pi r_{\text{edge}}$ , and the  $R_0$  is the major radius. The relation between two internodal transport times is

$$\tau_{P,\sigma}^{\text{core} \rightarrow \text{edge}} = \frac{V_{\text{core}}}{V_{\text{edge}}} \frac{V_{\text{edge}} \Delta r_{\text{core-edge}}}{A_{\text{core}} D_{\sigma}^{\text{core}}} = \frac{V_{\text{core}}}{V_{\text{edge}}} \tau_{P,\sigma}^{\text{edge} \rightarrow \text{core}}. \quad (2.16)$$

Hence, the particle transport term in the core node becomes

$$\bar{S}_{\sigma,\text{tran}}^{\text{core}} = -\frac{\bar{n}_{\sigma}^{\text{core}} - \bar{n}_{\sigma}^{\text{edge}}}{\tau_{P,\sigma}^{\text{core} \rightarrow \text{edge}}} = -\frac{\bar{n}_{\sigma}^{\text{core}}}{\tau_{P,\sigma}^{\text{core} \rightarrow \text{edge}}} + \frac{V_{\text{edge}}}{V_{\text{core}}} \frac{\bar{n}_{\sigma}^{\text{edge}}}{\tau_{P,\sigma}^{\text{edge} \rightarrow \text{core}}}. \quad (2.17)$$

### *Edge Particle Balance Equation*

Similarly, the particle balance equation for the edge node is

$$\frac{d\bar{n}_{\sigma}^{\text{edge}}}{dt} = \bar{S}_{\sigma}^{\text{edge}} + \bar{S}_{\sigma,\text{tran}}^{\text{edge}}, \quad (2.18)$$

where the particle transport term in the edge node is

$$\begin{aligned} \bar{S}_{\sigma,\text{tran}}^{\text{edge}} &= -\frac{1}{V_{\text{edge}}} \left( \int_{A_{\text{edge}}} \mathbf{\Gamma}_{\sigma} \cdot d\mathbf{S} - \int_{A_{\text{core}}} \mathbf{\Gamma}_{\sigma} \cdot d\mathbf{S} \right) \\ &= -\frac{1}{V_{\text{edge}}} \left[ (\mathbf{\Gamma}_{\sigma,r})_{A_{\text{edge}}} A_{\text{edge}} - (\mathbf{\Gamma}_{\sigma,r})_{A_{\text{core}}} A_{\text{core}} \right]. \end{aligned} \quad (2.19)$$

The radial flux at the edge-SOL interface is approximated by

$$(\Gamma_{\sigma,r})_{A_{\text{edge}}} = \left( -D_{\sigma} \frac{dn_{\sigma}}{dr} \right)_{A_{\text{edge}}} \approx -D_{\sigma}^{\text{edge}} \frac{\bar{n}_{\sigma}^{\text{sol}} - \bar{n}_{\sigma}^{\text{edge}}}{\Delta r_{\text{edge-sol}}}, \quad (2.20)$$

where  $D_{\sigma}^{\text{edge}}$  is the diffusion coefficient at the surface  $A_{\text{edge}}$  between the edge and SOL nodes. Then,

$$\begin{aligned} \bar{S}_{\sigma,\text{tran}}^{\text{edge}} &= -\frac{A_{\text{edge}}}{V_{\text{edge}}} (\Gamma_{\sigma,r})_{A_{\text{edge}}} + \frac{A_{\text{core}}}{V_{\text{edge}}} (\Gamma_{\sigma,r})_{A_{\text{core}}} \\ &= -\frac{A_{\text{edge}} D_{\sigma}^{\text{edge}}}{V_{\text{edge}} \Delta r_{\text{edge-sol}}} (\bar{n}_{\sigma}^{\text{edge}} - \bar{n}_{\sigma}^{\text{sol}}) + \frac{V_{\text{core}}}{V_{\text{edge}}} \frac{A_{\text{core}} D_{\sigma}^{\text{core}}}{V_{\text{core}} \Delta r_{\text{core-edge}}} (\bar{n}_{\sigma}^{\text{core}} - \bar{n}_{\sigma}^{\text{edge}}). \end{aligned} \quad (2.21)$$

Let internodal particle transport times between edge and SOL nodes be

$$\tau_{P,\sigma}^{\text{edge} \rightarrow \text{sol}} = \frac{V_{\text{edge}} \Delta r_{\text{edge-sol}}}{A_{\text{edge}} D_{\sigma}^{\text{edge}}} = \frac{r_{\text{edge}}^2 - r_{\text{core}}^2}{2r_{\text{edge}}} \frac{\Delta r_{\text{edge-sol}}}{D_{\sigma}^{\text{edge}}}, \quad (2.22)$$

$$\tau_{P,\sigma}^{\text{sol} \rightarrow \text{edge}} = \frac{V_{\text{sol}} \Delta r_{\text{edge-sol}}}{A_{\text{edge}} D_{\sigma}^{\text{edge}}} = \frac{r_{\text{sol}}^2 - r_{\text{edge}}^2}{2r_{\text{edge}}} \frac{\Delta r_{\text{edge-sol}}}{D_{\sigma}^{\text{edge}}}, \quad (2.23)$$

where the SOL volume is  $V_{\text{sol}} = 2\pi R_0 \cdot \pi (r_{\text{sol}}^2 - r_{\text{edge}}^2)$ , and the edge-SOL interface area is  $A_{\text{sol}} = 2\pi R_0 \cdot 2\pi r_{\text{sol}}$ . The relation between two internodal transport times is

$$\tau_{P,\sigma}^{\text{edge} \rightarrow \text{sol}} = \frac{V_{\text{edge}}}{V_{\text{sol}}} \frac{V_{\text{sol}} \Delta r_{\text{edge-sol}}}{A_{\text{edge}} D_{\sigma}^{\text{edge}}} = \frac{V_{\text{edge}}}{V_{\text{sol}}} \tau_{P,\sigma}^{\text{sol} \rightarrow \text{edge}}. \quad (2.24)$$

Hence, the particle transport term in the edge node becomes

$$\begin{aligned} \bar{S}_{\sigma,\text{tran}}^{\text{edge}} &= -\frac{\bar{n}_{\sigma}^{\text{edge}} - \bar{n}_{\sigma}^{\text{core}}}{\tau_{P,\sigma}^{\text{edge} \rightarrow \text{core}}} - \frac{\bar{n}_{\sigma}^{\text{edge}} - \bar{n}_{\sigma}^{\text{sol}}}{\tau_{P,\sigma}^{\text{edge} \rightarrow \text{sol}}} \\ &= -\frac{\bar{n}_{\sigma}^{\text{edge}}}{\tau_{P,\sigma}^{\text{edge} \rightarrow \text{core}}} + \frac{V_{\text{core}}}{V_{\text{edge}}} \frac{\bar{n}_{\sigma}^{\text{core}}}{\tau_{P,\sigma}^{\text{core} \rightarrow \text{edge}}} - \frac{\bar{n}_{\sigma}^{\text{edge}}}{\tau_{P,\sigma}^{\text{edge} \rightarrow \text{sol}}} + \frac{V_{\text{sol}}}{V_{\text{edge}}} \frac{\bar{n}_{\sigma}^{\text{sol}}}{\tau_{P,\sigma}^{\text{sol} \rightarrow \text{edge}}}. \end{aligned} \quad (2.25)$$

With the assumption  $\tau_{P,\sigma}^{\text{sol} \rightarrow \text{edge}} \rightarrow \infty$ , the particle transport term is simplified to

$$\begin{aligned}\bar{S}_{\sigma,\text{tran}}^{\text{edge}} &= \frac{V_{\text{core}}}{V_{\text{edge}}} \frac{\bar{n}_{\sigma}^{\text{core}} - \bar{n}_{\sigma}^{\text{edge}}}{\tau_{P,\sigma}^{\text{core} \rightarrow \text{edge}}} - \frac{\bar{n}_{\sigma}^{\text{edge}}}{\tau_{P,\sigma}^{\text{edge} \rightarrow \text{sol}}} \\ &= -\frac{\bar{n}_{\sigma}^{\text{edge}}}{\tau_{P,\sigma}^{\text{edge} \rightarrow \text{core}}} + \frac{V_{\text{core}}}{V_{\text{edge}}} \frac{\bar{n}_{\sigma}^{\text{core}}}{\tau_{P,\sigma}^{\text{core} \rightarrow \text{edge}}} - \frac{\bar{n}_{\sigma}^{\text{edge}}}{\tau_{P,\sigma}^{\text{edge} \rightarrow \text{sol}}}.\end{aligned}\quad (2.26)$$

### *SOL Particle Balance Equation*

Also, the particle balance equation for the SOL node is

$$\frac{d\bar{n}_{\sigma}^{\text{sol}}}{dt} = \bar{S}_{\sigma}^{\text{sol}} + \bar{S}_{\sigma,\text{tran}}^{\text{sol}}, \quad (2.27)$$

where the particle transport term in the SOL node is

$$\bar{S}_{\sigma,\text{tran}}^{\text{sol}} = -\frac{\bar{n}_{\sigma}^{\text{sol}}}{\tau_{P,\sigma}^{\text{sol} \rightarrow \text{edge}}} + \frac{V_{\text{edge}}}{V_{\text{sol}}} \frac{\bar{n}_{\sigma}^{\text{edge}}}{\tau_{P,\sigma}^{\text{edge} \rightarrow \text{sol}}} - \frac{\bar{n}_{\sigma}^{\text{sol}}}{\tau_{P,\sigma}^{\text{sol} \rightarrow \text{div}}} \approx \frac{V_{\text{edge}}}{V_{\text{sol}}} \frac{\bar{n}_{\sigma}^{\text{edge}}}{\tau_{P,\sigma}^{\text{edge} \rightarrow \text{sol}}} - \frac{\bar{n}_{\sigma}^{\text{sol}}}{\tau_{P,\sigma}^{\text{sol} \rightarrow \text{div}}}, \quad (2.28)$$

and  $\tau_{P,\sigma}^{\text{sol} \rightarrow \text{div}}$  is the particle transport time from the SOL node to the divertor and plenum nodes, which represents one effective particle confinement time of the SOL node. Here, we use the formula:

$$\tau_{P,\sigma}^{\text{sol}} = \frac{V_{\text{sol}} \Delta r_{\text{sol-div}}}{A_{\text{sol}} D_{\sigma}^{\text{sol}}} = \frac{r_{\text{sol}}^2 - r_{\text{edge}}^2}{2r_{\text{sol}}} \frac{\Delta r_{\text{sol-div}}}{D_{\sigma}^{\text{sol}}}, \quad (2.29)$$

where  $\Delta r_{\text{sol-div}}$  is the radial distance between the SOL center and its outer surface.

### 2.2.2 Energy Balance Equation and Energy Transport

From the fluid theory, the energy conservation equation [13] for the species  $\sigma$  is

$$\frac{3}{2} n_{\sigma} \left( \frac{\partial}{\partial t} + \mathbf{v}_{\sigma} \cdot \nabla \right) T_{\sigma} + p_{\sigma} \nabla \cdot \mathbf{v}_{\sigma} + \nabla \cdot \mathbf{q}_{\sigma} = P_{\sigma}, \quad \sigma \in \mathcal{S}, \quad (2.30)$$

where  $T_{\sigma}$  is the temperature (in the energy unit),  $p_{\sigma}$  is the pressure,  $\mathbf{q}_{\sigma}$  is the heat flux, and  $P_{\sigma}$  is the net energy source for the species  $\sigma$ . Let the energy density be  $U_{\sigma} = \frac{3}{2} n_{\sigma} T_{\sigma}$ .

Combining the energy conservation equation with the particle one, we get

$$\begin{aligned} \frac{3}{2}n_\sigma \frac{\partial T_\sigma}{\partial t} + \frac{3}{2}\mathbf{\Gamma}_\sigma \cdot \nabla T_\sigma + p_\sigma \nabla \cdot \mathbf{v}_\sigma + \nabla \cdot \mathbf{q}_\sigma + \frac{3}{2}T_\sigma \frac{\partial n_\sigma}{\partial t} + \frac{3}{2}T_\sigma \nabla \cdot \mathbf{\Gamma}_\sigma &= P_\sigma + \frac{3}{2}T_\sigma S_\sigma, \\ \frac{3}{2} \frac{\partial (n_\sigma T_\sigma)}{\partial t} &= P_\sigma + \frac{3}{2}S_\sigma T_\sigma - p_\sigma \nabla \cdot \mathbf{v}_\sigma - \nabla \cdot \left( \frac{3}{2}\mathbf{\Gamma}_\sigma T_\sigma + \mathbf{q}_\sigma \right). \end{aligned} \quad (2.31)$$

Since

$$\mathbf{\Gamma}_\sigma = -D_\sigma \nabla n_\sigma, \quad \mathbf{q}_\sigma = -k_\sigma \nabla \frac{T_\sigma}{k} = -\chi_\sigma n_\sigma c_{p,m,\sigma} \nabla \frac{T_\sigma}{k} = -\frac{5}{2}\chi_\sigma n_\sigma \nabla T_\sigma, \quad (2.32)$$

where  $k_\sigma$  is the thermal conductivity,  $k$  is the Boltzmann constant,  $c_{p,m,\sigma}$  is the molar heat capacity, and  $\chi_\sigma$  is the thermal diffusivity, then,

$$\frac{\partial U_\sigma}{\partial t} = \left( P_\sigma + \frac{3}{2}S_\sigma T_\sigma - p_\sigma \nabla \cdot \mathbf{v}_\sigma \right) + \nabla \cdot \left( \frac{3}{2}D_\sigma T_\sigma \nabla n_\sigma + \frac{5}{2}\chi_\sigma n_\sigma \nabla T_\sigma \right). \quad (2.33)$$

If we assume  $D_\sigma \approx \frac{5}{3}\chi_\sigma$ <sup>1</sup> and let the new notations of the effective thermal diffusivity and the power source term be

$$\chi_\sigma \leftarrow \frac{5}{3}\chi_\sigma \approx D_\sigma, \quad P_\sigma \leftarrow P_\sigma + \frac{3}{2}S_\sigma T_\sigma - p_\sigma \nabla \cdot \mathbf{v}_\sigma, \quad (2.34)$$

then the energy conservation equation becomes

$$\begin{aligned} \frac{\partial U_\sigma}{\partial t} &= P_\sigma + \nabla \cdot \left( \frac{3}{2}\chi_\sigma T_\sigma \nabla n_\sigma + \frac{3}{2}\chi_\sigma n_\sigma \nabla T_\sigma \right) \\ &= P_\sigma + \nabla \cdot (\chi_\sigma \nabla U_\sigma). \end{aligned} \quad (2.35)$$

---

<sup>1</sup>This assumption allows us avoiding handling densities and temperatures at the interface, which are not available in the multinodal model.

### Core Energy Balance Equation

For the core node, let the volume-averaged energy density, net energy source, and energy transport term be

$$\bar{U}_\sigma^{\text{core}} = \frac{1}{V_{\text{core}}} \int_{V_{\text{core}}} U_\sigma dV, \quad (2.36)$$

$$\bar{P}_\sigma^{\text{core}} = \frac{1}{V_{\text{core}}} \int_{V_{\text{core}}} P_\sigma dV, \quad (2.37)$$

$$\bar{P}_{\sigma,\text{tran}}^{\text{core}} = \frac{1}{V_{\text{core}}} \int_{V_{\text{core}}} \nabla \cdot (\chi_\sigma \nabla U_\sigma) dV. \quad (2.38)$$

The volume-averaged energy conservation equation or the energy balance equation for the core node is

$$\frac{d\bar{U}_\sigma^{\text{core}}}{dt} = \bar{P}_\sigma^{\text{core}} + \bar{P}_{\sigma,\text{tran}}^{\text{core}}. \quad (2.39)$$

By following a similar method as the particle balance equation, internodal energy transport times between core and edge nodes are defined as

$$\tau_{E,\sigma}^{\text{core} \rightarrow \text{edge}} = \frac{V_{\text{core}} \Delta r_{\text{core-edge}}}{A_{\text{core}} \chi_\sigma^{\text{core}}} = \frac{r_{\text{core}}^2}{2r_{\text{core}}} \frac{\Delta r_{\text{core-edge}}}{\chi_\sigma^{\text{core}}}, \quad (2.40)$$

$$\tau_{E,\sigma}^{\text{edge} \rightarrow \text{core}} = \frac{V_{\text{edge}} \Delta r_{\text{core-edge}}}{A_{\text{core}} \chi_\sigma^{\text{core}}} = \frac{r_{\text{edge}}^2 - r_{\text{core}}^2}{2r_{\text{core}}} \frac{\Delta r_{\text{core-edge}}}{\chi_\sigma^{\text{core}}}, \quad (2.41)$$

where  $\chi_\sigma^{\text{core}}$  is the thermal diffusivity at the surface  $A_{\text{core}}$  between the core and edge nodes.

The energy transport term in the core node is

$$\bar{P}_{\sigma,\text{tran}}^{\text{core}} = -\frac{\bar{U}_\sigma^{\text{core}} - \bar{U}_\sigma^{\text{edge}}}{\tau_{E,\sigma}^{\text{core} \rightarrow \text{edge}}} = -\frac{\bar{U}_\sigma^{\text{core}}}{\tau_{E,\sigma}^{\text{core} \rightarrow \text{edge}}} + \frac{V_{\text{edge}}}{V_{\text{core}}} \frac{\bar{U}_\sigma^{\text{edge}}}{\tau_{E,\sigma}^{\text{edge} \rightarrow \text{core}}}. \quad (2.42)$$



### Edge Energy Balance Equation

Similarly, the energy balance equation for the edge node is

$$\frac{d\bar{U}_\sigma^{\text{edge}}}{dt} = \bar{P}_\sigma^{\text{edge}} + \bar{P}_{\sigma,\text{tran}}^{\text{edge}}. \quad (2.43)$$

Let internodal energy transport times between edge and SOL nodes be

$$\tau_{E,\sigma}^{\text{edge} \rightarrow \text{sol}} = \frac{V_{\text{edge}} \Delta r_{\text{edge-sol}}}{A_{\text{edge}} \chi_\sigma^{\text{edge}}} = \frac{r_{\text{edge}}^2 - r_{\text{core}}^2}{2r_{\text{edge}}} \frac{\Delta r_{\text{edge-sol}}}{\chi_\sigma^{\text{edge}}}, \quad (2.44)$$

$$\tau_{E,\sigma}^{\text{sol} \rightarrow \text{edge}} = \frac{V_{\text{sol}} \Delta r_{\text{edge-sol}}}{A_{\text{edge}} \chi_\sigma^{\text{edge}}} = \frac{r_{\text{sol}}^2 - r_{\text{edge}}^2}{2r_{\text{edge}}} \frac{\Delta r_{\text{edge-sol}}}{\chi_\sigma^{\text{edge}}}, \quad (2.45)$$

where  $\chi_\sigma^{\text{edge}}$  is the thermal diffusivity at the surface  $A_{\text{edge}}$  between the edge and SOL nodes.

The energy transport term in the edge node is

$$\begin{aligned} \bar{P}_{\sigma,\text{tran}}^{\text{edge}} &= -\frac{\bar{U}_\sigma^{\text{edge}} - \bar{U}_\sigma^{\text{core}}}{\tau_{E,\sigma}^{\text{edge} \rightarrow \text{core}}} - \frac{\bar{U}_\sigma^{\text{edge}} - \bar{U}_\sigma^{\text{sol}}}{\tau_{E,\sigma}^{\text{edge} \rightarrow \text{sol}}} \\ &= -\frac{\bar{U}_\sigma^{\text{edge}}}{\tau_{E,\sigma}^{\text{edge} \rightarrow \text{core}}} + \frac{V_{\text{core}}}{V_{\text{edge}}} \frac{\bar{U}_\sigma^{\text{core}}}{\tau_{E,\sigma}^{\text{core} \rightarrow \text{edge}}} - \frac{\bar{U}_\sigma^{\text{edge}}}{\tau_{E,\sigma}^{\text{edge} \rightarrow \text{sol}}} + \frac{V_{\text{sol}}}{V_{\text{edge}}} \frac{\bar{U}_\sigma^{\text{sol}}}{\tau_{E,\sigma}^{\text{sol} \rightarrow \text{edge}}}. \end{aligned} \quad (2.46)$$

Again, with the assumption  $\tau_{E,\sigma}^{\text{sol} \rightarrow \text{edge}} \rightarrow \infty$ , the energy transport term is simplified to

$$\begin{aligned} \bar{P}_{\sigma,\text{tran}}^{\text{edge}} &= \frac{V_{\text{core}}}{V_{\text{edge}}} \frac{\bar{U}_\sigma^{\text{core}} - \bar{U}_\sigma^{\text{edge}}}{\tau_{E,\sigma}^{\text{core} \rightarrow \text{edge}}} - \frac{\bar{U}_\sigma^{\text{edge}}}{\tau_{E,\sigma}^{\text{edge} \rightarrow \text{sol}}} \\ &= -\frac{\bar{U}_\sigma^{\text{edge}}}{\tau_{E,\sigma}^{\text{edge} \rightarrow \text{core}}} + \frac{V_{\text{core}}}{V_{\text{edge}}} \frac{\bar{U}_\sigma^{\text{core}}}{\tau_{E,\sigma}^{\text{core} \rightarrow \text{edge}}} - \frac{\bar{U}_\sigma^{\text{edge}}}{\tau_{E,\sigma}^{\text{edge} \rightarrow \text{sol}}}. \end{aligned} \quad (2.47)$$

### SOL Energy Balance Equation

Also, the energy balance equation for the SOL node is

$$\frac{d\bar{U}_\sigma^{\text{sol}}}{dt} = \bar{P}_\sigma^{\text{sol}} + \bar{P}_{\sigma,\text{tran}}^{\text{sol}}, \quad (2.48)$$

where the energy transport term in the SOL node is

$$\bar{P}_{\sigma, \text{tran}}^{\text{sol}} = -\frac{\bar{U}_{\sigma}^{\text{sol}}}{\tau_{E, \sigma}^{\text{sol} \rightarrow \text{edge}}} + \frac{V_{\text{edge}}}{V_{\text{sol}}} \frac{\bar{U}_{\sigma}^{\text{edge}}}{\tau_{E, \sigma}^{\text{edge} \rightarrow \text{sol}}} - \frac{\bar{U}_{\sigma}^{\text{sol}}}{\tau_{E, \sigma}^{\text{sol} \rightarrow \text{div}}} \approx \frac{V_{\text{edge}}}{V_{\text{sol}}} \frac{\bar{U}_{\sigma}^{\text{edge}}}{\tau_{E, \sigma}^{\text{edge} \rightarrow \text{sol}}} - \frac{\bar{U}_{\sigma}^{\text{sol}}}{\tau_{E, \sigma}^{\text{sol} \rightarrow \text{div}}}. \quad (2.49)$$

The  $\tau_{E, \sigma}^{\text{sol} \rightarrow \text{div}}$  is the effective energy confinement time of the SOL node, which is calculated from

$$\tau_{E, \sigma}^{\text{sol} \rightarrow \text{div}} = \frac{V_{\text{sol}} \Delta r_{\text{sol-div}}}{A_{\text{sol}} \chi_{\sigma}^{\text{sol}}} = \frac{r_{\text{sol}}^2 - r_{\text{edge}}^2}{2r_{\text{sol}}} \frac{\Delta r_{\text{sol-div}}}{\chi_{\sigma}^{\text{sol}}}. \quad (2.50)$$

### 2.2.3 Particle and Thermal Diffusivities

In order to calculate internodal transport times, the formulas of particle and thermal diffusivities are required. Much research [14, 15, 16, 17, 18, 19, 20, 21, 22, 23, 24, 25, 26, 27, 28] has been done for this topic. One comprehensive empirical scaling for the effective thermal diffusivity in the ELMy H-mode tokamak plasma compatible with the ITER H-92 P(y) [18] is

$$\begin{aligned} \chi_{H92}(\rho) &= \alpha_H B_T^{-5/2} n_e(\rho)^{3/4} T_e(\rho) |\nabla T_e(\rho)|^{1/2} q(\rho)^{9/4} \\ &\times \epsilon(\rho)^{7/8} \kappa(\rho)^{-2} M^{-1} A^{-1/8} a^{-1/2} \text{ (m}^2/\text{s)}, \end{aligned} \quad (2.51)$$

where the coefficient  $\alpha_H = 3.08$ , normalized radius  $\rho = r/a$ , toroidal magnetic field  $B_T$  in T, electron density  $n_e$  in  $10^{19} \text{ m}^{-3}$ , electron temperature  $T_e$  in keV, electron temperature gradient  $\nabla T_e$  in keV/m, safety factor  $q = q_{\psi}$ , local toroidicity  $\epsilon = r/R$ , local elongation  $\kappa$ , hydrogenic atomic mass number  $M$ , aspect ratio  $A = R/a$ , and minor radius  $a$  in m. Another empirical scaling compatible with the ITER H-98 P(y,2) [17] is

$$\begin{aligned} \chi_{H98}(\rho) &= \alpha_H B_T^{-3.5} n_e(\rho)^{0.9} T_e(\rho) |\nabla T_e(\rho)|^{1.2} q(\rho)^{3.0} \\ &\times \kappa(\rho)^{-2.9} M^{-0.6} R^{0.7} a^{-0.2} \text{ (m}^2/\text{s)}, \end{aligned} \quad (2.52)$$

where the coefficient  $\alpha_H = 0.123$ . The particle and thermal diffusivities for electrons and ions [18] are computed by

$$\chi_e(\rho) = \chi_i(\rho) = \chi_{H92}(\rho) \quad (\text{or } \chi_{H98}(\rho)), \quad (2.53)$$

$$D_i(\rho) = 0.3(\chi_e(\rho) + \chi_i(\rho)) = 0.6\chi_{H92}(\rho) \quad (\text{or } 0.6\chi_{H98}(\rho)). \quad (2.54)$$

In the multinodal model, the particle diffusivity  $D_{\text{node}}$  and the thermal diffusivity  $\chi_{\text{node}}$  are evaluated at their corresponding internodal surfaces. The electron density  $n_e(\rho)$  and temperature  $T_e(\rho)$  are replaced by the corresponding  $n_e^{\text{node}}$  and  $T_e^{\text{node}}$ , and  $\nabla T_e(\rho)$  is approximated by a finite difference scheme between nodes. We will revisit the diffusivity formula when we discuss the computational methods in the next chapter.

## 2.3 Sources and Sinks

In this section, several important sources and sinks of particles and energies in the multinodal model are presented. These terms include external particle sources, ohmic and auxiliary heating, fusion alpha heating, radiation, Coulomb collisional energy transfer, ion orbit loss, and atomic and molecular processes. The superscript “node” is used for a general node. Some global source and sink terms for the whole plasma are also discussed, which could occasionally be used as approximations for the corresponding nodal terms.

### 2.3.1 External Particle Sources

The external particle source  $S_{\sigma,\text{ext}}^{\text{node}}$  represents one species  $\sigma$  particles from the outside of the tokamak plasma. Main external particle sources include neutral beam injection (NBI) and gas puffing (GAS), i.e.,

$$S_{\sigma,\text{ext}}^{\text{node}} = S_{\sigma,\text{NBI}}^{\text{node}} + S_{\sigma,\text{GAS}}^{\text{node}}. \quad (2.55)$$

The global external particle sources for deuterons [10] are calculated by

$$S_{D,NBI} = \frac{P_{NBI}}{E_{b0}V}, \quad S_{D,gas} = \frac{GAS \cdot N_A}{C_{gas}R_{gas}V}, \quad (2.56)$$

where  $P_{NBI}$  is the total injected neural beam power,  $E_{b0}$  is the initial beam energy, GAS is the calibrated gasflow in the unit of Torr · L/s,  $N_A$  is the Avogadro constant,  $R_{gas}$  is the gas constant,  $C_{gas}$  is the inverse of the gas puffing efficiency, and  $V$  is the plasma volume. Here,  $E_{b0} = 80$  keV is used for the DIII-D tokamak, and  $E_{b0} = 1$  MeV is for the ITER. Besides, the constant  $C_{gas} = 150$  [10] or  $C_{gas} = 200$  [29] can be used for the gas puffing.

When the deposition profiles are available, the nodal external particle sources are calculated by integrating the deposition profile over the node. For example, the nodal particle source from NBI [11] is

$$S_{\sigma,NBI}^{node} = \frac{1}{V_{node}} \sum_k \frac{F_{k,\sigma}}{E_{b0,k}} \int_{V_{node}} \frac{dP_{NBI,k}}{d\rho} d\rho, \quad (2.57)$$

where  $V_{node}$  is the volume of the node,  $k$  indicates the beam component,  $E_{b0,k}$  is the energy of the beam component  $k$ ,  $F_{k,\sigma}$  is the fraction of beam particles to species  $\sigma$ , and  $dP_{NBI,k}/d\rho$  is the total radial NBI power deposition profile. Similarly, the nodal particle source from shattered pellet injection (SPI) (or similarly gas puffing) [11] is

$$S_{\sigma,SPI}^{node} = \frac{F_{p,\sigma}}{V_{node}} \int_{V_{node}} \frac{dS_{SPI}}{d\rho} d\rho, \quad (2.58)$$

where  $F_{p,\sigma}$  is the fraction of species  $\sigma$  in pellets and  $dS_{SPI}/d\rho$  is the total radial SPI particle deposition profile.

In this research, one exponential fitting for the gas puffing source profile [29] is used as

$$S_{GAS} = S_{GAS,max} 10^{-20(1-\rho)}, \quad 0 \leq \rho \leq 1, \quad (2.59)$$

where  $S_{GAS,max}$  is the maximum particle injection rate at the edge, and  $\rho$  is the normalized

radius. This profile is shown in the Figure 2.2, which is used for calculating nodal particle source by the Equation 2.72.

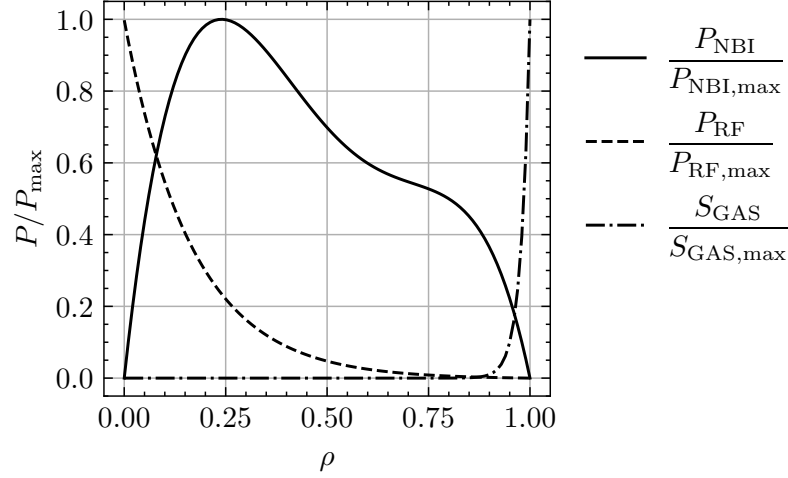


Figure 2.2: Several important deposition profiles in the tokamak plasma, where neutral beam injection and cyclotron heating power deposition profiles are fitted from Kessel et al. [30], and gas puffing profile is fitted from Baylor et al. [29].

### 2.3.2 Ohmic and Auxiliary Heating

In order to heat plasmas to a high enough temperature for fusion reactions, additional heating methods are required. The most common energy sources include ohmic heating, neutral beam injection (NBI), and radiofrequency (RF) radiation, where RF heating includes ion cyclotron heating (ICH), electron cyclotron heating (ECH), and lower hybrid heating (LH) [31, 32]. Among these heating methods, the ohmic heating  $P_{\Omega}^{\text{node}}$  supplies energy for electrons only, while the auxiliary heating terms can be included for both ions and electrons:

$$P_{i,\text{aux}}^{\text{node}} = P_{i,\text{NBI}}^{\text{node}} + P_{i,\text{ICH}}^{\text{node}}, \quad (2.60)$$

$$P_{e,\text{aux}}^{\text{node}} = P_{e,\text{NBI}}^{\text{node}} + P_{e,\text{ECH}}^{\text{node}} + P_{\sigma,\text{LH}}^{\text{node}}. \quad (2.61)$$

For the ohmic heating term, the global ohmic heating power  $P_{\Omega}$  can be accessed directly from the experiment data of DIII-D, where this global one can approximate the nodal term:

$$P_{\Omega}^{\text{node}} = P_{\Omega}. \quad (2.62)$$

For ITER, the ohmic heating power [33] is computed by

$$P_{\Omega}^{\text{node}} \text{ (W/m}^3\text{)} = 2.8 \times 10^{-9} \frac{Z_{\text{eff}} I_P^2}{a^4 T_e^{3/2}}, \quad (2.63)$$

where  $Z_{\text{eff}}$  is the effective atomic number, the plasma current  $I_P$  is in A, the minor radius  $a$  in m, and the nodal electron temperature  $T_e = T_e^{\text{node}}$  in keV.

The neutral beam injection (NBI) powers are gotten by multiplying the total NBI power  $P_{\text{NBI}}$  with the fraction of energy to one species. The fraction of the initial beam energy to ions [34] is

$$f_{bi} = \frac{1}{E_{b0}} \int P_i dt = \phi(E_{b0}/E_c), \quad (2.64)$$

where  $E_{b0}$  is the initial beam energy ( $E_{b0} \approx 80$  keV for the DIII-D tokamak, and  $E_{b0} \approx 1$  MeV for ITER),  $E_c$  is the critical beam energy [34] by

$$E_c = \left( \frac{3\sqrt{\pi}}{4} \right)^{2/3} \left( \frac{m_i}{m_e} \right)^{1/3} \frac{m_b T_e}{m_i}, \quad (2.65)$$

and the function  $\phi(x)$  [34] is

$$\phi(x) = \frac{1}{x} \left[ \frac{1}{3} \ln \frac{1 - x^{1/2} + x}{(1 + x^{1/2})^2} + \frac{2}{\sqrt{3}} \left( \tan^{-1} \frac{2x^{1/2} - 1}{\sqrt{3}} + \frac{\pi}{6} \right) \right]. \quad (2.66)$$

The NBI power fraction for electrons is gotten by  $f_{be} = 1 - f_{bi}$ . Hence,

$$P_{i,\text{NBI}} = f_{bi} \frac{P_{\text{NBI}}}{V}, \quad P_{e,\text{NBI}} = f_{be} \frac{P_{\text{NBI}}}{V}. \quad (2.67)$$

Then the NBI power to ions is distributed among different species by their particle densities.

Similarly, the nodal power sources are calculated by integrating them when the deposi-

tion profiles are available. The nodal NBI power [11] is

$$P_{\sigma, \text{NBI}}^{\text{node}} = \frac{1}{V_{\text{node}}} \sum_k \frac{U_{k, \sigma}}{E_{b0, k}} \int_{V_{\text{node}}} \frac{dP_{\text{NBI}, k}}{d\rho} d\rho, \quad (2.68)$$

where  $U_{k, \sigma}$  is the fraction of energy from beam particle  $k$  to species  $\sigma$ . Also, the nodal RF heating [11] is

$$P_{\sigma, \text{RF}}^{\text{node}} = \frac{F_{\text{RF}, \sigma}}{V_{\text{node}}} \int_{V_{\text{node}}} \frac{dP_{\text{RF}}}{d\rho} d\rho, \quad (2.69)$$

where  $F_{\text{RF}, \sigma}$  is the fraction of the deposited RF heating power to species  $\sigma$  and  $dP_{\text{RF}}/d\rho$  is the total radial RF power deposition profile.

In this research, predetermined deposition profiles of auxiliary heating powers are utilized. Suppose the power density from one energy source  $x$  is  $P_x(\rho)$ , and the total power is  $P_{x, \text{tot}}$ . Thus,

$$\begin{aligned} P_{x, \text{tot}} &= \int_0^a P_x(r) 2\pi R_0 \cdot 2\pi r dr = 4\pi^2 a^2 R_0 \int_0^1 P_x(\rho) \rho d\rho \\ &= 4\pi^2 a^2 R_0 P_{x, \text{max}} \int_0^1 p(\rho) \rho d\rho, \end{aligned} \quad (2.70)$$

where  $p(\rho)$  is the normalized power profile function and can be determined by simulations (e.g., TSC [35], ASTRA [36], and ONETWO [37]) or experiments [30, 38, 39]. Hence,

$$P_{x, \text{max}} = \frac{P_{x, \text{tot}}}{4\pi^2 a^2 R_0 \int_0^1 p(\rho) \rho d\rho} = \frac{P_{x, \text{tot}}}{V} \frac{1}{2 \int_0^1 p(\rho) \rho d\rho}. \quad (2.71)$$

Therefore, the nodal power density is

$$\begin{aligned} P_x^{\text{node}} &= \frac{1}{V_{\text{node}}} \int_{V_{\text{node}}} P_x(\rho) dV = \frac{1}{V_{\text{node}}} \int_{r_0}^{r_1} P_x(r) 2\pi R_0 \cdot 2\pi r dr \\ &= \frac{4\pi^2 a^2 R_0}{2\pi R_0 \cdot \pi a^2 (\rho_1^2 - \rho_0^2)} \int_{\rho_0}^{\rho_1} P_{x, \text{max}} p(\rho) \rho d\rho \\ &= P_{x, \text{max}} \frac{2}{\rho_1^2 - \rho_0^2} \int_{\rho_0}^{\rho_1} p(\rho) \rho d\rho = \frac{P_{x, \text{tot}}}{V} \frac{1}{\rho_1^2 - \rho_0^2} \frac{\int_{\rho_0}^{\rho_1} p(\rho) \rho d\rho}{\int_0^1 p(\rho) \rho d\rho}. \end{aligned} \quad (2.72)$$

One polynomial fitting for the neutral beam injection (NBI) power deposition profile [30] is

$$P_{\text{NBI}} = P_{\text{NBI,max}} (-20.44\rho^4 + 45.92\rho^3 - 35.89\rho^2 + 10.42\rho), \quad 0 \leq \rho \leq 1, \quad (2.73)$$

which is shown in the Figure 2.2. In addition, one exponential fitting for the cyclotron heating power deposition profile [30] is

$$P_{\text{CH}} = P_{\text{CH,max}} (e^{-6\rho} - e^{-6}), \quad 0 \leq \rho \leq 1, \quad (2.74)$$

which is also shown in the Figure 2.2.

### 2.3.3 Fusion and Alpha Heating

The next term to be considered is the fusion alpha heating. As we mentioned in the introduction, a deuterium-tritium (D-T) fusion generates a 14.1 MeV neutron and a 3.5 MeV alpha particle. While neutrons leave the plasma immediately, alpha particles are confined by the magnetic field and transfer their energy to electrons and ions. Following the neutral beam injection (NBI) formula in the Equation 2.64, the fraction of the initial fusion alpha particle energy to ions [34] is

$$f_{\alpha i} = \frac{1}{E_{\alpha}} \int P_i dt = \phi \left( \frac{E_{\alpha}}{E_c} \right) \approx 0.189, \quad (2.75)$$

where  $E_c = 0.281 \text{ MeV} < E_{\alpha} = 3.5 \text{ MeV}$  for  $T_e = 10 \text{ keV}$ . The illustration of this energy transfer process is shown in the Figure 2.3, where the radiation and transport losses are neglected. From this figure, the energetic alpha particles are found to transfer their energy first to core electrons and then to core ions. The figure shows most fusion heating to electrons for  $t < 0.253 \text{ s}$ . This delay could prevent the thermal instability, where an opportunity is provided to remove the electron energy from the core before electrons heat



the ions then lead to a higher fusion reactivity. The alpha heating from the fusion event is vital to the study of burning dynamics, which should be considered in the multinodal model.

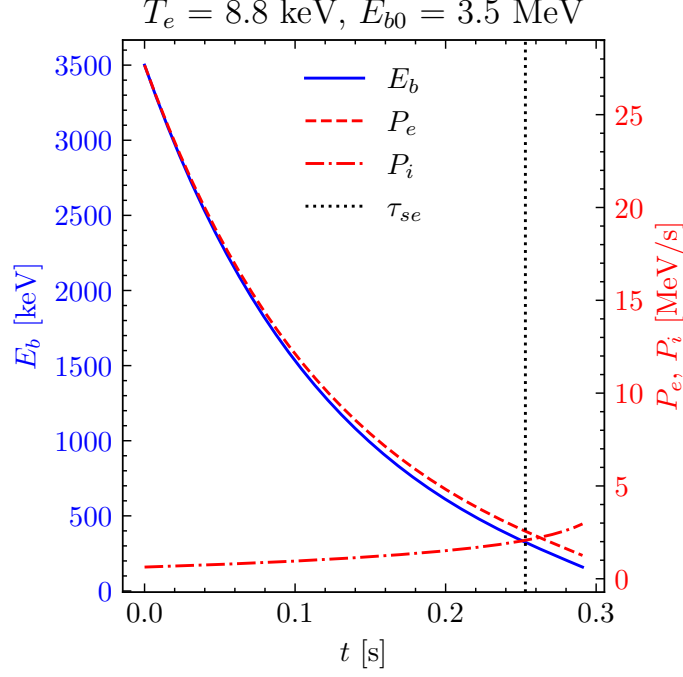


Figure 2.3: Fusion alpha heating without radiation and transport losses for a typical inductive operation scenario of ITER.

Since the threshold energies of D-D and D-<sup>3</sup>He fusions are much higher than the D-T fusion, only the D-T fusion is considered for the multinodal model in this research. The nodal fusion terms for D-T fusion are represented by

$$S_{D,\text{fus}}^{\text{node}} = S_{T,\text{fus}}^{\text{node}} = -n_D^{\text{node}} n_T^{\text{node}} \langle \sigma v \rangle_{\text{fus}}, \quad S_{\alpha,\text{fus}}^{\text{node}} = n_D^{\text{node}} n_T^{\text{node}} \langle \sigma v \rangle_{\text{fus}}, \quad (2.76)$$

$$P_{\sigma,\text{fus}}^{\text{node}} = n_D^{\text{node}} n_T^{\text{node}} \langle \sigma v \rangle_{\text{fus}} U_{f\sigma}, \quad \sigma \in \{D, T, \alpha\}, \quad (2.77)$$

where  $\langle \sigma v \rangle_{\text{fus}}$  is the fusion reactivity evaluated at the nodal ion temperature  $T_i^{\text{node}}$  and computed by the Bosch-Hale fusion reactivity fitting model [4], and  $U_{f\sigma}$  is the energy transferred from fusion alpha particles to the species  $\sigma$  per fusion reaction. However, the main drawback of these fusion power terms is that the fusion energy is assumed being trans-

ferred from the fusion alpha particles to the ions and electrons immediately. The delay effect between fusion alpha heating to electrons and to ions should be considered.

When the delay effect of fusion alpha heating is considered, the nodal fusion power can be written as an integral term of generated alpha particles from previous times multiplying the heating power:

$$P_{\sigma,\text{fus}}^{\text{node}}(t) = \int_{t_0}^t n_{\text{D}}^{\text{node}}(t') n_{\text{T}}^{\text{node}}(t') \langle \sigma v \rangle_{\text{fus}} (T_i^{\text{node}}(t')) P_{\alpha\sigma} (\mathcal{E}_{\alpha}^{\text{node}}(t - t'), T_e^{\text{node}}(t)) dt', \quad (2.78)$$

where  $t$  is the current time,  $t'$  is a previous term to be integrated, and  $t_0$  is the initial time. The  $P_{\alpha\sigma}$  is the power transferred from the fusion alpha particle to the species  $\sigma$ , which depends on the fusion alpha particle energy  $\mathcal{E}_{\alpha}^{\text{node}}$  and the electron temperature  $T_e^{\text{node}}$ . The fusion alpha particle energy can be calculated by the time evolution of beam energy in the NBI heating [34]:

$$\mathcal{E}_b(t) = \mathcal{E}_{b0} \left[ e^{-3t/\tau_{se}} - \left( \frac{\mathcal{E}_c}{\mathcal{E}_{b0}} \right) (1 - e^{-3t/\tau_{se}}) \right]^{2/3}, \quad (2.79)$$

where  $\mathcal{E}_{b0}$  is the initial beam energy at  $t = 0$ ,  $\tau_{se}$  the slowing-down time of beam particles in electrons [34] computed by

$$\tau_{se} = \frac{3(2\pi)^{1/2} T_e^{3/2}}{m_e^{1/2} m_b A_D}, \quad (2.80)$$

with

$$A_D = \frac{ne^4 Z_b^2 Z^2 \ln \Lambda}{2\pi \epsilon_0^2 m_b^2}. \quad (2.81)$$

The beam heating powers to electrons and ions [34] are

$$P_{be} = \frac{2m_e^{1/2} m_b A_D}{3(2\pi)^{1/2} T_e^{3/2}} \mathcal{E}_b, \quad P_{bi} = P_{be} \left( \frac{\mathcal{E}_c}{\mathcal{E}_b} \right)^{3/2}, \quad (2.82)$$

where the critical beam energy [34] is

$$\mathcal{E}_c = \left( \frac{3\sqrt{\pi}}{4} \right)^{2/3} \left( \frac{m_i}{m_e} \right)^{1/3} \frac{m_b}{m_i} T_e, \quad (2.83)$$

and the electron temperature  $T_e$  is evaluated at the current time  $t$ . To avoid solving the integro-differential equation (IDE), we approximate the integral term in the Equation 2.78 by a delayed fusion heating. By a sample computation with ITER conditions, most of fusion alpha particle energy is deposited to electrons at the beginning and to ions around  $\tau_{se}$ . So, we assume the ion temperature increasing linearly in  $[t - \tau_{se}, t]$ . Thus, the fusion reaction rate  $S_{\text{fus}}^{\text{node}}$  for ions is evaluated at

$$T_i^{\text{node}}(t - \tau_{se}) \approx T_i^{\text{node}}(t) - \left. \frac{dT_i^{\text{node}}}{dt} \right|_t \cdot \tau_{se}. \quad (2.84)$$

The delayed fusion reactions then give the fusion heating power  $P_{\sigma, \text{fus}}^{\text{node}}$  to ions.

### 2.3.4 Radiations

Once electrons and ions get energy from the fusion alpha particles, several kinds of radiation can be generated as energy losses. The substantial radiative energy losses in the burning plasma include electron cyclotron radiation (ECR), bremsstrahlung, and impurity radiation (line and recombination radiations), i.e.

$$P_R^{\text{node}} = P_{\text{rad}}^{\text{node}} = P_{\text{ECR}}^{\text{node}} + P_{\text{brem}}^{\text{node}} + P_{\text{imp}}^{\text{node}}. \quad (2.85)$$

These radiations are viewed as instantaneous energy transfer processes from the core to the edge or wall. However, radiations from different regions play various roles in energy coupling between these regions in tokamak plasmas.

### Electron Cyclotron Radiation

In tokamaks, charged particles (ions and electrons) are confined in magnetic fields with a gyro-frequency  $\Omega = -qB/m$  and a gyro-radius  $r_L = v_\perp / |\Omega|$ . When charged particles are centrifugally accelerated, cyclotron radiations can be generated, which are important for sufficiently high-temperature plasmas [11, 1]. The rate of energy loss from a single particle [1, 12] is

$$\frac{dW_{\text{rad}}}{dt} = \frac{e^2}{6\pi\epsilon_0 c^3} \frac{r_L^2 \Omega^4}{\left[1 - \left(\frac{r_L \Omega}{c}\right)^2\right]^2}, \quad (2.86)$$

where  $c$  is the speed of light and  $\epsilon_0$  is the vacuum permittivity. Since

$$\frac{r_{L,e} \Omega_e^2}{r_{L,i} \Omega_i^2} = \frac{v_{\perp,e} e B / m_e}{v_{\perp,i} z_i e B / m_i} = \frac{1}{z_i} \sqrt{\frac{m_i T_e}{m_e T_i}} \frac{m_i}{m_e} \approx \frac{1}{z_i} \left(\frac{m_i}{m_e}\right)^{3/2} \gg 1, \quad (2.87)$$

the electron cyclotron radiation (ECR) is much larger than the ion cyclotron radiation (ICR). In this research, only the ECR is considered.

Albajar et al. [40] proposed a practical formula for ECR in the tokamak including the estimation of wall reflection:

$$P_{\text{syn},r} (\text{W}) = 3.84 \times 10^{-2} (1-r)^{1/2} R_0 a^{1.38} \kappa^{0.79} B_0^{2.62} \left(\frac{n_{e0}}{10^{20}}\right)^{0.38} T_{e0} \\ \times (16 + T_{e0})^{2.61} \left(1 + 0.12 \frac{T_{e0}}{p_{a0}^{0.41}}\right)^{-1.51} K(\alpha_n, \alpha_T, \beta_T) G(A), \quad (2.88)$$

with pre-assumed density and temperature profiles

$$n_e = n_{e0} (1 - \rho^2)^{\alpha_n}, \quad (2.89)$$

$$T_e = (T_{e0} - T_{ea}) (1 - \rho^{\beta_T})^{\alpha_T} + T_{ea}, \quad (2.90)$$

where formal of parameters are

$$p_{a0} = 6.04 \times 10^3 \frac{a}{B_T} \frac{n_{e0}}{10^{20}}, \quad (2.91)$$

$$G(A) = 0.93 (1 + 0.85e^{-0.82A}), \quad (2.92)$$

$$K(\alpha_n, \alpha_T, \beta_T) = (\alpha_n + 3.87\alpha_T + 1.46)^{-0.79} (1.98 + \alpha_T)^{1.36} \beta_T^{2.14} \\ \times (\beta_T^{1.53} + 1.87\alpha_T - 0.16)^{-1.33}, \quad (2.93)$$

the central density  $n_{e0}$  is in  $\text{m}^3$ , the central temperature  $T_{e0}$  is in keV,  $r$  is the wall reflectivity, and  $A$  is the aspect ratio.

By using the practical formula in the Equation 2.88, Hill [11] showed that the power loss from ECR increases with the core temperature and can have a significant effect when the temperature of the core plasma is larger than 30 – 40 keV. Furthermore, this power loss from ECR can lead to greater thermal stability due to its instantaneous negative feedback mechanism. Hence, the ECR term should be considered in the multinodal model.

When the electron temperature is relatively small, the nodal ECR term can be approximated by the global one as

$$P_{\text{ECR}}^{\text{node}} = \frac{P_{\text{syn},r}}{V}, \quad (2.94)$$

where the central density  $n_{e0}$  and temperature  $T_{e0}$  are approximated by the core density  $n_e^{\text{core}}$  and temperature  $T_e^{\text{core}}$ . Also, the estimated parameters [11]  $\alpha_n = 0.5$ ,  $\alpha_T = 8.0$ ,  $\beta_T = 5.0$ , and  $r = 0.8$  can be used.

However, when the electron temperature is high, the more precise calculation is needed for a larger ECR power. From the integration of the density profile in the Equation 2.89 over the whole plasma, there is

$$\frac{V_{\text{core}} n_e^{\text{core}} + V_{\text{edge}} n_e^{\text{edge}}}{V} = 2 \int_0^1 n_e(\rho) \rho d\rho = \frac{n_{e0}}{1 + \alpha_n}. \quad (2.95)$$

Thus, the central density  $n_{e0}$  can be solved by

$$n_{e0} = (1 + \alpha_n) \frac{V_{\text{core}} n_e^{\text{core}} + V_{\text{edge}} n_e^{\text{edge}}}{V}. \quad (2.96)$$

Similarly, by integrating of the temperate profile in the Equation 2.90 over the core node, there is

$$\begin{aligned} T_e^{\text{core}} &= \frac{2}{\rho_{\text{core}}^2} \int_0^{\rho_{\text{core}}} T_e(\rho) \rho \, d\rho = \frac{2}{\rho_{\text{core}}^2} \int_0^{\rho_{\text{core}}} [(T_{e0} - T_{ea}) (1 - \rho^{\beta_T})^{\alpha_T} + T_{ea}] \rho \, d\rho \\ &= \frac{2}{\rho_{\text{core}}^2} (T_{e0} - T_{ea}) \int_0^{\rho_{\text{core}}} (1 - \rho^{\beta_T})^{\alpha_T} \rho \, d\rho + T_{ea} \\ &\equiv \frac{2I_1}{\rho_{\text{core}}^2} (T_{e0} - T_{ea}) + T_{ea}. \end{aligned} \quad (2.97)$$

Also, in the edge node, there is

$$\begin{aligned} T_e^{\text{edge}} &= \frac{2}{\rho_{\text{edge}}^2 - \rho_{\text{core}}^2} \int_{\rho_{\text{core}}}^{\rho_{\text{edge}}} T_e(\rho) \rho \, d\rho \\ &= \frac{2}{\rho_{\text{edge}}^2 - \rho_{\text{core}}^2} \int_{\rho_{\text{core}}}^{\rho_{\text{edge}}} [(T_{e0} - T_{ea}) (1 - \rho^{\beta_T})^{\alpha_T} + T_{ea}] \rho \, d\rho \\ &= \frac{2}{\rho_{\text{edge}}^2 - \rho_{\text{core}}^2} (T_{e0} - T_{ea}) \int_{\rho_{\text{core}}}^{\rho_{\text{edge}}} (1 - \rho^{\beta_T})^{\alpha_T} \rho \, d\rho + T_{ea} \\ &\equiv \frac{2I_2}{\rho_{\text{edge}}^2 - \rho_{\text{core}}^2} (T_{e0} - T_{ea}) + T_{ea}. \end{aligned} \quad (2.98)$$

Thus, the central and boundary temperatures can be solved from

$$T_{e0} = \frac{\rho_{\text{core}}^2 (\rho_{\text{core}}^2 - \rho_{\text{edge}}^2 + 2I_2)}{2\rho_{\text{core}}^2 (I_1 + I_2) - 2I_1 \rho_{\text{edge}}^2} T_e^{\text{core}} + \frac{(\rho_{\text{core}}^2 - \rho_{\text{edge}}^2) (2I_1 - \rho_{\text{core}}^2)}{2\rho_{\text{core}}^2 (I_1 + I_2) - 2I_1 \rho_{\text{edge}}^2} T_e^{\text{edge}}, \quad (2.99)$$

$$T_{ea} = \frac{I_2 \rho_{\text{core}}^2}{\rho_{\text{core}}^2 (I_1 + I_2) - I_1 \rho_{\text{edge}}^2} T_e^{\text{core}} + \frac{I_1 (\rho_{\text{core}}^2 - \rho_{\text{edge}}^2)}{\rho_{\text{core}}^2 (I_1 + I_2) - I_1 \rho_{\text{edge}}^2} T_e^{\text{edge}}, \quad (2.100)$$

where integrals are

$$I_1 = \int_0^{\rho_{\text{core}}} (1 - \rho^{\beta_T})^{\alpha_T} \rho \, d\rho, \quad I_2 = \int_{\rho_{\text{core}}}^{\rho_{\text{edge}}} (1 - \rho^{\beta_T})^{\alpha_T} \rho \, d\rho. \quad (2.101)$$

Then, the shape parameters  $\alpha_n = 0.037$ ,  $\alpha_T = 1.027$ , and  $\beta_T = 1.194$  are fitted from typical electron density and temperature profiles in the ITER inductive operation, which are shown in the Figure 2.4. Similarly, the shape parameters  $\alpha_n = 0.102$ ,  $\alpha_T = 4.079$ , and  $\beta_T = 3.278$  for the ITER non-inductive operation are shown in the Figure 2.5. Moreover, a ECR power profile is fitted from Albajar et al. [41] as

$$\frac{dP_{\text{ECR}}}{dV} \text{ (MW/m}^3\text{)} = -1.333\rho^4 + 3.314\rho^3 - 2.335\rho^2 + 0.118\rho + 0.238. \quad (2.102)$$

This ECR power profile is integrated and normalized to fractions of ECR power to the core and edge nodes, i.e.,  $f_{\text{ECR}}^{\text{core}}$  and  $f_{\text{ECR}}^{\text{edge}}$ . Hence, the nodal ECR power is computed by

$$P_{\text{ECR}}^{\text{core}} = f_{\text{ECR}}^{\text{core}} P_{\text{ECR}}, \quad P_{\text{ECR}}^{\text{edge}} = f_{\text{ECR}}^{\text{edge}} P_{\text{ECR}}, \quad (2.103)$$

where  $P_{\text{ECR}}$  is the global ECR power density with the central density in the Equation 2.96 and the central temperature in the Equation 2.99.

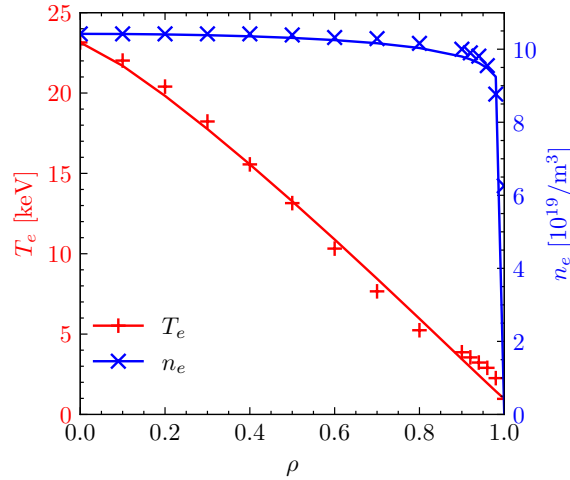


Figure 2.4: Electron temperature and density profiles fitted for the electron cyclotron radiation (ECR) calculation, where  $T_e$  and  $n_e$  are the typical electron temperatures and densities in the ITER inductive operation [31, 7].

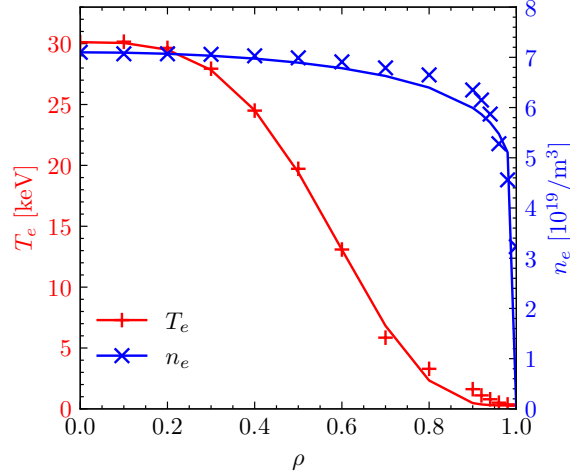


Figure 2.5: Electron temperature and density profiles fitted for the electron cyclotron radiation (ECR) calculation, where  $T_e$  and  $n_e$  are the typical electron temperatures and densities in the ITER non-inductive operation [7].

### *Bremsstrahlung and Impurity Radiations*

Radiations from electrons interacting with fusion ions and impurities are important energy sinks. These radiations will decrease the temperature of electrons, decreasing the ion temperature and limiting the thermal excursion.

When one charged particle is decelerated by a collision with another one, bremsstrahlung can happen, where a photon is produced for the energy loss. Since radiation fields from two one-kind particles are canceled [1], only the electron-ion collisions can generate bremsstrahlung. The power of bremsstrahlung radiation [1] is calculated from

$$P_{\text{brem}}^{\text{node}} = P_{\text{brem}} \text{ (W/m}^3\text{)} = 1.7 \times 10^{-38} z_{\text{eff}}^2 n_i n_e T_e^{1/2}, \quad (2.104)$$

where  $T_e$  is the electron temperature in keV and

$$z_{\text{eff}}^2 = \sum_{j \neq e} \frac{n_j z_j^2}{n_i} = \frac{n_i z_i^2}{n_i} + \frac{n_z z_z^2}{n_i} \quad (2.105)$$

is the effective atomic number.



Both fusion reactions and sputtering from walls bring impurity particles into the plasma. Those impurities can be partially ionized. When plasma electrons collide with partially ionized atoms, the electrons of these ions can be excited to higher states, followed by the de-excitation to lower states with emissions of energetic photons, which lead to line radiations. Also, free plasma electrons can recombine with these partially ionized atoms and emit photons, which give recombination radiations. Usually, elements with high atomic numbers have higher level radiations than the lower ones [1]. The impurity radiation [1, 42, 43] is calculated by

$$P_{\text{imp}}^{\text{node}} = P_{\text{imp}} \left( \text{W/m}^3 \right) = \sum_z (1 + 0.3T_e) \times 10^{-37} n_e n_z z^{3.7-0.33 \ln T_e}, \quad (2.106)$$

where  $T_e$  is in keV,  $z$  is the atomic number of the impurity ions, and the other quantities are in mks units.

Mandrekas et al. [44] simulated ITER Engineering Design Activities (EDA) model with self-consistent coupled transport scrape-off layer and divertor calculations. Their results suggest that impurity radiation can be considered to solve the divertor heat load problem in ITER. Becker [45] explored the confinement in the ignited ITER EDA by self-consistent calculations with a 1.5-D predictive transport code. This research shows a significant radiative loss from the confinement zone by bremsstrahlung. Pütterich et al. [46] calculated cooling factors for multiple elements from H to Bi at  $n_e = 5 \times 10^{19} \text{ m}^{-3}$  via ADAS. Pütterich et al. [46] also concluded a coarse reactor model is able to model impurities effectively. Besides, Hill [11] suggested active impurity seeding can be a possible way of controlling burn conditions. These conclusions prompt us to include impurity radiations into the multinodal model.

### 2.3.5 Collisional Energy Transfer

Coulomb collisions transfer energy between charged particles. Since the collision between one kind of species does not change the average species temperature, only the collisional energy transfer between different species is considered. The collisional energy transfer to the species  $\sigma$  is

$$Q_{\sigma}^{\text{node}} = \sum_{\sigma' \neq \sigma} Q_{\sigma\sigma'}^{\text{node}}, \quad (2.107)$$

where  $Q_{\sigma\sigma'}^{\text{node}} \equiv Q_{\sigma' \rightarrow \sigma}^{\text{node}}$  is the collisional energy transfer from the species  $\sigma'$  to the species  $\sigma$ .

For the collisions between ion species, the rate of collisional energy transfer from the species  $i'$  to  $i$  is

$$Q_{ii'} = \frac{3}{2} n_i (T_{i'} - T_i) \nu_{ii'}, \quad (2.108)$$

where the characteristic frequency for energy transfer between ions [1, 47] is

$$\begin{aligned} \nu_{ii'} &= \frac{2m_i}{m_i + m_{i'}} \frac{\sqrt{2}}{3\sqrt{\pi}} \left( \frac{q_i q_{i'}}{4\pi\epsilon_0} \right)^2 \frac{4\pi n_{i'}}{m_i T_i^{3/2}} \left( \frac{m_i m_{i'}}{m_i + m_{i'}} \right)^{1/2} \ln \Lambda_i, \\ &= \frac{2\sqrt{2}}{3\sqrt{\pi}} \left( \frac{q_i q_{i'}}{4\pi\epsilon_0} \right)^2 \frac{4\pi n_{i'}}{T_i^{3/2}} \frac{(m_i m_{i'})^{1/2}}{(m_i + m_{i'})^{3/2}} \ln \Lambda_i. \end{aligned} \quad (2.109)$$

This term is used for the collisional energy transfer between deuterons, tritons, and alpha particles, such as  $Q_{\alpha D}^{\text{node}}$ ,  $Q_{\alpha T}^{\text{node}}$ , and  $Q_{DT}^{\text{node}}$ .

When the collisions between ions and electrons are considered, the rate of ion-electron collisional energy transfer  $Q_{ie}$  [1] (from electrons to ions) is used:

$$Q_{ie} = \frac{n_i n_e (q_i q_e)^2 m_e \ln \Lambda \left( 1 - \frac{T_i}{T_e} \right)}{2\pi\epsilon_0^2 (2\pi m_e T_e)^{1/2} m_i \left[ 1 + \frac{4\sqrt{\pi}}{3} \left( \frac{3m_e T_i}{2m_i T_e} \right)^{3/2} \right]}, \quad (2.110)$$

and  $Q_{ei} = -Q_{ie}$ , where  $\ln \Lambda$  is the Coulomb logarithm. The  $Q_{ie}^{\text{node}}$  term is positive when  $T_i^{\text{node}} < T_e^{\text{node}}$  and negative when  $T_i^{\text{node}} > T_e^{\text{node}}$ . This term is applied for the collisional

energy transfer between ions and electrons, such as  $Q_{De}^{\text{node}}$ ,  $Q_{Te}^{\text{node}}$ , and  $Q_{\alpha e}^{\text{node}}$ .

To compute the collisional energy transfer, the Coulomb logarithm is needed. When temperatures among different species are approximately same, we apply [1]

$$\ln \Lambda = \ln \left[ 12\pi \sqrt{\frac{(\epsilon_0 T)^3}{n_e q_e^4 q_i^2}} \right], \quad (2.111)$$

where  $T$  is the common temperature, and  $q$  is the charge. However, when species have much different temperatures, the classical Coulomb logarithm for collisions between species [48] is

$$\begin{aligned} \ln \Lambda &= \ln \left[ 12\pi \left( \frac{\epsilon_0}{e} \right)^{3/2} \right] - \ln \left[ \frac{Z_1 Z_2 (A_1 + A_2)}{A_2 T_1 + A_1 T_2} \sqrt{\frac{n_*}{T_*}} \right] \\ &= 30.37 - \ln (Z_1 Z_2) - \ln \left[ \frac{A_1 + A_2}{A_2 T_1 + A_1 T_2} \sqrt{\frac{n_*}{T_*}} \right], \end{aligned} \quad (2.112)$$

where  $A$  is the mass number with respect to the proton mass, densities in  $\text{m}^{-3}$ , temperatures in eV, and

$$\frac{n_*}{T_*} = \frac{n_e}{T_e} + \sum_i \frac{Z_i^2 n_i}{T_i}. \quad (2.113)$$

### 2.3.6 Ion Orbit Loss

Ion orbit loss (IOL) [49, 50, 51, 52, 53, 54, 55] stands for one kind of ion loss. Ions on passing or banana-trapped orbits can leave the plasma by drifting outward across the last closed flux surface (LCFS), which is called the standard IOL. Another kind of IOL is for the ion loss through the X-point in the diverted plasma, which is called the X-loss IOL. We only consider the standard IOL in the multinodal model, but the X-loss IOL could be included in the future.

To compute the IOL terms in the multinodal model, the loss fractions are needed. The

ion particle loss fraction for the Maxwellian velocity distribution [49, 51] is

$$F_{\text{orb}} = \frac{\int_{-1}^1 \Gamma(3/2, \epsilon_{\min}(\rho_0, \zeta_0)) d\zeta_0}{2\Gamma(3/2)}, \quad (2.114)$$

where  $\zeta_0 = V_{\parallel 0}/V_0$  is the direction cosine,

$$\epsilon_{\min}(\rho_0, \zeta_0) = \frac{E_{\min}(\rho_0, \zeta_0)}{kT_i(\rho_0)} = \frac{mV_{\min}^2(\rho_0, \zeta_0)}{2kT_i(\rho_0)} \quad (2.115)$$

is the reduced energy corresponding to the minimum velocity of the IOL,  $\Gamma(n)$  is the gamma function, and  $\Gamma(n, x)$  is the upper incomplete gamma function. Similarly, the energy loss fraction [49, 51] is

$$E_{\text{orb}} = \frac{\int_{-1}^1 \Gamma(5/2, \epsilon_{\min}(\rho_0, \zeta_0)) d\zeta_0}{2\Gamma(5/2)}. \quad (2.116)$$

The minimum loss energy  $E_{\min}(\rho_0, \zeta_0)$  for ions is determined by proper computation strategies [51]. One method is using the GTEDGE code [51]. where a combination of conversations of canonical toroidal angular momentum, energy, and magnetic momentum is solved. This quadratic equation for the initial ion velocity  $V_0$  [51] is written as

$$\begin{aligned} V_0^2 \left[ \left( \left| \frac{B_s}{B_0} \right| \frac{f_{\phi 0}}{f_{\phi s}} \zeta_0 \right)^2 - 1 + (1 - \zeta_0^2) \left| \frac{B_s}{B_0} \right| \right] + V_0 \left[ \frac{2e(\psi_0 - \psi_s)}{Rm f_{\phi s}} \left( \left| \frac{B_s}{B_0} \right| \frac{f_{\phi 0}}{f_{\phi s}} \zeta_0 \right) \right] \\ + \left[ \left( \frac{e(\psi_0 - \psi_s)}{Rm f_{\phi s}} \right)^2 - \frac{2e(\phi_0 - \phi_s)}{m} \right] = 0, \end{aligned} \quad (2.117)$$

where  $R$  is the major radius,  $\phi$  is the electrostatic potential,  $f_{\phi} = |B_{\phi}/B|$ ,  $\psi$  is the flux surface. From the Ampere's law, the flux surface is calculated from

$$\psi = RA_{\phi} = \frac{1}{2} \left( \frac{\mu_0 I}{2\pi a^2} \right) R_0 r^2 \implies \psi(\rho) = \frac{\mu_0 I R_0}{4\pi} \rho^2. \quad (2.118)$$

The circular flux surface geometry is described as

$$R(r, \theta) = R_0 h(r, \theta), \quad h(r, \theta) = 1 + \frac{r}{R_0} \cos \theta, \quad B_\phi = \frac{B_{\phi 0}}{h(r, \theta)}. \quad (2.119)$$

As an approximation, we solve the Equation 2.117 at  $\zeta_0 = 1$  and take the  $\min_{-\pi \leq \theta_0 \leq \pi} V_0(\zeta_0, \rho_0, \theta_0)$  with average parameters of one shot. Also, the predetermined electrostatic potential profiles in the Appendix C are used. Two sample calculations are shown in the Figure 2.6 for DIII-D and the Figure 2.7 for ITER.

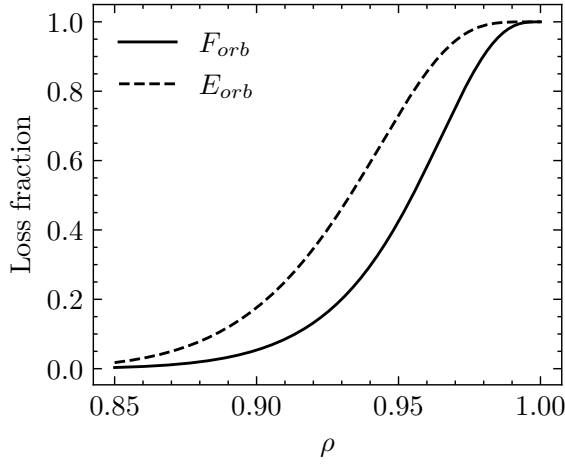


Figure 2.6: Ion particle and energy cumulative loss fractions for DIII-D, where  $I_P = 1.5$  MA,  $R_0 = 1.75$  m,  $a = 0.885$  m,  $T_i = 1$  keV,  $B_{\phi 0} = 1.98$  T, and the electrostatic potential is from the Appendix C.1.

Once the nodal particle and energy loss fractions are calculated from the IOL model, the nodal IOL for ion particles [11] is computed by

$$S_{\sigma, \text{IOL}}^{\text{node}} = - \frac{F_{\sigma, \text{orb}}(\rho_{\text{node}}^{\text{IOL}})}{\tau_{P, \sigma, \text{IOL}}^{\text{node}}} n_{\sigma}^{\text{node}}, \quad (2.120)$$

where  $\rho_{\text{node}}^{\text{IOL}}$  is evaluated at the center of one node,  $\tau_{P, \sigma, \text{IOL}}^{\text{node}}$  is the particle loss timescale of IOL. Also, the nodal IOL for ion energies [11] is

$$P_{\sigma, \text{IOL}}^{\text{node}} = - \frac{E_{\sigma, \text{orb}}(\rho_{\text{node}}^{\text{IOL}})}{\tau_{E, \sigma, \text{IOL}}^{\text{node}}} U_{\sigma}^{\text{node}}, \quad (2.121)$$

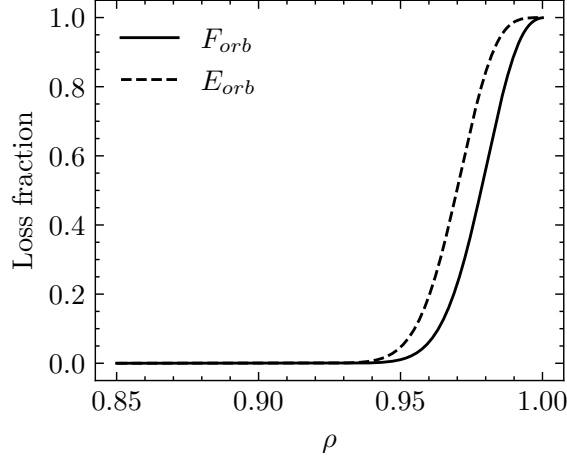
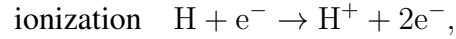
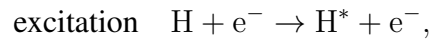


Figure 2.7: Ion particle and energy cumulative loss fractions for ITER, where  $I_P = 9.731$  MA,  $R_0 = 6.2$  m,  $a = 2$  m,  $T_i = 6$  keV,  $B_{\phi 0} = 5.3$  T, and the electrostatic potential is from the Appendix C.2.

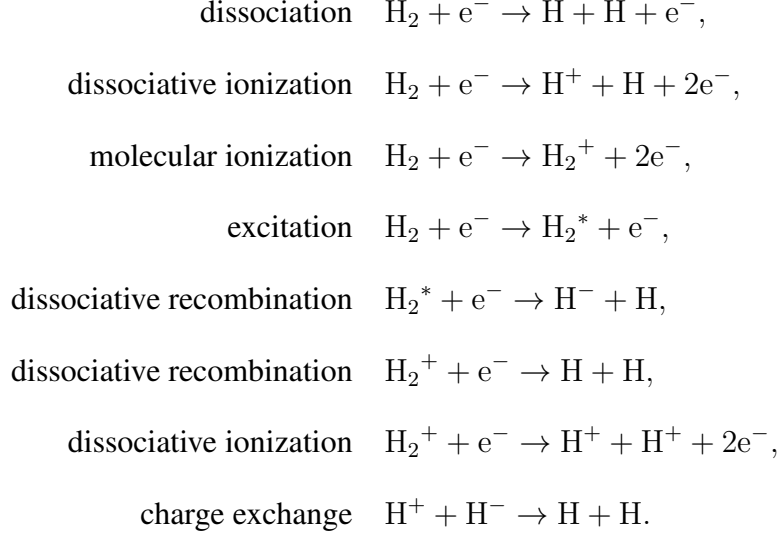
where  $\tau_{E,\sigma,\text{IOL}}^{\text{node}}$  is the energy loss timescale of IOL. The IOL timescales is approximated by transport times from the edge to the SOL.

### 2.3.7 Atomic and Molecular Processes

Atomic and molecular processes are important for the scrape-off layer and divertor regions. For the recycling hydrogen (or deuterium or tritium) atoms from the wall, the important atomic processes [1, 34] are excitation, ionization, charge exchange, and elastic scattering:



For the re-emitted and gas injected hydrogen (or deuterium or tritium) molecules, the important molecular processes [1, 34] are



In the multinodal model, we focus on the atomic reactions and ignore the molecular ones. Following the previous research [56, 57], we consider the ionization, recombination, charge exchange, and the elastic scattering processes in the SOL and divertor node. The cross sections and reaction rate coefficients for these processes can be found in previous research [58, 59, 60].

- Ionization: The particle sources for the ionization process are

$$S_{\sigma,\text{ion}}^{\text{sol}} = n_{\sigma 0}^{\text{sol}} n_e^{\text{sol}} \langle \sigma v \rangle_{\sigma,\text{ion}}^{\text{sol}}, \quad \sigma \in \{ \text{D}, \text{T} \}, \quad (2.122)$$

$$S_{e,\text{ion}}^{\text{sol}} = \sum_{\sigma} n_{\sigma 0}^{\text{sol}} n_e^{\text{sol}} \langle \sigma v \rangle_{\sigma,\text{ion}}^{\text{sol}}, \quad (2.123)$$

where  $\langle \sigma v \rangle_{\sigma,\text{ion}}^{\text{sol}}$  is the reaction rate coefficient for an ionization process [59], and the summation is over all ionization processes. The energy sink is

$$P_{e,\text{ion}}^{\text{sol}} = - \sum_{\sigma} E_{\sigma,\text{ion}} n_{\sigma 0}^{\text{sol}} n_e^{\text{sol}} \langle \sigma v \rangle_{\sigma,\text{ion}}^{\text{sol}}, \quad (2.124)$$

where the ionization energy is  $E_{\sigma,\text{ion}} = 13.6 \text{ eV}$  [59] or can be calculated by [56]

$$E_{\text{ion}} (\text{eV}) = 17.5 + \left[ 5.0 + \frac{35.5}{T_e (\text{eV})} \right] \log_{10} \left( \frac{10^{21}}{n_e (\text{m}^{-3})} \right). \quad (2.125)$$

- **Recombination:** The particle sinks for the recombination processes are

$$S_{\sigma,\text{rec}}^{\text{sol}} = -n_{\sigma}^{\text{sol}} n_e^{\text{sol}} \langle \sigma v \rangle_{\sigma,\text{rec}}^{\text{sol}}, \quad \sigma \in \{ \text{D}, \text{T} \}, \quad (2.126)$$

$$S_{e,\text{rec}}^{\text{sol}} = - \sum_{\sigma} n_{\sigma}^{\text{sol}} n_e^{\text{sol}} \langle \sigma v \rangle_{\sigma,\text{rec}}^{\text{sol}}, \quad (2.127)$$

where  $\langle \sigma v \rangle_{\sigma,\text{rec}}^{\text{sol}}$  is the reaction rate coefficient for a recombination process [59], and the summation is over all recombination processes. The energy source is

$$P_{e,\text{rec}}^{\text{sol}} = \sum_{\sigma} f_{\sigma,\text{rec}} E_{\sigma,\text{rec}} n_{\sigma}^{\text{sol}} n_e^{\text{sol}} \langle \sigma v \rangle_{\sigma,\text{rec}}^{\text{sol}}, \quad (2.128)$$

where  $f_{\sigma,\text{rec}}$  is the absorption fraction of the ionization potential released upon recombination, and the recombination energy is  $E_{\sigma,\text{rec}} = 13.6 \text{ eV}$ .

- **Charge exchange and elastic scattering:** The energy sink for the charge exchange and elastic scattering is

$$P_{\sigma,\text{at}}^{\text{sol}} = -\frac{3}{2} (T_{\sigma}^{\text{sol}} - T_{\sigma 0,c}^{\text{sol}}) n_{\sigma}^{\text{sol}} n_{\sigma 0,c}^{\text{sol}} \left( \langle \sigma v \rangle_{\sigma,\text{cx}}^{\text{sol}} + \langle \sigma v \rangle_{\sigma,\text{el}}^{\text{sol}} \right), \quad \sigma \in \mathcal{I}, \quad (2.129)$$

where  $\langle \sigma v \rangle_{\sigma,\text{cx}}^{\text{sol}}$  and  $\langle \sigma v \rangle_{\sigma,\text{el}}^{\text{sol}}$  are the reaction rate coefficients for the charge exchange and elastic scattering [60] respectively, and also  $n_{\sigma 0,c}^{\text{sol}}$  and  $T_{\sigma 0,c}^{\text{sol}}$  are the density and temperature of the cold recycling neutral atoms from the wall.

The neutral densities  $n_{\sigma 0}^{\text{sol}}$  and  $n_{\sigma 0,c}^{\text{sol}}$  can be measured from experiments or computed from Monte Carlo or neutral transport codes, such as the GTNEUT [61]. In this research, we assume  $n_{\text{D}0}^{\text{sol}} = 10^{15} \text{ m}^{-3}$ . The cold recycling neutral deuterium density can be approximated with the particle reflection from the wall. The particle reflection coefficient  $R_N$



and the energy reflection coefficient  $R_E$  are computed from Thomas et al. [62]. Once the particle reflection coefficient is computed, the cold recycling neutral density can be approximated by  $n_{D0,c}^{\text{sol}} \approx R_N n_{D0}^{\text{sol}}$ . We do not apply the approximation from  $R_N n_{D0}^{\text{sol}}$ , since the nodal particle density is usually much higher than the particles injected on the wall, which may lead to a much larger recycling neutral density. The temperature of these neutrals is assumed as  $T_{D0,c}^{\text{sol}} \approx 1 \text{ eV}$  for a convenience of using available data of the reaction rate coefficients [60], but the result is insensitive to this temperature.

## 2.4 Multinodal Model Framework

After discussions of essential processes in fusion plasmas, now the framework for the multinodal burning plasma dynamics model based on previous works [11, 12] can be presented. As introduced in the Section 2.1, a tokamak plasma is divided into multiple regions in the multinodal model, where each region is modeled as one separate node. A node has one system of dynamics equations for modeling particle and energy balances. Using the multinodal model, different phenomena in different regions are modeled with different timescales.

For convenience of dividing the tokamak plasma into multiple regions, the normalized minor radius is defined as  $\rho = r/a$ , where  $a$  is the minor radius. The tokamak plasma is split into the following four regions:

- Core region:  $0 \leq \rho \leq \rho_{\text{core}} = 0.9$ , where  $\rho_{\text{core}} = r_{\text{core}}/a$ .
- Edge region:  $\rho_{\text{core}} \leq \rho \leq \rho_{\text{edge}} = 1.0$ , where  $\rho_{\text{edge}} = r_{\text{edge}}/a$ .
- Scrape-off layer (SOL) region:  $\rho_{\text{edge}} \leq \rho \leq \rho_{\text{sol}} = 1.1$ , where  $\rho_{\text{sol}} = r_{\text{sol}}/a$ .
- Divertor region: the divertor and the private flux region.

Those numbers of  $\rho_{\text{core}}$ ,  $\rho_{\text{edge}}$ , and  $\rho_{\text{sol}}$  are pre-assumed here and could be adjusted in the future research. The first three regions in the DIII-D tokamak are shown in the Figure 2.8.

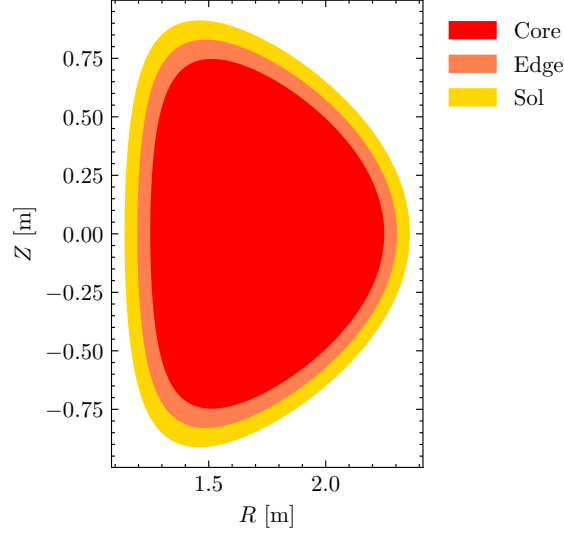


Figure 2.8: The cross section of the DIII-D plasma with the core, edge, and SOL regions in the multinodal model. The divertor region is omitted here.

The multinodal model contains density and energy balance equations for all regions. The  $n_{\sigma}^{\text{node}}$  and  $T_{\sigma}^{\text{node}}$  are used as the volume-averaged particle density and temperature in one node. For example, the volume-averaged electron density  $n_e^{\text{node}}$  in one node between  $\rho_0$  and  $\rho_1$  is calculated from the radial distribution function through

$$\begin{aligned}
 n_e^{\text{node}} &= \frac{1}{V} \int_V n_e(\rho) dV \\
 &= \frac{1}{\pi (\rho_1^2 - \rho_0^2) \cdot 2\pi R_0} \int_{\rho_0}^{\rho_1} d\rho \int_0^{2\pi} \rho d\theta \int_0^{2\pi} (R_0 + \rho \cos \theta) n_e(\rho) d\phi \quad (2.130) \\
 &= \frac{4\pi^2 R_0}{2\pi^2 (\rho_1^2 - \rho_0^2) R_0} \int_{\rho_0}^{\rho_1} n_e(\rho) \rho d\rho = \frac{2}{\rho_1^2 - \rho_0^2} \int_{\rho_0}^{\rho_1} n_e(\rho) \rho d\rho.
 \end{aligned}$$

This formula is used to obtain nodal values from experiment data. Also, the nodal species energy density is defined as

$$U_{\sigma}^{\text{core}} = \frac{3}{2} n_{\sigma}^{\text{core}} T_{\sigma}^{\text{core}}. \quad (2.131)$$

The particle and energy balance equations for all nodes are presented in the following subsections.

### 2.4.1 Core Region

The core region is where most fusion reactions happen. Fusion reactions generate energetic alpha particles, which introduce a vital energy source for further radiation and transport. Modeling the dynamics of the core node is important in the multinodal model.

#### *Core Particle Balance Equations*

In the core region, deuterons and tritons are injected through the neutral beam injection (NBI) and gas puffing. When the core temperature is high enough, the fusion reactions happen, which consume deuterons and tritons and produce alpha particles. Those particles are transported to the edge by diffusion or be lost by ion orbit loss (IOL). Hence, the particle balance equation for deuterons, tritons, and alpha particles is

$$\frac{dn_{\sigma}^{\text{core}}}{dt} = S_{\sigma}^{\text{core}} = S_{\sigma,\text{ext}}^{\text{core}} + S_{\sigma,\text{fus}}^{\text{core}} + S_{\sigma,\text{tran}}^{\text{core}} + S_{\sigma,\text{IOL}}^{\text{core}}, \quad \sigma \in \{D, T, \alpha\}. \quad (2.132)$$

The external particle sources and wall reactions also bring in impurity particles, which are transported or lost. Thus, the particle balance equation for impurities is presented as

$$\frac{dn_z^{\text{core}}}{dt} = S_z^{\text{core}} = S_{z,\text{ext}}^{\text{core}} + S_{z,\text{tran}}^{\text{core}} + S_{z,\text{IOL}}^{\text{core}}, \quad z \in \{z_1, z_2, \dots\}, \quad (2.133)$$

where when multiple impurities are considered, the single impurity  $z$  can be replaced by  $z_1, z_2, \dots$ . Similarly, the particle balance equation for electrons is

$$\frac{dn_e^{\text{core}}}{dt} = S_e^{\text{core}} = S_{e,\text{ext}}^{\text{core}} + S_{e,\text{tran}}^{\text{core}}, \quad (2.134)$$

which is replaced by the quasi-neutrality:

$$n_e^{\text{core}} = \sum_{\sigma \in \mathcal{I}} z_{\sigma} n_{\sigma}^{\text{core}} = n_D^{\text{core}} + n_T^{\text{core}} + z_{\alpha} n_{\alpha}^{\text{core}} + \sum_z z_z n_z^{\text{core}}. \quad (2.135)$$

Notice, the balance equations of electrons in other regions will also be replaced by their corresponding quasi-neutrality equations. The terms on the right-hand sides of these particle balance equations are the particle sources and sinks, which have been discussed thoroughly in the previous sections:

1. The external particle source  $S_{\sigma,\text{ext}}^{\text{core}}$  is presented in the Equation 2.55.
2. The fusion term for the D-T fusion  $S_{\sigma,\text{fus}}^{\text{core}}$  is presented in the Equation 2.76.
3. The particle transport term  $S_{\sigma,\text{tran}}^{\text{core}}$  is presented in the Equation 2.17.
4. And the ion orbit loss (IOL) term  $S_{\sigma,\text{IOL}}^{\text{core}}$  is presented in the Equation 2.120.

### *Core Energy Balance Equations*

In the core region, ions are heated by auxiliary heating and fusion alpha heating. The ions also redistribute their energies through Coulomb collisions. Such energetic ions then are transported to the edge or lost by the IOL. Therefore, the energy balance equation for ions is

$$\frac{dU_{\sigma}^{\text{core}}}{dt} = P_{\sigma}^{\text{core}} = P_{\sigma,\text{aux}}^{\text{core}} + P_{\sigma,\text{fus}}^{\text{core}} + Q_{\sigma}^{\text{core}} + P_{\sigma,\text{tran}}^{\text{core}} + P_{\sigma,\text{IOL}}^{\text{core}}, \quad \sigma \in \mathcal{I}. \quad (2.136)$$

Electrons are also heated through ohmic heating. Besides transport, the core electrons radiate their energy instantaneously through electron cyclotron radiation (ECR), bremsstrahlung, and impurity radiation. Hence, the energy balance equation for electrons is

$$\frac{dU_e^{\text{core}}}{dt} = P_e^{\text{core}} = P_{\Omega}^{\text{core}} + P_{e,\text{aux}}^{\text{core}} + P_{e,\text{fus}}^{\text{core}} - P_R^{\text{core}} + Q_e^{\text{core}} + P_{e,\text{tran}}^{\text{core}}. \quad (2.137)$$

These sources and sinks have been described in the previous sections:

1. The auxiliary heating term  $P_{\sigma,\text{aux}}^{\text{core}}$  is presented in the Equation 2.60 and 2.61.
2. The ohmic heating to electrons  $P_{\Omega}^{\text{core}}$  is presented in the Equation 2.62 and 2.63.

3. The D-T fusion term  $P_{\sigma,\text{fus}}^{\text{core}}$  is presented in the Equation 2.77.
4. The radiation term  $P_R^{\text{core}}$  is presented in the Equation 2.85.
5. The energy transport term  $P_{\sigma,\text{tran}}^{\text{core}}$  is presented in the Equation 2.42.
6. The Coulomb collisional energy transfer  $Q_{\sigma}^{\text{core}}$  term is presented in the Equation 2.107.
7. And the IOL term  $P_{\sigma,\text{IOL}}^{\text{core}}$  is presented in the Equation 2.121.

### 2.4.2 Edge Region

Once the particle and energy are transported from the core to the edge, the edge ions and electrons are heated. Also, the edge plasma has more impurities, which will have stronger impurity radiations. Besides, some edge effects, including the ion orbit loss (IOL), are significant. Hence, modeling the edge region is essential.

#### *Edge Particle Balance Equations*

In the edge region, the ions and electrons are also supplied by the neutral beam injection (NBI) and gas puffing. Usually, the gas puffing will introduce most particles to the edge node rather than to the core node. Also, particles are transported from the core to edge, and then to the SOL. The IOL will accelerate the particle loss in the edge node. The particle balance equations for deuterons, tritons, alpha particles, and impurities are

$$\frac{dn_{\sigma}^{\text{edge}}}{dt} = S_{\sigma}^{\text{edge}} = S_{\sigma,\text{ext}}^{\text{edge}} + S_{\sigma,\text{fus}}^{\text{edge}} + S_{\sigma,\text{tran}}^{\text{edge}} + S_{\sigma,\text{IOL}}^{\text{edge}}, \quad \sigma \in \mathcal{I}. \quad (2.138)$$

Most of sources and sinks in these equations are same as the corresponding terms in the core region, while the particle transport term  $S_{\sigma,\text{tran}}^{\text{edge}}$  is presented in the Equation 2.26.

### Edge Energy Balance Equations

The energetic ions and electrons are transported to the edge and then heat the edge plasma. Those heated electrons will lose their energies through transport and radiations. These processes will couple the edge equations with the core ones. Thus, the energy balance equations for deuterons, tritons, alpha particles, impurities, and electrons are

$$\frac{dU_{\sigma}^{\text{edge}}}{dt} = P_{\sigma}^{\text{edge}} = P_{\sigma,\text{aux}}^{\text{edge}} + P_{\sigma,\text{fus}}^{\text{edge}} + Q_{\sigma}^{\text{edge}} + P_{\sigma,\text{tran}}^{\text{edge}} + P_{\sigma,\text{IOL}}^{\text{edge}}, \quad \sigma \in \mathcal{I}, \quad (2.139)$$

$$\frac{dU_e^{\text{edge}}}{dt} = P_e^{\text{edge}} = P_{\Omega}^{\text{edge}} + P_{e,\text{aux}}^{\text{edge}} + P_{e,\text{fus}}^{\text{edge}} - P_R^{\text{edge}} + Q_e^{\text{edge}} + P_{e,\text{tran}}^{\text{edge}}. \quad (2.140)$$

Similar to the edge particle equations, most of terms are same as the corresponding terms in the core region, while the energy transport term  $P_{\sigma,\text{tran}}^{\text{edge}}$  is presented in the Equation 2.47.

### 2.4.3 Scrape-Off Layer Region

The scrape-off layer (SOL) [63, 58, 64, 65, 60, 56, 66, 57, 67, 68, 69, 70, 71, 72, 73] refers to the plasma outside the separatrix. The particle densities and temperatures in the SOL are relatively lower compared with the edge ones. Thus, the neutral and partially ionized particles cannot be ignored. Modeling the SOL is important for practical fusion reactors.

### SOL Particle Balance Equations

In the SOL region, particles are transported from the edge. Besides, the atoms can be injected from the external sources and then recycled from the wall, where the wall condition is vital. Also, the atomic and molecular processes are important in this region. Hence, the particle balance equations in the SOL region are

$$\frac{dn_{\sigma}^{\text{sol}}}{dt} = S_{\sigma}^{\text{sol}} = S_{\sigma,\text{ext}}^{\text{sol}} + S_{\sigma,\text{ion}}^{\text{sol}} + S_{\sigma,\text{rec}}^{\text{sol}} + S_{\sigma,\text{tran}}^{\text{sol}} + S_{\sigma,\text{IOL}}^{\text{sol}}, \quad \sigma \in \mathcal{I}, \quad (2.141)$$

where the particle sources and sinks are as follows.

1. The particle source term from external sources, such as the massive gas injection (MGI) [11], is

$$S_{\sigma,\text{ext}}^{\text{sol}} = S_{\sigma,\text{MGI}}^{\text{sol}} = \frac{S_{\sigma,\text{MGI}}^{\text{tot}} f_{\sigma,\text{MGI}}^{\text{sol}}}{V_{\text{sol}}}, \quad (2.142)$$

where  $S_{\sigma,\text{MGI}}^{\text{tot}}$  is the total MGI source of species  $\sigma$  and  $f_{\sigma,\text{MGI}}^{\text{sol}}$  is the fraction of  $S_{\sigma,\text{MGI}}^{\text{tot}}$  ionized in the SOL.

2. The particle source term for the ionization process  $S_{\sigma,\text{ion}}^{\text{sol}}$  is presented in the Equation 2.122.
3. The particle sink term for the recombination process  $S_{\sigma,\text{rec}}^{\text{sol}}$  is presented in the Equation 2.126.
4. The transport term  $S_{\sigma,\text{tran}}^{\text{sol}}$  is presented in the Equation 2.28.
5. And the IOL term  $S_{\sigma,\text{IOL}}^{\text{sol}}$  is the IOL particle from the edge to the SOL.

### *SOL Energy Balance Equations*

Similar to the edge node, the transport and radiation should be considered in the SOL node. Besides, the atomic and molecular processes are important. Thus, the energy balance equations in the SOL region are

$$\frac{dU_{\sigma}^{\text{sol}}}{dt} = P_{\sigma}^{\text{sol}} = P_{\sigma,\text{ext}}^{\text{sol}} + P_{\sigma,\text{at}}^{\text{sol}} + Q_{\sigma}^{\text{sol}} + P_{\sigma,\text{tran}}^{\text{sol}} + P_{\sigma,\text{IOL}}^{\text{sol}}, \quad \sigma \in \mathcal{I}, \quad (2.143)$$

$$\frac{dU_e^{\text{sol}}}{dt} = P_e^{\text{sol}} = P_{e,\text{ext}}^{\text{sol}} + P_{e,\text{ion}}^{\text{sol}} + P_{e,\text{rec}}^{\text{sol}} - P_R^{\text{sol}} + Q_e^{\text{sol}} + P_{e,\text{tran}}^{\text{sol}}, \quad (2.144)$$

where the energy sources and sinks are described as follows.

1. The  $P_{\sigma,\text{ext}}^{\text{sol}}$  is the power source term from external sources.
2. The power sink term from the ionization process  $P_{\sigma,\text{ion}}^{\text{sol}}$  is presented in the Equation 2.124.

3. The power source term from the recombination process  $P_{\sigma,\text{rec}}^{\text{sol}}$  is presented in the Equation 2.128.
4. The power sink term from the charge exchange and elastic scattering processes  $P_{\sigma,\text{at}}^{\text{sol}}$  is presented in the Equation 2.129.
5. The radiation term  $P_R^{\text{sol}}$  is the impurity radiation, which has been discussed before.
6. The collisional energy transfer term  $Q_{\sigma}^{\text{sol}}$  includes collisions of the species  $\sigma$  with both charged particles and neutral particles, i.e.

$$Q_{\sigma}^{\text{sol}} = \sum_{\sigma' \in \mathcal{I}, \sigma' \neq \sigma} Q_{\sigma' \rightarrow \sigma}^{\text{sol}} + \sum_{\sigma'_0} Q_{\sigma'_0 \rightarrow \sigma}^{\text{sol}}. \quad (2.145)$$

Notice that the elastic scattering with the recycling of neutral particles from the wall has already been considered in the atomic process term.

7. The transport term  $P_{\sigma,\text{tran}}^{\text{sol}}$  is presented in the Equation 2.49.
8. And the IOL term  $P_{\sigma,\text{IOL}}^{\text{sol}}$  is the IOL energy from the edge to the SOL.

#### 2.4.4 Divertor Region

The divertor [56, 66] is a magnetic device for removing impurities and ashes from the plasma when the reactor is operating. It can help control the buildup of fusion products and clean plasma impurities. Modeling dynamics in the divertor node is vital for practical fusion reactors.

##### *Divertor Particle Balance Equations*

The particle balance equations in the divertor region are

$$\frac{dn_{\sigma}^{\text{div}}}{dt} = S_{\sigma}^{\text{div}} = S_{\sigma,\text{ext}}^{\text{div}} + S_{\sigma,\text{ion}}^{\text{div}} + S_{\sigma,\text{rec}}^{\text{div}} + S_{\sigma,\text{tran}}^{\text{div}}, \quad \sigma \in \mathcal{I}. \quad (2.146)$$



The particle sources and sinks from external sources, ionization, and recombination are similar to those in the SOL region. The transport term is

$$S_{\sigma,\text{tran}}^{\text{div}} = \frac{V_{\text{sol}}}{V_{\text{div}}} \frac{n_{\sigma}^{\text{sol}}}{\tau_{P,\sigma}^{\text{sol} \rightarrow \text{div}}} + S_{\sigma,\text{tar}}^{\text{div}}, \quad (2.147)$$

where  $S_{\sigma,\text{tar}}^{\text{div}}$  is the particle sink for combinations with divertor targets. The  $S_{\sigma,\text{tar}}^{\text{div}}$  is computed by [11]:

$$S_{\sigma,\text{tar}}^{\text{div}} = -\frac{A_{\text{div}}}{V_{\text{div}}} n_{\sigma}^{\text{div}} c_{s,\sigma} (1 - R_{w,\sigma}), \quad (2.148)$$

where the  $A_{\text{div}}$  is the combined effective surface area of the divertor targets,  $V_{\text{div}}$  is the volume of the divertor region,  $c_{s,\sigma}$  is the sound speed of the species  $\sigma$  in the divertor as [56]:

$$c_{s,\sigma} = \sqrt{\frac{2T_{\sigma}^{\text{div}}}{m_{\sigma}}}, \quad (2.149)$$

and the  $R_{w,\sigma}$  is the reflection fraction of the species  $\sigma$  from the wall.

### *Divertor Energy Balance Equations*

The energy balance equations in the divertor region are

$$\frac{dU_{\sigma}^{\text{div}}}{dt} = P_{\sigma}^{\text{div}} = P_{\sigma,\text{ext}}^{\text{div}} + P_{\sigma,\text{at}}^{\text{div}} + Q_{\sigma}^{\text{div}} + P_{\sigma,\text{tran}}^{\text{div}}, \quad \sigma \in \mathcal{I}, \quad (2.150)$$

$$\frac{dU_e^{\text{div}}}{dt} = P_e^{\text{div}} = P_{e,\text{ext}}^{\text{div}} + P_{e,\text{ion}}^{\text{div}} + P_{e,\text{rec}}^{\text{div}} - P_R^{\text{div}} + Q_e^{\text{div}} + P_{e,\text{tran}}^{\text{div}}. \quad (2.151)$$

The power sources and sinks from the external sources, radiation, ionization, recombination, charge exchange, elastic scattering, and collisions are similar to those in the SOL region. The transport term is

$$P_{\sigma,\text{tran}}^{\text{div}} = \frac{V_{\text{sol}}}{V_{\text{div}}} \frac{U_{\sigma}^{\text{sol}}}{\tau_{E,\sigma}^{\text{sol} \rightarrow \text{div}}} + P_{\sigma,\text{tar}}^{\text{div}}, \quad (2.152)$$

where  $P_{\sigma,\text{tar}}^{\text{div}}$  is the energy sink for combinations with divertor targets. The  $P_{\sigma,\text{tar}}^{\text{div}}$  is computed by [11]:

$$P_{\sigma,\text{tar}}^{\text{div}} = -\frac{A_{\text{div}}}{V_{\text{div}}} U_{\sigma}^{\text{div}} c_{s,\sigma} \gamma_{\sigma,\text{sh}}, \quad (2.153)$$

where the sheath energy transmission coefficient  $\gamma_{\text{sh}}$  is gotten from [56, 11]:

$$\gamma_{\sigma,\text{sh}} = \frac{2T_{\sigma}^{\text{div}}}{T_e^{\text{div}}} + \frac{2}{1 - \delta_{\sigma,\text{sh}}} + \frac{1}{2} \ln \left[ \frac{(1 - \delta_{\sigma,\text{sh}}) m_{\sigma} / m_e}{2\pi(1 + T_{\sigma}^{\text{div}} / T_e^{\text{div}})} \right], \quad (2.154)$$

and  $\delta_{\sigma,\text{sh}}$  is the secondary sheath transmission coefficient.

## 2.5 Summary

In this chapter, a framework for a multi-region multi-timescale plasma transport model is proposed to simulate burning plasma dynamics in tokamaks. Regions including the core, edge, scrape-off layer (SOL), and divertor are modeled as separate nodes. The balanced equations and transport terms are derived from the fluid theory. Several essential terms in the burning plasma are introduced, including fusion alpha heating, electron cyclotron radiation (ECR), bremsstrahlung, impurity radiation, and collisional energy transfer. Moreover, other necessary terms, containing external particle sources, ohmic and auxiliary heating, and atomic and molecular processes, are discussed. One edge effect, ion orbit loss (IOL), is also considered. The framework of the multinodal model is proposed at the end of the chapter. In the next chapter, we will develop the computational methods for the multinodal model.

## CHAPTER 3

### COMPUTATIONAL METHODS

Before applying the multinodal model for simulating plasmas, we must properly compute the particle and energy transport between nodes. In this chapter, computational methods for the multinodal burning plasma dynamics model are built. Firstly, The limitations of previous methods for obtaining transport times are discussed. Next, we present a parametric diffusivity formula with transport times. Moreover, the machine learning algorithms involved in this research are visited, including back propagation and gradient descent. Finally, the GTBURN package and its modules are introduced at the end of the chapter.

#### 3.1 Limitations of Previous Works

In the multinodal burning plasma model, particles and energy are transferred through radiation and transport. Although radiations travel at the speed of light, which are treated as instantaneous energy transfer processes, the particle and energy transport should be characterized with finite transport times  $\tau_{x,\sigma}^{a \rightarrow b}$  from the region  $a$  to  $b$  for species  $\sigma$  particles (if  $x = P$ ) or energies (if  $x = E$ ). Modeling the transport times between adjacent nodes is critical for the multinodal model.

In order to determine the internodal transport time, the first way one can try is the energy confinement time  $\tau_E^{\text{exp}}$  from the steady-state energy balance equation [1]:

$$\frac{W_{\text{th}}}{\tau_E^{\text{exp}}} = P_{\text{heat}} - P_{\text{rad}} - \frac{dW_{\text{th}}}{dt} - \frac{dW_{\text{rot}}}{dt}, \quad (3.1)$$

where the thermal energy is  $W_{\text{th}} = \int \frac{3}{2} n T dV$ , the rotation energy is  $W_{\text{rot}} = \int \frac{1}{2} n m v^2 dV$ , also  $P_{\text{heat}}$  and  $P_{\text{rad}}$  are additional heating and radiation respectively. Through regression analysis over multiple experiments from various tokamaks, scaling laws are gotten for the

global (one-nodal) energy confinement time. One widely used scaling law is the ITER-98(y,2) energy confinement scaling law (ITER-98) [5]:

$$\begin{aligned} \frac{\tau_E^{\text{IPB98(y,2)}}}{1 \text{ s}} = & 0.056 \left( \frac{I_P}{1 \text{ MA}} \right)^{0.93} \left( \frac{B_T}{1 \text{ T}} \right)^{0.15} \left( \frac{n_e}{10^{19} \text{ m}^{-3}} \right)^{0.41} \left( \frac{P_{\text{tot}}}{1 \text{ MW}} \right)^{-0.69} \\ & \times \left( \frac{R_0}{1 \text{ m}} \right)^{1.97} \kappa^{0.78} A^{-0.58} \left( \frac{M}{1 \text{ amu}} \right)^{0.19}, \end{aligned} \quad (3.2)$$

where  $I_P$  (MA) is the plasma current,  $B_T$  (T) is the toroidal magnetic field,  $n_e$  ( $\text{m}^{-3}$ ) is the line averaged electron density,  $P_{\text{tot}}$  (MW) is the total absorbed power (heating power),  $R_0$  (m) is the major radius,  $\kappa$  is the elongation,  $A = R_0/a$  is the aspect ratio, and  $M$  (amu) is the hydrogen isotope mass ( $M = 2$  for the deuterium plasma and  $M = 2.5$  for the deuterium-tritium plasma). However, this equation does not measure the energy transport time directly, but determines a energy loss rate from the steady-state plasma. Additionally, this formula cannot be generalized to a transport time between nodes conveniently in theory.

The second way to determine internodal transport times is to perform tokamak experiments and infer transport times from them. This method has been suggested in previous research [12]. For example, by injecting pellets into the core plasma, one can measure the deuteron density change in the edge plasma to get the deuterium particle transport time from the core to the edge, i.e.,  $\tau_{P,D}^{\text{core} \rightarrow \text{edge}}$ . Similarly, by providing electron cyclotron heating to the core plasma, one can measure the electron temperature change in the edge plasma to get the electron energy transport time from the core to the edge, i.e.,  $\tau_{E,e}^{\text{core} \rightarrow \text{edge}}$ . The region-to-region particle and energy transport times can be determined by adjusting these coupling coefficients to make the predictions of the multinodal model consistent with measured densities and temperatures. However, there are several shortcomings of this direct measurement method:

- Firstly, directly measuring one particle or energy transport time for one species is hard in practice. In real tokamak experiments, multiple particle and energy sources

can exist during one shot, such as the gas puffing of deuterons at the beginning and then the neutral beam injection next. The interactions of multiple particle and energy sources are sometimes unavoidable. In such cases, the transport times are not independent of each other and hence cannot be determined from experiments separately.

- Besides, the direct measurement method can only determine one steady transport time from one shot, which will be a constant in that shot. However, the experimental conditions can be changed during one shot and among different shots. In fact, for a well-performed multinodal model, a proper model for dynamic transport times is required, where internodal transport times should depend on real-time experiment conditions such as the magnetic field, safety factor, and local temperature.
- Lastly, the direct measurement can only provide transport times for existing shots, while these transport times are hard and unreliable to be extrapolated to new shots. The purpose of this research is to obtain a predictive model, which can not only explain the existing shots, but also predict the new shots with new reasonable conditions. This raises a requirement for model generalization ability.

By visiting the drawbacks of previous methods for obtaining internodal transport times, we propose a novel way by taking advantage of state-of-the-art machine learning techniques. A parametric scaling law is given for the diffusivity model and then used for building the internodal transport times. The diffusivity model can be optimized by utilizing experiment data and used for predicting new experiments of both DIII-D and ITER. More details of this method are discussed in this chapter.

### **3.2 Multinodal Model Formulas**

In this section, the formulas in the multinodal model are presented. A parametric diffusivity model is proposed, and a vector form of internodal transport time computation is given. The

parameters in the diffusivity model are discussed, which will need optimizing based on the experiment data. Those optimization algorithms will be introduced in the next section.

### 3.2.1 Parametric Diffusivity Model

The diffusivity formula in the Equation 2.52 is rewritten as a parametric one:

$$\begin{aligned} \frac{\chi(\rho)}{1 \text{ m}^2/\text{s}} = & \alpha_H \left( \frac{B_T}{1 \text{ T}} \right)^{\alpha_B} \left( \frac{n_e(\rho)}{10^{19} \text{ m}^{-3}} \right)^{\alpha_n} \left( \frac{T_e(\rho)}{1 \text{ keV}} \right)^{\alpha_T} \left( \frac{|\nabla T_e(\rho)|}{1 \text{ keV/m}} \right)^{\alpha_{\nabla T}} q(\rho)^{\alpha_q} \\ & \times \kappa(\rho)^{\alpha_\kappa} \left( \frac{M}{1 \text{ amu}} \right)^{\alpha_M} \left( \frac{R}{1 \text{ m}} \right)^{\alpha_R} \left( \frac{a}{1 \text{ m}} \right)^{\alpha_a}, \end{aligned} \quad (3.3)$$

where  $\rho$  is the normalized radius by  $\rho = r/a$ ,  $B_T$  is the toroidal magnetic field,  $n_e$  is the electron density,  $T_e$  is the electron temperature,  $q$  is the safety factor,  $\kappa$  is the local elongation,  $M$  is the hydrogenic atomic mass number,  $R$  is the major radius, and  $a$  is the minor radius. Also,  $\alpha_H, \alpha_B, \dots, \alpha_a$  are undetermined parameters, which will be solved from the experiment data later. Now the diffusivity formula is reformulated into one vector form by taking logarithms in both sides:

$$\begin{aligned} \ln \left( \frac{\chi(\rho)}{1 \text{ m}^2/\text{s}} \right) = & \ln \alpha_H + \alpha_B \ln \left( \frac{B_T}{1 \text{ T}} \right) + \alpha_n \ln \left( \frac{n_e(\rho)}{10^{19} \text{ m}^{-3}} \right) + \alpha_T \ln \left( \frac{T_e(\rho)}{1 \text{ keV}} \right) \\ & + \alpha_{\nabla T} \ln \left( \frac{|\nabla T_e(\rho)|}{1 \text{ keV/m}} \right) + \alpha_q \ln q(\rho) + \alpha_\kappa \ln \kappa(\rho) \\ & + \alpha_M \ln \left( \frac{M}{1 \text{ amu}} \right) + \alpha_R \ln \left( \frac{R}{1 \text{ m}} \right) + \alpha_a \ln \left( \frac{a}{1 \text{ m}} \right) \\ = & b + \mathbf{w}^T \ln \mathbf{x}(\rho), \end{aligned} \quad (3.4)$$

where the notations are

$$b = \ln \alpha_H, \quad (3.5)$$

$$\mathbf{w} = \begin{bmatrix} \alpha_B & \alpha_n & \alpha_T & \alpha_{\nabla T} & \alpha_q & \alpha_\kappa & \alpha_M & \alpha_R & \alpha_a \end{bmatrix}^T, \quad (3.6)$$

$$\mathbf{x}(\rho) = \begin{bmatrix} \frac{B_T}{1 \text{ T}} & \frac{n_e(\rho)}{10^{19} \text{ m}^{-3}} & \frac{T_e(\rho)}{1 \text{ keV}} & \frac{|\nabla T_e(\rho)|}{1 \text{ keV/m}} & q(\rho) & \kappa(\rho) & \frac{M}{1 \text{ amu}} & \frac{R}{1 \text{ m}} & \frac{a}{1 \text{ m}} \end{bmatrix}^T. \quad (3.7)$$

Let the internodal particle diffusivity be  $D_\sigma^{\text{node}}$ , and the internodal thermal diffusivity be  $\chi_\sigma^{\text{node}}$ . Although we use the “node” in the superscripts here, those diffusivities represent transport between adjacent nodes. The diffusivity vector is defined as

$$\boldsymbol{\chi}_{\text{node}} = \begin{bmatrix} D_{\text{D}}^{\text{node}} & D_{\text{T}}^{\text{node}} & \dots & \chi_{\text{D}}^{\text{node}} & \chi_{\text{T}}^{\text{node}} & \dots \end{bmatrix}^T / (1 \text{ m}^2/\text{s}). \quad (3.8)$$

Also, let the nodal input vector  $\mathbf{x}(\rho)$  be  $\mathbf{x}_{\text{node}}$ . Hence, the diffusivity model becomes

$$\begin{aligned} \ln \boldsymbol{\chi}_{\text{node}} &= \ln \begin{bmatrix} D_{\text{D}}^{\text{node}} / (1 \text{ m}^2/\text{s}) \\ D_{\text{T}}^{\text{node}} / (1 \text{ m}^2/\text{s}) \\ \vdots \end{bmatrix} = \begin{bmatrix} b_{P,\text{D}}^{\text{node}} + (\mathbf{w}_{P,\text{D}}^{\text{node}})^T \ln \mathbf{x}_{\text{node}} \\ b_{P,\text{T}}^{\text{node}} + (\mathbf{w}_{P,\text{T}}^{\text{node}})^T \ln \mathbf{x}_{\text{node}} \\ \vdots \end{bmatrix} \\ &= \begin{bmatrix} b_{P,\text{D}}^{\text{node}} \\ b_{P,\text{T}}^{\text{node}} \\ \vdots \end{bmatrix} + \begin{bmatrix} (\mathbf{w}_{P,\text{D}}^{\text{node}})^T \\ (\mathbf{w}_{P,\text{T}}^{\text{node}})^T \\ \vdots \end{bmatrix} \ln \mathbf{x}_{\text{node}} \equiv \mathbf{b}_{\text{node}} + \mathbf{W}_{\text{node}} \ln \mathbf{x}_{\text{node}}. \end{aligned} \quad (3.9)$$

In general, the internodal diffusivity model can be defined as any parametric function:

$$\boldsymbol{\chi}_{\text{node}} = \mathbf{f}_{\text{node}}(\mathbf{x}_{\text{node}}). \quad (3.10)$$

where  $\boldsymbol{\chi}_{\text{node}} \in \mathbb{R}^{n_{\chi}^{\text{node}}}$ ,  $\mathbf{x}_{\text{node}} \in \mathbb{R}^{n_x^{\text{node}}}$ , and  $\mathbf{f}_{\text{node}} : \mathbb{R}^{n_x^{\text{node}}} \mapsto \mathbb{R}^{n_{\chi}^{\text{node}}}$ . Here we select one

exponentially linear function:

$$\chi_{\text{node}} = \mathbf{f}_{\text{node}}(\mathbf{x}_{\text{node}}; \mathbf{W}_{\text{node}}, \mathbf{b}_{\text{node}}) = \exp(\mathbf{b}_{\text{node}} + \mathbf{W}_{\text{node}} \ln \mathbf{x}_{\text{node}}), \quad (3.11)$$

where  $\mathbf{W}_{\text{node}} \in \mathbb{R}^{n_{\chi}^{\text{node}} \times n_x^{\text{node}}}$  and  $\mathbf{b}_{\text{node}} \in \mathbb{R}^{n_{\chi}^{\text{node}}}$ . Such an exponentially linear function gives a positive diffusivity as a power scaling of physical features  $\mathbf{x}_{\text{node}}$ . This function can be replaced with the multi-layer neural network (multilayer perceptron [74, 75]) in the future.

The nodal diffusivity models from the different nodes are combined and rewritten into one formula:

$$\begin{aligned} \chi &= \begin{bmatrix} \chi_{\text{core}}^T & \chi_{\text{edge}}^T & \cdots \end{bmatrix}^T \\ &= \begin{bmatrix} \mathbf{f}_{\text{core}}^T(\mathbf{x}_{\text{core}}; \mathbf{W}_{\text{core}}, \mathbf{b}_{\text{core}}) & \mathbf{f}_{\text{edge}}^T(\mathbf{x}_{\text{edge}}; \mathbf{W}_{\text{edge}}, \mathbf{b}_{\text{edge}}) & \cdots \end{bmatrix}^T, \\ &\equiv \mathbf{f}(\mathbf{x}), \end{aligned} \quad (3.12)$$

where  $\chi \in \mathbb{R}^{n_{\chi}}$  is the diffusivity vector,  $\mathbf{x} \in \mathbb{R}^{n_x}$  is the physical feature vector, and  $\mathbf{f} : \mathbb{R}^{n_x} \mapsto \mathbb{R}^{n_{\chi}}$  is a parametric function for the diffusivity model. This formula is convenient when the model is discussed theoretically. In practice, each nodal diffusivity model is implemented separately since each one has a different input vector.

### 3.2.2 Dynamical System

After defining the diffusivity model, we go back to the multinodal model, which is viewed as a dynamical system:

$$\frac{d\mathbf{y}}{dt} = \mathbf{S}(\mathbf{y}(t), \boldsymbol{\tau}(t), t), \quad t_0 \leq t \leq t_{nt}, \quad (3.13)$$



where  $t$  is the time variable,  $\mathbf{y} \in \mathbb{R}^{n_y}$  is a vector of nodal particle densities and energies, i.e.

$$\mathbf{y} = \begin{bmatrix} \mathbf{y}_{\text{core}}^T & \mathbf{y}_{\text{edge}}^T & \dots \end{bmatrix}^T, \quad (3.14)$$

$$\mathbf{y}_{\text{node}} = \begin{bmatrix} n_{\text{D}}^{\text{node}} & n_{\text{T}}^{\text{node}} & \dots & U_{\text{D}}^{\text{node}} & U_{\text{T}}^{\text{node}} & \dots \end{bmatrix}^T, \quad (3.15)$$

$\boldsymbol{\tau} \in \mathbb{R}^{n_\tau}$  is the vector of transport times, and  $\mathbf{S} \in \mathbb{R}^{n_y}$  is the vector of particle and energy sources for the corresponding  $\mathbf{y}$ . The internodal transport time vector is defined as

$$\boldsymbol{\tau} = \begin{bmatrix} \boldsymbol{\tau}_{\text{core}}^T & \boldsymbol{\tau}_{\text{edge}}^T & \dots \end{bmatrix}^T, \quad (3.16)$$

where  $\boldsymbol{\tau}_{\text{node}} \in \mathbb{R}^{n_\tau^{\text{node}}}$  is the vector of internodal transport times. For example, the core-edge transport time vector is

$$\boldsymbol{\tau}_{\text{core}} = \begin{bmatrix} \tau_{P,\text{D}}^{\text{core} \rightarrow \text{edge}} & \tau_{P,\text{T}}^{\text{core} \rightarrow \text{edge}} & \dots & \tau_{E,\text{D}}^{\text{core} \rightarrow \text{edge}} & \dots \end{bmatrix}^T, \quad (3.17)$$

and the edge-SOL transport time vector is

$$\boldsymbol{\tau}_{\text{edge}} = \begin{bmatrix} \tau_{P,\text{D}}^{\text{edge} \rightarrow \text{sol}} & \tau_{P,\text{T}}^{\text{edge} \rightarrow \text{sol}} & \dots & \tau_{E,\text{D}}^{\text{edge} \rightarrow \text{sol}} & \dots \end{bmatrix}^T. \quad (3.18)$$

Here the relation between two directions of adjacent nodes in the Equation 2.16 is used, so only one-direction transport times are needed. Besides, the internodal transport times depend on the corresponding diffusivities, which can be represented by a function:

$$\boldsymbol{\tau}_{\text{node}} = \mathbf{g}_{\text{node}}(\boldsymbol{\chi}_{\text{node}}), \quad (3.19)$$

where the function  $\mathbf{g}_{\text{node}} : \mathbb{R}^{n_\chi^{\text{node}}} \mapsto \mathbb{R}^{n_\tau^{\text{node}}}$  has been defined in the Section 2.2 such as the Equation 2.14, 2.15, 2.40, and 2.41. All nodal transport times can also be combined into

one function  $\mathbf{g} : \mathbb{R}^{n_x} \mapsto \mathbb{R}^{n_\tau}$  such that

$$\boldsymbol{\tau}(t) = \mathbf{g}(\boldsymbol{\chi}(t)). \quad (3.20)$$

Notice, the function  $\mathbf{g}$  is determined, which is different from the parametric function  $\mathbf{f}$  with undetermined parameters. To solve the dynamic system with the internodal transport times, we still need to obtain parameters in the diffusivity model first. The method will be discussed in the next section.

### 3.3 Optimization Algorithms

In this section, optimization algorithms from machine learning are introduced to obtain the parameters in the diffusivity model. Most of the concepts and methods can be found in the machine learning and deep learning materials [76, 77].

#### 3.3.1 Mean Squared Error Loss

After the dynamical system in the Equation 3.13 is formulated, it is solved for one shot (i.e., one experiment) at discrete time steps  $t = t_1, t_2, \dots, t_{n_t}$ , where the number of time steps  $n_t$  is determined by the experiment measurement or burning length. In this research, the Runge-Kutta of order 5 of Dormand-Prince-Shampine method [78] is used for solving this system of ordinary differential equations (ODEs). The solution of the dynamical system is given as  $\hat{\mathbf{Y}} \in \mathbb{R}^{n_t \times n_y}$ , where one row of  $\hat{\mathbf{Y}}$  is one solution  $\mathbf{y}(t_i)$  at the time step  $t_i$ . Here, the energy densities have been replaced by their corresponding temperatures. Let the experiment measurement be  $\mathbf{Y} \in \mathbb{R}^{n_t \times n_y}$ . The error between multinodal model solutions (predictions) and experiment measurements (targets) for this shot is defined by the mean squared error (MSE):

$$\mathcal{L} = \frac{1}{n_t n_y} \left\| \hat{\mathbf{Y}} - \mathbf{Y} \right\|_F^2, \quad (3.21)$$

where the Frobenius norm is used for matrices. This error is also used as the loss function in the optimization process. The regularization term is added to the loss function for preventing overfitting:

$$\mathcal{L} = \frac{1}{n_t n_y} \left\| \hat{\mathbf{Y}} - \mathbf{Y} \right\|_F^2 + \sum_{\text{node}} \left( \lambda_W^{\text{node}} \left\| \mathbf{W}_{\text{node}} \right\|_F^2 + \lambda_b^{\text{node}} \left\| \mathbf{b}_{\text{node}} \right\|_2^2 \right), \quad (3.22)$$

where  $\lambda_W^{\text{node}}$  and  $\lambda_b^{\text{node}}$  are regularization hyperparameters.

### 3.3.2 Back Propagation Algorithm

To get the optimized diffusivity model, one needs to minimize the MSE loss over all given shots in the training dataset. In this process, the parameters in the diffusivity model are updated by following the gradient descent algorithm, where the back propagation algorithm is used to compute gradients of the MSE loss over model parameters.

The back propagation algorithm [76, 77] is widely used for training feed-forward neural networks. The gradient of the loss over the model parameters is computed by the chain rule. In the multinodal model, the gradient of the MSE loss on the nodal weight  $\mathbf{W}_{\text{node}}$  is

$$\begin{aligned} \nabla_{\mathbf{W}_{\text{node}}} \mathcal{L} &= \frac{\partial \mathcal{L}}{\partial \mathbf{W}_{\text{node}}} \\ &= \frac{2}{n_t n_y} \left( \hat{\mathbf{Y}} - \mathbf{Y} \right)^T \frac{\partial \hat{\mathbf{Y}}}{\partial \mathbf{T}_{\text{node}}} \frac{\partial \mathbf{T}_{\text{node}}}{\partial \mathbf{C}_{\text{node}}} \frac{\partial \mathbf{C}_{\text{node}}}{\partial \mathbf{W}_{\text{node}}} \in \mathbb{R}^{n_{\chi}^{\text{node}} \times n_x^{\text{node}}}, \end{aligned} \quad (3.23)$$

where  $\partial \hat{\mathbf{Y}} / \partial \mathbf{T}_{\text{node}} \in \mathbb{R}^{n_t \times n_y}$  is the gradient of the ODE solver computed by the adjoint sensitivity method [78],  $\mathbf{T}_{\text{node}} \in \mathbb{R}^{n_t \times n_{\tau}^{\text{node}}}$  and  $\mathbf{C}_{\text{node}} \in \mathbb{R}^{n_t \times n_{\chi}^{\text{node}}}$  are  $\boldsymbol{\tau}_{\text{node}}$  and  $\boldsymbol{\chi}_{\text{node}}$  at all time steps respectively, and

$$\frac{\partial \mathbf{C}_{\text{node}}}{\partial \mathbf{W}_{\text{node}}} = \mathbf{C}_{\text{node}}^T \ln \mathbf{X}_{\text{node}} \in \mathbb{R}^{n_{\chi}^{\text{node}} \times n_x^{\text{node}}}. \quad (3.24)$$

Similarly, we can calculate the gradient of MSE loss on the nodal bias term as  $\nabla_{\mathbf{b}_{\text{node}}} \mathcal{L}$ . In this research, we utilize an automatic differentiation engine in the PyTorch [79], a Python

library for deep learning, to automatically compute these gradients. Also, the gradient of the ODE solver has been built in the `torchdiffeq` [78]. So, we do not have to implement these gradient formulas ourselves.

When the gradients are available, the weight and bias are updated through the gradient descent algorithm [77]:

$$\mathbf{W}_{\text{node}} \leftarrow \mathbf{W}_{\text{node}} - \eta_{\mathbf{W}_{\text{node}}} \nabla_{\mathbf{W}_{\text{node}}} \mathcal{L}, \quad (3.25)$$

$$\mathbf{b}_{\text{node}} \leftarrow \mathbf{b}_{\text{node}} - \eta_{\mathbf{b}_{\text{node}}} \nabla_{\mathbf{b}_{\text{node}}} \mathcal{L}, \quad (3.26)$$

where  $\eta_{\mathbf{W}_{\text{node}}}$  and  $\eta_{\mathbf{b}_{\text{node}}}$  are learning rates, which can control step sizes in the gradient descent algorithm. After enough iterations, this algorithm can find a local minimum of the MSE loss. By combining the gradient descent with the back propagation, we are able to optimize the parameters in the diffusivity time model (i.e.,  $\alpha_H, \alpha_B, \dots, \alpha_a$  in the Equation 3.3).

### 3.3.3 Vanishing and Exploding Gradient Problem

However, this is one issue to be addressed. When the back propagation is processed in the ODE solver, the gradient can explode, which is similar to the Recurrent Neural Network (RNN). Intuitively, let  $\mathbf{A} \in \mathbb{R}^{n \times n}$  be a square matrix, and its eigenvalue decomposition is  $\mathbf{A} = \mathbf{Q}\mathbf{\Lambda}\mathbf{Q}^{-1}$ , where  $\mathbf{Q} \in \mathbb{R}^{n \times n}$  whose columns are eigenvectors of  $\mathbf{A}$ , and  $\mathbf{\Lambda}$  is the diagonal matrix for eigenvalues of  $\mathbf{A}$  and  $|\lambda_1| \geq |\lambda_2| \geq \dots \geq |\lambda_n|$ . Then,

$$\mathbf{A}^k = (\mathbf{Q}\mathbf{\Lambda}\mathbf{Q}^{-1}) (\mathbf{Q}\mathbf{\Lambda}\mathbf{Q}^{-1}) \dots (\mathbf{Q}\mathbf{\Lambda}\mathbf{Q}^{-1}) = \mathbf{Q}\mathbf{\Lambda}^k\mathbf{Q}^{-1}. \quad (3.27)$$

When  $|\lambda_1| > 1$ ,  $\lim_{k \rightarrow \infty} \|\mathbf{A}^k\| \rightarrow \infty$ , which can lead to exploding gradient when the sequence is overlong. It is also similar to the vanishing gradient. There are some methods to avoid the gradient exploding or vanishing. In this work, we simply limit the length of the time sequence of one shot, so that the gradients will not vanish or explode. Better methods can

be implemented in the future.

Collecting all pieces in the previous sections together, we can build the multinodal model with the diffusivity and transport time models, solve it to get solutions, then optimize the diffusivity model for better predictions. All these things give the algorithm inside the GTBURN package, which is introduced in the next section.

### 3.4 GTBURN Package

In this section, the framework of GTBURN, a Python package developed for burning plasma dynamics models, is described. Although the GTBURN package can be used for solving the one nodal model as the Appendix A, only the multinodal model is focused on here.

The GTBURN package includes the following modules.

- **Data:** A module reads in the experiment data such as the DIII-D data from the OM-FIT (One Modeling Framework for Integrated Tasks) [80], including two-dimensional data  $n_e$ ,  $n_z$ ,  $T_e$ ,  $T_i$  (depending on  $\rho$  and  $t$ ), and one-dimensional data  $a$ ,  $R_0$ ,  $\kappa$ ,  $B_T$ ,  $I_P$ ,  $P_{\text{tot}}$ ,  $P_\Omega$ ,  $P_{\text{NBI}}$ , etc. (depending on  $t$  only). For ITER, the conditions of design scenarios from the ITER design book [31] are used.
- **Preprocessor:** A module preprocesses data into time sequences. Since the original signal can be sampled at different times, we need this module to interpolate all signals at one consistent time list. Also, the volume-averaging is done for the two-dimensional signals by the Equation 2.130 to get the nodal particle densities and temperatures.
- **Diffusivity model:** A module implements the model for particle and thermal diffusivities. The Equation 3.11 is built for each node with its corresponding parameters. The shot conditions are combined into input vectors, and the diffusivities are given

from the model as output vectors. Several undetermined parameters are contained in this module, which are initialized properly from empirical formulas.

- **Transport time model:** A module computes the particle and energy transport times as the Equation 3.19. The particle and thermal diffusivities from the diffusivity model are used as inputs, and the internodal transport times are given out from this module.
- **Reactor:** A module simulates the tokamak by the multinodal burning plasma dynamics model. The particle and energy sources and sinks are computed from the experiment data. The internodal transport times are utilized for building the transport terms. Then, these terms are assembled together into one dynamical system and are ready to be solved by an ordinary differential equation (ODE) solver.
- **Dynamical system solver:** A module solves the dynamical system from the reactor. Solutions of this solver are the estimated particle densities and temperatures. This solver is designed to be differentiable, which means the back propagation algorithm is allowed for computing gradients through it.
- **Optimizer:** A module calculates the mean square error (MSE) between the estimated particle densities and temperatures and experiment ones. The back propagation algorithm is used to allow the gradient of MSE to flow back to the diffusivity model, where parameters are updated with the gradient descent algorithm.

The workflow chart for GTBURN is shown in the Figure 3.1, where cylinders are represented dataset, rectangles are for modules, solid lines are for forward flows to solve the problem, and blue dash lines are for the back propagation to optimize the parameters in the diffusivity model. Python packages including NumPy [81], SciPy [82], Matplotlib [83], PyTorch [79], and torchdiffeq [78] are used. In GTBURN, plasma data from datasets are preprocessed in the preprocessor first, then inputted into the parametric diffusivity model to get particle and thermal diffusivities. Those diffusivities are then inputted

into the transport time model to get particle and energy transport times between different nodes. All particle and energy source and sink terms are inputted into the multinodal model, which is then solved by the dynamical system solver to obtain simulated nodal densities and temperatures. The optimizer takes both estimations and measurements to optimize parameters in the diffusivity model. Once the diffusivity model is optimized based on the experiment data, the whole multinodal model is used to predict results for new shots.

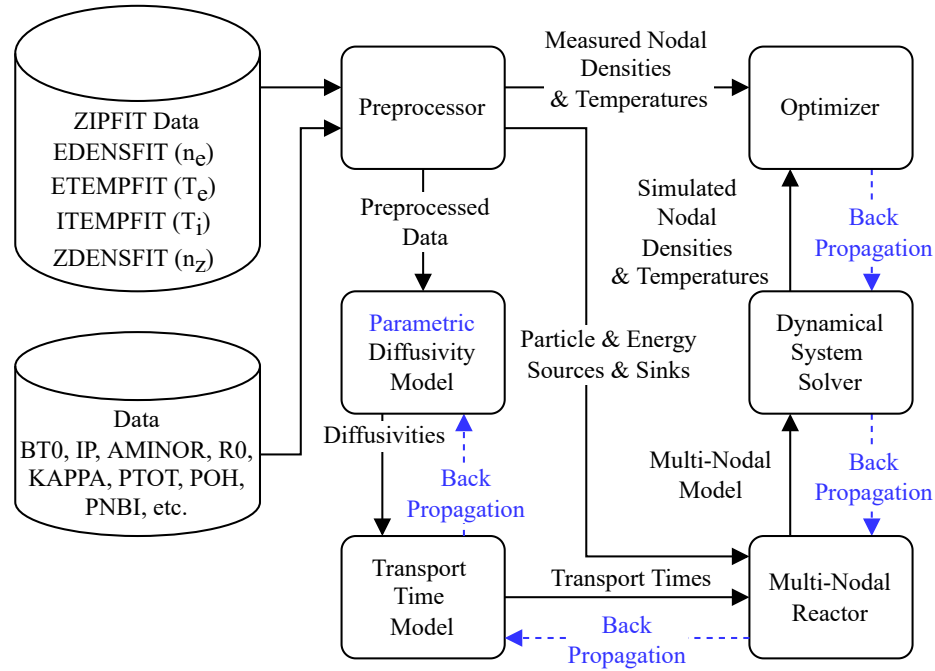


Figure 3.1: Workflow chart for the GTBURN, where solid lines are for the forward flow to solve the problem and dash lines are for back propagation to optimize the parameters in the diffusivity model.

### 3.5 Summary

This chapter proposes several computational methods for the multinodal burning plasma model. The main question answered in this chapter is how to obtain the internodal transport times. Firstly, previous methods based on global energy confinement times and experiment measurements are reviewed, and their limitations are discussed. Then, one novel method based on machine learning is proposed, where the parametric diffusivity model is initialized

by scaling laws and optimized using experimental data. Next, the relevant machine learning algorithms are explained, including back propagation and gradient descent. Finally, several modules in the GTBURN package are introduced for simulating plasmas with the multinodal model. In the following chapters, this package is used for DIII-D deuterium plasmas and ITER deuterium-tritium plasmas.



## CHAPTER 4

### MULTINODAL MODEL SIMULATIONS FOR DIII-D PLASMAS

In order to validate the proposed multinodal burning plasma dynamics model, it is crucial to apply the model for DIII-D non-fusion plasmas. In this chapter, the multinodal model is simplified to a three-nodal model and then simulated for DIII-D shots. Several necessary assumptions are made for the model's application to deuterium plasmas. The particle and energy balance equations are presented with the corresponding diffusivities and transport times. Experiment data and simulation settings are also explained. The data are split into training and testing datasets, where the diffusivity model is trained on the training dataset and then evaluated on the testing dataset. Finally, the simulation results are presented and analyzed for testing shots, and the strengths and weaknesses of the multinodal model for DIII-D plasmas are discussed at the end of this chapter.

#### 4.1 Assumptions for Modeling DIII-D Plasmas

In DIII-D experiments, deuterium plasmas are used. Due to a lower cross section and a higher energy threshold, the deuterium-deuterium (D-D) fusion reaction is neglected. Therefore, the multinodal model can be simplified to a non-reaction one. Several assumptions utilized to simplify the multinodal model for the DIII-D deuterium plasma are as follows.

1. Only the core, edge, and scrape-off layer (SOL) regions are modeled as nodes. The divertor, private flux region, plenum, and other regions are neglected.
2. Only the deuteron, electron, and one effective impurity particle (carbon) are considered. The triton, alpha particle, and other impurities are neglected.
3. Only  $n_D^{\text{node}}$ ,  $T_D^{\text{node}}$ , and  $T_e^{\text{node}}$  in the corresponding nodes are solved in the dynamics

model. The  $n_z^{\text{node}}$  is obtained from the experimental measurements, and the  $n_e^{\text{node}}$  is gotten from the charge neutrality.

4. The deuterium-deuterium (D-D), deuterium-tritium (D-T), and other fusion reactions are neglected.
5. Only atomic processes of ionization, recombination, charge exchange, and elastic scattering of deuterons are considered. Other atomic processes and all molecular processes are neglected.
6. The ohmic heating, neutral beam injection (NBI), electron cyclotron heating (ECH), ion cyclotron heating (ICH), and gas puffing deposition profiles are predetermined for all shots.
7. In the electron cyclotron radiation (ECR) formula (i.e., the Equation 2.88) , ITER coefficients  $\alpha_n = 0.5$ ,  $\alpha_T = 8.0$ ,  $\beta_T = 5.0$ , and  $r = 0.8$  are used.
8. The ion orbit loss (IOL) term is only included for the edge deuterons. Besides, the IOL timescales are approximated by the corresponding transport times from the edge to the SOL.

Most assumptions mentioned above allow us to take advantage of the DIII-D deuterium plasma data from OMFIT (One Modeling Framework for Integrated Tasks) [80] conveniently. However, some assumptions will be removed when the ITER plasma is studied in the next chapter.

## 4.2 Particle and Energy Balance Equations

The multinodal plasma dynamics model for DIII-D plasmas has two groups of equations, including particle balance equations and energy balance equations.

Particle balance equations for deuterons in the core, edge, and SOL nodes are

$$\frac{dn_D^{\text{core}}}{dt} = S_{D,\text{ext}}^{\text{core}} + S_{D,\text{tran}}^{\text{core}}, \quad (4.1)$$

$$\frac{dn_D^{\text{edge}}}{dt} = S_{D,\text{ext}}^{\text{edge}} + S_{D,\text{tran}}^{\text{edge}} + S_{D,\text{IOL}}^{\text{edge}}, \quad (4.2)$$

$$\frac{dn_D^{\text{sol}}}{dt} = S_{D,\text{ion}}^{\text{sol}} + S_{D,\text{rec}}^{\text{sol}} + S_{D,\text{tran}}^{\text{sol}} + S_{D,\text{IOL}}^{\text{sol}}. \quad (4.3)$$

The electron densities are solved from the charge neutrality equations:

$$n_e^{\text{core}} = z_D n_D^{\text{core}} + z_z n_z^{\text{core}}, \quad (4.4)$$

$$n_e^{\text{edge}} = z_D n_D^{\text{edge}} + z_z n_z^{\text{edge}}, \quad (4.5)$$

$$n_e^{\text{sol}} = z_D n_D^{\text{sol}} + z_z n_z^{\text{sol}}, \quad (4.6)$$

where atomic numbers are  $z_D = 1$  and  $z_z = 6$ . The particle sources and sinks on the right-hand sides of the particle balance equations are presented as follows.

1. The nodal external source term is  $S_{D,\text{ext}}^{\text{node}} = S_{D,\text{NBI}}^{\text{node}} + S_{D,\text{GAS}}^{\text{node}}$ .
2. The nodal ionization term is  $S_{D,\text{ion}}^{\text{sol}} = n_{D0}^{\text{sol}} n_e^{\text{sol}} \langle \sigma v \rangle_{D,\text{ion}}^{\text{sol}}$ , and the nodal recombination term is  $S_{D,\text{rec}}^{\text{sol}} = -n_D^{\text{sol}} n_e^{\text{sol}} \langle \sigma v \rangle_{D,\text{rec}}^{\text{sol}}$ .
3. The nodal transport terms are

$$S_{D,\text{tran}}^{\text{core}} = -\frac{n_D^{\text{core}} - n_D^{\text{edge}}}{\tau_{P,D}^{\text{core} \rightarrow \text{edge}}}, \quad (4.7)$$

$$S_{D,\text{tran}}^{\text{edge}} = \frac{V_{\text{core}}}{V_{\text{edge}}} \frac{n_D^{\text{core}} - n_D^{\text{edge}}}{\tau_{P,D}^{\text{core} \rightarrow \text{edge}}} - \frac{n_D^{\text{edge}}}{\tau_{P,D}^{\text{edge} \rightarrow \text{sol}}}, \quad (4.8)$$

$$S_{D,\text{tran}}^{\text{sol}} = \frac{V_{\text{edge}}}{V_{\text{sol}}} \frac{n_D^{\text{edge}}}{\tau_{P,D}^{\text{edge} \rightarrow \text{sol}}} - \frac{n_D^{\text{sol}}}{\tau_{P,D}^{\text{sol} \rightarrow \text{div}}}, \quad (4.9)$$

where  $\tau_{P,D}^{\text{core} \rightarrow \text{edge}}$  is the particle transport time from the core node to the edge node,  $\tau_{P,D}^{\text{edge} \rightarrow \text{sol}}$  is the particle transport time from the edge node to the SOL node, and

$\tau_{P,\sigma}^{\text{sol} \rightarrow \text{div}}$  is the particle confinement time from the SOL node to the divertor and plenum. The formulas of particle transport times are

$$\tau_{P,\sigma}^{\text{core} \rightarrow \text{edge}} = \frac{r_{\text{core}}^2}{2r_{\text{core}}} \frac{\Delta r_{\text{core-edge}}}{D_{\sigma}^{\text{core}}}, \quad (4.10)$$

$$\tau_{P,\sigma}^{\text{edge} \rightarrow \text{sol}} = \frac{r_{\text{edge}}^2 - r_{\text{core}}^2}{2r_{\text{edge}}} \frac{\Delta r_{\text{edge-sol}}}{D_{\sigma}^{\text{edge}}}, \quad (4.11)$$

$$\tau_{P,\sigma}^{\text{sol} \rightarrow \text{div}} = \frac{r_{\text{sol}}^2 - r_{\text{edge}}^2}{2r_{\text{sol}}} \frac{\Delta r_{\text{sol-div}}}{D_{\sigma}^{\text{sol}}}, \quad (4.12)$$

where  $D_{\sigma}^{\text{core}}$ ,  $D_{\sigma}^{\text{edge}}$ , and  $D_{\sigma}^{\text{sol}}$  are particle diffusivities.

4. The IOL terms are

$$S_{\text{D,IOL}}^{\text{edge}} = -\frac{F_{\text{D,orb}}^{\text{edge}}}{\tau_{P,\text{D,IOL}}^{\text{edge}}} n_{\text{D}}^{\text{edge}}, \quad S_{\text{D,IOL}}^{\text{sol}} = -\frac{V_{\text{edge}}}{V_{\text{sol}}} S_{\text{D,IOL}}^{\text{edge}}, \quad (4.13)$$

where the particle loss fraction  $F_{\text{D,orb}}^{\text{edge}}$  is evaluated at the center of the edge node  $\rho_{\text{edge}}^{\text{IOL}} = (\rho_{\text{edge}} + \rho_{\text{core}})/2$ , and the particle loss timescale is approximated by the particle transport time:  $\tau_{P,\text{D,IOL}}^{\text{edge}} \approx \tau_{P,\text{D}}^{\text{edge} \rightarrow \text{sol}}$ .

Energy balance equations for deuterons and electrons in the core, edge, and SOL nodes are

$$\frac{dU_{\text{D}}^{\text{core}}}{dt} = P_{\text{D,aux}}^{\text{core}} + Q_{\text{D}}^{\text{core}} + P_{\text{D,tran}}^{\text{core}}, \quad (4.14)$$

$$\frac{dU_{\text{D}}^{\text{edge}}}{dt} = P_{\text{D,aux}}^{\text{edge}} + Q_{\text{D}}^{\text{edge}} + P_{\text{D,tran}}^{\text{edge}} + P_{\text{D,IOL}}^{\text{edge}}, \quad (4.15)$$

$$\frac{dU_{\text{D}}^{\text{sol}}}{dt} = P_{\text{D,at}}^{\text{sol}} + Q_{\text{D}}^{\text{sol}} + P_{\text{D,tran}}^{\text{sol}} + P_{\text{D,IOL}}^{\text{sol}}, \quad (4.16)$$

$$\frac{dU_e^{\text{core}}}{dt} = P_{\Omega}^{\text{core}} + P_{e,\text{aux}}^{\text{core}} - P_R^{\text{core}} + Q_e^{\text{core}} + P_{e,\text{tran}}^{\text{core}}, \quad (4.17)$$

$$\frac{dU_e^{\text{edge}}}{dt} = P_{\Omega}^{\text{edge}} + P_{e,\text{aux}}^{\text{edge}} - P_R^{\text{core}} + Q_e^{\text{edge}} + P_{e,\text{tran}}^{\text{edge}}, \quad (4.18)$$

$$\frac{dU_e^{\text{sol}}}{dt} = P_{e,\text{ion}}^{\text{sol}} + P_{e,\text{rec}}^{\text{sol}} - P_R^{\text{sol}} + Q_e^{\text{sol}} + P_{e,\text{tran}}^{\text{sol}}, \quad (4.19)$$

where for  $\sigma \in \{D, e\}$  and  $\text{node} \in \{\text{core}, \text{edge}, \text{sol}\}$ , the nodal energy is  $U_\sigma^{\text{node}} = \frac{3}{2} n_\sigma^{\text{node}} T_\sigma^{\text{node}}$ .

The energy sources and sinks on the right-hand sides are presented as follows.

1. The nodal ohmic heating term is approximated by the global averaged one:  $P_\Omega^{\text{node}} \approx P_\Omega$ .
2. The nodal auxiliary heating term is  $P_{\sigma,\text{aux}}^{\text{node}} = P_{\sigma,\text{NBI}}^{\text{node}} + P_{\sigma,\text{RF}}^{\text{node}}$ .
3. The nodal Coulomb collisional energy transfer terms are

$$Q_D^{\text{node}} = Q_{De}^{\text{node}} = \frac{n_D^{\text{node}} n_e^{\text{node}} (q_D q_e)^2 m_e \ln \Lambda \left(1 - \frac{T_D^{\text{node}}}{T_e^{\text{node}}}\right)}{2\pi\epsilon_0^2 (2\pi m_e T_e^{\text{node}})^{1/2} m_D \left[1 + \frac{4\sqrt{\pi}}{3} \left(\frac{3m_e T_D^{\text{node}}}{2m_D T_e^{\text{node}}}\right)^{3/2}\right]}, \quad (4.20)$$

and  $Q_e^{\text{node}} = -Q_{De}^{\text{node}}$ .

4. The nodal radiation term for the core and edge nodes is  $P_R^{\text{node}} = P_{\text{ECR}}^{\text{node}} + P_{\text{brem}}^{\text{node}} + P_{\text{imp}}^{\text{node}}$ , where radiation terms on the right-hand side are calculated by the Equation 2.94, 2.104, and 2.106 respectively. The radiation term for the SOL node is  $P_R^{\text{sol}} = P_{\text{brem}}^{\text{sol}} + P_{\text{imp}}^{\text{sol}}$ .
5. The nodal charge exchange and elastic scattering term is

$$P_{D,\text{at}}^{\text{sol}} = -\frac{3}{2} (T_D^{\text{sol}} - T_{D0,c}^{\text{sol}}) n_D^{\text{sol}} n_{D0,c}^{\text{sol}} \left( \langle \sigma v \rangle_{D,\text{cx}}^{\text{sol}} + \langle \sigma v \rangle_{D,\text{el}}^{\text{sol}} \right), \quad (4.21)$$

where  $\langle \sigma v \rangle_{D,\text{cx}}^{\text{sol}}$  and  $\langle \sigma v \rangle_{D,\text{el}}^{\text{sol}}$  are charge exchange and elastic scattering reaction rate coefficients,  $n_{D0,c}^{\text{sol}} \approx R_N n_{D0}^{\text{sol}}$ , and  $T_{D0,c}^{\text{sol}} \approx 1 \text{ eV}$ .

6. The nodal ionization term is  $P_{e,\text{ion}}^{\text{sol}} = -E_{D,\text{ion}} n_{D0}^{\text{sol}} n_e^{\text{sol}} \langle \sigma v \rangle_{D,\text{ion}}^{\text{sol}}$ , where the  $\langle \sigma v \rangle_{D,\text{ion}}^{\text{sol}}$  is the ionization reaction rate coefficient, the  $E_{D,\text{ion}}$  is the ionization energy, and  $n_{D0}^{\text{sol}} = 10^{15} \text{ m}^{-3}$ . The nodal recombination term is  $P_{e,\text{rec}}^{\text{sol}} = E_{D,\text{rec}} n_D^{\text{sol}} n_e^{\text{sol}} \langle \sigma v \rangle_{D,\text{rec}}^{\text{sol}}$ ,

where the  $\langle\sigma v\rangle_{D,\text{rec}}^{\text{sol}}$  is the recombination reaction rate coefficient and the  $E_{D,\text{rec}}$  is the recombination energy.

## 7. The nodal transport terms are

$$P_{\sigma,\text{tran}}^{\text{core}} = -\frac{U_{\sigma}^{\text{core}} - U_{\sigma}^{\text{edge}}}{\tau_{E,\sigma}^{\text{core}\rightarrow\text{edge}}}, \quad (4.22)$$

$$P_{\sigma,\text{tran}}^{\text{edge}} = \frac{V_{\text{core}}}{V_{\text{edge}}} \frac{U_{\sigma}^{\text{core}} - U_{\sigma}^{\text{edge}}}{\tau_{E,\sigma}^{\text{core}\rightarrow\text{edge}}} - \frac{U_{\sigma}^{\text{edge}}}{\tau_{E,\sigma}^{\text{edge}\rightarrow\text{sol}}}, \quad (4.23)$$

$$P_{\sigma,\text{tran}}^{\text{sol}} = \frac{V_{\text{edge}}}{V_{\text{sol}}} \frac{U_{\sigma}^{\text{edge}}}{\tau_{E,\sigma}^{\text{edge}\rightarrow\text{sol}}} - \frac{U_{\sigma}^{\text{sol}}}{\tau_{E,\sigma}^{\text{sol}\rightarrow\text{div}}}, \quad (4.24)$$

where  $\tau_{E,\sigma}^{\text{core}\rightarrow\text{edge}}$  is the energy transport time from the core node and to the edge node,  $\tau_{E,\sigma}^{\text{edge}\rightarrow\text{sol}}$  is the energy transport time from the edge node to the SOL node, and the  $\tau_{E,\sigma}^{\text{sol}\rightarrow\text{div}}$  is the energy confinement time for the SOL node. The formulas of energy transport times are

$$\tau_{E,\sigma}^{\text{core}\rightarrow\text{edge}} = \frac{r_{\text{core}}^2}{2r_{\text{core}}} \frac{\Delta r_{\text{core-edge}}}{\chi_{\sigma}^{\text{core}}}, \quad (4.25)$$

$$\tau_{E,\sigma}^{\text{edge}\rightarrow\text{sol}} = \frac{r_{\text{edge}}^2 - r_{\text{core}}^2}{2r_{\text{edge}}} \frac{\Delta r_{\text{edge-sol}}}{\chi_{\sigma}^{\text{edge}}}, \quad (4.26)$$

$$\tau_{E,\sigma}^{\text{sol}\rightarrow\text{div}} = \frac{r_{\text{sol}}^2 - r_{\text{edge}}^2}{2r_{\text{sol}}} \frac{\Delta r_{\text{sol-div}}}{\chi_{\sigma}^{\text{sol}}}, \quad (4.27)$$

where  $\chi_{\sigma}^{\text{core}}$ ,  $\chi_{\sigma}^{\text{edge}}$  and  $\chi_{\sigma}^{\text{sol}}$  are thermal diffusivities.

## 8. The IOL terms are

$$P_{D,\text{IOL}}^{\text{edge}} = -\frac{E_{D,\text{orb}}^{\text{edge}}}{\tau_{E,D,\text{IOL}}^{\text{edge}}} U_D^{\text{edge}}, \quad P_{D,\text{IOL}}^{\text{sol}} = -\frac{V_{\text{edge}}}{V_{\text{sol}}} P_{D,\text{IOL}}^{\text{edge}}, \quad (4.28)$$

where  $E_{D,\text{orb}}^{\text{edge}}$  is the energy loss fraction evaluated at the edge center, and the energy loss timescale is approximated by the energy transport time:  $\tau_{E,D,\text{IOL}}^{\text{edge}} \approx \tau_{E,D}^{\text{edge}\rightarrow\text{sol}}$ .

### 4.3 Diffusivity and Transport Time Models

In this section, the diffusivity and internodal transport time formulas are simplified for the DIII-D plasma based on the assumptions in the Section 4.1. Only particle diffusivities for deuterons and thermal diffusivities for deuterons and electrons in the core, edge, and SOL nodes are considered. Other diffusivities are neglected in the multinodal model for DIII-D. Besides, only particle transport times for deuterons and energy transport times for deuterons and electrons are modeled.

Let the diffusivity vectors at the core-edge, edge-SOL, and SOL-plenum/divertor surfaces be

$$\chi_{\text{core}} = \begin{bmatrix} D_{\text{D}}^{\text{core}} & \chi_{\text{D}}^{\text{core}} & \chi_e^{\text{core}} \end{bmatrix}^{\text{T}}, \quad (4.29)$$

$$\chi_{\text{edge}} = \begin{bmatrix} D_{\text{D}}^{\text{edge}} & \chi_{\text{D}}^{\text{edge}} & \chi_e^{\text{edge}} \end{bmatrix}^{\text{T}}, \quad (4.30)$$

$$\chi_{\text{sol}} = \begin{bmatrix} D_{\text{D}}^{\text{sol}} & \chi_{\text{D}}^{\text{sol}} & \chi_e^{\text{sol}} \end{bmatrix}^{\text{T}}, \quad (4.31)$$

where the unit of diffusivities is  $1 \text{ m}^2/\text{s}$ . The parametric diffusivity models are

$$\chi_{\text{core}} = \exp(\mathbf{b}_{\text{core}} + \mathbf{W}_{\text{core}} \ln \mathbf{x}_{\text{core}}), \quad (4.32)$$

$$\chi_{\text{edge}} = \exp(\mathbf{b}_{\text{edge}} + \mathbf{W}_{\text{edge}} \ln \mathbf{x}_{\text{edge}}), \quad (4.33)$$

$$\chi_{\text{sol}} = \exp(\mathbf{b}_{\text{sol}} + \mathbf{W}_{\text{sol}} \ln \mathbf{x}_{\text{sol}}), \quad (4.34)$$

where  $\mathbf{W}_{\text{core}}$ ,  $\mathbf{W}_{\text{edge}}$ ,  $\mathbf{W}_{\text{sol}}$ ,  $\mathbf{b}_{\text{core}}$ ,  $\mathbf{b}_{\text{edge}}$ , and  $\mathbf{b}_{\text{sol}}$  are model parameters. The input vectors of the diffusivity models are

$$\mathbf{x}_{\text{core}} = \left[ \frac{B_T}{1 \text{ T}} \quad \frac{n_e^{\text{core}}}{10^{19} \text{ m}^{-3}} \quad \frac{T_e^{\text{core}}}{1 \text{ keV}} \quad \frac{|\nabla T_e|_{\text{core}}}{1 \text{ keV/m}} \quad q_{\text{core}} \quad \kappa_{\text{core}} \quad \frac{M}{1 \text{ amu}} \quad \frac{R}{1 \text{ m}} \quad \frac{a}{1 \text{ m}} \right], \quad (4.35)$$

$$\mathbf{x}_{\text{edge}} = \left[ \frac{B_T}{1 \text{ T}} \quad \frac{n_e^{\text{edge}}}{10^{19} \text{ m}^{-3}} \quad \frac{T_e^{\text{edge}}}{1 \text{ keV}} \quad \frac{|\nabla T_e|_{\text{edge}}}{1 \text{ keV/m}} \quad q_{\text{edge}} \quad \kappa_{\text{edge}} \quad \frac{M}{1 \text{ amu}} \quad \frac{R}{1 \text{ m}} \quad \frac{a}{1 \text{ m}} \right], \quad (4.36)$$

$$\mathbf{x}_{\text{sol}} = \left[ \frac{B_T}{1 \text{ T}} \quad \frac{n_e^{\text{sol}}}{10^{19} \text{ m}^{-3}} \quad \frac{T_e^{\text{sol}}}{1 \text{ keV}} \quad \frac{|\nabla T_e|_{\text{sol}}}{1 \text{ keV/m}} \quad q_{\text{sol}} \quad \kappa_{\text{sol}} \quad \frac{M}{1 \text{ amu}} \quad \frac{R}{1 \text{ m}} \quad \frac{a}{1 \text{ m}} \right], \quad (4.37)$$

where  $q_{\text{core}} \approx q_{\text{edge}} \approx q_{\text{sol}} \approx q_{95}$  (the safety factor at the 95% flux surface),  $\kappa_{\text{node}} \approx \kappa$  (the global elongation), and

$$|\nabla T_e|_{\text{core}} \approx \frac{|T_e^{\text{core}} - T_e^{\text{edge}}|}{\Delta r_{\text{core-edge}}}, \quad |\nabla T_e|_{\text{edge}} \approx \frac{|T_e^{\text{edge}}|}{\Delta r_{\text{edge-sol}}}, \quad |\nabla T_e|_{\text{sol}} \approx \frac{|T_e^{\text{sol}}|}{\Delta r_{\text{sol-div}}}. \quad (4.38)$$

Here the core and edge gradients only depend on the core and edge electron temperatures, so that the core and edge nodes can be decoupled from the SOL node for convenience in model training. Also, when the burning plasma physics in the core and edge nodes is focused on, the SOL can be removed from the multinodal model. This simplification will be helpful when multinodal model is applied for ITER.

The internodal transport times are built based on the nodal diffusivities. The core transport time vector containing internodal transport times from the core to edge is

$$\boldsymbol{\tau}_{\text{core}} = \begin{bmatrix} \tau_{P,D}^{\text{core} \rightarrow \text{edge}} \\ \tau_{E,D}^{\text{core} \rightarrow \text{edge}} \\ \tau_{E,e}^{\text{core} \rightarrow \text{edge}} \end{bmatrix} = \begin{bmatrix} \frac{r_{\text{core}}^2}{2r_{\text{core}}} \frac{\Delta r_{\text{core-edge}}}{D_D^{\text{core}}} \\ \frac{r_{\text{core}}^2}{2r_{\text{core}}} \frac{\Delta r_{\text{core-edge}}}{\chi_D^{\text{core}}} \\ \frac{r_{\text{core}}^2}{2r_{\text{core}}} \frac{\Delta r_{\text{core-edge}}}{\chi_e^{\text{core}}} \end{bmatrix} = \frac{r_{\text{core}}^2}{2r_{\text{core}}} \Delta r_{\text{core-edge}} \oslash \boldsymbol{\chi}_{\text{core}}, \quad (4.39)$$

where  $\oslash$  is the componentwise division. The edge transport time vector for transport times



from the edge to SOL is

$$\boldsymbol{\tau}_{\text{edge}} = \begin{bmatrix} \tau_{P,D}^{\text{edge} \rightarrow \text{sol}} \\ \tau_{E,D}^{\text{edge} \rightarrow \text{sol}} \\ \tau_{E,e}^{\text{edge} \rightarrow \text{sol}} \end{bmatrix} = \begin{bmatrix} \frac{r_{\text{edge}}^2 - r_{\text{core}}^2}{2r_{\text{edge}}} \frac{\Delta r_{\text{edge-sol}}}{D_D^{\text{edge}}} \\ \frac{r_{\text{edge}}^2 - r_{\text{core}}^2}{2r_{\text{edge}}} \frac{\Delta r_{\text{edge-sol}}}{\chi_D^{\text{edge}}} \\ \frac{r_{\text{edge}}^2 - r_{\text{core}}^2}{2r_{\text{edge}}} \frac{\Delta r_{\text{edge-sol}}}{\chi_e^{\text{edge}}} \end{bmatrix} = \frac{r_{\text{edge}}^2 - r_{\text{core}}^2}{2r_{\text{edge}}} \Delta r_{\text{edge-sol}} \odot \boldsymbol{\chi}_{\text{edge}}. \quad (4.40)$$

And the SOL transport time vector for transport times from the SOL to divertor and plenum (or the effective confinement times of SOL to the outside of plasma) is

$$\boldsymbol{\tau}_{\text{sol}} = \begin{bmatrix} \tau_{P,D}^{\text{sol} \rightarrow \text{div}} \\ \tau_{E,D}^{\text{sol} \rightarrow \text{div}} \\ \tau_{E,e}^{\text{sol} \rightarrow \text{div}} \end{bmatrix} = \begin{bmatrix} \frac{r_{\text{sol}}^2 - r_{\text{edge}}^2}{2r_{\text{sol}}} \frac{\Delta r_{\text{sol-div}}}{D_D^{\text{sol}}} \\ \frac{r_{\text{sol}}^2 - r_{\text{edge}}^2}{2r_{\text{sol}}} \frac{\Delta r_{\text{sol-div}}}{\chi_D^{\text{sol}}} \\ \frac{r_{\text{sol}}^2 - r_{\text{edge}}^2}{2r_{\text{sol}}} \frac{\Delta r_{\text{sol-div}}}{\chi_e^{\text{sol}}} \end{bmatrix} = \frac{r_{\text{sol}}^2 - r_{\text{edge}}^2}{2r_{\text{sol}}} \Delta r_{\text{sol-div}} \odot \boldsymbol{\chi}_{\text{sol}}. \quad (4.41)$$

All these formulas have been built in the GTBURN package.

#### 4.4 Experiment Data and Simulation Settings

After the multinodal model and the parametric diffusivity formula are formalized, the experiment data used for the DIII-D plasma simulations can be presented. The shots used in this work are listed in the Table 4.1 with the signals in Table 4.2. These data selections follow Hill et al. [10]. The selected shots are limited to the ELMing non-RMP (non-resonant magnetic perturbation) H-mode with the standard magnetic field configuration. Basic descriptions of these shots, including the ohmic heating power, electron cyclotron heating (ECH) power, ion cyclotron heating (ICH) power, neutral beam injection (NBI) power, gas puffing, magnetic field at the magnetic axis, electron density and temperature, are listed in the Table 4.1. Besides, several signals for these shots are used, including geometric parameters (e.g., minor radius, major radius, plasma volume, etc.), electromagnetic parameters (e.g., plasma current, toroidal field, etc.), powers (e.g., ohmic heating power, NBI power,

etc.). The particle density and temperature profiles are collected from the ZIPFIT [84, 80], which fits profiles using EFIT data and Thomson data. The profiles are integrated to get nodal densities and temperatures.

Table 4.1: Experiment shots [10] from DIII-D used in this study, where densities and temperatures are volume-averaged over the whole plasma.

Shot	$P_{\Omega}/\text{MW}$	$P_{\text{ECH}}/\text{MW}$	$P_{\text{ICH}}/\text{MW}$	$P_{\text{NBI}}/\text{MW}$	$\text{GAS}/(\text{Torr} \cdot \text{L/s})$	$ B_0 /\text{T}$	$n_e/10^{19} \text{ m}^{-3}$	$T_e/\text{keV}$
131190*	-0.18-0.57	0.00-2.44	0.00	2.01-9.21	11.29-162.33	1.72-1.92	1.25-4.65	0.50-2.80
131191	-0.11-0.26	0.00-2.38	0.00	2.57-9.20	14.11-87.21	1.73-1.87	1.08-3.89	0.46-3.24
131195	0.07-0.43	0.00-2.23	0.00	2.61-9.65	7.99-76.45	1.77-1.86	1.14-3.27	0.89-2.29
131196	0.00-0.78	0.00-1.27	0.00	2.02-9.79	11.35-84.68	1.76-1.87	1.14-3.63	0.49-2.63
134350	-0.22-0.82	0.00-3.15	0.00	2.39-9.27	0.00-90.14	1.73-1.93	1.11-6.60	0.45-2.96
135837	-0.06-0.58	0.00	0.00	0.00-14.44	0.05-46.83	1.73-2.04	1.22-4.85	0.35-1.65
135843	0.16-1.43	0.00	0.00	0.06-7.12	0.05-115.68	1.82-2.13	0.65-6.55	0.29-1.80
140417	0.02-0.89	0.00	0.00	0.61-4.37	0.00-70.65	1.90-2.02	1.82-5.18	0.48-1.44
140418*	-0.07-0.85	0.00	0.00	0.61-4.13	0.00-64.55	1.87-2.05	1.70-5.00	0.43-1.30
140419	-0.12-0.82	0.00	0.00	0.61-4.12	0.00-39.96	1.92-2.05	1.43-5.26	0.48-1.49
140420*	0.10-0.98	0.00-3.34	0.00	0.61-4.12	0.00-21.69	1.88-2.07	0.96-6.94	0.45-1.76
140421	-0.23-0.84	0.00-3.23	0.00	0.61-4.11	0.00-17.94	1.90-2.06	0.99-5.77	0.57-1.76
140422	-0.20-0.89	0.00	0.00	0.61-4.13	0.00-23.60	1.92-2.06	0.93-4.85	0.51-1.78
140423	-0.13-0.86	0.00	0.00	0.61-4.11	0.00-30.99	1.93-2.06	0.96-4.44	0.50-1.88
140424	-0.02-0.85	0.00	0.00	0.61-4.14	0.05-104.98	1.92-2.05	1.22-6.94	0.51-1.66
140425	0.05-0.84	0.00	0.00	0.61-4.14	0.02-112.07	1.90-2.06	1.19-7.73	0.42-1.49
140427*	0.09-0.96	0.00	0.00	0.61-4.15	0.02-109.97	1.93-2.05	1.94-7.15	0.42-1.19
140428	0.10-0.87	0.00	0.00	0.61-4.15	0.00-0.20	1.91-2.06	1.50-7.06	0.48-1.13
140429	0.16-0.84	0.00	0.00	0.61-4.15	0.00-6.46	1.92-2.05	1.09-6.82	0.46-1.24
140430	0.00-0.88	0.00	0.00-0.04	0.61-4.15	0.00-26.28	1.93-2.08	1.08-4.24	0.48-1.61
140431	-0.06-0.95	0.00	0.00-0.04	0.61-4.16	0.00-38.34	1.91-2.09	1.00-4.17	0.53-1.86
140432	-0.08-0.95	0.00	0.00	0.61-4.13	0.00-50.36	1.90-2.09	0.98-3.85	0.48-2.06
140440	0.12-1.03	0.00	0.00	0.61-4.14	0.03-108.87	1.95-2.09	1.47-7.43	0.49-1.29
140535*	0.18-0.69	0.00	0.00-0.03	0.63-4.48	0.07-118.15	1.92-2.10	1.13-2.11	0.23-1.29
140673	0.00-0.49	0.00-3.38	0.00-0.29	1.95-11.26	0.00-102.17	1.65-1.78	1.16-4.76	0.34-1.39

\* Shots in the testing dataset.

In order to prevent over-fitting for a particular shot and also obtain a general multinodal to cover a wide range of shots, the selected shots in the Table 4.1 are divided into two datasets: one training dataset including 20 shots, which are in the Table 4.1 without stars, and another testing dataset including 5 shots, which are in the Table 4.1 with stars. The training dataset is used to optimize the parametric diffusivity model, while the testing dataset is used to evaluate the performances of the optimized model. In detail, the computational experiment is done as follows:

Table 4.2: DIII-D experimental signals from OMFIT [80] used in the multinodal model.

Name	Units	Tree	Description
AMINOR	m	EFIT	Minor radius
R0	m	EFIT	Major radius of magnetic axis
VOLUME	m <sup>3</sup>	EFIT	Plasma volume
KAPPA0	-	EFIT	Elongation at magnetic axis
TRITOP	-	EFIT	Top triangularity
TRIBOT	-	EFIT	Bottom triangularity
IP	A	N/A	Plasma current measured with Rogowski loops
BT0	T	EFIT	Toroidal field at magnetic axis
LI	-	EFIT	Internal inductance
Q0	-	EFIT	$q$ at magnetic axis
Q95	-	EFIT	$q$ at 95% flux surface
PTOT	W	EFIT	Total input power, including NBI, Ohmic, ECH, and ICH
POH	W	EFIT	Ohmic power
PNBI	W	EFIT	Total Injected neutral beam power
ECHPWRC	W	N/A	Total ECH power
ICHPWRC	W	N/A	Total RF power
GASA_CAL	Torr · L/s	NEUTRALS	Calibrated gasflow measurements from the 5 gas valves (A-E)
EDENSFIT	10 <sup>19</sup> m <sup>-3</sup>	ZIPFIT01	Electron density
ETEMPFIT	keV	ZIPFIT01	Electron temperature
ITEMPFIT	keV	ZIPFIT01	Ion temperature
ZDENSFIT	10 <sup>19</sup> m <sup>-3</sup>	ZIPFIT01	Impurity density

- Training process: The dynamical system of the multinodal model is solved on the training dataset by following the black arrows in the Figure 3.1. During this process, the data are preprocessed into time sequences. Then the nodal diffusivities are gotten and inputted into the internodal transport time model, where the parameters from the  $\chi_{H98}$  model [17] are used for initializing the diffusivity model. Next, the nodal source terms with the transport times are integrated into a multinodal model. This model is solved in a dynamical system solver to get the simulated nodal densities  $\hat{n}_\sigma^{\text{node}}$  and temperatures  $\hat{T}_\sigma^{\text{node}}$ . After it, the mean squared error (MSE) is computed as

$$\text{MSE} = \frac{1}{n_t n_y} \sum_{t_i} \|\mathbf{y}_{t_i} - \hat{\mathbf{y}}_{t_i}\|_2^2, \quad (4.42)$$

where for each time step, the simulation solution from the multinodal model is

$$\hat{\mathbf{y}}_{t_i} = \left[ \begin{array}{ccc} \frac{\hat{n}_D^{\text{node}}}{10^{19} \text{ m}^{-3}} & \frac{\hat{T}_D^{\text{node}}}{1 \text{ keV}} & \frac{\hat{T}_e^{\text{node}}}{1 \text{ keV}} \end{array} \right]_{\text{node} \in \{ \text{core}, \text{edge}, \text{sol} \}}, \quad (4.43)$$

and the measurement from the DIII-D experiment is

$$\mathbf{y}_{t_i} = \left[ \begin{array}{ccc} \frac{n_D^{\text{node}}}{10^{19} \text{ m}^{-3}} & \frac{T_D^{\text{node}}}{1 \text{ keV}} & \frac{T_e^{\text{node}}}{1 \text{ keV}} \end{array} \right]_{\text{node} \in \{ \text{core}, \text{edge}, \text{sol} \}}. \quad (4.44)$$

Once the MSE is calculated, the gradients of error flow back by following the blue arrows in the Figure 3.1 to the parametric diffusivity model. The parameters in the diffusivity model are updated by using the gradient descent algorithm. The shots in the training dataset are iterated through this process one by one. Such one iteration all shots is called an epoch. Multiple epochs are done until the convergence, where the MSE is small enough.

- Testing process: Once the parameters in the nodal diffusivity model are converged to a local optimum, the dynamical system of the multinodal model is solved on the testing dataset. Then, the solutions are compared with the experimental measurements. Also, the errors from both the original diffusivity model and the optimized model are compared to analyze the effectiveness of the whole computational method.

There are several hyperparameters used to control the training and testing processes. Those hyperparameters in the solver and optimizer are listed in the Table 4.3. Unlike the parameters, which can be learned (or solved) from the data, the hyperparameters are predetermined by researchers.

The absolute and relative tolerances are used in the in the ordinary differential equation (ODE) solver [78, 85], where the total tolerance is computed by

$$\text{atol} + \text{rtol} * \text{norm of the current state}.$$

The learning rate and the regularization rate (weight decay) in the optimizer are set 0.01

Table 4.3: Hyperparameters in the solver and optimizer.

Hyper-parameter	Number
Solver absolute tolerance	$10^{-5}$
Solver relative tolerance	$10^{-5}$
Optimizer learning rate	0.01
Optimizer regularization rate	$10^{-5}$
Training time step	0.2 s
Testing time step	0.02 s
Moving average window size	5
Training epoch number	24

and  $10^{-5}$  respectively. A higher learning rate can increase the convergence speed but may result in a worse local minimum (larger MSE). For shortening the running time of the optimization process and stabilizing the convergence, the training time step is selected as 0.2 s, while the testing time step is 0.02 s for the better evaluations. Also, to smooth the oscillations in experimental measurements, the simple moving average is implemented with a window size of 5. Since the core and edge nodes can be decoupled from the multinodal model, the core and edge nodes are trained firstly with 12 epochs. Then the SOL node is trained for another 12 epochs to get an optimized multinodal model. This method can help the model converge and stabilize.

One important issue during the training process is the stiffness, where the multinodal model can be stiff for some shots. The multinodal model can be viewed as a system of ordinary differential equations (ODEs). A stiff equation [86] means a differential equation becomes numerically unstable for a normal step size, since some terms in the equation change too rapidly. The stiffness of a system can be evaluated the stiffness ratio. For a linear constant coefficient system  $\mathbf{y}' = \mathbf{A}\mathbf{y} + \mathbf{f}(t)$ , where  $\mathbf{y}, \mathbf{f} \in \mathbb{R}^n$  and  $\mathbf{A} \in \mathbb{R}^{n \times n}$ , let the eigenvalues of  $\mathbf{A}$  be  $\lambda_i \in \mathbb{C}$ ,  $i = 1, \dots, n$ . Then sort the eigenvalues by  $|\operatorname{Re}(\bar{\lambda})| \geq |\operatorname{Re}(\lambda_i)| \geq |\operatorname{Re}(\underline{\lambda})|$ . The stiffness ratio is defined as  $|\operatorname{Re}(\bar{\lambda})| / |\operatorname{Re}(\underline{\lambda})|$ . Since usually a multinodal model is a nonlinear system, we can linearize the multinodal model at one point and then access its stiffness ratio. This research can be done in future. Also, since an

adaptive-step ODE solver is used in this research, the solver will automatically cut the step size when rapid changes are seen in the source terms. This can lead to an extremely small time step and a long-time solving procedure. However, the fixed-step ODE solver cannot be applied, since it can lead to a divergent solution. Hence, some specific stiff ODE solvers may be applied for solving the multinodal model in the future.

#### 4.5 Computation Results

After the parametric diffusivity model in the multinodal model is trained on the training shots, the simulation results of testing shots are presented in this section. The parameters in the optimized diffusivity model are listed in the Table 4.4 for the core, edge, and scrape-off layer (SOL) nodes. The particle diffusivities of deuterons and the thermal diffusivities of deuterons and electrons are included. We also listed the parameters in the original  $\chi_{H98}$  [17] model in the Equation 2.52 for the comparison, which are used as initial parameters in the diffusivity model. The performances of the optimized parametric diffusivity model for testing shots will be analyzed in the following subsections.

Table 4.4: Parameters in the nodal particle and thermal diffusivities for the DIII-D plasma.

	$\alpha_H$	$\alpha_B$	$\alpha_n$	$\alpha_T$	$\alpha_{\nabla T}$	$\alpha_q$	$\alpha_\kappa$	$\alpha_M$	$\alpha_R$	$\alpha_a$
$D_{H98}$	0.0738	-3.5000	0.9000	1.0000	1.2000	3.0000	-2.9000	-0.6000	0.7000	-0.2000
$\chi_{H98}$	0.1230	-3.5000	0.9000	1.0000	1.2000	3.0000	-2.9000	-0.6000	0.7000	-0.2000
$D_D^{\text{core}}$	0.0401	-4.2589	1.0426	-0.8033	-0.4398	2.5829	-3.2690	-1.2093	0.0965	0.2555
$\chi_D^{\text{core}}$	0.0827	-3.5729	-0.1225	3.2578	1.1600	2.3382	-2.7806	-1.0380	0.1285	0.3878
$\chi_e^{\text{core}}$	0.0784	-3.9093	0.6392	2.3133	1.6147	2.4419	-3.3836	-1.0507	0.2298	0.2593
$D_D^{\text{edge}}$	0.0370	-4.2804	3.2465	0.6073	-0.3878	2.4128	-3.1978	-1.2910	-0.0161	0.2778
$\chi_D^{\text{edge}}$	0.1129	-3.5983	0.2251	1.4056	1.1128	2.9299	-3.0591	-0.6859	0.6195	-0.0464
$\chi_e^{\text{edge}}$	0.1270	-3.3745	-0.9212	1.4332	1.4935	2.9131	-3.0735	-0.5680	0.7330	-0.1191
$D_D^{\text{sol}}$	0.0602	-3.6842	1.5414	0.2547	0.8641	2.7684	-3.1355	-0.8030	0.4916	0.0138
$\chi_D^{\text{sol}}$	0.1267	-3.4738	0.6007	1.2647	1.2567	3.0425	-2.8686	-0.5700	0.7319	-0.2312
$\chi_e^{\text{sol}}$	0.1196	-3.5343	0.7191	1.2305	1.2152	2.9764	-2.9216	-0.6284	0.6721	-0.1760

To evaluate the overall performance of the optimized model, the mean squared error

(MSE) is used. Shots in the testing dataset are simulated with the optimized model, including the shot 131190, 140418, 140420, 140427, and 140535. The performances of the original  $\chi_{H98}$  diffusivity model [15, 17, 25] and the optimized parametric diffusivity model are shown in the Table 4.5. The average MSE of testing shots is also computed. The relative decreases of the errors are over 96% after the optimization, and the average MSE on the testing dataset decreases over 98%. Since the diffusivity model was only trained on the training dataset rather than on the testing dataset, these decreases in errors prove the effectiveness of the computational method. The multinodal model with the optimized diffusivity formula can be generalized for predicting new shots that the multinodal model has never seen before.

Table 4.5: Mean squared errors for shots in the testing set.

Shot	Mean squared error (MSE)		Relative decrease of MSE
	$\chi_{H98}$ model	Optimized model	
131190	11.5861	0.4075	96.48%
140418	56.6859	0.3170	99.44%
140420	70.3650	0.5876	99.16%
140427	29.7967	0.7105	97.62%
140535	88.4208	0.7348	99.17%
Average	51.3709	0.5515	98.93%

In order to obtain insights into the strengths and shortcomings of the multinodal model, shots in the testing dataset are analyzed in the following subsections. Several necessary signals changing with time are presented first. Then the solutions of the multinodal model over the core, edge, and SOL nodes are given. Also, the diffusivities and transport times are displayed. Finally, a summary of all results is given at the end.

#### 4.5.1 Shot 131190

The first shot in the testing dataset is the shot 131190. Some signals, including the plasma current, toroidal magnetic field, safety factor, gas puffing rate, ohmic heating power, neutral

beam injection (NBI) power, electron cyclotron heating (ECH) power, and ion cyclotron heating (ICH) power, are presented in the Figure 4.1. In this shot, particles are puffed to the plasma edge at the beginning, and then the plasma is heated by ohmic heating. The NBI is turned on for the whole shot with a higher power around 3-5 s. The ECH power is used to heat the electrons during 2.5-4.5 s, while the ICH power is zero in this shot.

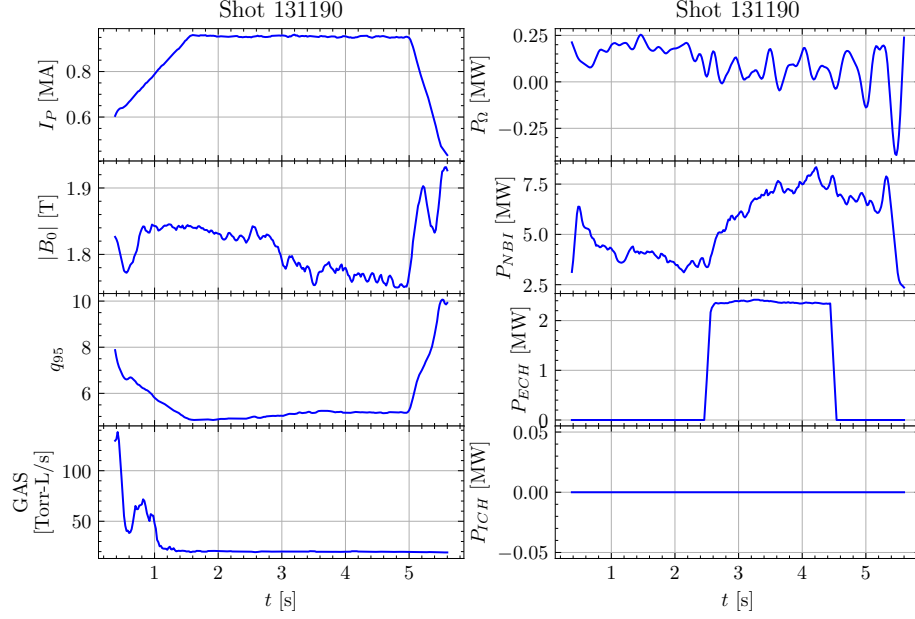


Figure 4.1: Signals of the shot 131190 from the DIII-D tokamak, where the plasma current, toroidal magnetic field, safety factor, gas puffing, ohmic heating, neutral beam injection (NBI), electron cyclotron heating (ECH), and ion cyclotron heating (ICH) are included.

To directly compare the original diffusivity model and optimized diffusivity model, we plot the densities and temperatures of the deuterons and electrons in the core, edge, and SOL nodes in the Figure 4.2, 4.4, and 4.6 respectively. The left column is the solution from the original model in each figure, and the right column is from the optimized model. The densities are presented in the top row, and the temperatures are in the bottom row. The  $\hat{n}_\sigma^{\text{node}}$  and  $\hat{T}_\sigma^{\text{node}}$  are from the simulations of the multinodal model, and  $n_\sigma^{\text{node}}$  and  $T_\sigma^{\text{node}}$  are from the experimental measurements (ZIPFIT). The multinodal model performances over the core, edge and SOL nodes are analyzed one by one next.



### *Core Node*

The core particle densities and temperatures of the deuterons and electrons for the shot 131190 are shown in the Figure 4.2, with the diffusivities and internodal transport times from the core to edge in the Figure 4.3. The overall performance of the optimized diffusivity is better than the original diffusivity model. After optimizations, the particle densities increase at the beginning of the shot when the gas puffing is on and then with the NBI. However, a small jump of the electron temperature is found at the beginning of the shot, probably due to an overestimated NBI power. When the ECH is turned on round 2.5 s, the increases of the core temperatures are lower than the experiment measured ones. An amplification factor can be multiplied by the ECH term in the electron energy balance equation. This factor can also be learned from the data automatically. Besides, the increases in thermal diffusivities of deuterons and electrons are observed around 2.5 s, which will also lead to lower temperatures. At the end of the shot, the densities and temperatures decrease as expected.

### *Edge Node*

The edge particle densities and temperatures of the deuterons and electrons for the shot 131190 are shown in the Figure 4.4, with the diffusivities and transport times from the edge to SOL in the Figure 4.5. Again, the optimized diffusivity model has a better performance than the original model in the edge node. Jumps of the particle densities are observed at the beginning of the shot since most of the gas puffing is assumed to be deposited at the edge node. The gas puffing coefficient can be adjusted with experiment conditions or a gas puffing code in the future. The experiment data have more oscillations due to the measurement issues, but the multinodal model solutions are much smoother. The deuteron and electron particle densities can basically track the experiment data. However, the temperatures are lower than in the experiment due to higher thermal diffusivities. More heating power depositions to the edge node with lower thermal diffusivities can give higher temperatures

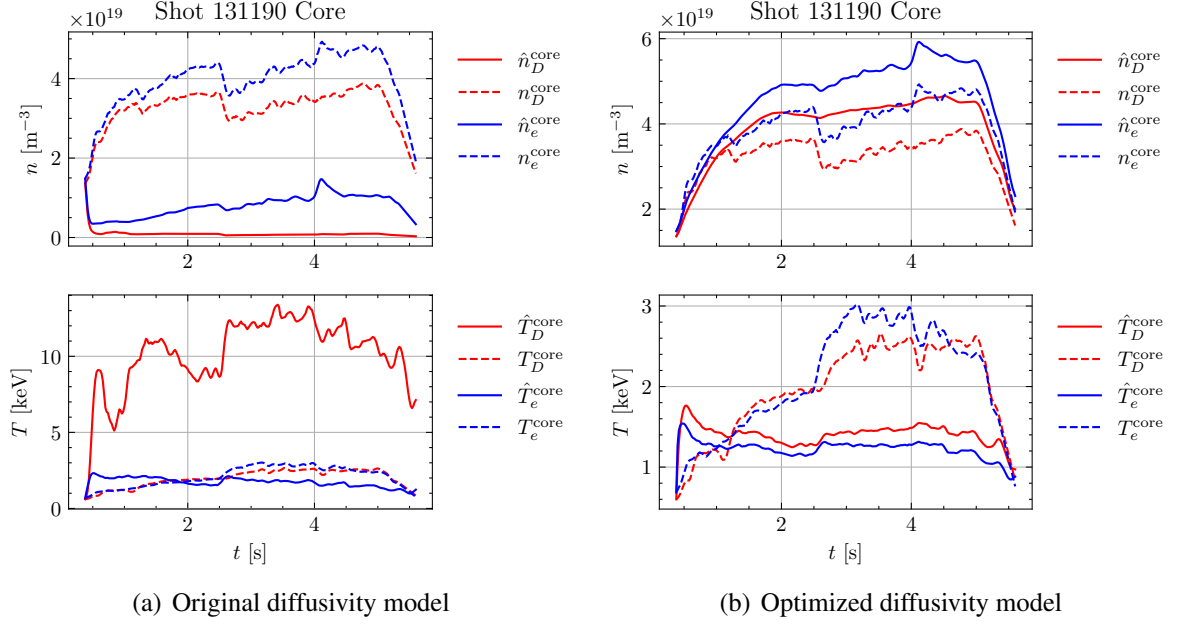


Figure 4.2: Simulation results of the shot 131190 for the core node, where  $\hat{n}_\sigma^{\text{node}}$  and  $\hat{T}_\sigma^{\text{node}}$  are from the multinodal model, while  $n_\sigma^{\text{node}}$  and  $T_\sigma^{\text{node}}$  are from the experimental measurement.

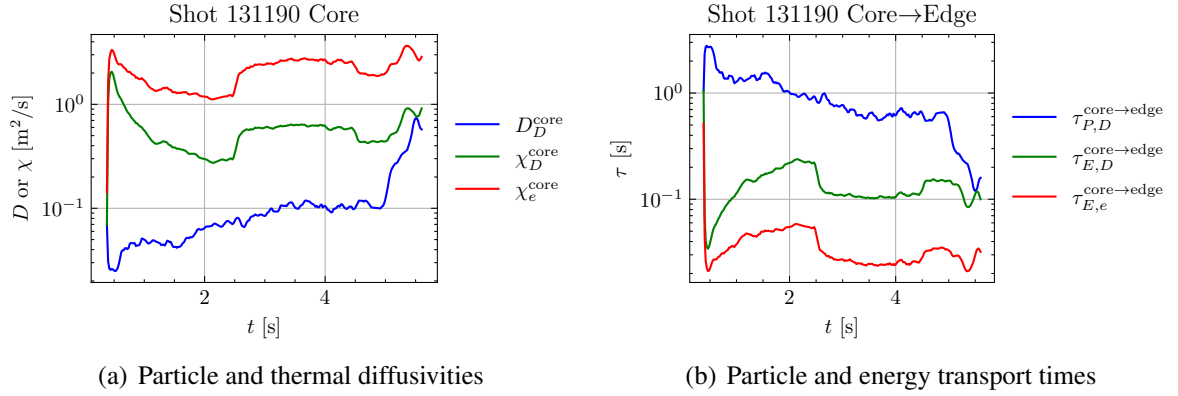


Figure 4.3: Diffusivities and transport times from the core to the edge for the shot 131190 with the optimized diffusivity model.

during the middle of the shot. The multinodal model can track the decrease in densities and temperatures at the end of the shot.

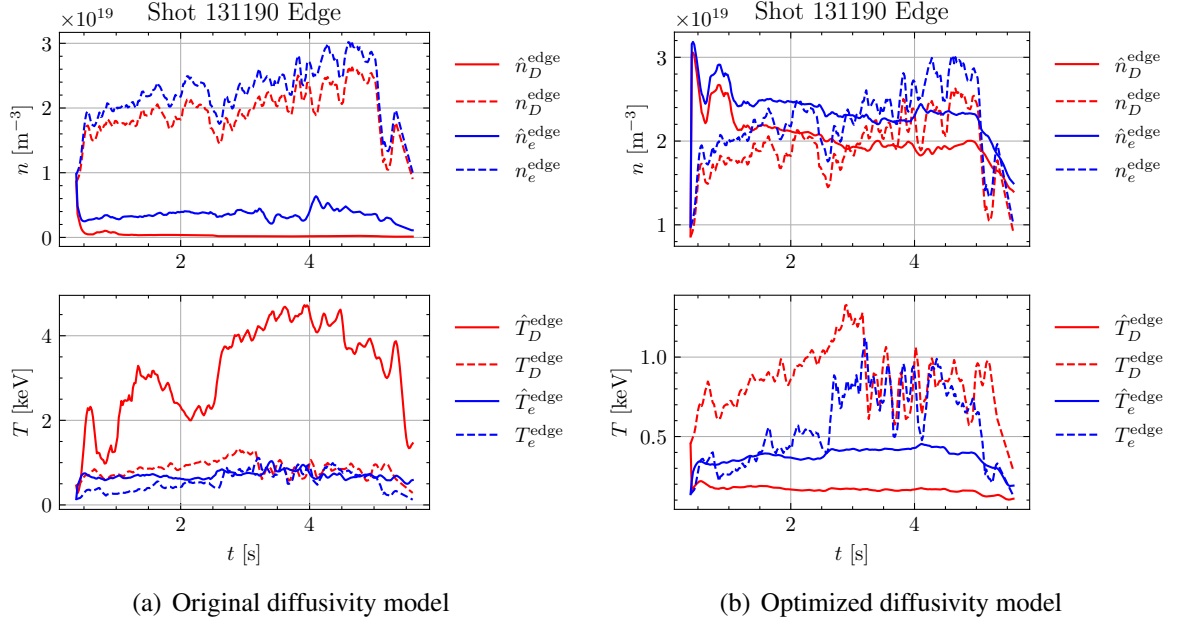


Figure 4.4: Simulation results of the shot 131190 for the edge node, where  $\hat{n}_\sigma^{\text{node}}$  and  $\hat{T}_\sigma^{\text{node}}$  are from the multinodal model, while  $n_\sigma^{\text{node}}$  and  $T_\sigma^{\text{node}}$  are from the experimental measurement.

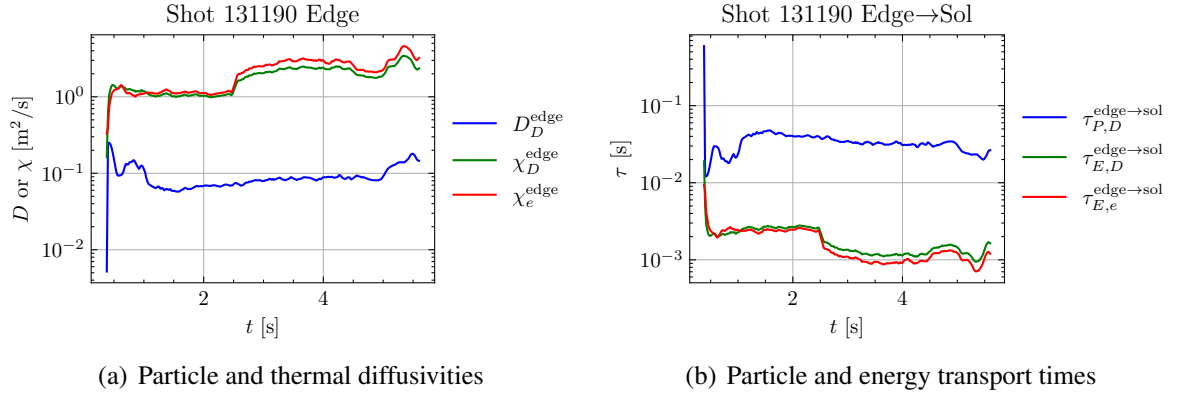


Figure 4.5: Diffusivities and transport times from the edge to the SOL for the shot 131190 with the optimized diffusivity model.

### SOL Node

The SOL particle densities and temperatures of the deuterons and electrons for the shot 131190 are shown in the Figure 4.6, with the diffusivities and transport times in the Figure 4.7. Similar to the core and edge nodes, the performance of the multinodal model becomes better after the optimization. Although the particle densities can track the experimental

measurement tendencies, the deuteron temperature is lower than the experiment data, and the electron temperature is higher than the measurement. A lower deuteron thermal diffusivity can help mitigate this deviation. However, the problem with the electron temperature may be caused by some ignored processes in the SOL, such as more atomic and molecular reactions. Also, neutral particle densities in the SOL should be adjusted, so the number of electrons generated from the ionization process can be properer. Therefore, a neutral and charged particle code [56, 57, 61] for the SOL, divertor, plenum, and other necessary regions is required to be connected with the multinodal model code for better performance in the SOL region.

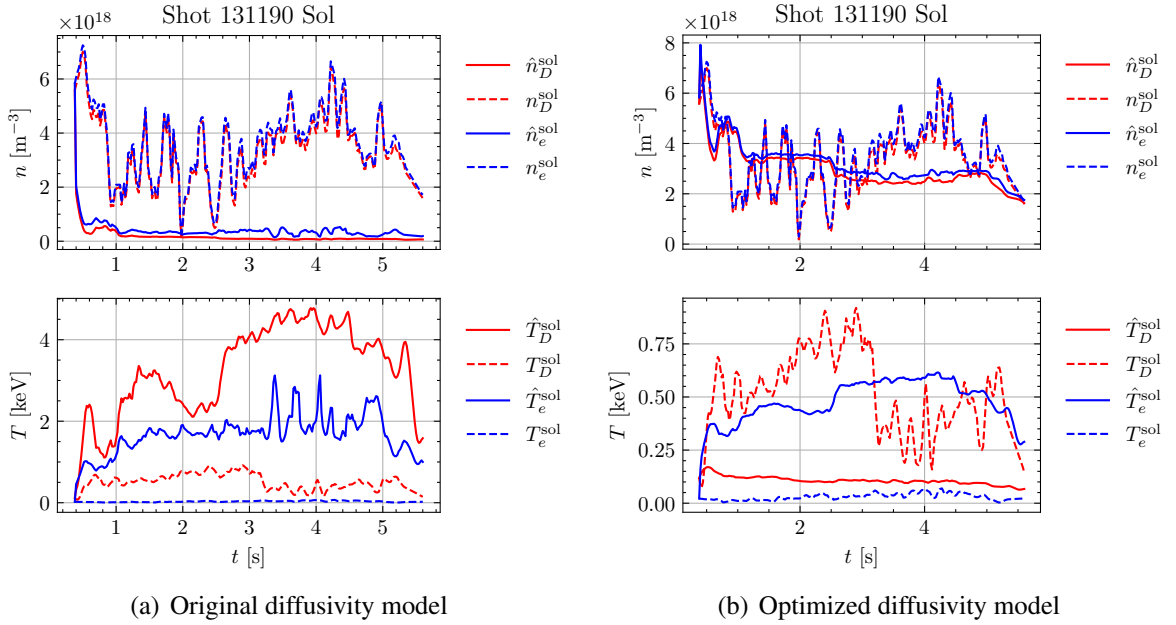


Figure 4.6: Simulation results of the shot 131190 for the SOL node, where  $\hat{n}_\sigma^{\text{node}}$  and  $\hat{T}_\sigma^{\text{node}}$  are from the multinodal model, while  $n_\sigma^{\text{node}}$  and  $T_\sigma^{\text{node}}$  are from the experimental measurement.

#### 4.5.2 Shot 140418

The second shot in the testing dataset is the shot 140418, and its signals are shown in the Figure 4.8. The gas particles are puffed to the plasma edge at the beginning of the shot. Then the neutral particles are injected from the beginning around 1.2 s to the end. The ECH

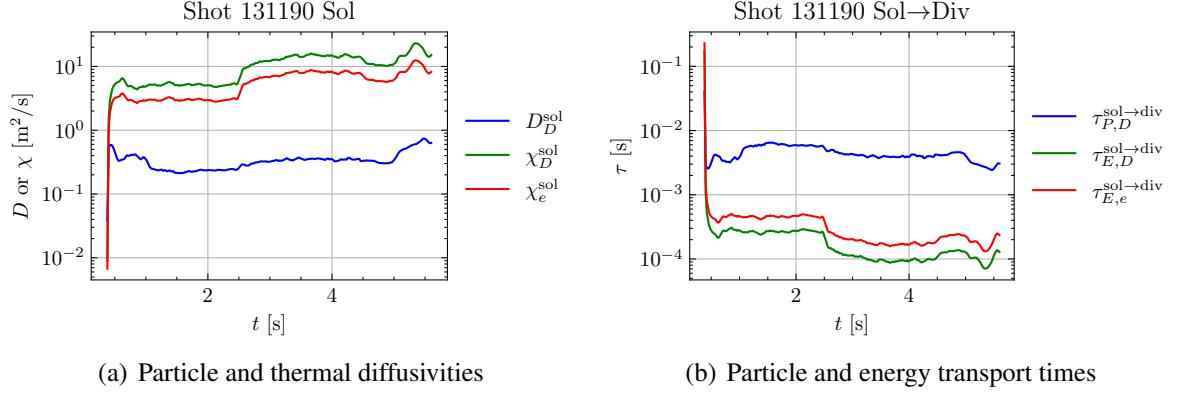


Figure 4.7: Diffusivities and transport times from the SOL to the divertor for the shot 131190 with the optimized diffusivity model.

and ICH are zeros for this shot. This shot is a good example of analyzing the response of the multinodal model with only the NBI power, since there is only one primary energy source during the most time of the shot.

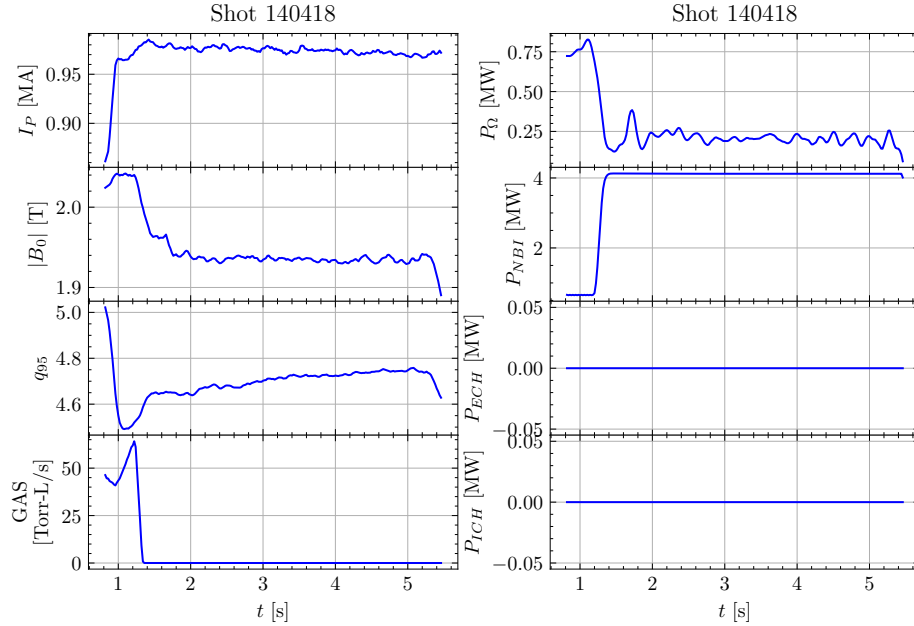


Figure 4.8: Signals of the shot 140418 from the DIII-D tokamak, where the plasma current, toroidal magnetic field, safety factor, gas puffing, ohmic heating, neutral beam injection (NBI), electron cyclotron heating (ECH), and ion cyclotron heating (ICH) are included.

### Core Node

The core particle densities and temperatures of the deuterons and electrons for the shot 140418 are shown in the Figure 4.9, with the diffusivities and transport times in the Figure 4.10. The performance of the multinodal model becomes much better after the optimization. The particle densities increase as expected with the NBI, although the increasing speed is lower than the measurement. However, bumps are observed at the beginning of the core temperatures, which shows an overestimation of the ohmic heating. Also, a larger thermal diffusivity of core electrons can help mitigate this bump. Similar to the particle densities, the core temperatures can also increase with the NBI power, which shows the thermal diffusivities are appropriately determined. The overall performance of the multinodal model is good in the core node with only the NBI power.

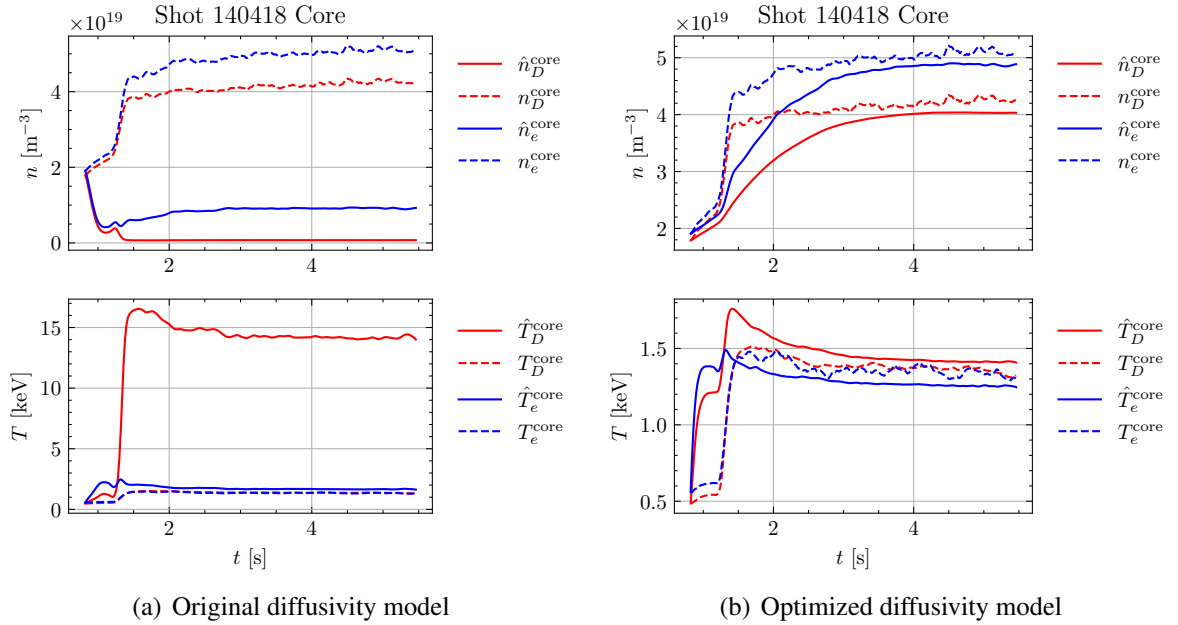


Figure 4.9: Simulation results of the shot 140418 for the core node, where  $\hat{n}_\sigma^{\text{node}}$  and  $\hat{T}_\sigma^{\text{node}}$  are from the multinodal model, while  $n_\sigma^{\text{node}}$  and  $T_\sigma^{\text{node}}$  are from the experimental measurement.

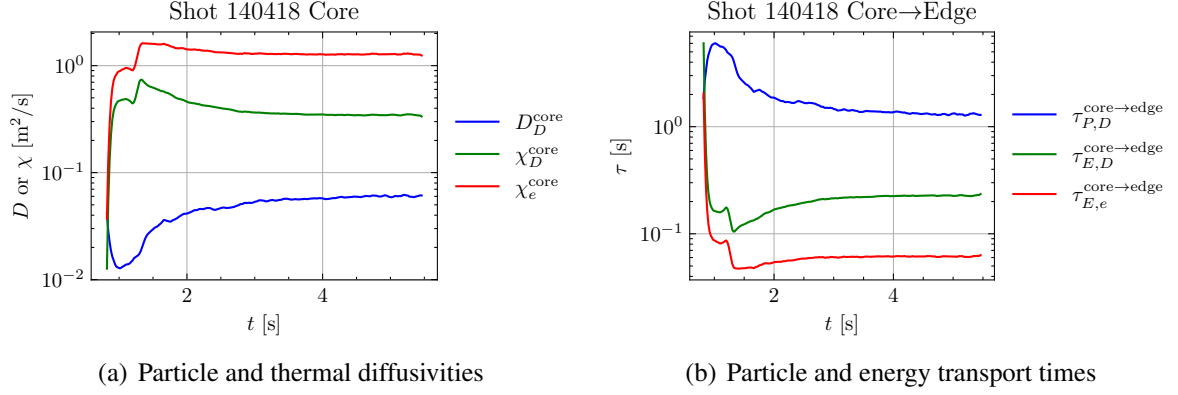


Figure 4.10: Diffusivities and transport times from the core to the edge for the shot 140418 with the optimized diffusivity model.

### Edge Node

The edge particle densities and temperatures of the deuterons and electrons for the shot 140418 are shown in the Figure 4.11, with the diffusivities and transport times in the Figure 4.12. A jump in the particle densities is noticed at the beginning, which is from the overestimation of the gas puffing at the edge node. However, when NBI is turned on, a decrease in particle density is found. This may be because of the over-long transport time from the core to the edge or the over-short transport and the ion orbit loss from the edge to the SOL. The edge temperatures can track the tendencies of the NBI. However, the deuteron thermal diffusivity should be lower, while the electron thermal diffusivity should be higher.

### SOL Node

The SOL particle densities and temperatures of the deuterons and electrons for the shot 140418 are shown in the Figure 4.13, with the diffusivities and transport times in the Figure 4.14. The particle densities of SOL deuterons and electrons jump at the beginning of the shot, which is from the gas puffing at the edge node then transported to the SOL, and can be flattened by increasing the transport time from the edge to the SOL. The SOL temperatures follow the increases from the NBI, although the thermal diffusivity of electrons should be much larger than the current solution.

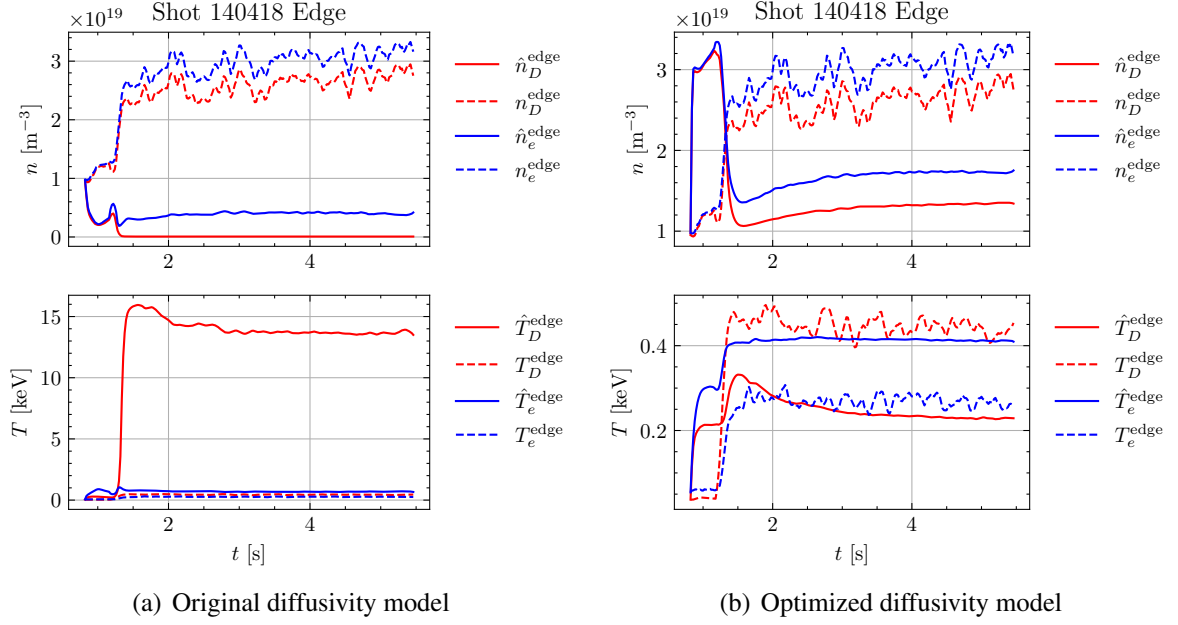


Figure 4.11: Simulation results of the shot 140418 for the edge node, where  $\hat{n}_\sigma^{\text{node}}$  and  $\hat{T}_\sigma^{\text{node}}$  are from the multinodal model, while  $n_\sigma^{\text{node}}$  and  $T_\sigma^{\text{node}}$  are from the experimental measurement.

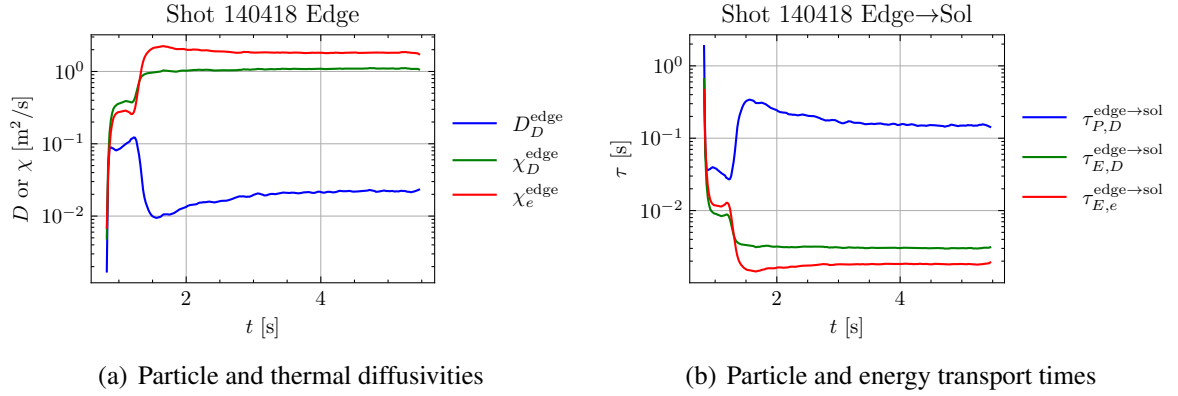


Figure 4.12: Diffusivities and transport times from the edge to the SOL for the shot 140418 with the optimized diffusivity model.

#### 4.5.3 Shot 140420

The third testing shot is the shot 140420, where the signals are shown in the Figure 4.15. This shot has gas puffing at the beginning of the shot. Then NBI is turned on at the 1.2 s. The ECH starts at the 2 s and ends at the 5 s, with a slight decrease around the 3.1 s. The ICH is zero during the shot. This shot is a good example for analyzing the multinodal



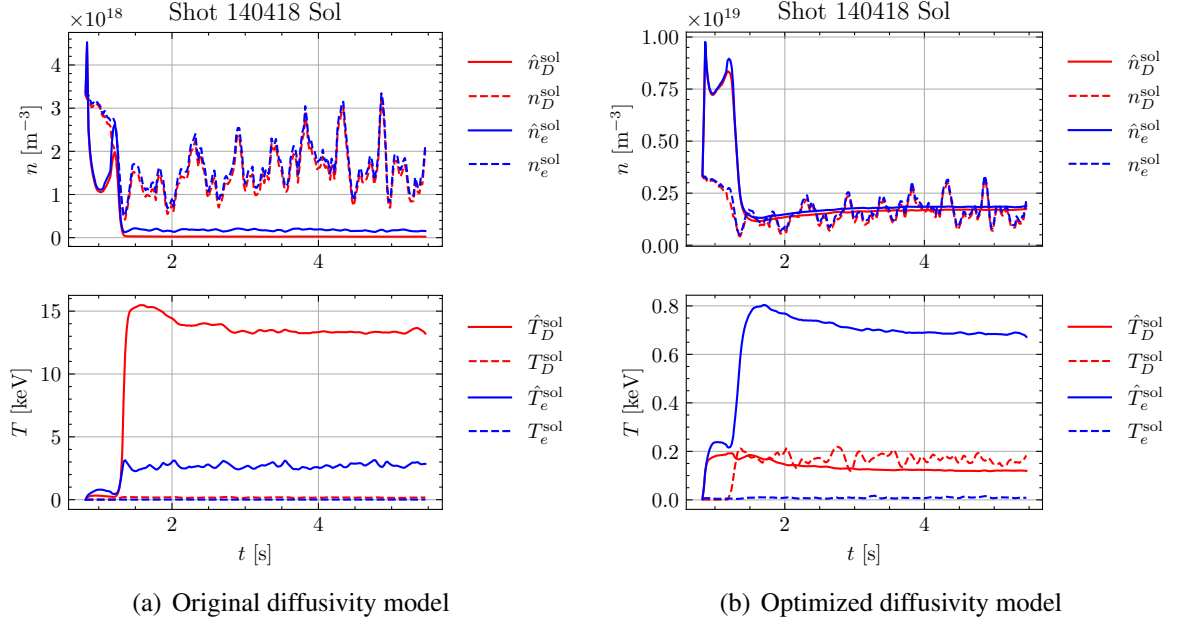


Figure 4.13: Simulation results of the shot 140418 for the SOL node, where  $\hat{n}_\sigma^{\text{node}}$  and  $\hat{T}_\sigma^{\text{node}}$  are from the multinodal model, while  $n_\sigma^{\text{node}}$  and  $T_\sigma^{\text{node}}$  are from the experimental measurement.

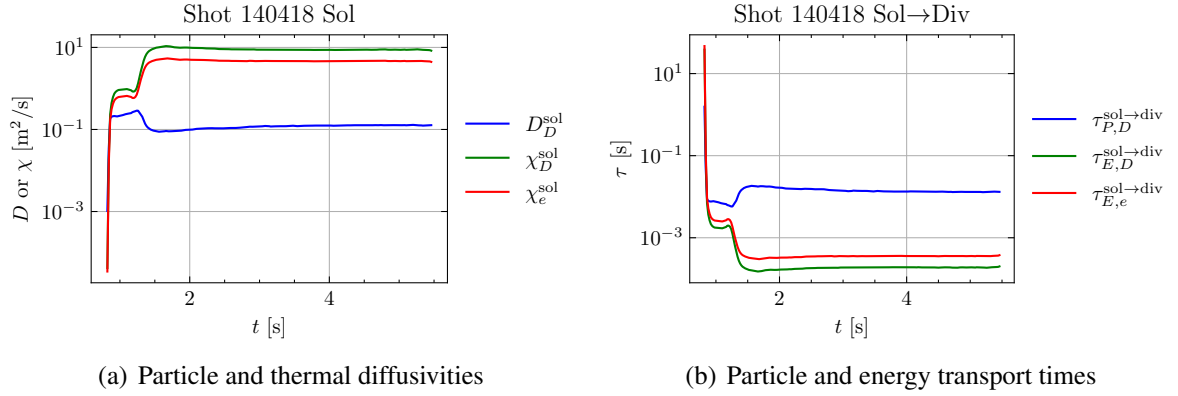


Figure 4.14: Diffusivities and transport times from the SOL to the divertor for the shot 140418 with the optimized diffusivity model.

model performance with two kinds of power sources, i.e., NBI and ECH.

### Core Node

The core particle densities and temperatures of the deuterons and electrons for the shot 140420 are shown in the Figure 4.16, with the diffusivities and transport times in the Figure

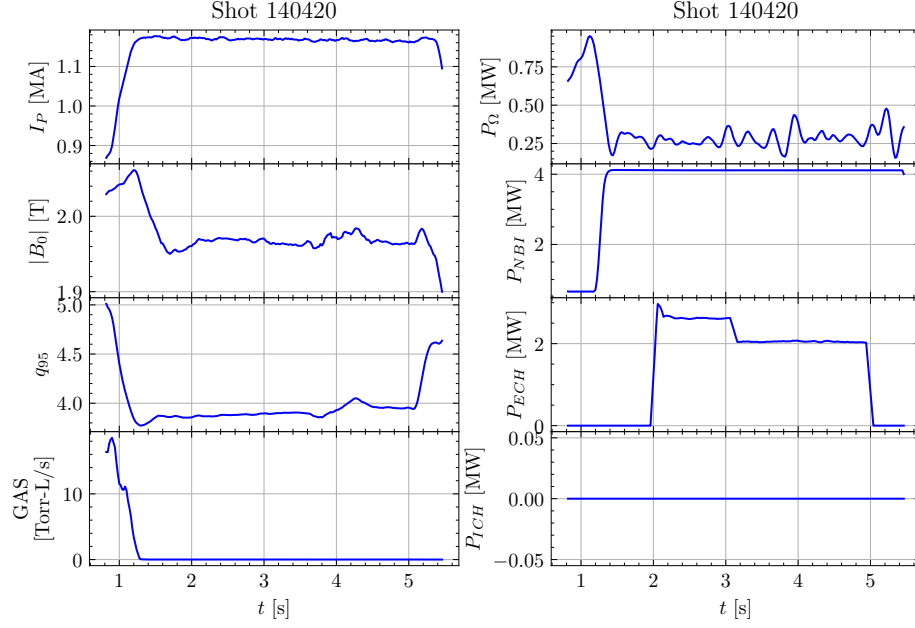


Figure 4.15: Signals of the shot 140420 from the DIII-D tokamak, where the plasma current, toroidal magnetic field, safety factor, gas puffing, ohmic heating, neutral beam injection (NBI), electron cyclotron heating (ECH), and ion cyclotron heating (ICH) are included.

4.17. We can see a considerable improvement in the overall performance in the simulation results of core densities and temperatures. The deuteron and electron densities increase as expected when the gas puffing and NBI are turned on. The core temperatures also increase with the NBI and ECH during the shot, where the deuteron temperature has a more accurate result than the electron temperature. These results prove that the multinodal model can correctly handle the NBI and ECH powers in the core node.

### *Edge Node*

The edge particle densities and temperatures of the deuterons and electrons for the shot 140420 are shown in the Figure 4.18, with the diffusivities and transport times in the Figure 4.19. Similar to previous shots, the particle densities are higher than the measurement at the beginning while lower at the middle and end. The higher particle densities at the beginning can be because of overestimating the gas puffing in the edge node or a short transport time from the edge to SOL. The lower particle densities later may be due to an overly strong

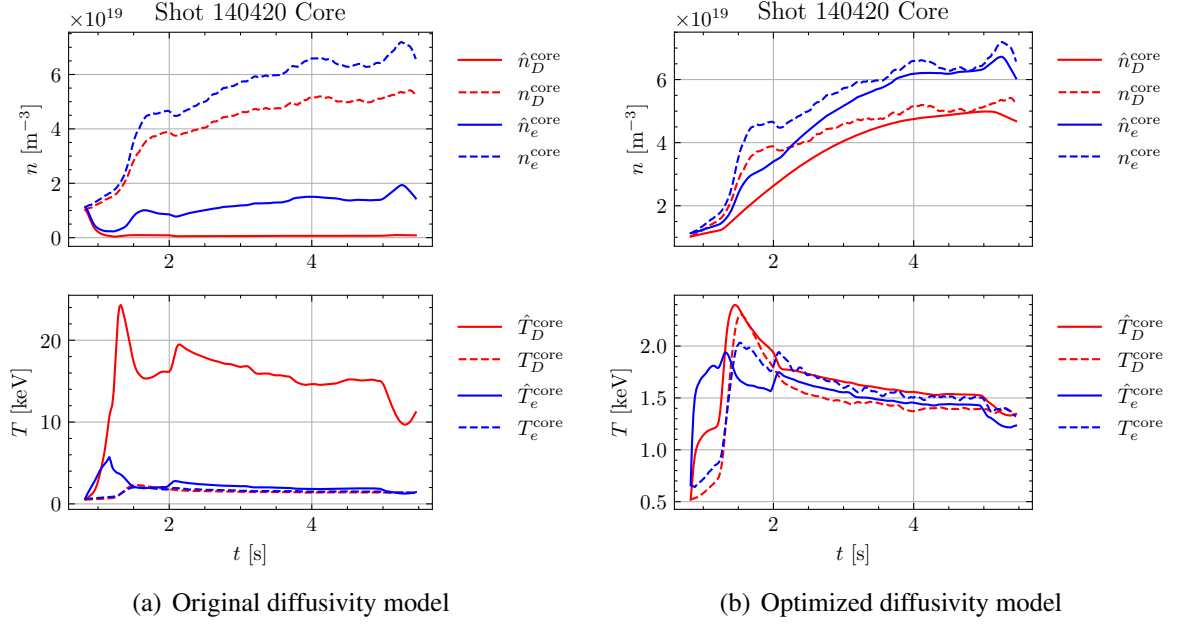


Figure 4.16: Simulation results of the shot 140420 for the core node, where  $\hat{n}_\sigma^{\text{node}}$  and  $\hat{T}_\sigma^{\text{node}}$  are from the multinodal model, while  $n_\sigma^{\text{node}}$  and  $T_\sigma^{\text{node}}$  are from the experimental measurement.

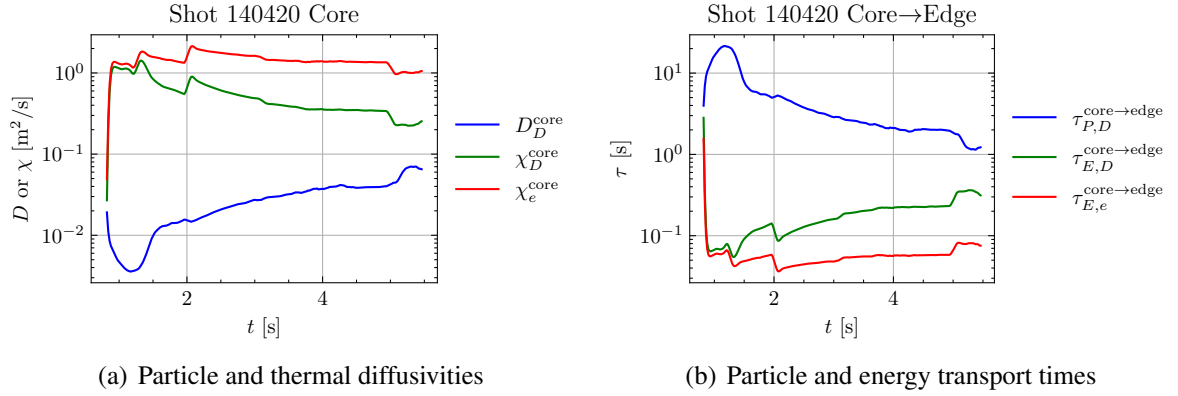


Figure 4.17: Diffusivities and transport times from the core to the edge for the shot 140420 with the optimized diffusivity model.

transport and ion orbit loss from the edge to the SOL. A longer deuteron transport time from the edge to SOL can help increase the particle densities in the edge node. The edge temperatures can track the measurements, although the electron thermal diffusivity should be larger to get a lower electron temperature in the edge node. The overall performance of the optimized multinodal model is better than the original one with the  $\chi_{H98}$  diffusivity,

although the core node has a better result than the edge node.

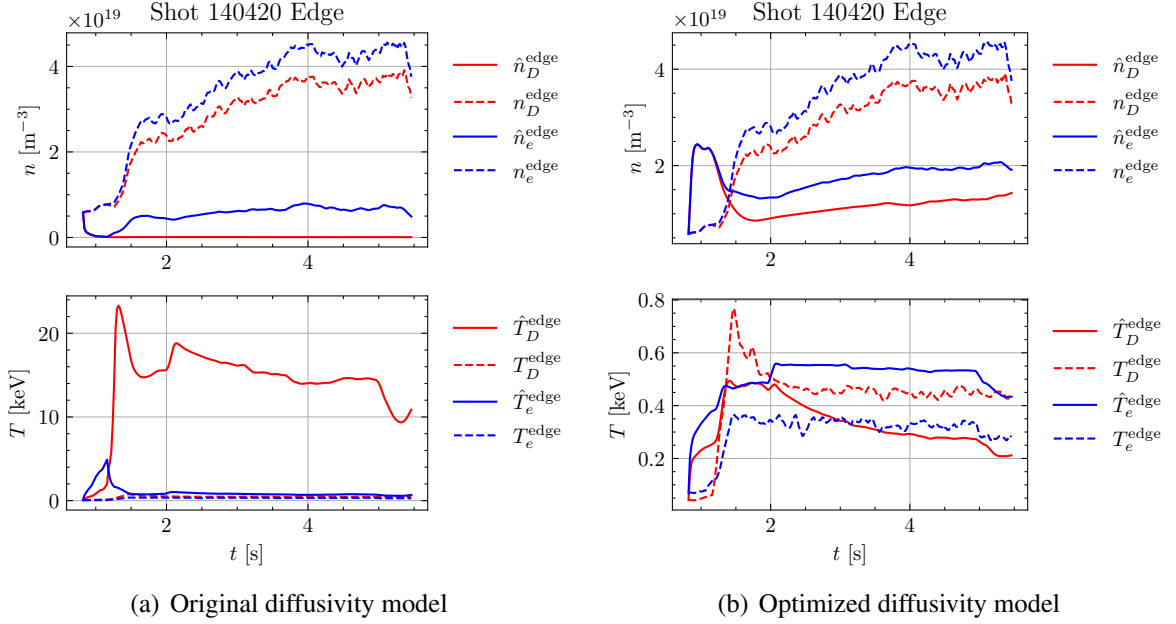


Figure 4.18: Simulation results of the shot 140420 for the edge node, where  $\hat{n}_\sigma^{\text{node}}$  and  $\hat{T}_\sigma^{\text{node}}$  are from the multinodal model, while  $n_\sigma^{\text{node}}$  and  $T_\sigma^{\text{node}}$  are from the experimental measurement.

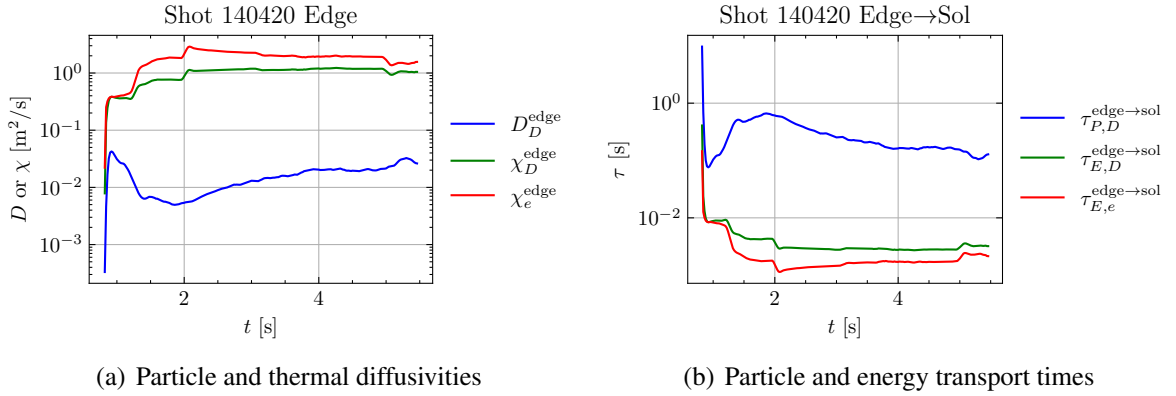


Figure 4.19: Diffusivities and transport times from the edge to the SOL for the shot 140420 with the optimized diffusivity model.

### SOL Node

The SOL particle densities and temperatures of the deuterons and electrons for the shot 140420 are shown in the Figure 4.20, with the diffusivities and transport times in the Figure

4.21. The overall performance of the multinodal model increases in the SOL node after the optimization. However, due to a stronger transport from the edge to the SOL, the particle densities are overestimated at the beginning. Besides, the electron temperature is found to be too high in the SOL node. Therefore, a larger thermal diffusivity should be assigned, and more atomic and molecular reactions should be considered with proper neutral particle densities.

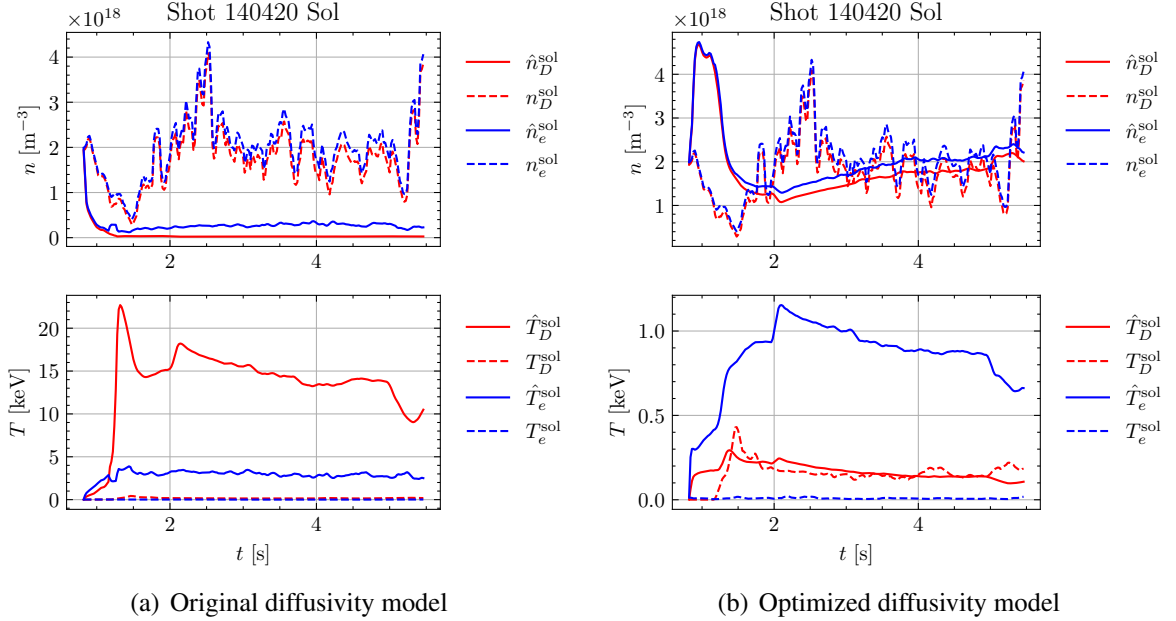


Figure 4.20: Simulation results of the shot 140420 for the SOL node, where  $\hat{n}_\sigma^{\text{node}}$  and  $\hat{T}_\sigma^{\text{node}}$  are from the multinodal model, while  $n_\sigma^{\text{node}}$  and  $T_\sigma^{\text{node}}$  are from the experimental measurement.

#### 4.5.4 Shot 140427

The fourth testing shot is the shot 140427, whose signals are shown in the Figure 4.22. The NBI is turned on at the beginning of the shot around 1.2 s to the end. The gas puffing is given at 3 s-5 s. The ECH and ICH are zeros during this shot. This shot can be used for analyzing the multinodal model performance with both the gas puffing and NBI.

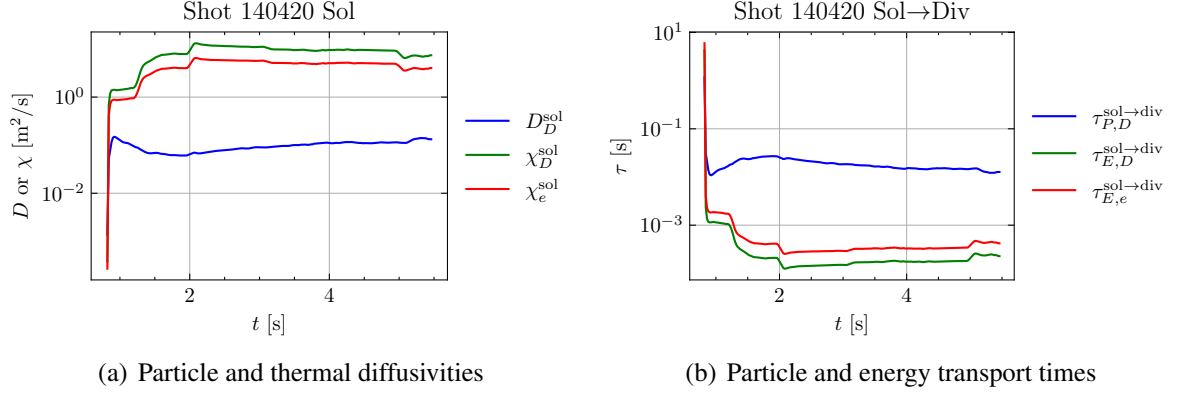


Figure 4.21: Diffusivities and transport times from the SOL to the divertor for the shot 140420 with the optimized diffusivity model.

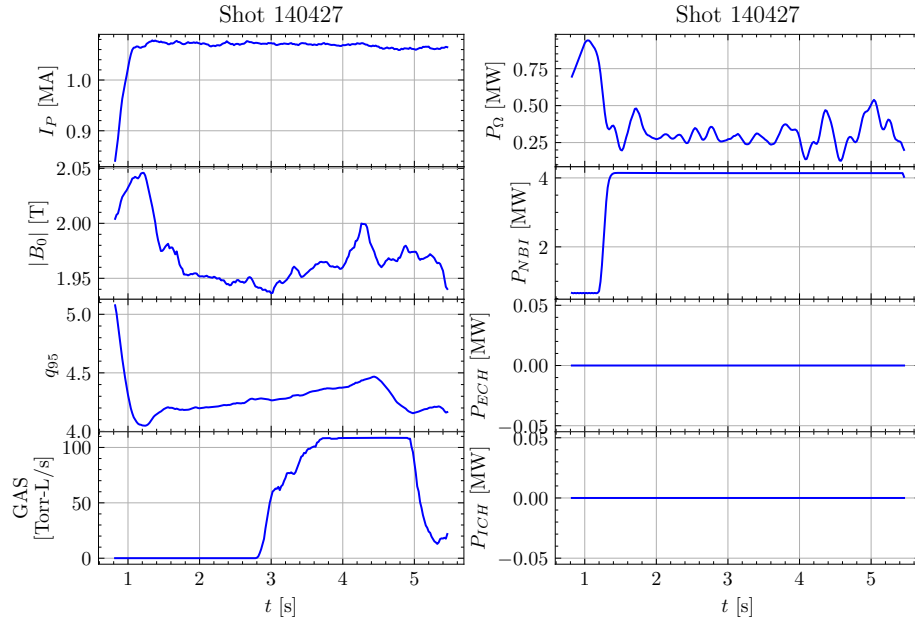


Figure 4.22: Signals of the shot 140427 from the DIII-D tokamak, where the plasma current, toroidal magnetic field, safety factor, gas puffing, ohmic heating, neutral beam injection (NBI), electron cyclotron heating (ECH), and ion cyclotron heating (ICH) are included.

### Core Node

The core particle densities and temperatures of the deuterons and electrons for the shot 140427 are shown in the Figure 4.23, with the diffusivities and transport times in the Figure 4.24. The overall performance of the optimized diffusivity model is better than the original one. When the NBI is turned on, the deuteron particle in the core region can increase

with time. However, the increase speed is lower than the measurement. A lower particle diffusivity can help decrease the transport from the core to the edge and hence accelerate this process. The deuteron and electron temperatures can also track the jump when the NBI is on. However, besides a bump at the beginning, a small overshoot is observed in the deuteron temperature. A larger thermal diffusivity will eliminate this overshoot from the NBI.

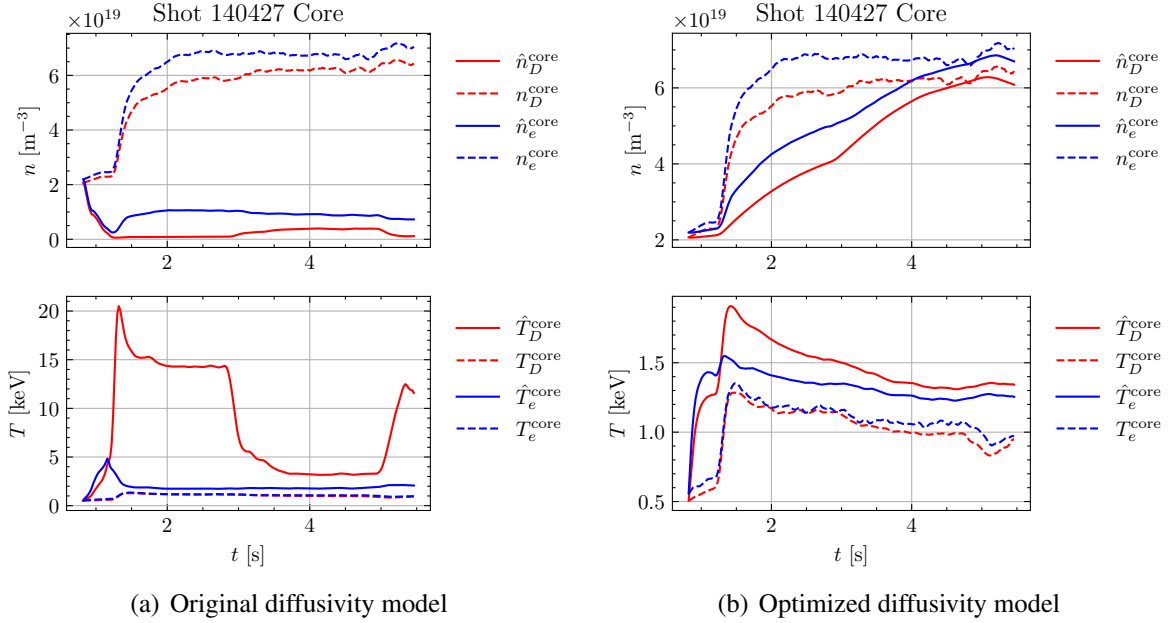


Figure 4.23: Simulation results of the shot 140427 for the core node, where  $\hat{n}_\sigma^{\text{node}}$  and  $\hat{T}_\sigma^{\text{node}}$  are from the multinodal model, while  $n_\sigma^{\text{node}}$  and  $T_\sigma^{\text{node}}$  are from the experimental measurement.

### Edge Node

The edge particle densities and temperatures of the deuterons and electrons for the shot 140427 are shown in the Figure 4.25, with the diffusivities and transport times in the Figure 4.26. Although the performance of the multinodal model improves after the optimization, the effect of the NBI is underestimated in the edge densities. More particles should be deposited to the edge deuterons when the NBI is turned on. This issue can be solved by using a more accurate NBI simulation code. The deuteron and electron temperatures can

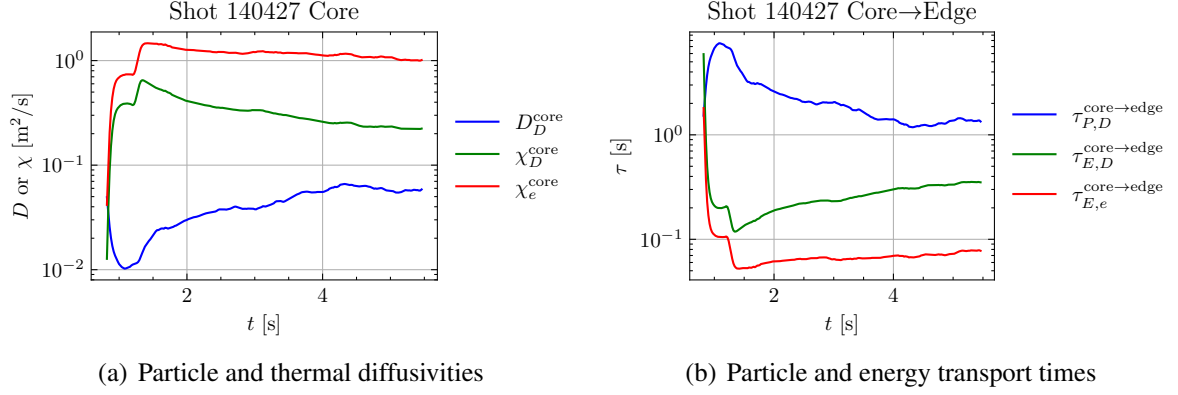


Figure 4.24: Diffusivities and transport times from the core to the edge for the shot 140427 with the optimized diffusivity model.

increase as expected when the NBI is turned on. However, the thermal diffusivity of the edge electron should be higher than the current result to have a lower electron temperature.

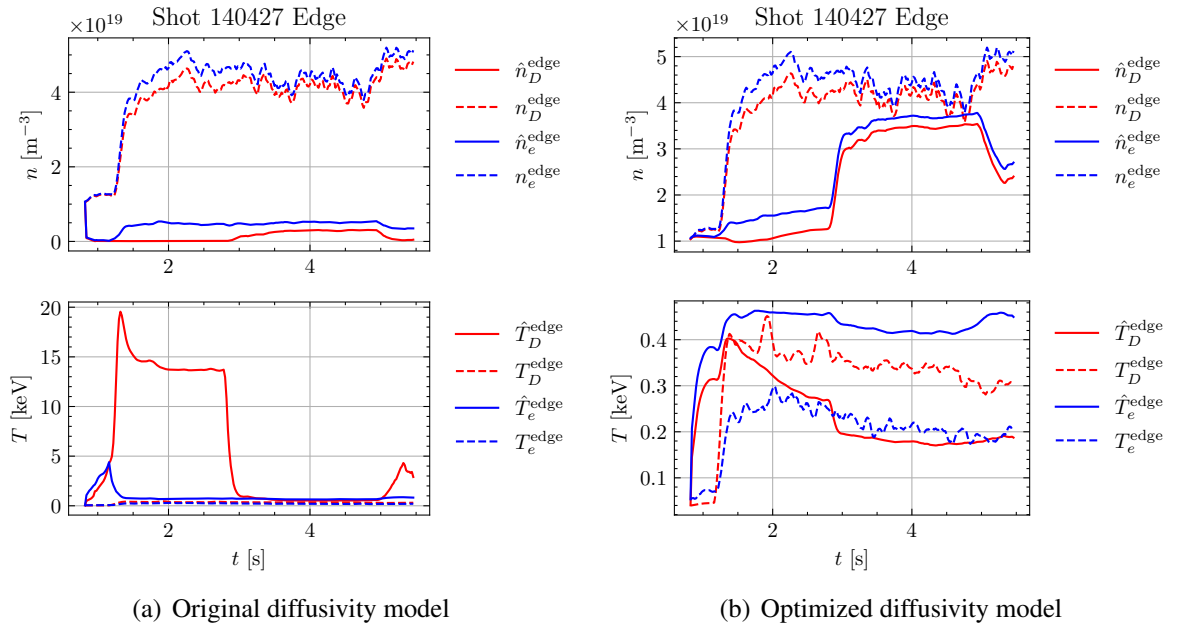


Figure 4.25: Simulation results of the shot 140427 for the edge node, where  $\hat{n}_\sigma^{\text{node}}$  and  $\hat{T}_\sigma^{\text{node}}$  are from the multinodal model, while  $n_\sigma^{\text{node}}$  and  $T_\sigma^{\text{node}}$  are from the experimental measurement.



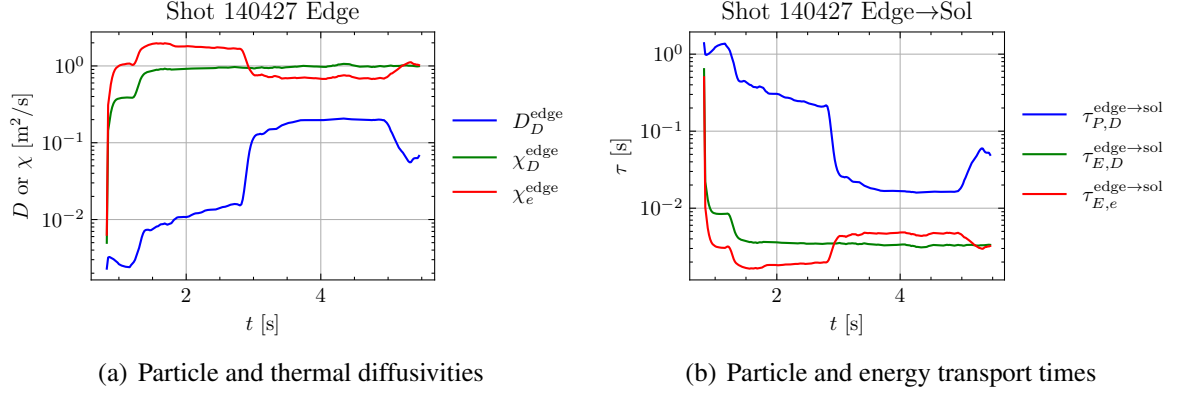


Figure 4.26: Diffusivities and transport times from the edge to the SOL for the shot 140427 with the optimized diffusivity model.

### *SOL Node*

The SOL particle densities and temperatures of the deuterons and electrons for the shot 140427 are shown in the Figure 4.27, with the diffusivities and transport times in the Figure 4.28. The bump in the particle densities shows that the particle transport from the edge to the SOL is overestimated. When gas puffing is turned on, a large transport from the edge to the SOL leads to higher SOL densities than the experimental measurements. For temperatures, the electron temperature is found to be much higher than the measurement. This can be explained by a longer confinement time of the SOL electrons, and some ignored SOL reactions. Again, a more accurate SOL-divertor code with the multinodal model can mitigate this problem.

### 4.5.5 Shot 140535

The last testing shot is the shot 140535, whose signals are shown in the Figure 4.29. The gas particles are puffed at the beginning of the shot. The neutral beams are injected in 0.4-3 s, with the ICH to the core ions in 1-3 s. This shot is a good example of analyzing the performance of ion temperatures in the multinodal model since it is the only testing shot with ICH.

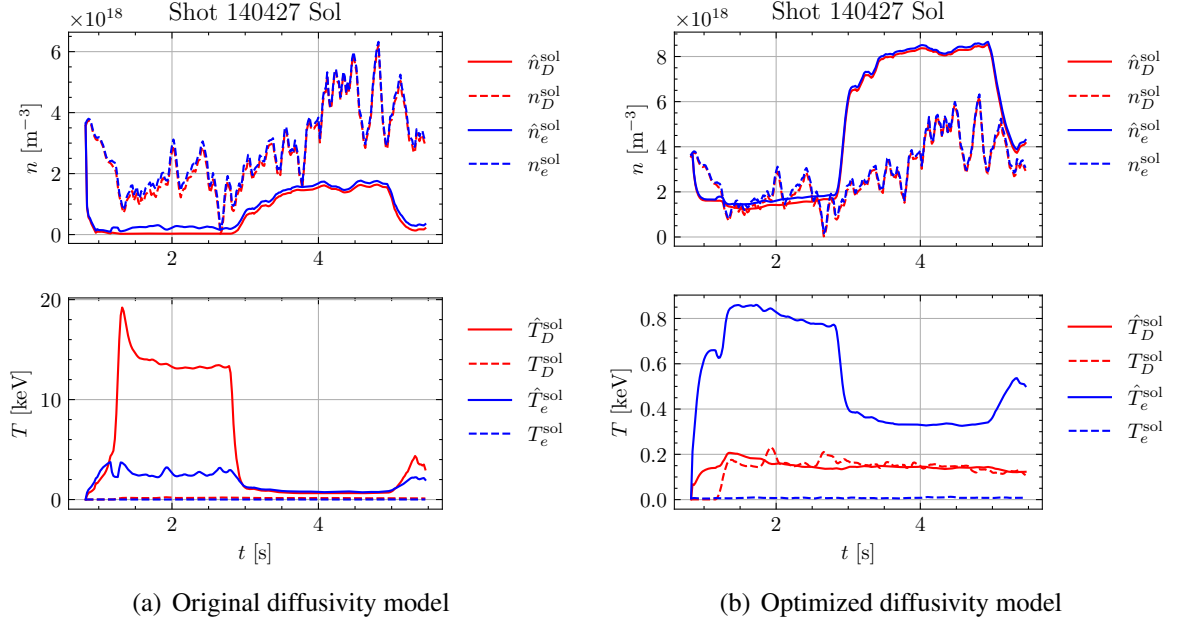


Figure 4.27: Simulation results of the shot 140427 for the SOL node, where  $\hat{n}_\sigma^{\text{node}}$  and  $\hat{T}_\sigma^{\text{node}}$  are from the multinodal model, while  $n_\sigma^{\text{node}}$  and  $T_\sigma^{\text{node}}$  are from the experimental measurement.

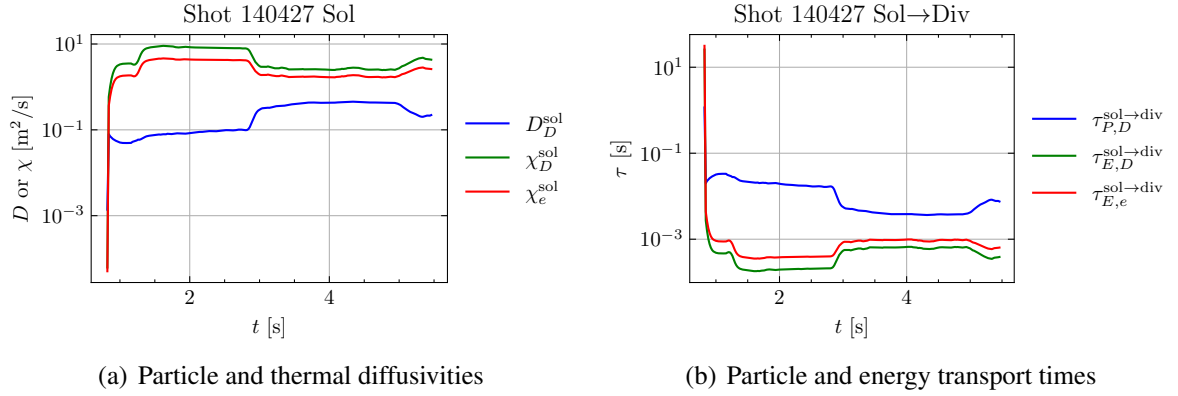


Figure 4.28: Diffusivities and transport times from the SOL to the divertor for the shot 140427 with the optimized diffusivity model.

### Core Node

The core particle densities and temperatures of the deuterons and electrons for the shot 140535 are shown in the Figure 4.30, with the diffusivities and transport times in the Figure 4.31. The core particle densities are larger than the experimental measurement. Thus, the particle diffusivity of the core deuteron should be larger than the current value, so the extra

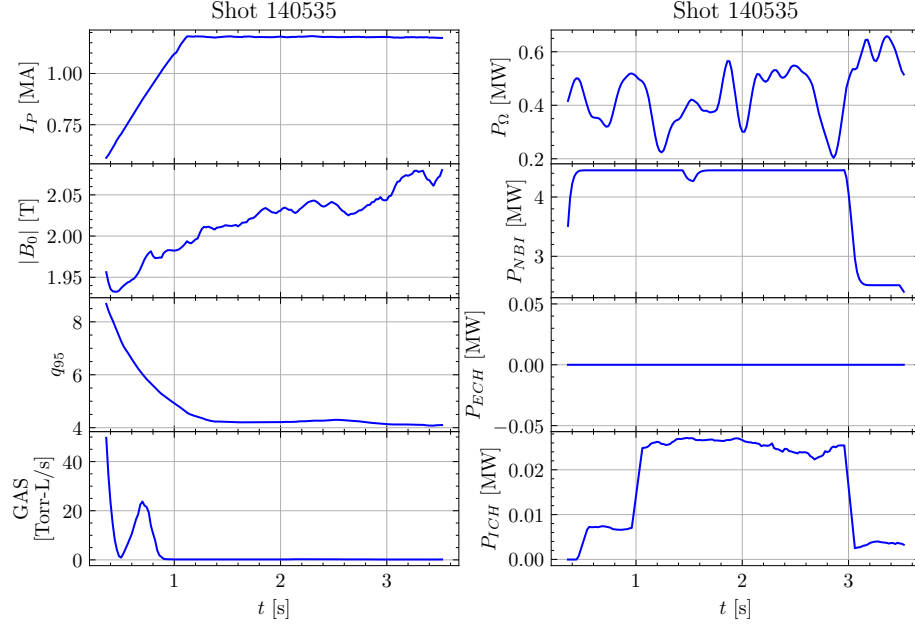


Figure 4.29: Signals of the shot 140535 from the DIII-D tokamak, where the plasma current, toroidal magnetic field, safety factor, gas puffing, ohmic heating, neutral beam injection (NBI), electron cyclotron heating (ECH), and ion cyclotron heating (ICH) are included.

particles can be transported from the core to the edge. The core temperatures track the tendencies of the experiment data. However, the thermal diffusivities at the beginning of the shot should be larger, so the temperatures can increase more slowly due to the NBI.

#### *Edge Node*

The edge particle densities and temperatures of the deuterons and electrons for the shot 140535 are shown in the Figure 4.32, with the diffusivities and transport times in the Figure 4.33. Similar to the core node, the particle diffusivity of the edge deuteron should be larger than the current value to have small edge densities compared with the experimental measurement. For edge temperatures, the ICH power deposited to the edge deuterons should be larger to have a higher deuteron temperature. An over higher electron temperature is observed for the edge electrons. The energy transport time of electrons from the core to the edge should be larger.

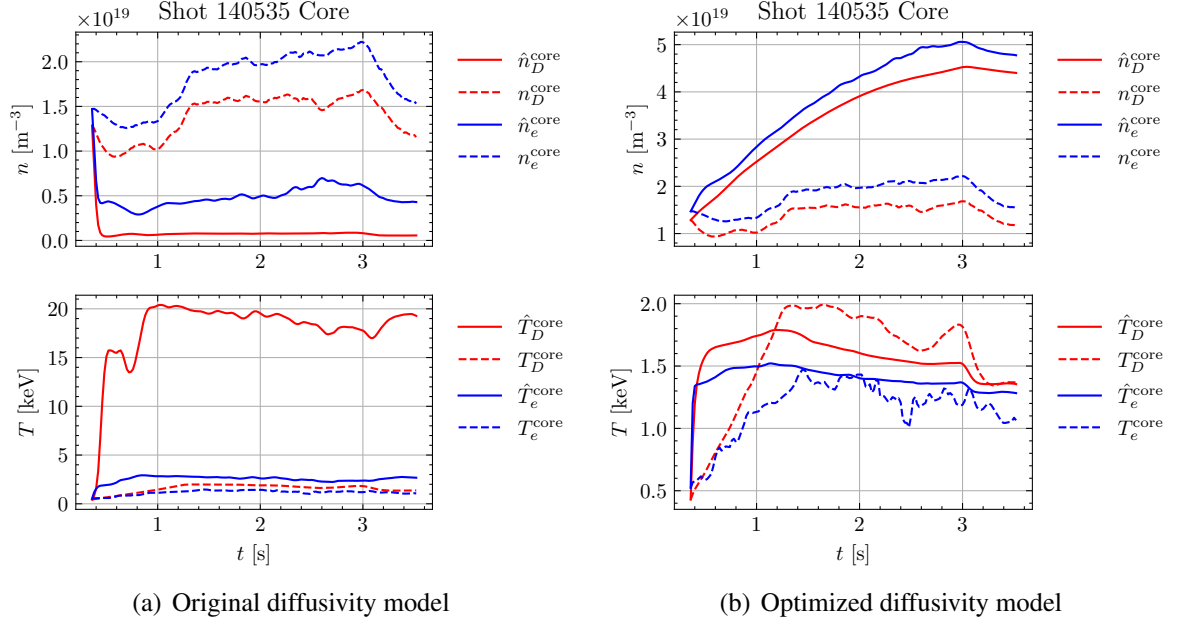


Figure 4.30: Simulation results of the shot 140535 for the core node, where  $\hat{n}_\sigma^{\text{node}}$  and  $\hat{T}_\sigma^{\text{node}}$  are from the multinodal model, while  $n_\sigma^{\text{node}}$  and  $T_\sigma^{\text{node}}$  are from the experimental measurement.

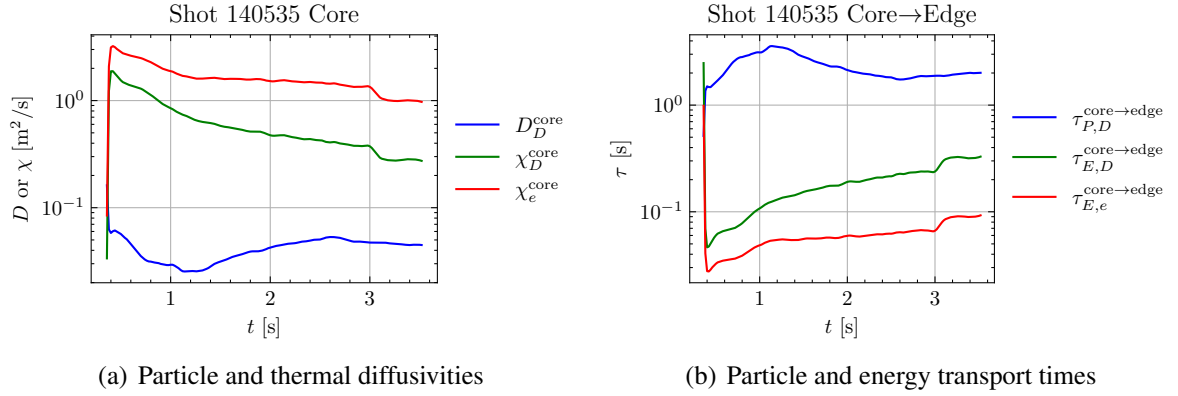


Figure 4.31: Diffusivities and transport times from the core to the edge for the shot 140535 with the optimized diffusivity model.

### SOL Node

The SOL particle densities and temperatures of the deuterons and electrons for the shot 140535 are shown in the Figure 4.34, with the diffusivities and transport times in the Figure 4.35. The overall performance of the multinodal model in the SOL particle densities improves after the optimization, although the particle density result is better than the tem-

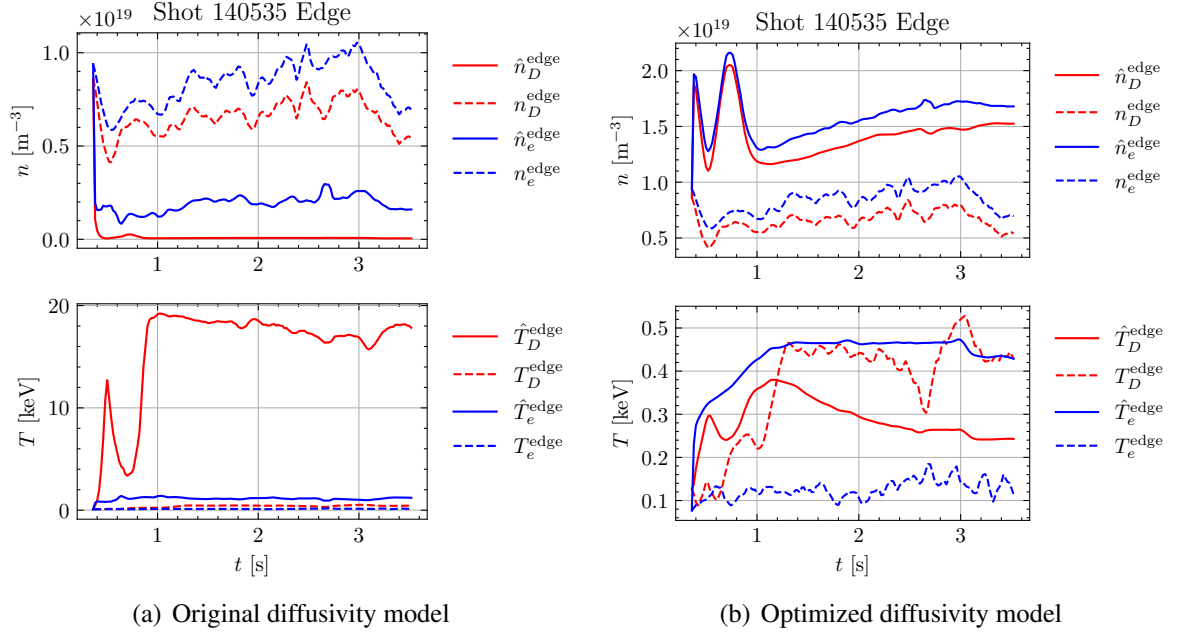


Figure 4.32: Simulation results of the shot 140535 for the edge node, where  $\hat{n}_\sigma^{\text{node}}$  and  $\hat{T}_\sigma^{\text{node}}$  are from the multinodal model, while  $n_\sigma^{\text{node}}$  and  $T_\sigma^{\text{node}}$  are from the experimental measurement.

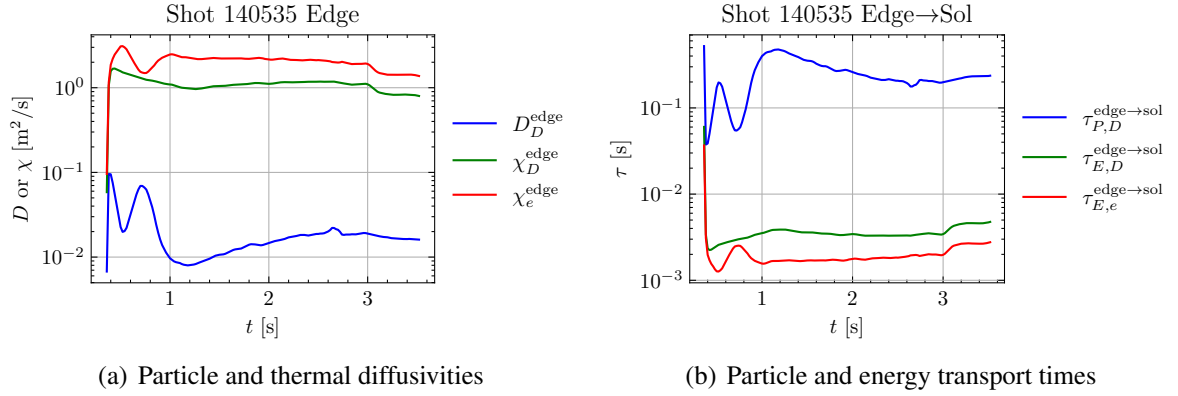


Figure 4.33: Diffusivities and transport times from the edge to the SOL for the shot 140535 with the optimized diffusivity model.

perature one. However, the effective energy confinement time of the SOL electrons should be lower, so the electron temperature can be smaller than the current simulation result compared with the experimental measurement.

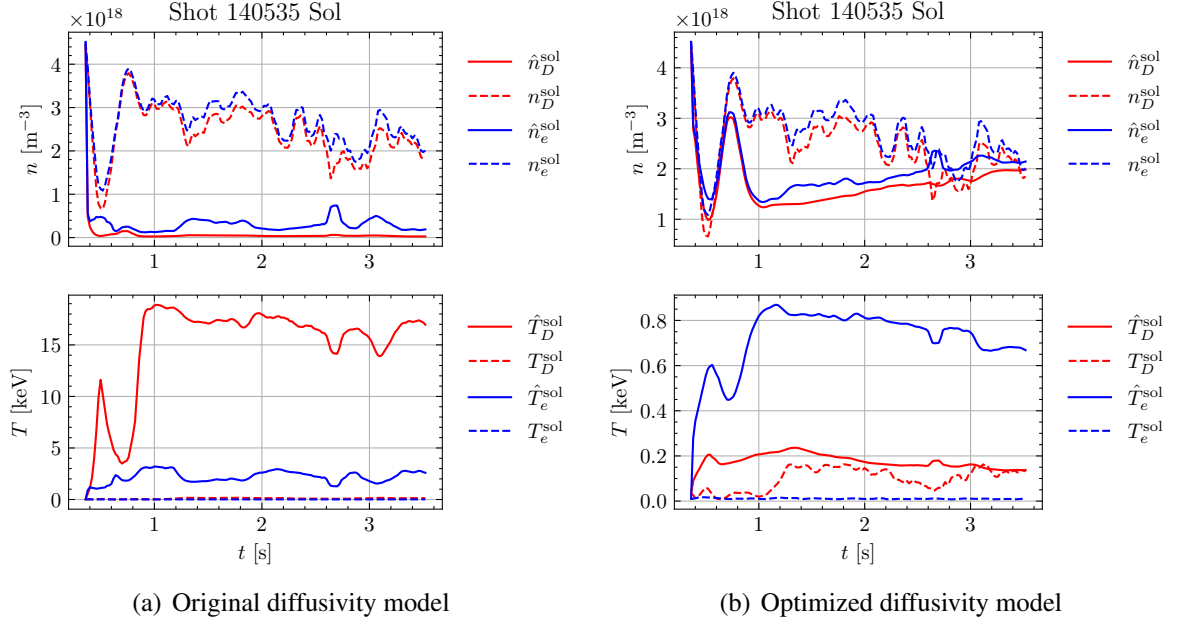


Figure 4.34: Simulation results of the shot 140535 for the SOL node, where  $\hat{n}_\sigma^{\text{node}}$  and  $\hat{T}_\sigma^{\text{node}}$  are from the multinodal model, while  $n_\sigma^{\text{node}}$  and  $T_\sigma^{\text{node}}$  are from the experimental measurement.

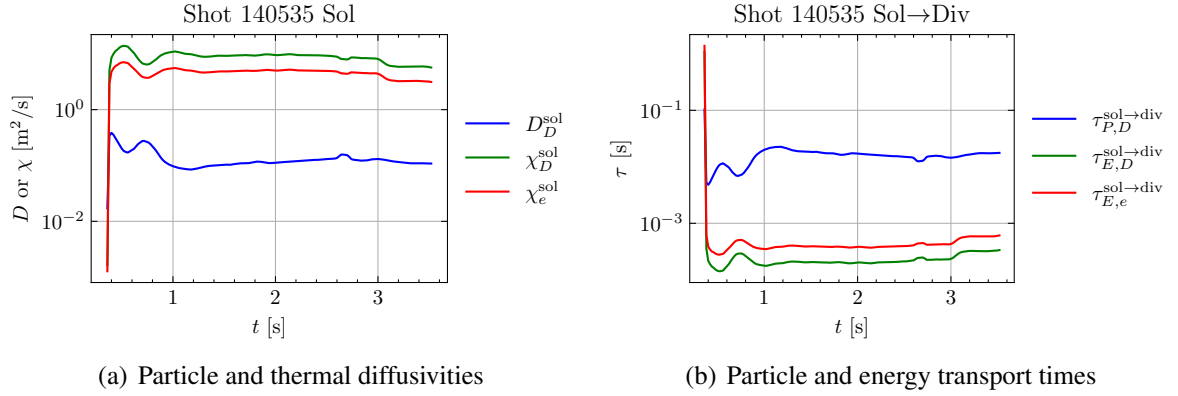


Figure 4.35: Diffusivities and transport times from the SOL to the divertor for the shot 140535 with the optimized diffusivity model.

## 4.6 Summary

This chapter presents a simplified multinodal model for DIII-D deuterium plasmas. Three nodes are modeled, including the core, edge, and scrape-off layer (SOL). These nodes' particle and energy balance equations are given with the proper sources and sinks. A paramet-

ric diffusivity model is formulated with the internodal transport times. Among the DIII-D experiment data, 25 ELMing non-RMP H-mode shots are selected and split into training and testing datasets. The multinodal model is optimized on the training set and evaluated on the testing set. The evaluation results' mean squared error (MSE) is presented with the optimized diffusivity model parameters. The particle densities, temperatures, diffusivities, and transport times are presented for the testing shots.

After analyzing the model performances, several strengths and shortcomings of the multinodal model are concluded:

- The overall performance of the multinodal model with optimized diffusivity parameters is better than the original one with the  $\chi_{H98}$  diffusivity [17, 18]. This observation proves the effectiveness of the proposed computational methods based on machine learning and optimization algorithms.
- The performance of the multinodal model is better in the core and edge nodes than in the SOL node. Since the core and edge nodes can be decoupled from the multinodal model, we can use such a two-nodal model when we simulate burning plasmas in ITER.
- The multinodal model can track the density and temperature tendencies more accurately with only one power source than the multiple sources. More interaction terms can be considered in future work.
- The neutral beam injection (NBI) is dealt with more appropriately than the ion and electron cyclotron heating (ICH and ECH). This observation requires more accurate computations for the deposition profiles rather than the predetermined ones currently used.
- The distributions and efficiencies of the gas puffing among nodes should be adjusted by the experiment data. So the particle densities in the edge node will not have a jump at the shot beginning.

- The ion orbit loss (IOL) and other edge effects in the edge nodes should be revisited in the future to get a better result of edge transport.

After discussing the strengths and shortcomings of the multinodal model for DIII-D non-fusion plasmas, we can now apply the model to ITER fusion plasmas, where deuterium-tritium (D-T) fusion reactions should be included in the model. This target will be focused on in the next chapter. The limitations of the current multinodal model can also be addressed in future work, which will be discussed in the last chapter.



## **CHAPTER 5**

### **MULTINODAL MODEL SIMULATIONS FOR ITER PLASMAS**

In order to study the thermal runaway instability of burning plasmas, it is important to apply the multinodal burning plasma model for ITER deuterium-tritium (D-T) plasmas in this chapter. Several proper assumptions are made for simplifying the multinodal model. The particle and energy balance equations are presented for deuterons, tritons, alpha particles, and electrons. The simplified multinodal model is then applied to simulate inductive and non-inductive operation scenarios. Sensitivity analyses are also done for diffusivity, electron cyclotron radiation, impurity radiation, and ion orbit loss parameters. The simulation results show that radiation and transport processes can quickly remove extra energy from fusion alpha heating and prevent potential thermal runaway instability.

#### **5.1 Assumptions for Modeling ITER Plasmas**

In order to be used for simulating ITER deuterium-tritium (D-T) plasmas, the multinodal burning plasma model needs several necessary simplifications, which are postulated as follows. With these assumptions, this study's research can focus on the burning plasma and its critical involved timescales with a balance of solution accuracy and computation efficiency.

1. Only the core and edge regions are modeled as nodes in the multinodal model. Other regions are neglected, including the scrape-off layer (SOL), divertor, and plenum. The geometry of the multinodal model for ITER is shown in the Figure 5.1. This assumption can let us focus on the important burning processes in the plasma core and the transport and radiation from the core to the edge.
2. Only the deuteron, triton, alpha particle, and electron are computed in the model.

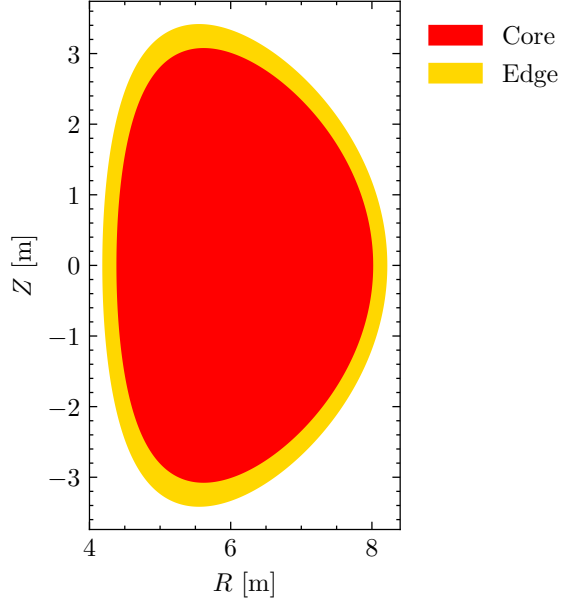


Figure 5.1: The cross section of the ITER plasma with the core and edge regions in the multinodal model.

Particle densities and temperatures of these species are solved from the multinodal model besides electron densities, which are computed from the charge neutrality.

3. Only the helium (He, around 3%), beryllium (Be, 2%), and argon (Ar, 0.12%) are considered as impurity particles, where helium is generated from D-T fusion reactions, beryllium is the first wall material, and argon is seeded for increasing radiation loss and reduce the heat load to the divertor [7]. Besides the helium density directly solved from the multinodal model, other impurity densities are assumed as constant fractions of the electron density in one region. This assumption can let us avoid modeling complicated impurity mechanisms and wall conditions.
4. Only the deuterium-tritium (D-T) fusion reaction is considered. Other fusion reactions, including D-D and D- $^3\text{He}$  reactions, are neglected due to their lower reaction rates than the D-T reactions under ITER conditions.
5. The delay mechanism of the fusion alpha heating is implemented for the core node. The fusion alpha particles can transfer energy to electrons immediately but have to

wait for a slowing-down timescale before heating ions. Besides, the ion temperature is assumed to increase linearly within this timescale.

6. All atomic processes and molecular processes are neglected, which are usually crucial in the neglected SOL and divertor nodes. Neutral particles and recycling particles from the wall are also ignored. The particles passing through the last closed flux surface (LCFS) are assumed lost.
7. When auxiliary heating is applied, the predetermined energy deposition profiles of neutral beam injection (NBI) and radiofrequency (RF) heating [30], including electron cyclotron heating (ECH), ion cyclotron heating (ICH), and lower hybrid (LH) heating, are used. These deposition profiles have been included in the previous research. This assumption can decrease the computation burden, while more accurate computations for auxiliary heating can be implemented in the future.
8. The triton particle and thermal diffusivities are assumed equal to the deuteron corresponding ones, i.e.  $D_D^{\text{node}} = D_T^{\text{node}}$  and  $\chi_D^{\text{node}} = \chi_T^{\text{node}}$ , where  $\text{node} \in \{\text{core}, \text{edge}\}$ . Thus, only two ion particle diffusivities ( $D_D^{\text{node}}$  and  $D_\alpha^{\text{node}}$ ), two ion thermal diffusivities ( $\chi_D^{\text{node}}$  and  $\chi_\alpha^{\text{node}}$ ), and one electron thermal diffusivity ( $\chi_e^{\text{node}}$ ) are needed for each node.
9. When the electron cyclotron radiation (ECR) [40] is computed, the parameters including the density profile  $\alpha_n = 0.037$  and temperature profile  $\alpha_T = 1.027$ ,  $\beta_T = 1.194$  fitted from the typical ITER profiles of inductive scenario [7], and also the reflection coefficient  $r = 0.8$  [11, 41] are used in the ECR formula. For the non-inductive scenario, the parameter  $\alpha_n = 0.102$ ,  $\alpha_T = 4.079$ ,  $\beta_T = 3.278$ ,  $r = 0.8$  are applied. Besides, one ECR power profile fitted from Albajar et al. [41] is used..
10. The ion orbit loss (IOL [49, 50, 51, 52, 53, 54, 55]) term is only included for the edge node, where the particle and energy loss timescales are approximated by the

corresponding transport times from the edge to the SOL. The sample IOL computation with ITER conditions [11] has shown that the IOL in the plasma core can be neglected.

## 5.2 Particle and Energy Balance Equations

With the above assumptions, the multinodal burning plasma model proposed in the Section 2.4 can be simplified into the following particle and energy balance equations.

Particle balance equations for deuterons, tritons, and alpha particles in the core and edge nodes are

$$\frac{dn_D^{\text{core}}}{dt} = S_{D,\text{ext}}^{\text{core}} + S_{D,\text{fus}}^{\text{core}} + S_{D,\text{tran}}^{\text{core}}, \quad (5.1)$$

$$\frac{dn_T^{\text{core}}}{dt} = S_{T,\text{ext}}^{\text{core}} + S_{T,\text{fus}}^{\text{core}} + S_{T,\text{tran}}^{\text{core}}, \quad (5.2)$$

$$\frac{dn_\alpha^{\text{core}}}{dt} = S_{\alpha,\text{ext}}^{\text{core}} + S_{\alpha,\text{fus}}^{\text{core}} + S_{\alpha,\text{tran}}^{\text{core}}, \quad (5.3)$$

$$\frac{dn_D^{\text{edge}}}{dt} = S_{D,\text{ext}}^{\text{edge}} + S_{D,\text{fus}}^{\text{edge}} + S_{D,\text{tran}}^{\text{edge}} + S_{D,\text{IOL}}^{\text{edge}}, \quad (5.4)$$

$$\frac{dn_T^{\text{edge}}}{dt} = S_{T,\text{ext}}^{\text{edge}} + S_{T,\text{fus}}^{\text{edge}} + S_{T,\text{tran}}^{\text{edge}} + S_{T,\text{IOL}}^{\text{edge}}, \quad (5.5)$$

$$\frac{dn_\alpha^{\text{edge}}}{dt} = S_{\alpha,\text{ext}}^{\text{edge}} + S_{\alpha,\text{fus}}^{\text{edge}} + S_{\alpha,\text{tran}}^{\text{edge}} + S_{\alpha,\text{IOL}}^{\text{edge}}. \quad (5.6)$$

The electron densities are computed from the charge neutrality:

$$n_e^{\text{core}} = z_D n_D^{\text{core}} + z_T n_T^{\text{core}} + z_\alpha n_\alpha^{\text{core}} + \sum_z z_z n_z^{\text{core}}, \quad (5.7)$$

$$n_e^{\text{edge}} = z_D n_D^{\text{edge}} + z_T n_T^{\text{edge}} + z_\alpha n_\alpha^{\text{edge}} + \sum_z z_z n_z^{\text{edge}}. \quad (5.8)$$

The particle source and sink terms on the right-hand sides of the particle balance equations are as follows.

1. The external particle source term is computed by summing the neutral beam injection (NBI), gas puffing (GAS), shatter pellet injection (SPI), and other external particle

sources:  $S_{\sigma,\text{ext}}^{\text{node}} = S_{\sigma,\text{NBI}}^{\text{node}} + S_{\sigma,\text{GAS}}^{\text{node}} + S_{\sigma,\text{SPI}}^{\text{node}} + \dots$ , where  $\sigma \in \{D, T, \alpha\}$ . In this chapter, only the particles from the NBI are considered.

2. The fusion terms are computed from the D-T fusion reactions as in the Equation 2.76:

$$S_{D,\text{fus}}^{\text{node}} = S_{T,\text{fus}}^{\text{node}} = -n_D^{\text{node}} n_T^{\text{node}} \langle \sigma v \rangle_{\text{fus}}, \quad S_{\alpha,\text{fus}}^{\text{node}} = n_D^{\text{node}} n_T^{\text{node}} \langle \sigma v \rangle_{\text{fus}}. \quad (5.9)$$

3. The transport terms considering the transport between the core and edge, and also between the edge and SOL are computed by

$$S_{\sigma,\text{tran}}^{\text{core}} = -\frac{n_{\sigma}^{\text{core}} - n_{\sigma}^{\text{edge}}}{\tau_{P,\sigma}^{\text{core} \rightarrow \text{edge}}}, \quad S_{\sigma,\text{tran}}^{\text{edge}} = \frac{V_{\text{core}}}{V_{\text{edge}}} \frac{n_{\sigma}^{\text{core}} - n_{\sigma}^{\text{edge}}}{\tau_{P,\sigma}^{\text{core} \rightarrow \text{edge}}} - \frac{n_{\sigma}^{\text{edge}}}{\tau_{P,\sigma}^{\text{edge} \rightarrow \text{sol}}}, \quad (5.10)$$

where  $\tau_{P,\sigma}^{\text{core} \rightarrow \text{edge}}$  is the particle transport time from the core node to the edge node, and  $\tau_{P,\sigma}^{\text{edge} \rightarrow \text{sol}}$  is the particle transport time from the edge node to the SOL node. These particle transport times are calculated by

$$\tau_{P,\sigma}^{\text{core} \rightarrow \text{edge}} = \frac{r_{\text{core}}^2}{2r_{\text{core}}} \frac{\Delta r_{\text{core-edge}}}{D_{\sigma}^{\text{core}}}, \quad \tau_{P,\sigma}^{\text{edge} \rightarrow \text{sol}} = \frac{r_{\text{edge}}^2 - r_{\text{core}}^2}{2r_{\text{edge}}} \frac{\Delta r_{\text{edge-sol}}}{D_{\sigma}^{\text{edge}}} \quad (5.11)$$

where  $D_{\sigma}^{\text{core}}$  and  $D_{\sigma}^{\text{edge}}$  are the core and edge particle diffusivities respectively.

4. The ion orbit loss (IOL) term is only included for the edge node, which is computed by

$$S_{\sigma,\text{IOL}}^{\text{edge}} = -\frac{F_{\sigma,\text{orb}}^{\text{edge}}}{\tau_{P,\sigma,\text{IOL}}^{\text{edge}}} n_{\sigma}^{\text{edge}}, \quad (5.12)$$

where  $F_{\sigma,\text{orb}}^{\text{edge}}$  is the particle loss fraction, and  $\tau_{P,\sigma,\text{IOL}}^{\text{edge}}$  is the particle IOL timescale.

Energy balance equations for deuterons, tritons, alpha particles, and electrons in the

core and edge nodes are

$$\frac{dU_D^{\text{core}}}{dt} = P_{D,\text{aux}}^{\text{core}} + P_{D,\text{fus}}^{\text{core}} + Q_D^{\text{core}} + P_{D,\text{tran}}^{\text{core}}, \quad (5.13)$$

$$\frac{dU_T^{\text{core}}}{dt} = P_{T,\text{aux}}^{\text{core}} + P_{T,\text{fus}}^{\text{core}} + Q_T^{\text{core}} + P_{T,\text{tran}}^{\text{core}}, \quad (5.14)$$

$$\frac{dU_\alpha^{\text{core}}}{dt} = P_{\alpha,\text{aux}}^{\text{core}} + P_{\alpha,\text{fus}}^{\text{core}} + Q_\alpha^{\text{core}} + P_{\alpha,\text{tran}}^{\text{core}}, \quad (5.15)$$

$$\frac{dU_e^{\text{core}}}{dt} = P_\Omega^{\text{core}} + P_{e,\text{aux}}^{\text{core}} + P_{e,\text{fus}}^{\text{core}} - P_R^{\text{core}} + Q_e^{\text{core}} + P_{e,\text{tran}}^{\text{core}}, \quad (5.16)$$

$$\frac{dU_D^{\text{edge}}}{dt} = P_{D,\text{aux}}^{\text{edge}} + P_{D,\text{fus}}^{\text{edge}} + Q_D^{\text{edge}} + P_{D,\text{tran}}^{\text{edge}} + P_{D,\text{IOL}}^{\text{edge}}, \quad (5.17)$$

$$\frac{dU_T^{\text{edge}}}{dt} = P_{T,\text{aux}}^{\text{edge}} + P_{T,\text{fus}}^{\text{edge}} + Q_T^{\text{edge}} + P_{T,\text{tran}}^{\text{edge}} + P_{T,\text{IOL}}^{\text{edge}}, \quad (5.18)$$

$$\frac{dU_\alpha^{\text{edge}}}{dt} = P_{\alpha,\text{aux}}^{\text{edge}} + P_{\alpha,\text{fus}}^{\text{edge}} + Q_\alpha^{\text{edge}} + P_{\alpha,\text{tran}}^{\text{edge}} + P_{\alpha,\text{IOL}}^{\text{edge}}, \quad (5.19)$$

$$\frac{dU_e^{\text{edge}}}{dt} = P_\Omega^{\text{edge}} + P_{e,\text{aux}}^{\text{edge}} + P_{e,\text{fus}}^{\text{edge}} - P_R^{\text{core}} + Q_e^{\text{edge}} + P_{e,\text{tran}}^{\text{edge}}, \quad (5.20)$$

where the nodal energy density is defined as  $U_\sigma^{\text{node}} = \frac{3}{2} n_\sigma^{\text{node}} T_\sigma^{\text{node}}$  for  $\sigma \in \{D, T, \alpha, e\}$  and node  $\in \{\text{core}, \text{edge}\}$ . The energy source and sink terms on the right-hand sides of the energy balance equations are as follows.

1. Ohmic heating power is computed from the plasma current by the Equation 2.63:

$$P_\Omega^{\text{node}} (\text{W/m}^3) = 2.8 \times 10^{-9} \frac{Z_{\text{eff}} I_P^2}{a^4 T_e^{3/2}}, \quad (5.21)$$

where  $I_P$  is in A,  $a$  in m, and  $T_e$  in keV.

2. The auxiliary heating term is calculated by summing the neutral beam injection (NBI) and radiofrequency (RF) energy:  $P_{\sigma,\text{aux}}^{\text{node}} = P_{\sigma,\text{NBI}}^{\text{node}} + P_{\sigma,\text{RF}}^{\text{node}}$ .

3. Fusion power is directly deposited to the ions and electrons as the Equation 2.77:

$$P_{\sigma,\text{fus}}^{\text{node}} = n_D^{\text{node}} n_T^{\text{node}} \langle \sigma v \rangle_{\text{fus}} U_{f\sigma}, \quad \sigma \in \{D, T, \alpha\}, \quad (5.22)$$

where  $U_{f\sigma}$  is the fusion energy transferred from the fusion alpha particles to the species  $\sigma$ , and it is computed by viewing the fusion alpha particles as an energetic beam in NBI formulas. The delay effect between fusion alpha heating to electrons and ions is considered by using a slowing-down timescale  $\tau_{se}^{\text{node}}$  in the Equation 2.80:

$$\tau_{se} = \frac{3(2\pi)^{1/2} T_e^{3/2}}{m_e^{1/2} m_b A_D}. \quad (5.23)$$

The fusion heating to ions is postponed by this timescale compared with electrons. So fusion alpha particles will transfer their energy to electrons first before to ions.

#### 4. Collisional energy terms transferred between ions and electrons are

$$Q_{\alpha}^{\text{node}} = Q_{\alpha D}^{\text{node}} + Q_{\alpha T}^{\text{node}} + Q_{\alpha e}^{\text{node}}, \quad (5.24)$$

$$Q_D^{\text{node}} = -Q_{\alpha D}^{\text{node}} + Q_{DT}^{\text{node}} + Q_{De}^{\text{node}}, \quad (5.25)$$

$$Q_T^{\text{node}} = -Q_{\alpha T}^{\text{node}} - Q_{DT}^{\text{node}} + Q_{Te}^{\text{node}}, \quad (5.26)$$

$$Q_e^{\text{node}} = -Q_{\alpha e}^{\text{node}} - Q_{De}^{\text{node}} - Q_{Te}^{\text{node}}, \quad (5.27)$$

where  $Q_{\sigma\sigma'}^{\text{node}}$  is the energy transferred from the species  $\sigma'$  to  $\sigma$  collisionality. The  $Q_{\alpha D}^{\text{node}}$ ,  $Q_{\alpha T}^{\text{node}}$ , and  $Q_{DT}^{\text{node}}$  terms are computed from the Equation 2.108 as the ion-ion collisions:

$$Q_{ii'} = \frac{3}{2} n_i (T_{i'} - T_i) \nu_{ii'}, \quad (5.28)$$

where  $\nu_{ii'}$  is the characteristic frequency for energy transfer between ions as in the Equation 2.109. Also the  $Q_{De}^{\text{node}}$ ,  $Q_{Te}^{\text{node}}$ , and  $Q_{\alpha e}^{\text{node}}$  terms are computed from the Equation 2.110 as the ion-electron collisions:

$$Q_{ie} = \frac{n_i n_e (q_i q_e)^2 m_e \ln \Lambda \left( 1 - \frac{T_i}{T_e} \right)}{2\pi \epsilon_0^2 (2\pi m_e T_e)^{1/2} m_i \left[ 1 + \frac{4\sqrt{\pi}}{3} \left( \frac{3m_e T_i}{2m_i T_e} \right)^{3/2} \right]}. \quad (5.29)$$

5. The radiation term including electron cyclotron radiation (ECR [40]), bremsstrahlung [1], and impurity radiation [1, 42, 43] is computed by  $P_R^{\text{node}} = P_{\text{ECR}}^{\text{node}} + P_{\text{brem}}^{\text{node}} + P_{\text{imp}}^{\text{node}}$ .
6. The energy transport terms considering the transport between the core and edge, and the edge and SOL are obtained by

$$P_{\sigma,\text{tran}}^{\text{core}} = -\frac{U_{\sigma}^{\text{core}} - U_{\sigma}^{\text{edge}}}{\tau_{E,\sigma}^{\text{core} \rightarrow \text{edge}}}, \quad P_{\sigma,\text{tran}}^{\text{edge}} = \frac{V_{\text{core}}}{V_{\text{edge}}} \frac{U_{\sigma}^{\text{core}} - U_{\sigma}^{\text{edge}}}{\tau_{E,\sigma}^{\text{core} \rightarrow \text{edge}}} - \frac{U_{\sigma}^{\text{edge}}}{\tau_{E,\sigma}^{\text{edge} \rightarrow \text{sol}}}, \quad (5.30)$$

where  $\tau_{E,\sigma}^{\text{core} \rightarrow \text{edge}}$  is the energy transport time from the core node to the edge node, and  $\tau_{E,\sigma}^{\text{edge} \rightarrow \text{sol}}$  is the energy transport time from the edge node to the SOL node. These energy transport times are solved from

$$\tau_{E,\sigma}^{\text{core} \rightarrow \text{edge}} = \frac{r_{\text{core}}^2}{2r_{\text{core}}} \frac{\Delta r_{\text{core-edge}}}{\chi_{\sigma}^{\text{core}}}, \quad \tau_{E,\sigma}^{\text{edge} \rightarrow \text{sol}} = \frac{r_{\text{edge}}^2 - r_{\text{core}}^2}{2r_{\text{edge}}} \frac{\Delta r_{\text{edge-sol}}}{\chi_{\sigma}^{\text{edge}}}, \quad (5.31)$$

where  $\chi_{\sigma}^{\text{core}}$  and  $\chi_{\sigma}^{\text{edge}}$  are the core and edge thermal diffusivities respectively.

7. The IOL term is computed by

$$P_{\sigma,\text{IOL}}^{\text{edge}} = -\frac{E_{\sigma,\text{orb}}^{\text{edge}}}{\tau_{E,\sigma,\text{IOL}}^{\text{edge}}} U_{\sigma}^{\text{edge}}, \quad (5.32)$$

where  $E_{\sigma,\text{orb}}^{\text{edge}}$  is the energy loss fraction, and  $\tau_{E,\sigma,\text{IOL}}^{\text{edge}}$  is the energy IOL timescale.

### 5.3 Computation Results of Inductive Operation Scenarios

Once the multinodal burning plasma model is simplified for the ITER deuterium-tritium (D-T) plasmas, it can be used for simulating the ITER operation scenarios in the following sections. The ITER tokamak can be operating in not only the inductive case [31, 7], where the ohmic current contributes to the most of total toroidal current compared with the beam-driven current and the bootstrap current, but also the non-inductive case [31, 7], where highly energetic neutral atom injection and powerful radiofrequency radiation drive the



most toroidal current. In this section, the inductive and hybrid scenarios are simulated. The inductive operation scenario 2 is discussed firstly with more details, while the inductive scenario 1 and hybrid scenario 3 are visited briefly later.

### 5.3.1 Inductive Operation Scenario 2

The design scenario 2 of the inductive operation is selected to be simulated first, and its typical operating conditions [7] are shown in the Table 5.1 with the inductive scenario 1 and hybrid scenario 3. The typical parameters, including geometries, electromagnetic values, auxiliary heating powers, averaged densities, averaged temperatures, and impurity fractions, are contained. Although a helium fraction is mentioned in this table, the helium density will be solved from the multinodal model directly. These operation conditions are used for multinodal model simulations. Besides, the typical radial profiles of the electron and ion temperatures, and the electron and helium densities [7] are shown in the Figure 5.2. These profiles are integrated over the core and edge nodes to get nodal densities and temperatures, which are used as benchmarks for optimizing the diffusivity parameters in the multinodal model.

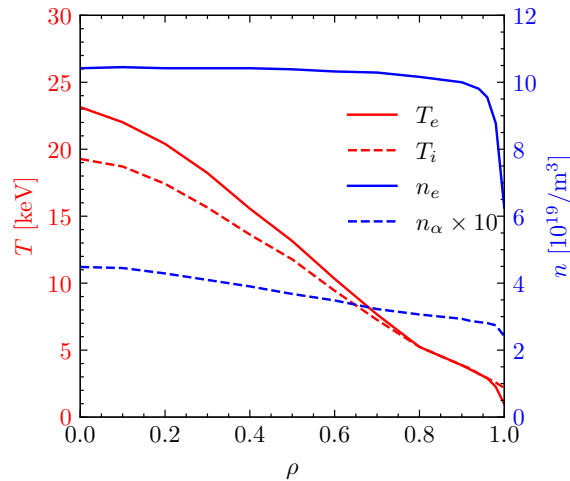


Figure 5.2: Plasma temperature and density profiles at the current flat-top phase for the inductive operational scenario. Reproduced with permission from the ITER Technical Basis [31].

Table 5.1: Typical parameters of ITER inductive and hybrid operation scenarios. Reproduced with permission from the ITER Technical Basis [31].

Parameter	Symbol	Scenario 1 Inductive	Scenario 2 Inductive	Scenario 3 Hybrid
Major radius	$R_0$ (m)	6.2	6.2	6.2
Minor radius	$a$ (m)	2.0	2.0	2.0
Volume	$V$ (m <sup>3</sup> )	831	831	831
Surface	$S$ (m <sup>2</sup> )	683	683	683
Elongation at the 95% flux surface	$\kappa_{95}$	1.70	1.70	1.70
Triangularity at the 95% flux surface	$\delta_{95}$	0.33	0.33	0.33
Toroidal magnetic field at the magnetic axis	$B_T$ (T)	5.3	5.3	5.3
Plasma current	$I_P$ (MA)	15	15	13.8
Safety factor at the 95% flux surface	$q_{95}$	3.0	3.0	3.3
Volume-averaged electron density	$\langle n_e \rangle$ (10 <sup>19</sup> m <sup>-3</sup> )	11.3	10.1	9.3
Volume-averaged ion temperature	$\langle T_i \rangle$ (keV)	8.1	8.0	8.4
Volume-averaged electron temperature	$\langle T_e \rangle$ (keV)	8.9	8.8	9.6
Fusion power	$P_{\text{fus}}$ (MW)	500	400	400
Auxiliary heating power	$P_{\text{aux}}$ (MW)	50	40	73
Radiofrequency heating power	$P_{\text{RF}}$ (MW)	17	7	40
Neutral beam heating power	$P_{\text{NBI}}$ (MW)	33	33	33
Fusion energy gain factor	$Q$	10	10	5.4
Energy confinement time	$\tau_E$ (s)	3.4	3.7	2.73
Plasma pulse length & burning time	$t$ (s)	500	400	1070
Helium fraction	$f_{\text{He}}$ (%)	3.2	3.2	2.5
Beryllium fraction	$f_{\text{Be}}$ (%)	2.0	2.0	2.0
Argon fraction	$f_{\text{Ar}}$ (%)	0.14	0.12	0.19
Effective impurity charge	$Z_{\text{eff}}$	1.72	1.66	1.85
Radiation power	$P_{\text{rad}}$ (MW)	61	47	55

Before simulating the inductive scenario 2, we need to model several necessary particle and energy sources. For external particle sources, the neutral beam injection (NBI) injects negative deuteron particles into the tokamak plasma. At the same time, the same amount of tritons is supplied for a balance of deuteron and triton particles. For external energy sources, neutral beam and radiofrequency radiation systems are used for auxiliary heating. ITER heating and current drive system [31, 87, 32] (H&CD) includes 33 MW neutral beam injection (NB, 1 MeV), 20 WM ion cyclotron heating (IC, 40-50 MHz), and 20MW

electron cyclotron heating (EC, 170 GHz) in the first campaign, and also 40MW lower hybrid heating (LH, 5 GHz) [32] with 50 MW NB, 40 MW IC, and 40 MW EC as potential upgrades in the future. Much studies [88, 89, 90, 91, 92] have been done for the ITER H&CD systems. For the inductively driven scenario 2, Wagner et al. [91] concluded that the exact heating mixture proportions of NB, IC, and EC are not critical. However, the IC should be utilized for heating ions directly. Thus, we assume all RF heating power is deposited to ions in this scenario.

In order to model the ITER burning plasma more accurately, the parameters in the diffusivity model need tuning properly by machine learning algorithms. In previous simulations of DIII-D plasmas, the experiment data are split into a training dataset and a testing dataset. The training dataset is used for tuning parameters in the diffusivity model. And once the diffusivity parameters are optimized properly, the multinodal model is evaluated on the testing dataset. However, since the ITER reactor is still under construction, we cannot obtain the ITER experiment data and use it to train the parametric diffusivity model directly. Thus, enlightened by the transfer learning [93], the parameters learned in the multinodal model of the DIII-D deuterium plasma are transferred to the diffusivity model for the ITER plasma. Then, we apply a fine-tuning method to these diffusivity parameters by using burning simulation results from the previous research [31, 7] as optimization targets. The parameters in the diffusivity model are adjusted for ITER operation conditions, so the simulation results of the ITER multinodal model can match these design scenarios during the current flat-top region.

During the optimization, the inductive scenario 2 is used as a training set, while the inductive scenario 1 and the hybrid scenario 3 are viewed as a testing set. The training set is used to train the parametric diffusivity model, while the testing set evaluates model performances. This method allows the optimized model to be generalized for new data in prediction tasks. This idea has been discussed thoroughly in the previous research for the DIII-D deuterium plasma. For the ITER D-T plasma, the optimization object is set as a

Table 5.2: Optimized parameters in the nodal particle and thermal diffusivities for the ITER inductive scenarios.

	$\alpha_H$	$\alpha_B$	$\alpha_n$	$\alpha_T$	$\alpha_{\nabla T}$	$\alpha_q$	$\alpha_\kappa$	$\alpha_M$	$\alpha_R$	$\alpha_a$
$D_D^{\text{core}}$	0.0623	-3.8193	1.4726	-0.3682	-0.0086	3.0048	-2.8187	-0.7748	0.5270	0.6836
$D_\alpha^{\text{core}}$	0.0749	-3.6346	1.6613	-0.1922	0.1712	3.1992	-2.6402	-0.5874	0.7167	0.8744
$\chi_D^{\text{core}}$	0.0699	-3.7410	-0.2917	3.1220	1.0357	2.1694	-2.9481	-1.2062	-0.0400	0.2193
$\chi_\alpha^{\text{core}}$	0.0774	-3.6392	-0.1908	3.2190	1.1267	2.2702	-2.8457	-1.1047	0.0613	0.3204
$\chi_e^{\text{core}}$	0.0492	-4.3936	0.0319	1.6794	0.9890	1.7566	-3.6844	-1.5747	-0.3684	-0.3237
$D_D^{\text{edge}}$	0.0276	-4.5754	2.9503	0.3002	-0.6916	2.1044	-3.4817	-1.5889	-0.3185	-0.0250
$D_\alpha^{\text{edge}}$	0.0347	-4.3454	3.1718	0.5397	-0.4552	2.3442	-3.2601	-1.3569	-0.0831	0.2106
$\chi_D^{\text{edge}}$	0.1117	-3.6094	0.2137	1.4591	1.1279	2.9174	-3.0692	-0.6974	0.6077	-0.0581
$\chi_\alpha^{\text{edge}}$	0.1106	-3.6189	0.1774	1.4062	1.0864	2.8513	-3.0361	-0.7233	0.5688	-0.0918
$\chi_e^{\text{edge}}$	0.1126	-3.4947	-0.9932	1.4032	1.4071	2.7817	-3.1842	-0.6915	0.6069	-0.2435

vector of

$$\left[ \frac{n_D^{\text{node}}}{10^{19} \text{ m}^{-3}} \quad \frac{n_\alpha^{\text{node}}}{10^{18} \text{ m}^{-3}} \quad \frac{n_e^{\text{node}}}{10^{19} \text{ m}^{-3}} \quad \frac{T_D^{\text{node}}}{1 \text{ keV}} \quad \frac{T_e^{\text{node}}}{1 \text{ keV}} \right]_{\text{node} \in \{\text{core, edge}\}}, \quad (5.33)$$

where both densities and temperatures in the core and edge nodes are considered. The parameters in the nodal diffusivity model are initialized as the corresponding DIII-D deuterium plasma parameters. Besides, only the current flat-top region of the inductive scenario 2 is simulated during the optimization. The densities and temperatures are initialized at the flat-top values instead of a cold plasma. The time step is set as 0.2 s and the total time length is 10 s. After 14 epochs, the mean squared error (MSE) loss of the scenario 2 at the current flat-top region drops from 6.7085 to 0.0016 with a learning rate of 0.02. The optimized diffusivity parameters are shown in the Table 5.2.

After optimizing the diffusivity parameters, the initial temperatures are reset to 2 keV in the core node and 1 keV in the edge node for all species. The particle densities are same as the Table 5.1 and the Figure 5.2, but the alpha particle densities become  $10^{17} \text{ m}^{-3}$ . The multinodal modal with this initial condition is then simulated for the ITER inductive scenario 2 and a total time 15 s.

The simulation results of the scenario 2 are shown in the Figure 5.3, where densities and

temperatures of deuterons, alpha particles, and electrons are presented. The triton densities and temperatures are omitted since their values are roughly the same as deuteron ones. Also, the temperatures of alpha particles are only for cold ones, where the fusion alpha particles at 3.5 MeV are excluded until they transfer their energy to electrons and ions. The simulation results show that the core and edge temperatures reach a steady state at about 11 s. The energy excursion from the fusion alpha heating is not found in this simulation.

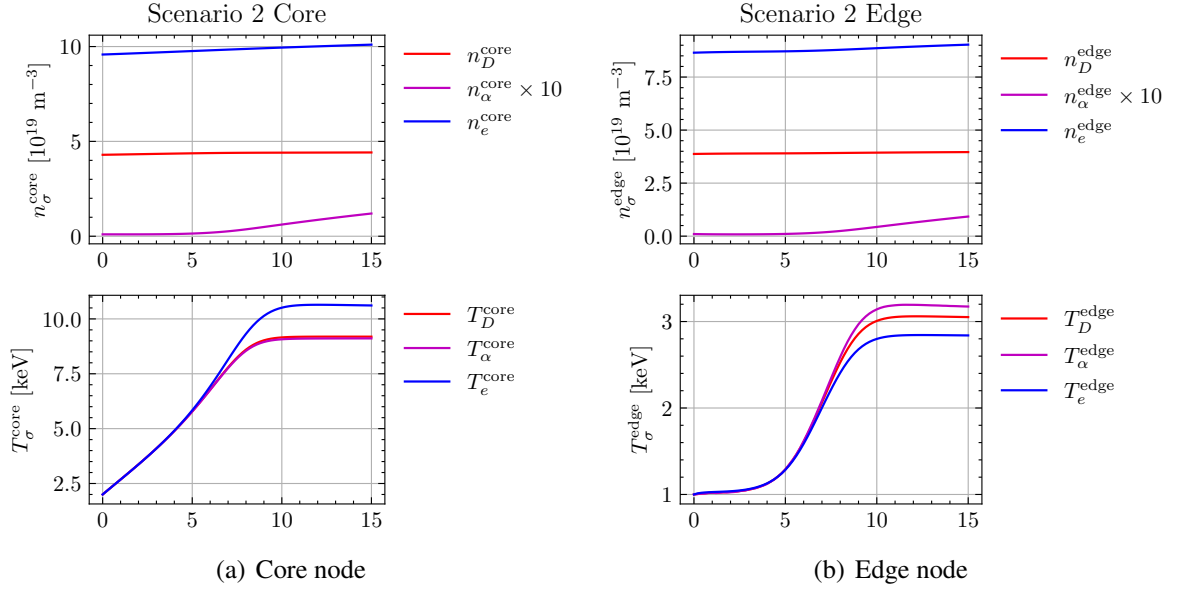


Figure 5.3: Densities and temperatures of the ITER design scenario 2.

The powers changing with time are shown in Figure 5.4, where for  $\sigma \in \{e, i\}$  and  $\text{node} \in \{\text{core}, \text{edge}\}$ ,  $P_{\text{oh}}^{\text{node}}$  is the ohmic heating,  $P_{\sigma, \text{aux}}^{\text{node}}$  is the auxiliary heating,  $P_{\sigma, \text{fus}}^{\text{node}}$  is the fusion heating,  $Q_\sigma^{\text{node}}$  is the Coulomb collisional energy transfer to the species  $\sigma$ ,  $P_{\text{rad}}^{\text{node}}$  is the radiation power,  $P_{\sigma, \text{tran}}^{\text{node}}$  is the energy transport, and  $P_{\sigma, \text{iol}}^{\text{node}}$  is the IOL energy loss. In these figures for powers, a positive value means a energy gain, while a negative value means a energy loss. At the beginning of the simulation, the ohmic heating  $P_{\text{oh}}^{\text{core}}$  and auxiliary heating  $P_{\sigma, \text{aux}}^{\text{core}}$  supply the most of energy to core electrons and ions, until the core ion temperature is higher enough to initiate fusion reactions. The fusion alpha particles heat the electrons in  $P_{e, \text{fus}}^{\text{core}}$  first, then the heated electrons transfer their energy to ions through Coulomb collisions  $Q_i^{\text{core}} = -Q_e^{\text{core}}$ . Meanwhile, the fusion heating is also deposited to

core ions through  $P_{i,\text{fus}}^{\text{core}}$ . The fusion heating is removed by the radiation power  $P_{\text{rad}}^{\text{core}}$  and transport loss  $P_{\sigma,\text{tran}}^{\text{core}}$ .

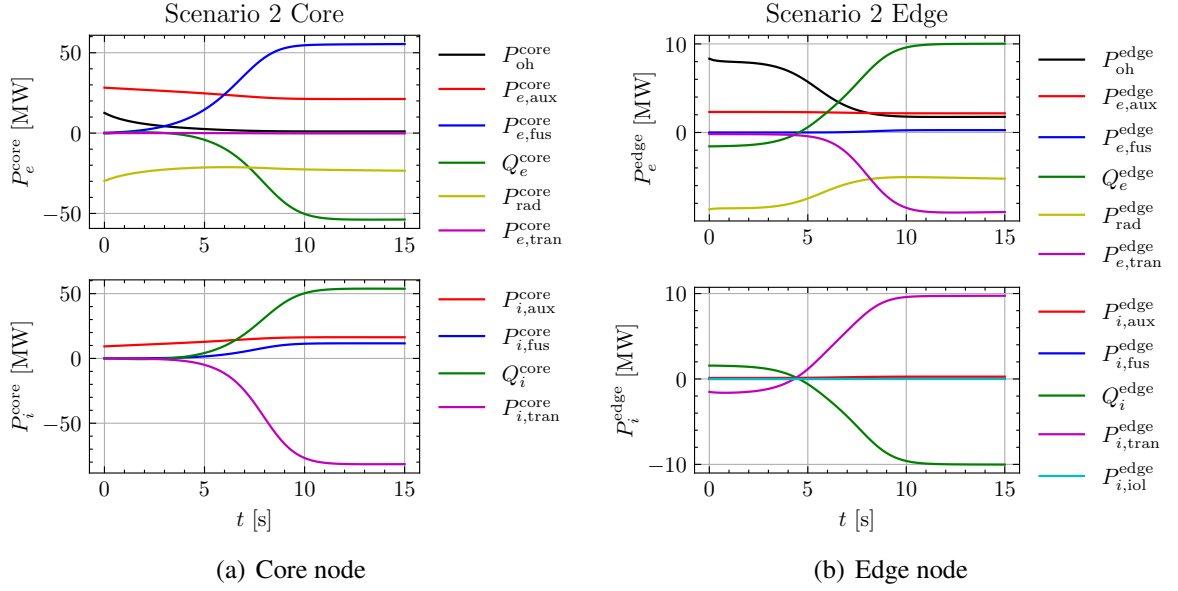


Figure 5.4: Powers of the ITER design scenario 2.

To present how the energy is produced and transferred, a picture of the energy flows at the 15 s for the scenario 2 is shown in the Figure 5.5. This picture presents an overview of how fusion energy is transferred between different species and transported between different regions by different mechanisms. Firstly, the fusion alpha particles born at 3.5 MeV are mostly deposited to the core electrons in 55.41 MW compared with ions in 11.65 MW. Notice that the multinodal model has considered a time delay between fusion heating to electrons and ions. However, it is not shown here since this energy flow figure is for an approximately steady state. Then, once the electrons are heated through fusion and auxiliary heating, they transfer energy to the core ions through Coulomb collisions in 53.80 MW. The core electrons also lose their energy through radiation and transport. The impurity radiation in 19.53 MW plays an important role among several radiation processes, compared with electron cyclotron radiation (ECR) in 3.26 MW and bremsstrahlung radiation in 0.62 MW. The ECR power is less than the impurity radiation due to a lower  $T_e^{\text{core}}$ . Besides, the energy transport to the edge electrons in 0.19 MW is relatively small due to a

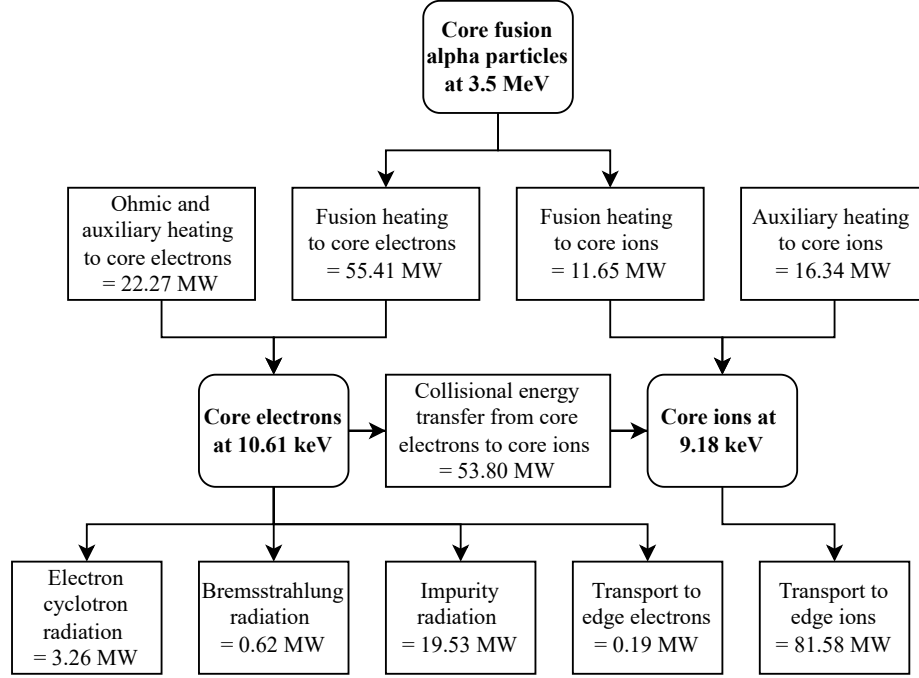


Figure 5.5: Energy flows for the ITER inductive scenario 2 simulated by the multinodal model at 15 s.

small electron diffusivity between the core and edge nodes. Moreover, after core ions are heated from fusion and auxiliary heating, they also transport their energy to the edge ones in 81.58 MW. These radiation and transport processes are quick and strong enough to remove extra energy from fusion alpha heating. Hence, the power excursion does not happen in this inductive scenario.

### 5.3.2 Inductive Operation Scenario 1

To evaluate the performance of the multinodal model with optimized diffusivity parameters for ITER inductive operations, one more inductive case, the scenario 1, is used as a testing scenario. The operation conditions of this scenario have been shown in the Table 5.1, where the expected fusion power 500 MW is higher than the scenario 2 with 400 MW. Also, larger radiofrequency (RF) heating power is applied with the same neutral beam injection (NBI) power as the scenario 2. A longer burning time in 500 s is planned with a higher electron temperature and density.

The simulation results of the multinodal model for the inductive operation scenario 1 are shown in the Figure 5.6. The ion and electron temperatures are comparable with the scenario 2 when they reach a steady state around 11 s. Similarly, the power excursion is not observed in this scenario.

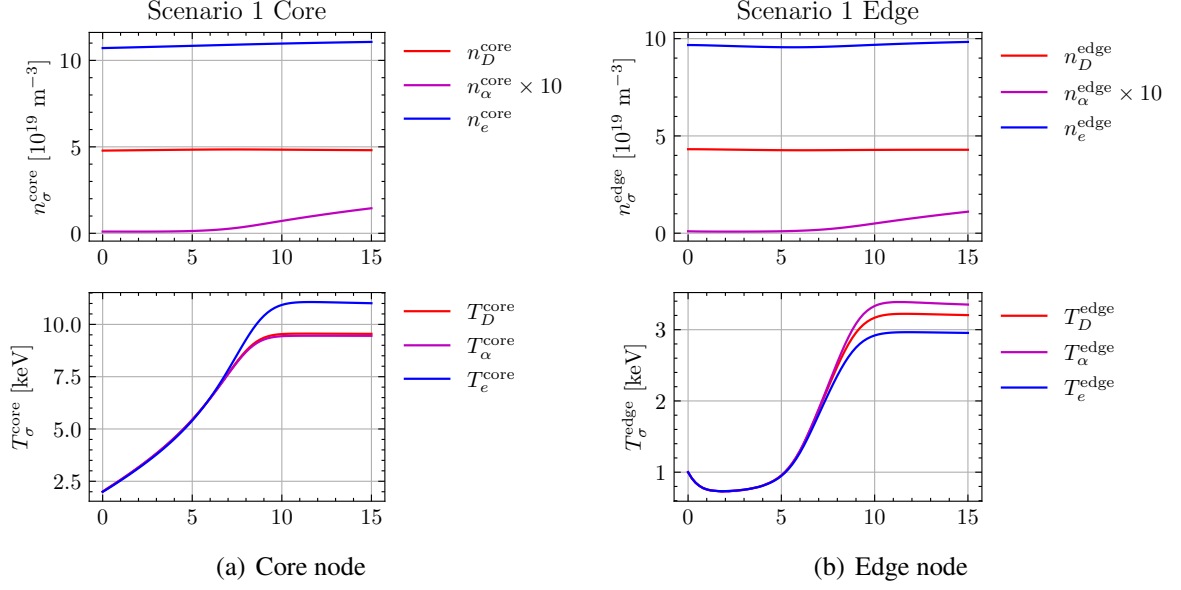


Figure 5.6: Densities and temperatures of the ITER design scenario 1.

### 5.3.3 Hybrid Operation Scenario 3

A hybrid mode of operation [31], where a substantial fraction of the plasma current is driven by non-inductive current drive power and the bootstrap current, is one of the promising routes towards the establishment of ITER operation in steady-state or non-inductive modes. One hybrid operation case, the scenario 3, is selected for verifying its thermal stability with fusion alpha heating by using the multinodal burning plasma model for inductive scenarios. The typical operation parameters have been listed in the Table 5.1. In this hybrid scenario, 25% plasma current is supplied by the current drive (i.e.  $I_{CD}/I_P = 25\%$ ), while 17% is by the bootstrap current (i.e.  $I_{BS}/I_P = 17\%$ ).

The simulation results of the hybrid operation scenario 3 with the multinodal model are shown in the Figure 5.7 and 5.8, where the densities and temperatures are shown firstly,



while the powers are presented next. The ion and electron temperatures reach a steady state in about 6 s, which is shorter than the inductive scenarios due to higher auxiliary heating power. The increased auxiliary heating is then removed by higher radiation and transport terms. Thus, no power excursion is observed in this hybrid scenario simulation.

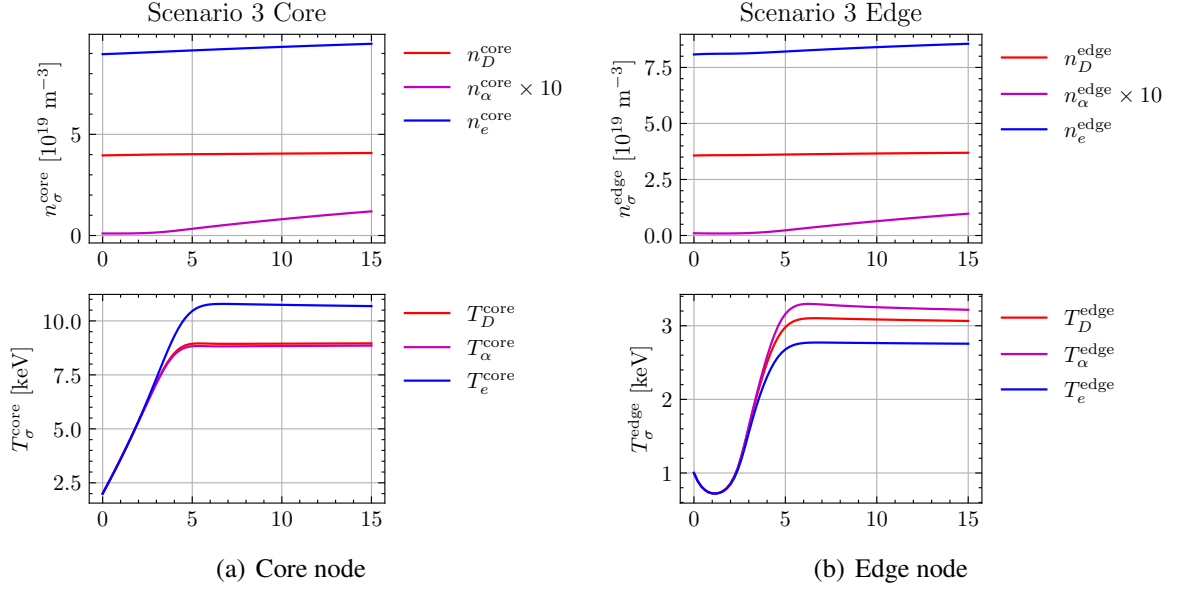


Figure 5.7: Densities and temperatures of the ITER design scenario 3.

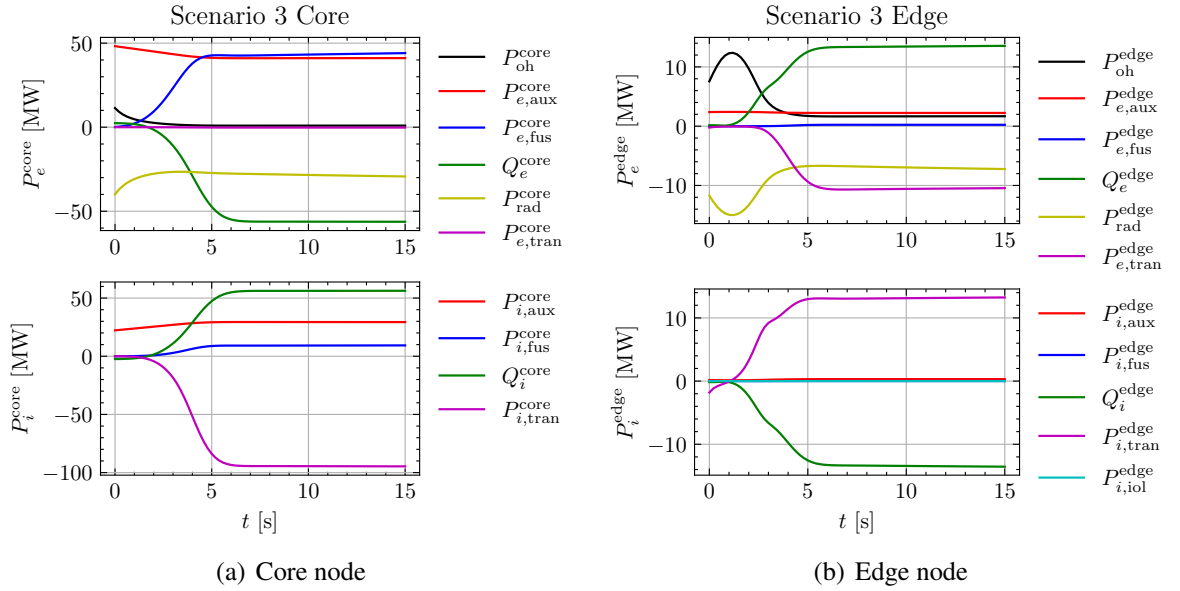


Figure 5.8: Powers of the ITER design scenario 3.

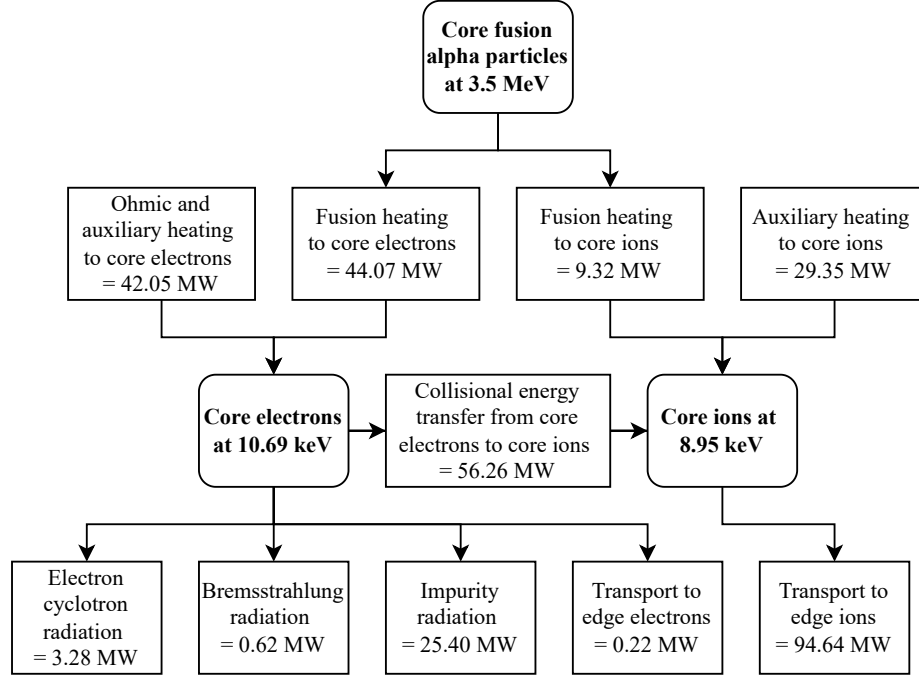


Figure 5.9: Energy flows for the ITER hybrid scenario 3 simulated by the multinodal model at 15 s.

Same as the inductive scenario 2, energy flows of the hybrid scenario 3 at the 15 s are shown in the Figure 5.9. Compared with the Figure 5.5, a lower fusion alpha heating to core electrons is observed, but the auxiliary heating is higher due to more RF power. Thus, the energy transfer to ions and radiation loss through impurities also become more extensive. Besides, due to more energy from auxiliary heating to core ions, they transport more heat to edge ions. These transport and radiation processes are sufficient to remove extra fusion energy and prevent power excursion in this hybrid scenario.

#### 5.4 Computation Results of Non-Inductive Operation Scenarios

Besides inductive scenarios, where most of the plasma current are supplied inductively, the ITER tokamak can also operate in steady-state non-inductive scenarios [31], where the total plasma current at the current flat-top phase is generated non-inductively by the additional current drive and bootstrap current. In ITER, four kinds of heating and current drive (H&CD) systems [7, 32] are used, including:

- Neutral beam (NB), which provides central plasma heating and can be adjusted to provide on-axis or near ( $r/a \leq 0.6$ ) off-axis current-drive,
- Ion cyclotron (IC) radiofrequency (RF), which provides the heating of ions and current-drive in the central plasma,
- Electron cyclotron (EC) RF, which provides central plasma heating and current-drive both on and off-axis, and
- Lower hybrid (LH) RF, which provides off-axis heating and current-drive.

Among these H&CD systems, the off-axis current-drive [7] is more appealing since this system can be used to provide favorable magnetic shear configurations for stability.

As representations for non-inductive operation conditions, three typical scenarios are selected, including the weak negative shear (WNS) scenario 4, the strong negative shear (SNS) scenario 6, and the weak positive shear (WPS) scenario 7. Their typical parameters are shown in the Table 5.3, where most of parameter names can be found in the Table 5.1. The percentages of current drive, bootstrap current, and ohmic heating in the plasma current are also included.

In order to simulate the non-inductive scenarios properly, we transfer the diffusivity parameters from the multinodal model of inductive scenarios to the multinodal model of non-inductive scenarios. These three non-inductive scenarios are split into a training dataset with the scenario 4 and a testing dataset with the scenario 6 and 7. Again, the training dataset is used for tuning diffusivity parameters, while the testing dataset is for evaluating model performances. The non-inductive multinodal model is trained on the training dataset with 2 epochs and a learning rate 0.02, where the mean squared error (MSE) loss of the scenario 4 drops from 13.2741 to 0.6333. The optimized parameters in the particle and thermal diffusivities for the non-inductive scenarios are shown in the Table 5.4. The multinodal model with optimized diffusivity parameters is then used to simulate non-inductive scenario 4, 6, and 7.

Table 5.3: Parameters of ITER non-inductive operation scenarios, where WNS is for weak negative shear, SNS is for strong negative shear, and WPS is for weak positive shear. Reproduced with permission from the ITER Technical Basis [31].

Parameter	Scenario 4 WNS	Scenario 6 SNS	Scenario 7 WPS
$R_0$ (m)	6.35	6.35	6.35
$a$ (m)	1.85	1.85	1.85
$\kappa_{95}$	1.85	1.86	1.86
$\delta_{95}$	0.40	0.41	0.41
$B_T$ (T)	5.18	5.18	5.18
$I_P$ (MA)	9.0	9.0	9.0
$q_0$	3.5	5.9	2.7
$q_{95}$	5.3	5.4	5.3
$\langle n_e \rangle$ ( $10^{19} \text{ m}^{-3}$ )	6.7	6.5	6.7
$\langle T_i \rangle$ (keV)	12.5	12.1	12.5
$\langle T_e \rangle$ (keV)	12.3	13.3	12.1
$P_{\text{fus}}$ (MW)	356	340	352
$P_{\text{LH}}$ (MW)	29	40	29
$P_{\text{NBI}}$ (MW)	30	20	28
$Q$	6.0	5.7	6.2
$\tau_E$ (s)	3.1	3.13	3.07
$f_{\text{He}}$ (%)	4.1	4.0	4.0
$f_{\text{Be}}$ (%)	2.0	2.0	2.0
$f_{\text{Ar}}$ (%)	0.26	0.2	0.23
$Z_{\text{eff}}$	2.07	1.89	1.99
$P_{\text{rad}}$ (MW)	37.6	36.2	34.6
$I_{\text{CD}}/I_P$ (%)	51.9	53.7	50.2
$I_{\text{BS}}/I_P$ (%)	48.1	46.3	49.8
$I_{\text{OH}}/I_P$ (%)	0	0	0

#### 5.4.1 Non-Inductive Operation Scenario 4

The first non-inductive ITER operation scenario simulated by the multinodal burning plasma model is the weak negative shear (WNS) scenario 4. Its typical conditions are listed in the Table 5.3, and its typical radial profiles are presented in the Figure 5.10. Compared with the inductive profiles in the Figure 5.2, a larger core temperature with a steeper temperature gradient can be observed. The plasma current of the non-inductive scenario is lower than

Table 5.4: Optimized parameters in the nodal particle and thermal diffusivities for the ITER non-inductive scenarios.

	$\alpha_H$	$\alpha_B$	$\alpha_n$	$\alpha_T$	$\alpha_{\nabla T}$	$\alpha_q$	$\alpha_\kappa$	$\alpha_M$	$\alpha_R$	$\alpha_a$
$D_D^{\text{core}}$	0.0709	-3.6915	1.5921	-0.2904	0.0625	3.1264	-2.6872	-0.6488	0.6514	0.8070
$D_\alpha^{\text{core}}$	0.0885	-3.4674	1.8260	-0.0281	0.3347	3.3629	-2.4712	-0.4213	0.8820	1.0389
$\chi_D^{\text{core}}$	0.0515	-4.0476	-0.5981	2.8100	0.7229	1.8626	-3.2547	-1.5129	-0.3467	-0.0875
$\chi_\alpha^{\text{core}}$	0.0568	-3.9486	-0.5002	2.9044	0.8117	1.9601	-3.1545	-1.4142	-0.2484	0.0106
$\chi_e^{\text{core}}$	0.0687	-4.0671	0.2988	1.9584	1.2788	1.9781	-3.2958	-1.2677	-0.0972	-0.0464
$D_D^{\text{edge}}$	0.0287	-4.5364	2.9882	0.3103	-0.6636	2.1400	-3.4399	-1.5506	-0.2814	0.0120
$D_\alpha^{\text{edge}}$	0.0358	-4.3141	3.2030	0.5623	-0.4266	2.3741	-3.2279	-1.3260	-0.0526	0.2410
$\chi_D^{\text{edge}}$	0.0975	-3.7455	0.0778	1.3422	0.9980	2.7811	-3.2051	-0.8336	0.4714	-0.1943
$\chi_\alpha^{\text{edge}}$	0.0941	-3.7818	0.0085	1.2420	0.9190	2.6745	-3.1888	-0.8902	0.3985	-0.2607
$\chi_e^{\text{edge}}$	0.1261	-3.3826	-0.8945	1.6105	1.5562	2.8887	-3.0679	-0.5809	0.7164	-0.1334

the inductive one, while the safety factor at the 95% flux surface is higher. Moreover, the plasma current is divided into two roughly equal halves by the current drive and bootstrap current.

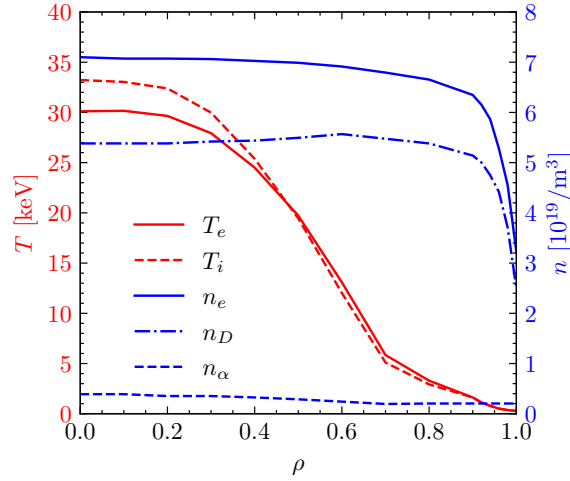


Figure 5.10: Plasma temperature and density profiles at the current flat-top phase for the steady state weak negative shear (WNS) operational scenario. Reproduced with permission from the ITER Technical Basis [31].

The simulation results for the non-inductive scenario 4 are shown in the Figure 5.11 and 5.12 for the core and edge nodes. The particle densities and temperatures are shown in the first figure, while the power terms are presented in the second figure. The ion and electron

temperatures reach a steady state at about 12 s. Compared with the inductive scenario 2, the non-inductive scenario 4 has larger fusion and auxiliary heating. Also, the energy transported from the core electrons to the edge ones is much larger now. However, the Coulomb collisional energy is transferred from ions to electrons since the temperature of core electrons is lower than the temperature of core ions. The energy excursion due to the fusion alpha heating is not found in this simulation.

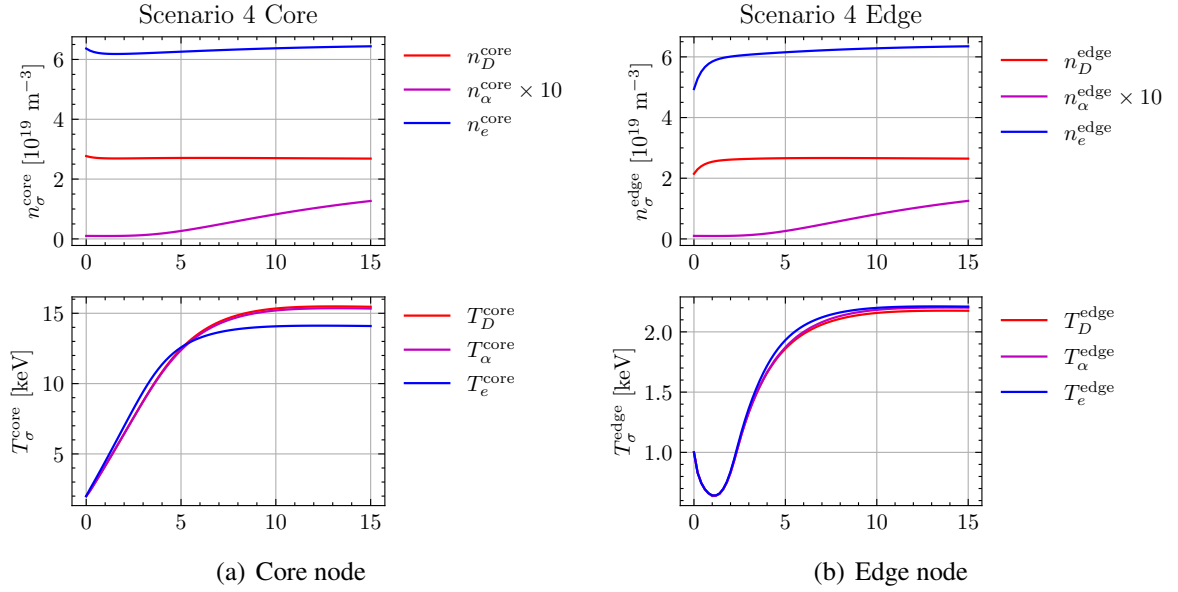


Figure 5.11: Densities and temperatures of the ITER design scenario 4.

To study the radiation and transport processes of the non-inductive scenario 4 quantitatively, energy flows at 15 s are shown in the Figure 5.13. Due to a higher ion temperature, larger fusion heating powers are observed for both ions and electrons. However, since the temperature of core electrons is lower than the temperature of core ions, the collisional energy transfer is from ions to electrons now. The energy transport from core electrons to the edge is much stronger than the inductive scenario to remove extra heating, but the energy transport of core ions is smaller now. Overall, the radiation and transport processes in the non-inductive scenario are sufficiently fast and strong to prevent power excursion of fusion alpha heating.

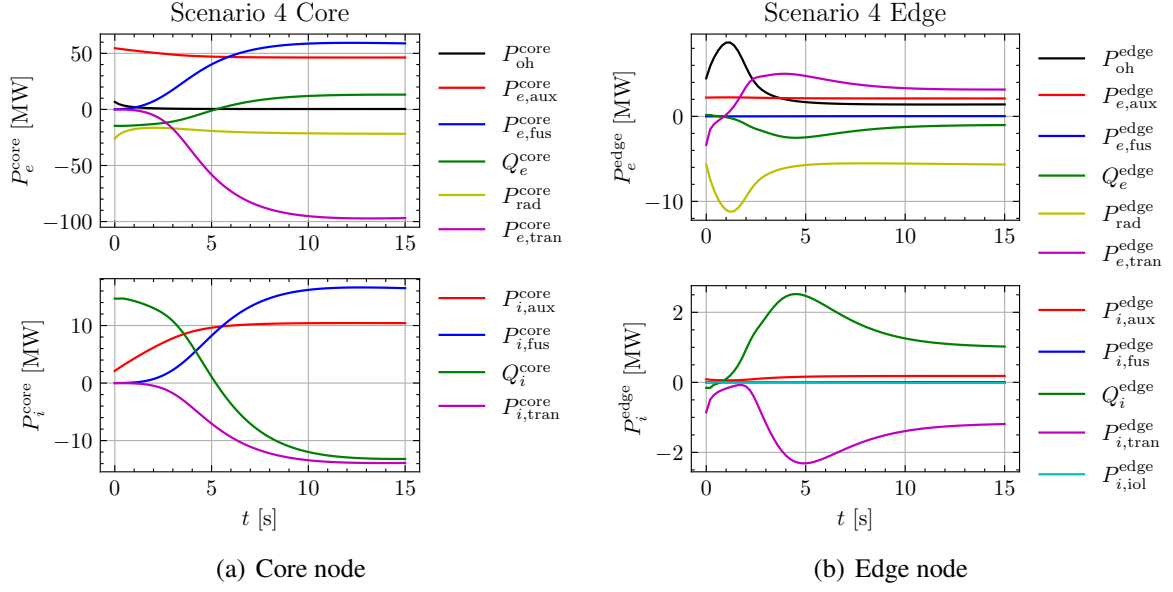


Figure 5.12: Powers of the ITER design scenario 4.

#### 5.4.2 Non-Inductive Operation Scenario 6 and 7

To evaluate the performance of the multinodal model for non-inductive operation, we select two more scenarios: one is the strong negative shear (SNS) scenario 6, and another is the weak positive shear (WPS) scenario 7. The simulation result for the scenario 6 is shown in the Figure 5.14, while the result for the scenario 7 is in the Figure 5.15. Similar to the WNS scenario 4, the ion and electron temperatures reach steady states around 12 s, and power excursion is not observed.

### 5.5 Sensitivity Analyses

To analyze how the density and temperature change with model parameters, we implement several sensitivity analyses in this section. The normalized sensitivities of densities and temperatures with respect to diffusivities, electron cyclotron radiation (ECR) parameters, impurity fractions, and ion orbit loss (IOL) timescales are computed for the inductive scenario 2. The dynamic processes of burning plasmas are also visualized by perturbing these parameters.

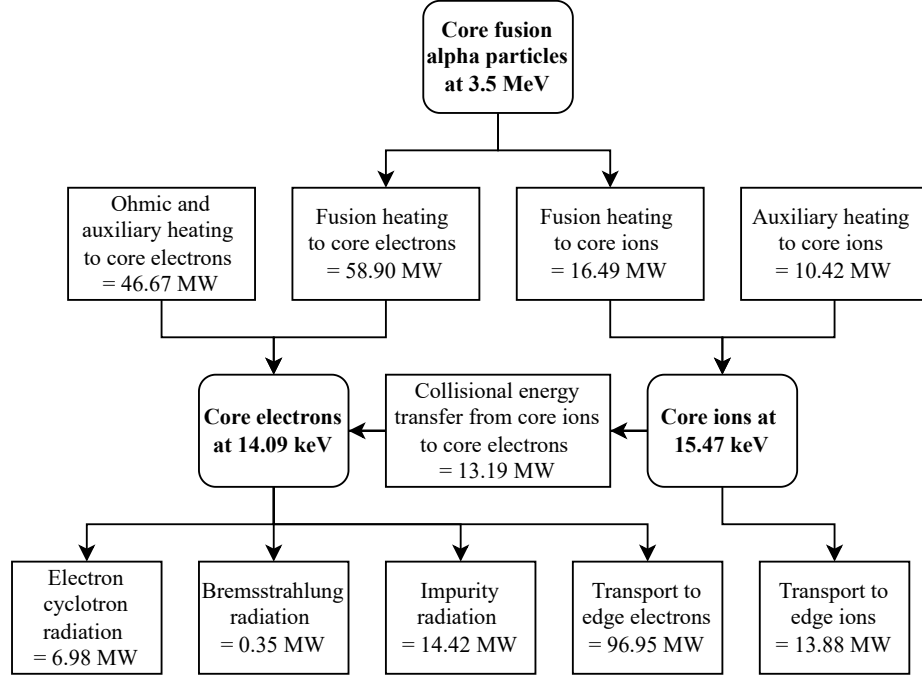


Figure 5.13: Energy flows for the ITER non-inductive scenario 4 simulated by the multi-odal model at 15 s.

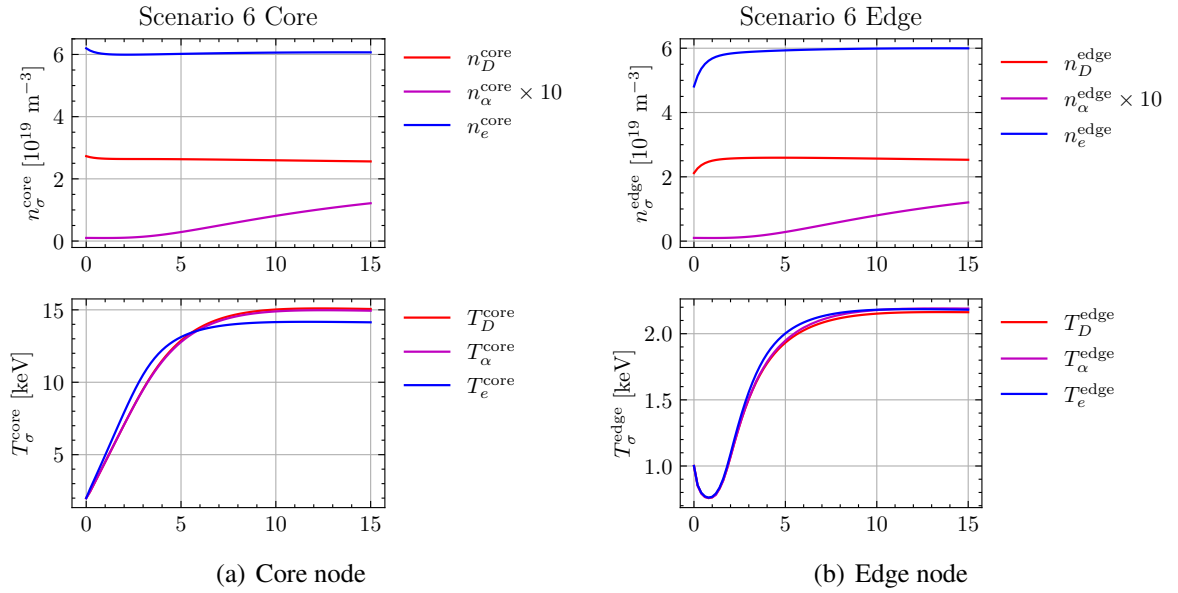


Figure 5.14: Densities and temperatures of the ITER design scenario 6.



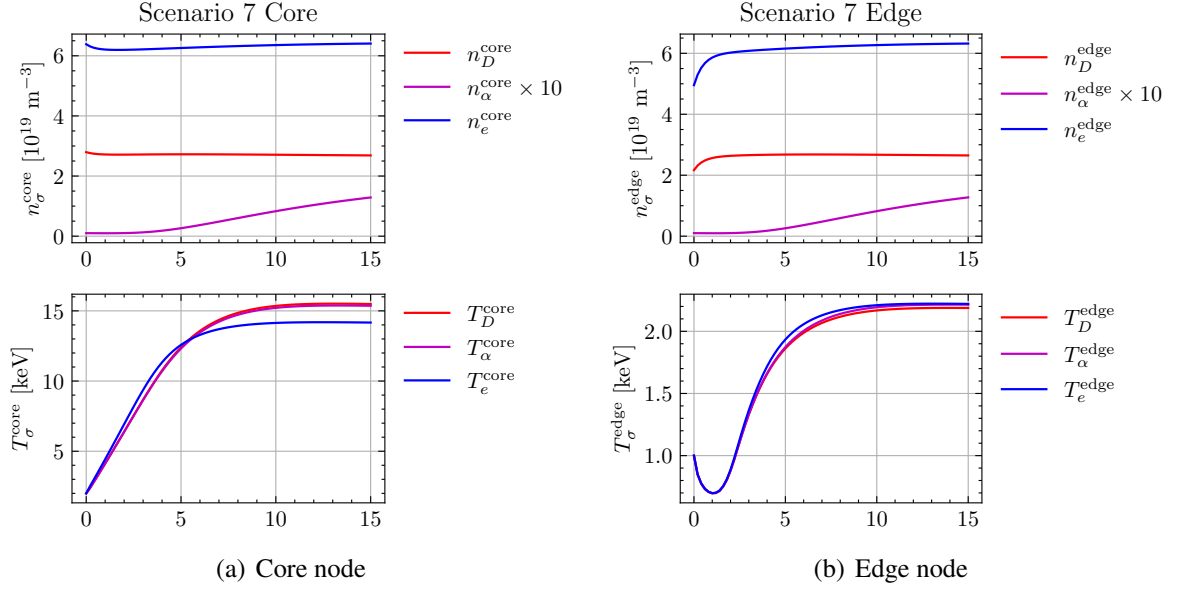


Figure 5.15: Densities and temperatures of the ITER design scenario 7.

### 5.5.1 Sensitivity Analysis of Diffusivities

The first sensitivity analysis is done for the diffusivity parameters in the Table 5.2. To avoid the impact of physical value scales and units, we utilize normalized sensitivities. For example, the normalized sensitivity of the core electron temperature  $T_e^{\text{core}}$  with respect to the temperature power  $\alpha_T$  in the electron thermal diffusivity  $\chi_e^{\text{core}}$  is computed by

$$S(T_e^{\text{core}}|\alpha_T) = \frac{\alpha_T}{T_e^{\text{core}}} \frac{\partial T_e^{\text{core}}}{\partial \alpha_T}. \quad (5.34)$$

The normalized sensitivities of the diffusivity parameters are shown in the Table 5.5. Several observations can be drawn from this table:

- The particle diffusivities of alpha particles are more sensitive to the change of parameters than the deuteron particle diffusivities in both the core and edge nodes.
- The core deuteron particle diffusivity is more sensitive to the magnetic field, nodal particle density, and safety factor.
- The thermal diffusivities of core deuterons are more sensitive to parameters than

Table 5.5: Sensitivities of the diffusivity parameters for the ITER design scenario 2.

Sensitivity	$\alpha_H$	$\alpha_B$	$\alpha_n$	$\alpha_T$	$\alpha_{\nabla T}$	$\alpha_q$	$\alpha_\kappa$	$\alpha_M$	$\alpha_R$	$\alpha_a$
$n_D^{\text{core}}$	-0.0172	0.1098	-0.0582	0.0127	0.0002	-0.0569	0.0258	0.0122	-0.0166	-0.0082
$n_\alpha^{\text{core}}$	-0.0729	0.4417	-0.2791	0.0326	-0.0252	-0.2561	0.1021	0.0392	-0.0953	-0.0442
$T_D^{\text{core}}$	-0.1751	1.0922	0.1180	-1.2921	-0.3722	-0.4172	0.2739	0.1935	0.0128	-0.0266
$T_\alpha^{\text{core}}$	-0.0199	0.1210	0.0088	-0.1516	-0.0461	-0.0497	0.0301	0.0202	-0.0022	-0.0044
$T_e^{\text{core}}$	-0.0006	0.0041	-0.0000	-0.0022	-0.0011	-0.0011	0.0011	0.0008	0.0004	0.0001
$n_D^{\text{edge}}$	-0.0905	0.6905	-0.5816	-0.0191	0.1448	-0.2092	0.1672	0.1317	0.0526	0.0016
$n_\alpha^{\text{edge}}$	-0.2759	1.9995	-1.9186	-0.1479	0.3268	-0.7106	0.4773	0.3430	0.0418	-0.0403
$T_D^{\text{edge}}$	-0.3151	1.8965	-0.1481	-0.4806	-0.9434	-1.0098	0.5131	0.2013	-0.3493	0.0127
$T_\alpha^{\text{edge}}$	-0.0085	0.0512	-0.0033	-0.0125	-0.0245	-0.0266	0.0137	0.0056	-0.0088	0.0005
$T_e^{\text{edge}}$	0.0190	-0.1450	0.1225	0.0048	-0.0323	0.0439	-0.0351	-0.0277	-0.0110	-0.0003

alpha particles and electrons.

- The core deuteron and electron thermal diffusivities are more sensitive to the nodal temperature, magnetic field, and safety factor.

Overall, the magnetic field and safety factor are important parameters to control particle and energy transport between core and edge nodes.

To visualize how the burning plasma dynamics changes due to the heat coefficients between the core and edge, we multiple and divide these heat coefficients ( $\chi_\sigma^{\text{core}}$ , where  $\sigma \in \{D, \alpha, e\}$ ) by two. The results are shown in the Figure 5.16. When heat coefficients become smaller, less energy can be transported from the core to the edge, leading to a higher core temperature and higher fusion power. However, since the heat coefficients have strong positive dependencies on temperatures and temperature gradients, the heat transport from the core to the edge becomes larger when the core temperature is high enough. Then such increasing in heat transport can balance the increase of fusion heating and thus prevent thermal instability. The change in core temperatures is included in the summary of sensitivity analyses as the Table 5.6.

### Scenario 2 Core

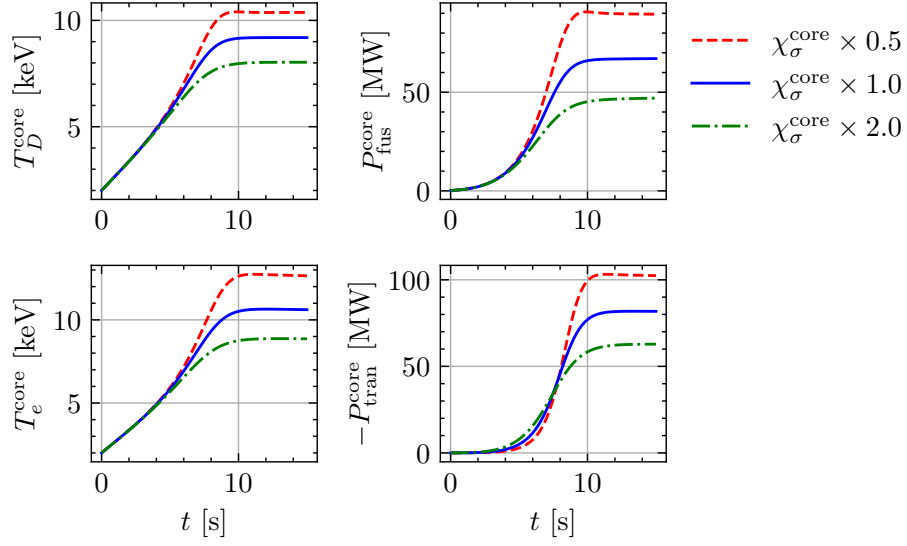


Figure 5.16: Sensitivity of the thermal diffusivity between the core and edge for the ITER design scenario 2.

Table 5.6: Summary of sensitivity analyses for the ITER design scenario 2.

Parameter	Change of the parameter	$\Delta T_D^{\text{core}}(\text{keV})$	$\Delta T_e^{\text{core}}(\text{keV})$
Core-edge thermal diffusivities $\chi_\sigma^{\text{core}}$	$\times 0.5$	+1.184	+2.038
	$\times 2.0$	-1.159	-1.751
Wall reflection coefficient of ECR $r = 0.8$	-0.1	-0.002	-0.025
	+0.1	+0.002	+0.033
Beryllium fraction $f_{\text{Be}} = 2.0\%$	-1.0%	-0.063	+0.059
	+1.0%	+0.058	-0.072
Argon fraction $f_{\text{Ar}} = 0.12\%$	-0.04%	-0.005	+0.165
	+0.04%	-0.008	-0.184
IOL timescales $\tau_{p,\sigma,\text{IOL}}^{\text{edge}}$ and $\tau_{E,\sigma,\text{IOL}}^{\text{edge}}$	$\times 0.1$	-0.000	-0.000
	$\times 10.0$	+0.000	+0.000

#### 5.5.2 Sensitivity Analysis of Electron Cyclotron Radiation Parameters

The second sensitivity analysis is done for electron cyclotron radiation (ECR). The normalized sensitivities of the ECR parameters are shown in the Table 5.7. Here only the core and edge electron temperatures with respect to the density shape parameter  $\alpha_n$ , the temperature

shape parameters  $\alpha_T$  and  $\beta_T$ , and the reflection coefficient  $r$  in Albajar et al. [40] are considered. The results show that the electron temperatures are more sensitive to the reflection coefficient  $r$  and the temperature shape factor  $\beta_T$  than other parameters. As mentioned by Albajar et al. [40], the wall reflection coefficient is still needed more research for ITER, which will be an important coefficient for modeling energy transport from core electrons to the edge and wall.

Table 5.7: Sensitivities of the ECR parameters for the ITER design scenario 2.

Sensitivity	$\alpha_n$	$\alpha_T$	$\beta_T$	$r$
$T_e^{\text{core}}$	-0.0001	0.0100	-0.0135	0.0212
$T_e^{\text{edge}}$	-0.0001	0.0098	-0.0132	0.0208

To visualize how the burning plasma dynamics changes by the wall reflection coefficient  $r$ , the results with different reflection coefficients are shown in the Figure 5.17, where  $P_{\text{ECR}}^{\text{core}}$  is the ECR loss in the core node, and  $r = 0.8$  is the original one. As we can see, a higher wall reflection coefficient means more ECR power being reflected back and thus a smaller value of ECR loss. However, since the ECR power is relatively small due to the low electron temperature  $T_e^{\text{core}}$ , the electron and ion temperatures do not change much by changing the wall reflection coefficient. The values of temperature changes are included in the Table 5.6.

### 5.5.3 Sensitivity Analysis of Impurity Fractions

The third sensitivity analysis is done for impurity fractions. The normalized sensitivities of the electron temperatures to impurity fractions, including beryllium and argon, are shown in the Table 5.8. Negative values mean the increase of impurity fractions will lead to lower electron temperatures. The argon impurity fraction is found to have a more substantial effect on the core electron temperature than the beryllium one.

The sensitivities of deuteron and electron temperatures' dynamics with respect to the beryllium and argon impurities are shown in the Figure 5.18 and 5.19 respectively. A higher

### Scenario 2 Core

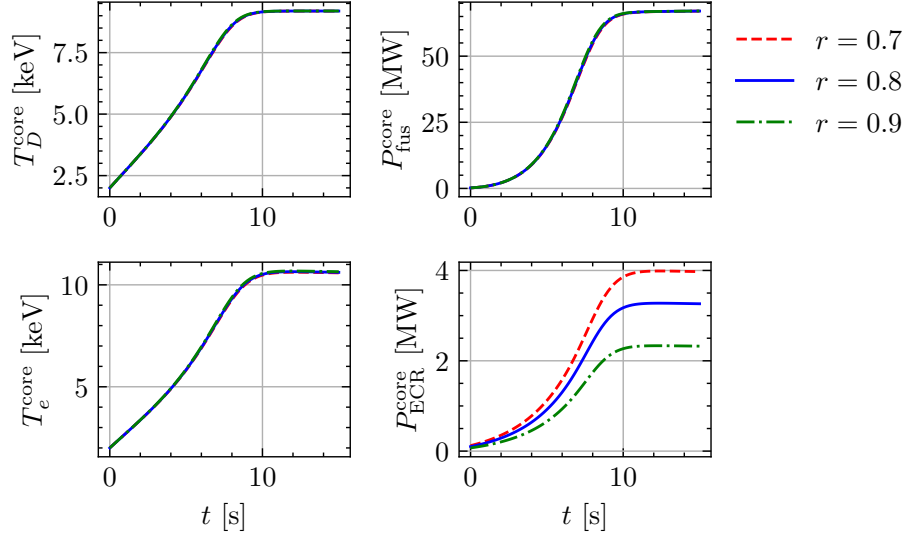


Figure 5.17: Sensitivity of the wall reflection coefficient in the electron cyclotron radiation for the ITER design scenario 2.

Table 5.8: Sensitivities of the impurity fractions for the ITER design scenario 2.

Sensitivity	$f_{\text{Be}}$	$f_{\text{Ar}}$
$T_e^{\text{core}}$	-0.0120	-0.0469
$T_e^{\text{edge}}$	-0.0184	-0.0693

impurity fraction leads to more impurity radiation and then causes a slower increase in core temperatures. However, as the core electron temperatures increase, the impurity radiation becomes smaller, and the temperatures at the steady state do not change much. The values of temperature changes have been presented in the Table 5.6.

#### 5.5.4 Sensitivity Analysis of Ion Orbit Loss Timescales

The last sensitivity analysis is done for ion orbit loss (IOL[49, 50, 51, 52, 53, 54, 55]) timescales. The normalized sensitivities of the IOL parameters are shown in the Table 5.9. The results show that the edge densities and temperatures are not sensitive to the IOL timescales, which is because of relatively small IOL values in the ITER edge node. This observation has been confirmed by computations with typical ITER parameters [11]. Since

### Scenario 2 Core

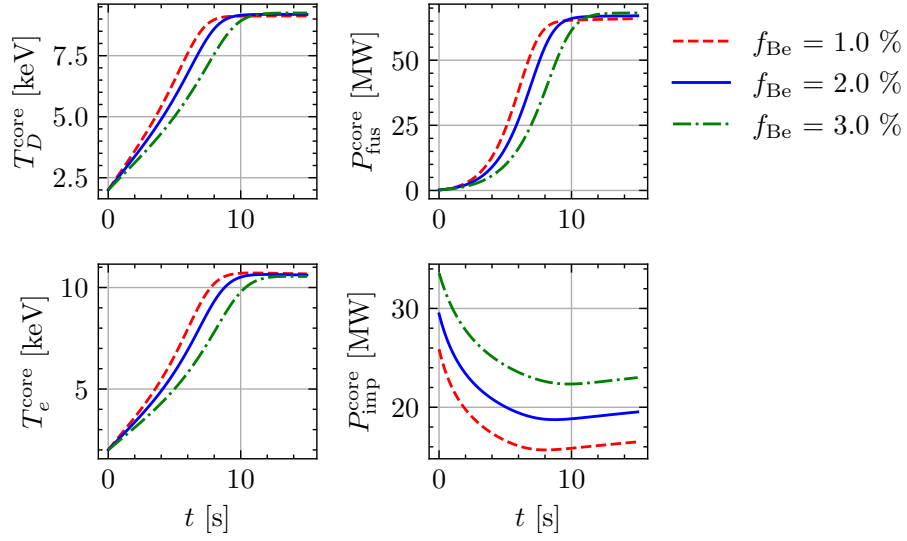


Figure 5.18: Sensitivity of the beryllium impurity fraction for the ITER design scenario 2.

### Scenario 2 Core

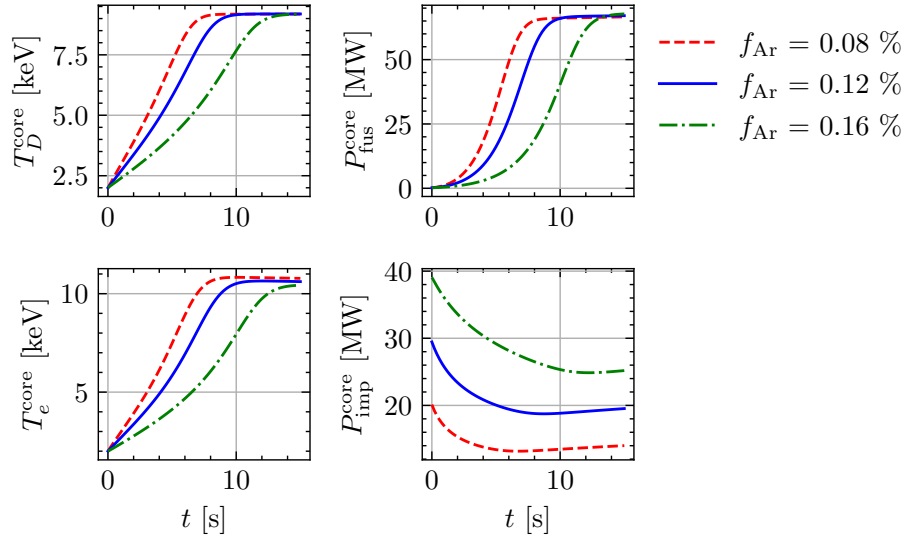


Figure 5.19: Sensitivity of the argon impurity fraction for the ITER design scenario 2.

the IOL timescales have fewer effects on the core temperatures, we do not need to simulate the burning plasma with different IOL timescales.

Table 5.9: Sensitivities of the IOL parameters for the ITER design scenario 2.

Sensitivity	$\tau_{p,\text{IOL}}^{\text{edge}}$	$\tau_{e,\text{IOL}}^{\text{edge}}$
$n_{\text{D}}^{\text{edge}}$	$-5.4127 \times 10^{-9}$	$4.3326 \times 10^{-9}$
$n_{\alpha}^{\text{edge}}$	$3.4776 \times 10^{-6}$	$8.9833 \times 10^{-8}$
$T_{\text{D}}^{\text{edge}}$	$-3.0381 \times 10^{-8}$	$5.7944 \times 10^{-7}$
$T_{\alpha}^{\text{edge}}$	$-1.7795 \times 10^{-7}$	$1.4968 \times 10^{-6}$

## 5.6 Summary

In this chapter, the multinodal burning plasma model is applied for simulating ITER deuterium-tritium (D-T) plasmas. Assumptions are made firstly to simplify the multinodal model, where only the deuteron, triton, alpha particle, and electron in the core and edge nodes are computed. Several significant impurities, including helium, beryllium, and argon, are considered for impurity radiation. Next, the delayed fusion heating, electron cyclotron radiation (ECR), and ion orbit loss (IOL) are modeled. Finally, the particle and energy balance equations are presented based on previous assumptions.

The simplified multinodal model is used for solving D-T plasmas in both inductive and non-inductive operation scenarios of ITER. In the inductive scenario, ohmic current contributes the most to plasma current. By simulating with the multinodal model, fusion alpha particles, born at 3.5 MeV from D-T fusion reactions, are observed transferring most of their energy to core electrons first. Then, when core electrons are heated, their energy is removed by impurity radiation, ECR, and Coulomb energy transfer to core ions quickly enough. Next, when the core ions are heated by fusion alpha particles, core electrons, and auxiliary heating, they transport their energy to edge ions. The radiation and transport processes are strong and fast enough to prevent energy excursion.

Compared with the inductive scenarios, most of the total plasma current is generated non-inductively by additional current drive and bootstrap current in the ITER steady-state operation. Simulations of non-inductive scenarios with the multinodal model show higher core electron and ion temperatures, with stronger energy transport from the core electrons

to the edge.

Several sensitivity analyses are done for the diffusivities, ECR parameters, impurity fractions, and IOL timescales on the inductive scenario 2. The magnetic field and safety factor are found important for controlling transport processes between nodes. Besides, the temperature shape factor and the wall reflection coefficient are essential in the ECR calculation, while the fractions of beryllium and argon are also critical to the burning plasma dynamics. The IOL timescale is not crucial in the ITER inductive operation.

In summary, the radiation and transport processes can promptly remove extra core energy from fusion alpha heating and prevent power excursion for both inductive and non-inductive operation scenarios in ITER.



## **CHAPTER 6**

### **CONCLUSION**

In this thesis, we develop a multi-region multi-timescale burning plasma dynamics model for tokamaks. This model is used for simulating DIII-D non-fusion plasmas and ITER fusion plasmas. Simulation results indicate that radiation and transport can promptly remove extra heat from the core plasma, thereby inhibiting the thermal runaway instability from fusion alpha heating. Also, research about multinodal model applications in burning plasma control can be done in the future.

#### **6.1 Research Conclusions**

This research develops a multi-region multi-timescale transport model to simulate burning plasma dynamics in tokamaks. Deuterium-tritium fusion generates 3.5 MeV alpha particles, which transfer their energy mainly to core electrons. The heated electrons and lower-energy fusion alpha particles then heat core ions, which will increase the fusion reaction rate and may conceivably lead to a thermal runaway instability. Meanwhile, core energy is transported to the edge and radiated to the wall. Multiple timescales of such processes between different tokamak regions determine the burning plasma dynamics.

A multinodal burning plasma dynamics model is proposed for studying such coupling effects between different tokamak regions. A tokamak plasma is divided into four regions: core, edge, scrape-off layer (SOL), and divertor, where each region is viewed as a separate node. The nodal particle and energy balance equations are derived from the conservation equations of the fluid theory, where the internodal transport terms are also obtained. Fusion alpha heating is modeled with a time delay between electrons and ions. Radiations, including electron cyclotron radiation (ECR), bremsstrahlung, and impurity radiation, are contained in the model as immediate energy transport from the core to the edge and wall. The ion

orbit loss (IOL) is incorporated as an edge plasma effect. Other essential mechanisms in burning plasmas are also visited. After assembling source and sink terms into particle and energy balance equations, a framework for the multinodal model is proposed. In summary, the multinodal model includes:

- Nodes: core, edge, scrape-off layer (SOL), and divertor.
- Terms: fusion alpha heating, ohmic heating, ion cyclotron heating (ICH), electron cyclotron heating (ECH), neutral beam injection (NBI), gas puffing, electron cyclotron radiation (ECR), bremsstrahlung, impurity radiation, internodal transport, Coulomb collisional energy transfer, ion orbit loss (IOL), and atomic and molecular processes.

In order to calculate the transport times between nodes, computational methods are presented for the multinodal model. The shortcoming and drawbacks of previous work have been summarized and discussed. Instead of directly obtaining the internodal transport times from experiments, we propose one parametric diffusivity model. The undetermined parameters are initialized from empirical laws and then optimized based on the experiment data. The machine learning and optimization algorithms used in this research are described thoroughly. The mean squared error is used as the loss and the optimization object. The back propagation is applied to get gradients through the solver, and the gradient descent is implemented to update diffusivity parameters. A computational framework for the multinodal model, GTBURN, is brought up. Several modules in this code package are also described.

In order to evaluate model performances, the multinodal model is applied for DIII-D non-fusion plasmas. Several assumptions are made to simplify the model for deuterium plasmas. The particle and energy balance equations are presented with the parametric diffusivity model and internodal transport times. Among DIII-D experiment data, 25 ELMing non-RMP H-mode shots are selected, where 20 shots are included in the training dataset, and 5 shots are held in the testing dataset. The training dataset is used to tune the parameters inside the diffusivity model, while the testing dataset is applied to evaluate the model

performance and its generalization ability for new shots. Then, the computation results of the multinodal model on the testing dataset are analyzed. The simulations show the overall performance of the multinodal model with the optimized diffusivities is better than the original model. The multinodal model can track tendencies of experimental densities and temperatures. It is found that the multinodal model performs better in shots with only one power source than with multiple sources. Also, the model performance in the core node is better than in the edge and SOL nodes. Other strengths and shortcomings of the multinodal model are also visited.

For analyzing the thermal stability of the ITER, the multinodal model is applied for ITER deuterium-tritium (D-T) plasmas. Firstly, several assumptions are introduced to simplify the model, and then particle and energy balance equations are given for the core and edge nodes. The D-T fusion heating is included with a reasonable time delay between fusion alpha heating to electrons and ions. The impurity radiation, bremsstrahlung, and ECR are considered. Also, the particle and energy transport between the core and edge are revisited. Both inductive and non-inductive scenarios are simulated, with time-dependent powers and energy flows presented. The simulation results indicate that radiation and transport processes are strong and fast enough to remove extra core energy from fusion alpha heating and prevent potential thermal instability. Moreover, sensitivity analyses for diffusivities, ECR parameters, impurity fractions, and IOL timescales exhibit the reliability of simulations. No tendency suggests the possibility of the fusion thermal excursion in our research.

## **6.2 Future Research**

For evaluating the multinodal model for ITER, it is crucial to perform a similar analysis for the deuterium-deuterium (D-D) phase of ITER to prepare a model for the deuterium-tritium (D-T) phase of ITER. Besides that, more future research can be done to improve the multinodal burning plasma dynamics model. We will discuss several potential direc-

tions for multinodal model improvements. Lastly, a framework for the multinodal model application in the burning D-T plasma control is proposed.

### 6.2.1 Improvement Directions of the Multinodal Model

The applications of the current multinodal model to DIII-D and ITER plasmas show its limitations and shortcomings. It is necessary to obtain a more accurate and delicate model in further work. The framework of the multinodal model can be developed in the following directions:

- **More regions:** The current research only considers the core, edge, scrape-off layer (SOL), and divertor regions of a tokamak. The model can also include the private flux region (PFR), plenum, and other tokamak regions. The transport processes among the SOL, divertor, PFR, and plenum have been shown to be essential in modeling practical tokamaks [65, 56, 66, 94], which should be considered in the future.
- **More species:** The current research only includes deuterons, tritons, alpha particles, electrons, and several impurities in the multinodal model, which are usually enough for an approximate model of deuterium-tritium (D-T) plasmas. However, more impurities might be needed when the wall effect is considered. The list of species in the multinodal model can be determined by the gas puffing, pellet injection, fusion, atomic and molecular reactions, and wall conditions.
- **More dimensions:** The current research only models each toroidal shell as one node since the main spatial dependence of plasma energy transport processes is essentially the radial direction [12]. However, the divertor in tokamaks can introduce visible poloidal asymmetry in the plasma temperature distribution. Hence, one toroidal shell can be divided into multiple nodes at different angles, and the current one-dimensional model can be developed into a two-dimensional model in the future.
- **More fusion reactions:** The current research only includes D-T fusion reactions.

However, when the ion temperature is high enough, other fusion events [4] such as D-D and D-<sup>3</sup>He reactions might also be worth considering.

- **More atomic and molecular processes:** The current research models the several critical atomic hydrogen processes in the DIII-D SOL node, including the ionization, recombination, charge exchange, and elastic scattering. More atomic and molecular processes [60, 1] can be included in the multinodal model for simulating the SOL and divertor nodes more accurately.
- **More accurate deposition profiles:** The current research applies predetermined particle source and power deposition profiles of the gas puffing, neutral beam injection, and cyclotron heating. However, these deposition profiles can be obtained from the experiment or relevant codes, such as ONETWO [95] and FREYA [96]. They will allow the multinodal model to have more precise source terms when distributing the external sources among different nodes.
- **More accurate radiation terms:** The current research implements fitting parameters  $\alpha_n$ ,  $\alpha_T$ , and  $\beta_T$  from ITER profiles with a predetermined wall reflection coefficient  $r$  for computing electron cyclotron radiation (ECR) [40]. However, these parameters can be estimated from experiments or simulations since the ECR has been shown to be important in the fusion plasma [11] during higher electron temperatures. Also, when multiple impurity particles are included in the model, a more accurate impurity radiation code such as ImpRad [97] can be utilized.
- **Multi-groups of  $\alpha$  particles:** When simulating ITER D-T plasmas, alpha particles are divided into two groups. The energetic alpha particles are only viewed as a heating source, while the lower energy alpha particles are modeled as an impurity species. However, the energy distribution of alpha particles calculated by kinetic models [98, 99] is far from a Maxwellian distribution. Hence, a model of multiple energy groups of alpha particles could be studied later.

- **Neutral particle transport:** The current simulations of DIII-D plasmas use the pre-assumed neutral particle density and temperature in the SOL. Nevertheless, a neutral particle transport code such as GTNEUT [57, 61] can be used to compute neutral particle densities in the SOL, divertor, and plenum. Such a neutral particle computation framework could be incorporated into the current model.
- **More edge phenomena:** The only edge phenomenon included in the current multi-nodal model is the ion orbit loss (IOL) [49, 51]. More plasma phenomena, such as edge-localized modes (ELMs) [100], multifaceted asymmetric radiations from the edge (MARFES) [101, 102, 94, 103], and non-diffusive transport [104], can be considered in the future.
- **More diffusivity formulas:** This research applies a linearly exponential diffusivity formula. More diffusivity formulas, including high-order exponential diffusivity formulas and neural networks, can be implemented and compared with the current formula in the future. Those formulas can catch the interactions between different physical values.
- **Physical constraints:** When the diffusivity parameters are optimized, the unconstrained optimization problem is solved, where only the mean squared error (MSE) is minimized. More physical constraints between variables can be contained to preserve physics during the optimization.
- **Multivariate optimization:** This research uses a sum of normalized nodal densities and temperatures, where those physical variables are divided by proper constants with units. Those constants are predetermined by the researcher's experience. In the future, these constants can be adjusted based on experimental conditions, and a better diffusivity model may be obtained. Besides, the stopping criterion can be revisited to find better minima of the MSE loss.

- **Adaptive-step stiff equation solvers:** The multinodal model has been observed to become stiff when external particle and energy sources change too rapidly. The current research uses an adaptive-step ordinary differential equation (ODE) solver, the Runge-Kutta of order 5 of Dormand-Prince-Shampine [78], which has been shown its limitations for solving stiff equations for DIII-D plasmas. Specialized stiff equation solvers, such as methods based on backward differentiation formulas (BDF) [105], can be applied for solving stiff equations in the multinodal model in the future.

### 6.2.2 Burning Plasma Control

One potential application of the multinodal model is the burning D-T plasma control. When particular nodal particle densities and temperatures are demanded, the multinodal model can be used to obtain the required external particle and energy sources.

Here we use a simplified example for the illustration purpose. Suppose the multinodal model only considers the core deuteron density and NBI power, i.e.,

$$\frac{dn_D^{\text{core}}(t)}{dt} = f(D_D^{\text{core}}, P_{D,\text{NBI}}^{\text{core}}, t). \quad (6.1)$$

In previous chapters, we calculated the gradient of the loss between the measured particle density and the simulated one over the particle diffusivity, i.e.,  $\frac{\partial \mathcal{L}_{n_D}^{\text{core}}}{\partial D_D^{\text{core}}}$ , and used it to update the diffusivity. However, given one particular wanted  $\tilde{n}_D^{\text{core}}$ , one can also compute the  $\mathcal{L}_{n_D}$  as the MSE loss between the given  $\tilde{n}_D^{\text{core}}$  and the multinodal model solution  $n_D^{\text{core}}$ . Then, we can use  $\frac{\partial \mathcal{L}_{n_D}^{\text{core}}}{\partial P_{D,\text{NBI}}^{\text{core}}}$  to update the NBI source term  $P_{D,\text{NBI}}^{\text{core}}$ . At the end, we can get the required NBI power changing with time.

The current GTBURN package can be modified for this burning control task. The workflow chart is shown in the Figure 6.1. Similarly, the black arrows are the forward directions to solve the multinodal model, and the blue arrows are the backward directions to optimize the parameters. Now the nodal densities and temperatures are predetermined

by researchers, and the required particle and energy sources are undetermined. Once those sources are initialized from empirical formulas, we can use the back propagation algorithm with gradient descent to update these source terms. After the optimization is finished, we can use these optimized sources to achieve the desired densities and temperatures. This work can be done in the future.

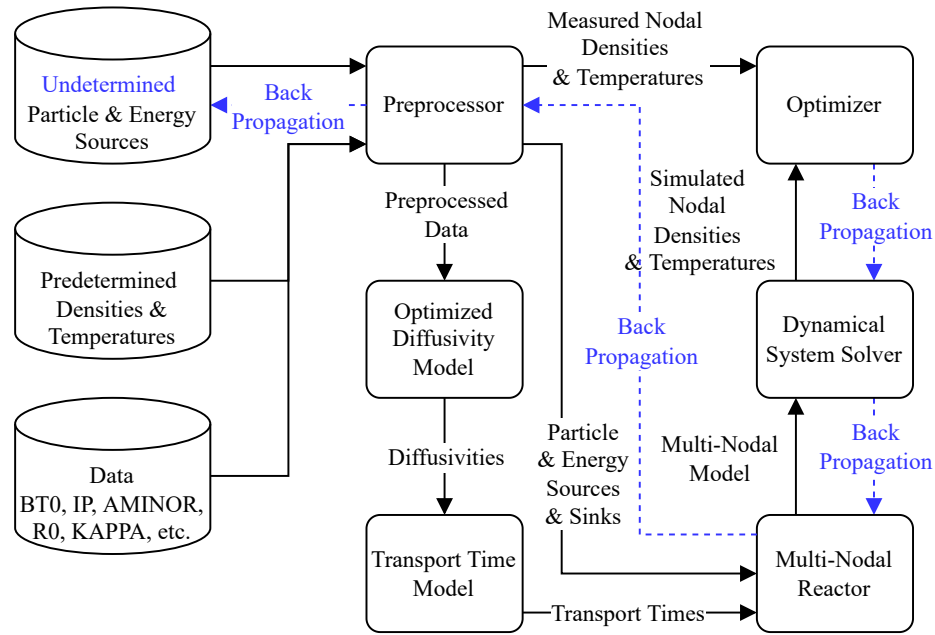


Figure 6.1: Workflow chart for the GTBURN for determining particle and energy sources, where solid lines are for the forward flow to solve the problem and dash lines are for back propagation to update undetermined particle and energy sources.



# Appendices

## APPENDIX A

### ONE-NODAL BURNING PLASMA DYNAMICS MODEL

In this appendix, we introduce a one-nodal burning plasma dynamics model with a particle and energy confinement time model. The code package, GTBURN, is used. Parameters in the confinement time model are tuned by DIII-D experiment data. The tuned model is compared with the original model with an energy confinement time from steady-state regressions. Simulation results show the advantages of the tuned model and indicate improvement directions for future work.

#### A.1 Global Dynamics Equations

The one-nodal burning plasma dynamics model views the tokamak as a zero-dimension reactor, where space-dependent variables, such as densities and temperatures, are replaced by volume-averaged ones. The zero-dimension volume-averaged particle and energy balance equations [106, 10, 1] for the D-T fusion can be represented by

$$\frac{dn_i}{dt} = S_i - \frac{1}{2}n_i^2 \langle \sigma v \rangle_f - \frac{n_i}{\tau_{P,i}}, \quad (\text{A.1})$$

$$\frac{dn_\alpha}{dt} = S_\alpha + \frac{1}{4}n_i^2 \langle \sigma v \rangle_f - \frac{n_\alpha}{\tau_{P,\alpha}}, \quad (\text{A.2})$$

$$\frac{dn_z}{dt} = S_z - \frac{n_z}{\tau_{P,z}}, \quad (\text{A.3})$$

$$\frac{3}{2} \frac{d}{dt} (n_i T_i) = P_{\text{aux},i} + \frac{1}{4}n_i^2 \langle \sigma v \rangle_f U_{\alpha i} + Q_{ie} - \frac{3}{2} \frac{n_i T_i}{\tau_{E,i}}, \quad (\text{A.4})$$

$$\frac{3}{2} \frac{d}{dt} (n_e T_e) = P_\Omega + P_{\text{aux},e} + \frac{1}{4}n_i^2 \langle \sigma v \rangle_f U_{\alpha e} - Q_{ie} - P_R - \frac{3}{2} \frac{n_e T_e}{\tau_{E,e}}, \quad (\text{A.5})$$

where  $n_i$ ,  $n_\alpha$ , and  $n_z$  are volume-averaged ion,  $\alpha$  particle, and impurity densities,  $T_i$  and  $T_e$  are volume-averaged ion and electron temperatures. Ions here are assumed to be half deuterons and half tritons. Those terms on the right hand sides of the balance equations

are particle and energy sources, where  $S_i$ ,  $S_\alpha$ , and  $S_z$  are the ion,  $\alpha$  particle, and impurity external particle source;  $\frac{1}{2}n_i^2 \langle \sigma v \rangle_f$  and  $\frac{1}{4}n_i^2 \langle \sigma v \rangle_f$  are the fusion particle terms, where  $\langle \sigma v \rangle_f$  is the D-T fusion reactivity;  $\frac{n_i}{\tau_{P,i}}$ ,  $\frac{n_\alpha}{\tau_{P,\alpha}}$ , and  $\frac{n_z}{\tau_{P,z}}$  are particle diffusion terms, where  $\tau_{P,i}$ ,  $\tau_{P,\alpha}$ , and  $\tau_{P,z}$  are ion,  $\alpha$  particle, and impurity particle confinement times;  $P_{\text{aux},i}$  and  $P_{\text{aux},e}$  are auxiliary heating to ions and electrons;  $P_\Omega$  is the ohmic heating to electrons;  $\frac{1}{4}n_i^2 \langle \sigma v \rangle_f U_{\alpha i}$  and  $\frac{1}{4}n_i^2 \langle \sigma v \rangle_f U_{\alpha e}$  are the fusion energy to ions and electrons;  $Q_{ie}$  is the Coulomb collisional energy transfer from electrons to electrons to ions;  $P_R$  is the radiation term; and  $\frac{3}{2} \frac{n_i T_i}{\tau_{E,i}}$  and  $\frac{3}{2} \frac{n_e T_e}{\tau_{E,e}}$  are energy diffusion terms, where  $\tau_{E,i}$  and  $\tau_{E,e}$  are ion and electron energy confinement times.

In one DIII-D tokamak plasma modeled, ions are assumed to be full deuterons, where tritons and  $\alpha$  particles are neglected. Hence, the Equation A.2 will not be solved, and the D-D fusion replaces the D-T fusion. Besides, instead of solving one particle balance for electrons, we can get the electron density from the charge neutrality, i.e.

$$n_e = Z_i n_i + Z_z n_z = n_i + 6n_z, \quad (\text{A.6})$$

where the effective impurity particle is assumed to be the carbon due to its availability in the DIII-D data. By using these impurity density data, we will not solve the Equation A.3 either. Combining the above assumptions, we can list the simplified global dynamics equations as follows:

$$\frac{dn_i}{dt} = S_i - S_{i,\text{fus}} - S_{i,\text{dif}}, \quad (\text{A.7})$$

$$\frac{3}{2} \frac{d}{dt} (n_i T_i) = P_{i,\text{aux}} + P_{i,\text{fus}} + Q_{ie} - P_{i,\text{dif}}, \quad (\text{A.8})$$

$$\frac{3}{2} \frac{d}{dt} (n_e T_e) = P_\Omega + P_{e,\text{aux}} + P_{e,\text{fus}} - P_R - Q_{ie} - P_{e,\text{dif}}, \quad (\text{A.9})$$

where fusion and diffusion terms have been placed with symbols. All particle and energy source terms have been modeled in the Section 2.3.

## A.2 Volume-Averaged Quantities

Since the dynamics equations to be solved are global in one tokamak but the available density and temperature data from DIII-D are radius dependent, these physics quantities need to be averaged over volume first. We take the electron density  $n_e$  as an example here. Suppose  $n_e$  is symmetric in toroidal and poloidal axes, i.e.,  $n_e(\rho)$ , where  $\rho$  is the normalized radius. The volume averaged  $n_e$  becomes  $\bar{n}_e = \frac{1}{V} \int_V n_e(\rho) dV$ . Instead of using one pre-assumed profile function [10], we make use of the numerical integral. In a torus geometry,

$$\begin{aligned} \bar{n}_e &= \frac{1}{V} \int_V n_e(\rho) dV \\ &= \frac{1}{\pi \rho_a^2 \cdot 2\pi R_0} \int_0^{\rho_a} d\rho \int_0^{2\pi} \rho d\theta \int_0^{2\pi} (R_0 + \rho \cos \theta) n_e(\rho) d\phi \\ &= \frac{4\pi^2 R_0}{2\pi^2 \rho_a^2 R_0} \int_0^{\rho_a} n_e(\rho) \rho d\rho = \frac{2}{\rho_a^2} \int_0^{\rho_a} n_e(\rho) \rho d\rho, \end{aligned} \quad (\text{A.10})$$

where  $\rho_a = 1$  is the normalized minor radius,  $R_0$  is the major radius, and  $\theta$  and  $\phi$  are poloidal and toroidal angles respectively. This integral will be done numerically with the trapezoidal rule. Similar processes can be done for  $\bar{T}_e$ ,  $\bar{T}_i$ , and  $\bar{n}_z$ . The averaged ion density  $\bar{n}_i$  can be calculated from the averaged electron and impurity densities with the assumption of charge neutrality in the Equation A.6. In the remaining of this appendix, we drop the bars over physical quantities and assume  $n_e, n_i, n_z, T_i, T_e$ , etc. are volume averaged.

## A.3 Particle and Energy Diffusion

Since most terms have been modeled in the multinodal model, we focus on the diffusion term here. The particle and energy diffusion terms are

$$S_{i,\text{dif}} = \frac{n_i}{\tau_{P,i}}, \quad P_{i,\text{dif}} = \frac{3}{2} \frac{n_i T_i}{\tau_{E,i}}, \quad P_{e,\text{dif}} = \frac{3}{2} \frac{n_e T_e}{\tau_{E,e}}. \quad (\text{A.11})$$

The original method to get the confinement times is to use the ITER-98(y,2) energy confinement scaling law (ITER-98) [5], which is built on the regression over multiple tokamaks data. The energy confinement time in the ITER-98 model is defined by

$$\begin{aligned} \frac{\tau_E^{\text{IPB98(y,2)}}}{1 \text{ s}} = & 0.056 \left( \frac{I_P}{1 \text{ MA}} \right)^{0.93} \left( \frac{B_0}{1 \text{ T}} \right)^{0.15} \left( \frac{n}{10^{19} \text{ m}^{-3}} \right)^{0.41} \left( \frac{P_{\text{tot}}}{1 \text{ MW}} \right)^{-0.69} \\ & \times \left( \frac{R_0}{1 \text{ m}} \right)^{1.97} \kappa^{0.78} A^{-0.58} \left( \frac{M}{1 \text{ amu}} \right)^{0.19}, \end{aligned} \quad (\text{A.12})$$

where  $I_P$  (MA) is the plasma current,  $B_0$  (T) is the toroidal magnetic field,  $n_e$  ( $\text{m}^{-3}$ ) is the line averaged electron density,  $P_{\text{tot}}$  (MW) is the total absorbed power,  $R_0$  (m) is the major radius,  $\kappa$  is the elongation,  $A = R_0/a$  is the aspect ratio, and  $M$  (amu) is the hydrogen isotope mass ( $M = 2$  here). The particle and energy confinement times can be gotten by assuming  $\tau_{P,i} = \tau_{E,i} = \tau_{E,e} = \tau_{E,98} \equiv \tau_E^{\text{IPB98(y,2)}}$ . In the next section, we will remove this assumption by allowing each confinement time to have a model with different parameters.

#### A.4 Confinement Time Models

As mentioned before, in order to get the diffusion terms  $S_{i,\text{dif}}$ ,  $P_{i,\text{dif}}$ ,  $P_{e,\text{dif}}$ , we need their confinement times. In the previous work [10], the confinement times,  $\tau_{P,i}$ ,  $\tau_{E,i}$ , and  $\tau_{E,e}$ , were modeled with a scaled ITER-98, i.e.,  $\tau_{P,\sigma} = C_{P,\sigma} \tau_{E,98}$  and  $\tau_{E,\sigma} = C_{E,\sigma} \tau_{E,98}$ , where  $C$  multipliers are confinement-tuning parameters (CTPs). The CTP is formulated as

$$\begin{aligned} C = & b_1 + b_2 P_{\text{NBI,vol}} + b_3 P_{\text{NBI,counter-frac}} + b_4 P_{\text{NBI,short-frac}} + b_5 P_{\text{ECH,vol}} + b_6 P_{\text{FW,vol}} \\ & + b_7 q_{95} + b_8 q_0 + b_9 I_{P,\text{xsec}} + b_{10} B_{T,0} + b_{11} S_{i,\text{GAS,vol}} + b_{12} \delta_{\text{divertor}} \\ & + b_{13} \delta_{\text{non-divertor}} + b_{14} \kappa, \end{aligned} \quad (\text{A.13})$$

where physical quantities can be found in [10] and  $b_1$ - $b_{14}$  are fitted through experiment data for  $\tau_{P,i}$ ,  $\tau_{E,i}$ , and  $\tau_{E,e}$ . This model requires physical quantities to be non-dimensional, and additions of terms are not consistent with multiplications in the original ITER-98 model.

Also, the previous work [10] presents results of energy confinement times and particle confinement times separately, but not at the same time.

To overcome these drawbacks of the previous work, we model confinement times by one tuned confinement time scaling law:

$$\begin{aligned} \frac{\tau}{1\text{ s}} = C & \left( \frac{I_P}{1\text{ MA}} \right)^{\alpha_{I_P}} \left( \frac{B_0}{1\text{ T}} \right)^{\alpha_{B_0}} \left( \frac{n}{10^{19}\text{ m}^{-3}} \right)^{\alpha_n} \left( \frac{P_{\text{tot}}}{1\text{ MW}} \right)^{\alpha_{P_{\text{tot}}}} \left( \frac{R_0}{1\text{ m}} \right)^{\alpha_{R_0}} \\ & \times \kappa^{\alpha_\kappa} A^{\alpha_A} \left( \frac{M}{1\text{ amu}} \right)^{\alpha_M}, \end{aligned} \quad (\text{A.14})$$

where  $C$ ,  $\alpha_{I_P} - \alpha_M$  are model parameters to be obtained through fitting the experiment data. By taking the natural logarithm in both sides, we can get

$$\begin{aligned} \ln \left( \frac{\tau_\sigma}{1\text{ s}} \right) = \ln C_\sigma & + \alpha_{\sigma, I_P} \ln \left( \frac{I_P}{1\text{ MA}} \right) + \alpha_{\sigma, B_0} \ln \left( \frac{B_0}{1\text{ T}} \right) + \alpha_{\sigma, n} \ln \left( \frac{n}{10^{19}\text{ m}^{-3}} \right) \\ & + \alpha_{\sigma, P_{\text{tot}}} \ln \left( \frac{P_{\text{tot}}}{1\text{ MW}} \right) + \alpha_{\sigma, R_0} \ln \left( \frac{R_0}{1\text{ m}} \right) + \alpha_{\sigma, \kappa} \ln \kappa + \alpha_{\sigma, A} \ln A \\ & + \alpha_{\sigma, M} \ln \left( \frac{M}{1\text{ amu}} \right), \end{aligned} \quad (\text{A.15})$$

where  $\tau_\sigma$  can be  $\tau_{P,i}$ ,  $\tau_{E,i}$ , and  $\tau_{E,e}$ . Let

$$b_\sigma = \ln C_\sigma, \quad (\text{A.16})$$

$$\mathbf{w}_\sigma = \left[ \alpha_{\sigma, I_P} \quad \alpha_{\sigma, B_0} \quad \alpha_{\sigma, n} \quad \alpha_{\sigma, P_{\text{tot}}} \quad \alpha_{\sigma, R_0} \quad \alpha_{\sigma, \kappa} \quad \alpha_{\sigma, A} \quad \alpha_{\sigma, M} \right]^T, \quad (\text{A.17})$$

$$\ln \mathbf{x} = \ln \left( \left[ \frac{I_P}{1\text{ MA}} \quad \frac{B_0}{1\text{ T}} \quad \frac{n}{10^{19}\text{ m}^{-3}} \quad \frac{P_{\text{tot}}}{1\text{ MW}} \quad \frac{R_0}{1\text{ m}} \quad \kappa \quad A \quad \frac{M}{1\text{ amu}} \right]^T \right). \quad (\text{A.18})$$

Then the Equation A.15 can be rewritten as  $\ln \left( \frac{\tau_\sigma}{1\text{ s}} \right) = \mathbf{w}_\sigma^T \ln \mathbf{x} + b_\sigma$ . If we put all three

confinement times into one formula, we have

$$\ln \boldsymbol{\tau} = \ln \begin{pmatrix} \frac{\tau_{P,i}}{1 \text{ s}} \\ \frac{\tau_{E,i}}{1 \text{ s}} \\ \frac{\tau_{E,e}}{1 \text{ s}} \end{pmatrix} = \begin{bmatrix} \mathbf{w}_{P,i}^T \\ \mathbf{w}_{E,i}^T \\ \mathbf{w}_{E,e}^T \end{bmatrix} \ln \mathbf{x} + \begin{bmatrix} b_{P,i} \\ b_{E,i} \\ b_{E,e} \end{bmatrix} \equiv \mathbf{W} \ln \mathbf{x} + \mathbf{b}, \quad (\text{A.19})$$

which can be viewed as a linear model. The model parameters  $\mathbf{W}$  and  $\mathbf{b}$  can be solved through back propagation algorithm, where the parameters are initialized by coefficients from the ITER-98 model then optimized by the gradient descent algorithm. The details of mathematical backgrounds and optimization algorithms can be found in the Section 3.3.

## A.5 Computation Results

In this section, we simulate shots from DIII-D experiments with a tuned confinement time model and compare its results with the original model. The GTBURN is used here for both simulation and optimization. The shots used in this work are listed in the Table 4.1 which follow [10]. Those shots are limited to ELMing H-mode non-RMP (non-resonant magnetic perturbation) shots with the standard magnetic field configuration. The shots are divided into two datasets: one training dataset including 20 shots, in the Table 4.1 without starts; another testing dataset including 5 shots, in the Table 4.1 with starts. The training set is used to optimize the confinement time model, and the testing set is used to validate the optimized model. In detail, the computational experiment is done as follows.

- **Training:** The dynamical system of the one-nodal model is solved on the training set by following the black arrows in the Figure 3.1. The MSE is calculated, then the gradients of error flow back by following the blue arrows in the Figure 3.1 to the confinement time model. The parameters in the confinement time model are updated. The settings for the optimizer are listed in the Table A.1.

- Testing: The dynamical system of the one-nodal model is solved on the testing set only in the forward direction. The solution is compared with the experiment measurement.

Table A.1: Hyperparameters in the solver and optimizer.

Hyper-parameter	Number
Solver absolute tolerance	$10^{-5}$
Solver relative tolerance	$10^{-3}$
Optimizer learning rate	0.05
Optimizer regularization rate	$10^{-5}$
Training time step	0.2 s
Testing time step	0.02 s
Moving average window size	5
Training epoch number	20

After optimizing the time confinement time model with the training set, we get the tuned coefficients, which are listed in the Table A.2, where the coefficients of the ITER-98 law are also shown for the comparison. For density confinement times, the ion density confinement time is found to be heavily dependent on the  $I_P$ . Besides, the signs of coefficients of  $\alpha_n$  and  $\alpha_{P_{\text{tot}}}$  are flipped, which shows the physical dependency of the density confinement time can be different from the energy one. For energy confinement times, the signs before  $\alpha_{B_0}$  and  $\alpha_M$  flipped, which shows a higher toroidal magnetic field can lead to a lower energy confinement time in the H-mode. Also, the  $\alpha_{I_P}$  for the  $\tau_{E,e}$  becomes negative now.

Table A.2: Tuned coefficients in the density and energy confinement time scaling laws as the Equation A.14.

	$C$	$\alpha_{I_P}$	$\alpha_{B_0}$	$\alpha_n$	$\alpha_{P_{\text{tot}}}$	$\alpha_{R_0}$	$\alpha_\kappa$	$\alpha_A$	$\alpha_M$
$\tau_{E,98}$	0.0562	0.9300	0.1500	0.4100	-0.6900	1.9700	0.7800	-0.5800	0.1900
$\tau_{P,i}$	0.1076	1.9214	0.8653	-1.3130	0.4209	2.6744	0.6771	-0.0352	0.8391
$\tau_{E,i}$	0.0494	0.6719	-0.0461	1.0544	-0.8528	1.8454	0.7878	-0.6815	0.0616
$\tau_{E,e}$	0.0426	1.0045	-0.2126	0.6868	-0.4626	1.7194	0.5302	-0.7969	-0.0862

The MSEs of the ITER-98 model and the tuned (optimized) model are shown in the Table A.3. Significant decreases of MSEs (over 92%) are found on the testing set after



optimizing parameters on the training set. These results can prove the effectiveness of our model. Although the confinement time model is trained on the training set, the optimized model can be generalized to solve the unseen shots in the testing set. This allows the one-nodal model to be used for prediction tasks.

Table A.3: Mean square errors for shots in the testing set.

Shot	Mean Square Error (MSE)		Relative decrease of MSE
	ITER-98 model	Tuned model	
131190	14.3232	1.1346	92.08%
140418	243.1307	1.2956	99.47%
140420	317.8486	1.6628	99.48%
140427	112.4497	2.3621	97.90%
140535	314.3537	0.4664	99.85%
Average	200.4212	1.3843	99.31%

The simulation results on the testing set are shown in the Figure A.1-A.5. The toroidal magnetic field, plasma current,  $q_{95}$ , particle and energy sources are shown in the Figure 4.1-4.29. For simulation results, the results from the original ITER-98 model are shown on the left-hand side, and the optimized model ones are shown on the right-hand side. Also, the ion and electron densities are shown on the first rows, and the temperatures are on the second rows. The analyses for each shot are as follows.

- Shot 131190: After the optimization, the densities are close to the experimental measurements, but the temperatures are lower than the measured ones. When the NBI and ECH powers are supplied to the plasma,  $T_i$  and  $T_e$  should be higher, which suggests the  $\alpha_{P_{tot}}$  can be higher, so larger power can lead to longer confinement time and high temperatures. Another way is to add the  $P_{ECH}$  to the confinement time model for modeling this positive effect on energies.
- Shot 140418: With the optimization, temperatures can catch the step jump, which can be explained as the transition from L-mode to H-mode. However, the particle density fails to do so, suggesting a switch term can be added to the confinement

time model. When the plasma transits from L-mode to H-mode, the switch can be turned on to increase the particle confinement time. Also, we can add the  $P_{\text{NBI}}$  to the confinement time model, which will allow it to model the jump in energy supply.

- Shot 140420: After the optimization, both density and temperature results improve but are under-estimated. As mentioned above, we can add  $P_{\text{NBI}}$  and  $P_{\text{ECH}}$  to the confinement time model.
- Shot 140427: The bump shape of the density shows the particle source from the gas is over-estimated. This problem can be solved by increasing  $C_{\text{gas}}$  hence decreasing the  $S_{i,\text{gas}}$  in the Equation 2.56. We also can let the  $C_{\text{gas}}$  be one learning parameter and optimize it with experiment data.
- Shot 140535: The results improve after optimization. Similarly, we can add  $P_{\text{ICH}}$  to the confinement time model.

In summary, by comparing the original and optimized results, we find we can add more terms, such as  $P_{\text{NBI}}$ ,  $P_{\text{ECH}}$ , and  $P_{\text{ICH}}$ , to the confinement time model. Also, the  $C_{\text{gas}}$  in the Equation 2.56 can be a learning parameter, which will be tuned by the experiment data.

## A.6 Summary

In this work towards the one-nodal burning plasma dynamics model, we present the system of equations at the beginning and the confinement time model next. The GTBURN package is used for simulating DIII-D plasmas. Finally, the advantages and limitations of the one-nodal model with the linear confinement time model are listed. Such drawbacks motivate us to develop a multinodal burning plasma dynamics model as in the thesis.

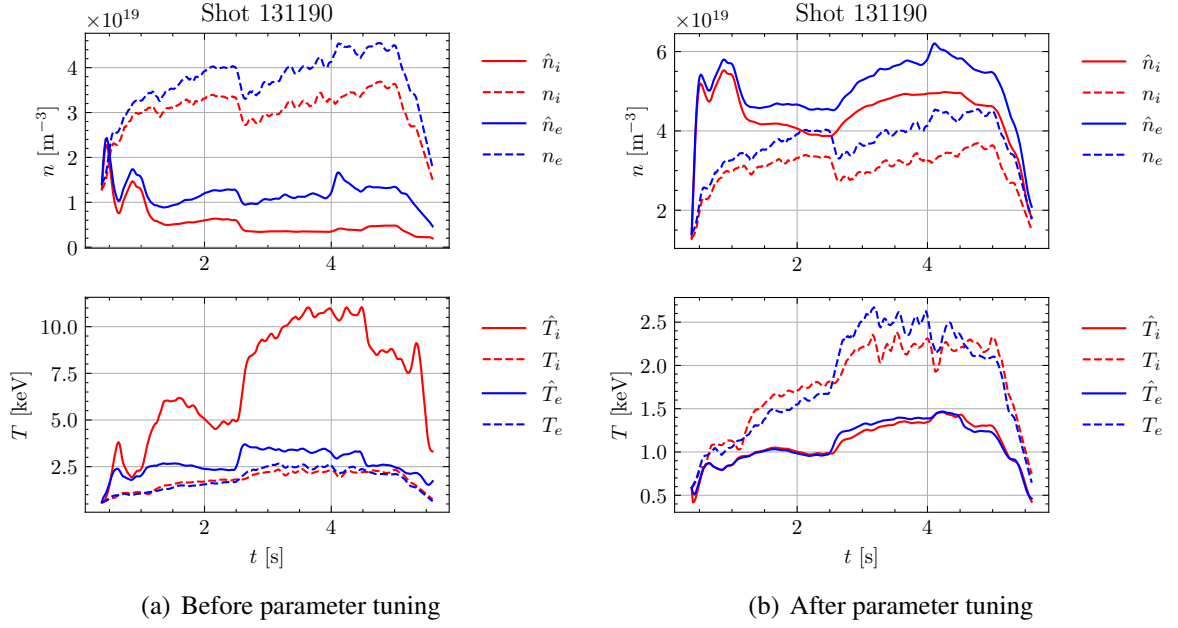


Figure A.1: Simulation results of the shot 131190, where  $\hat{n}_\sigma$  and  $\hat{T}_\sigma$  are from the one-nodal model, while  $n_\sigma$  and  $T_\sigma$  are from the experimental measurement.

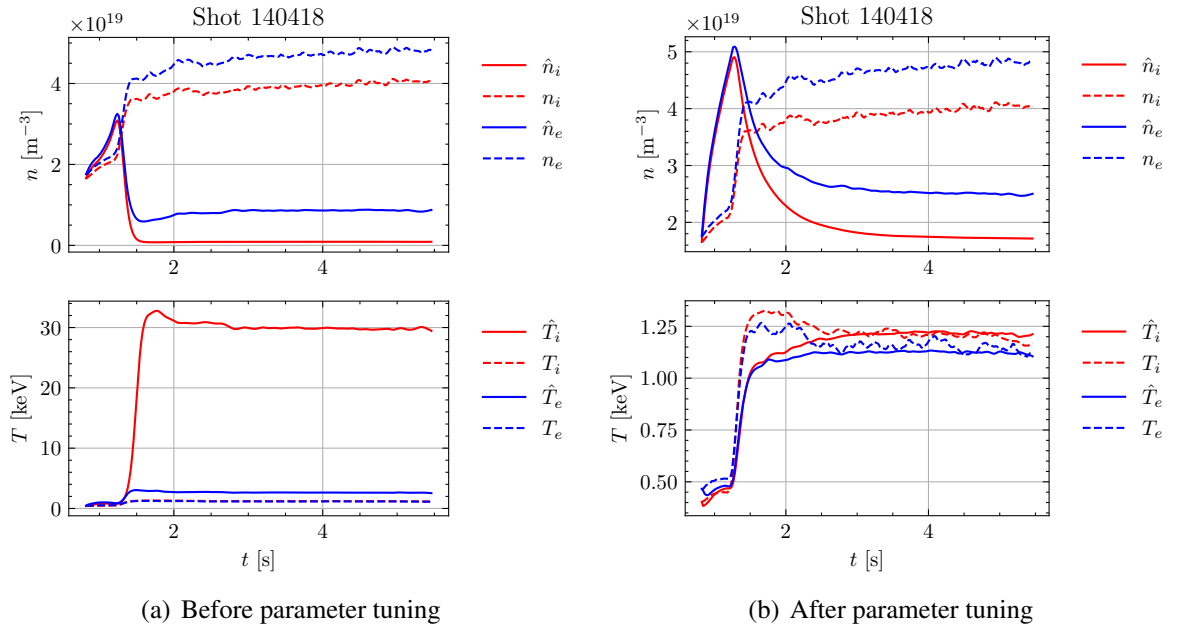


Figure A.2: Simulation results of the shot 140418, where  $\hat{n}_\sigma$  and  $\hat{T}_\sigma$  are from the one-nodal model, while  $n_\sigma$  and  $T_\sigma$  are from the experimental measurement.

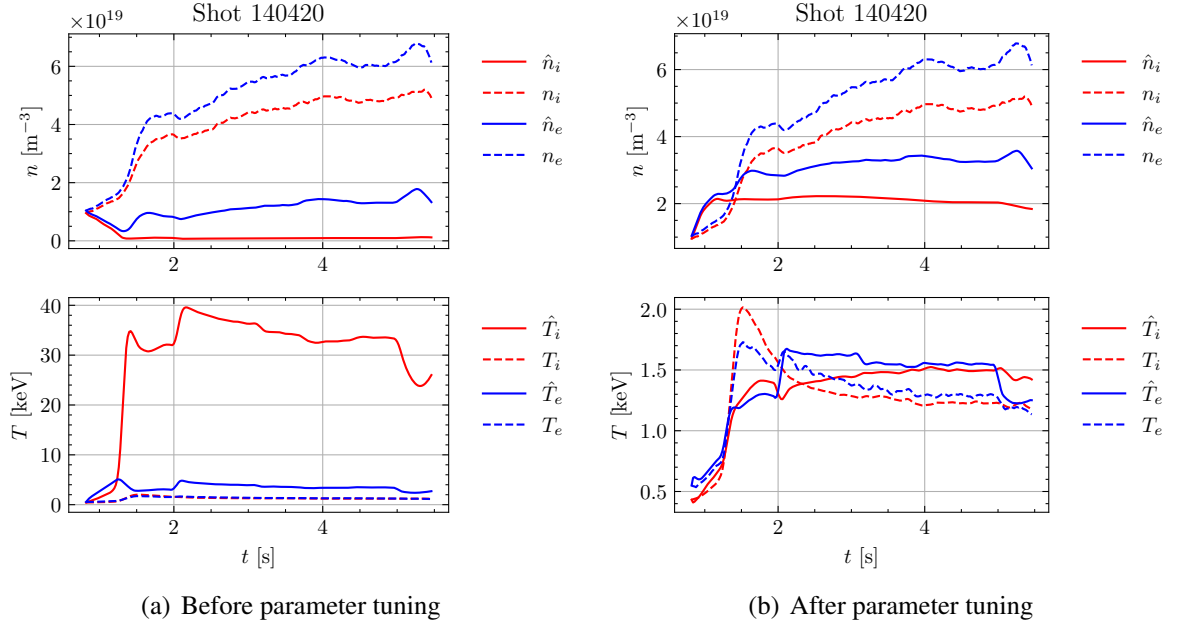


Figure A.3: Simulation results of the shot 140420, where  $\hat{n}_\sigma$  and  $\hat{T}_\sigma$  are from the one-nodal model, while  $n_\sigma$  and  $T_\sigma$  are from the experimental measurement.

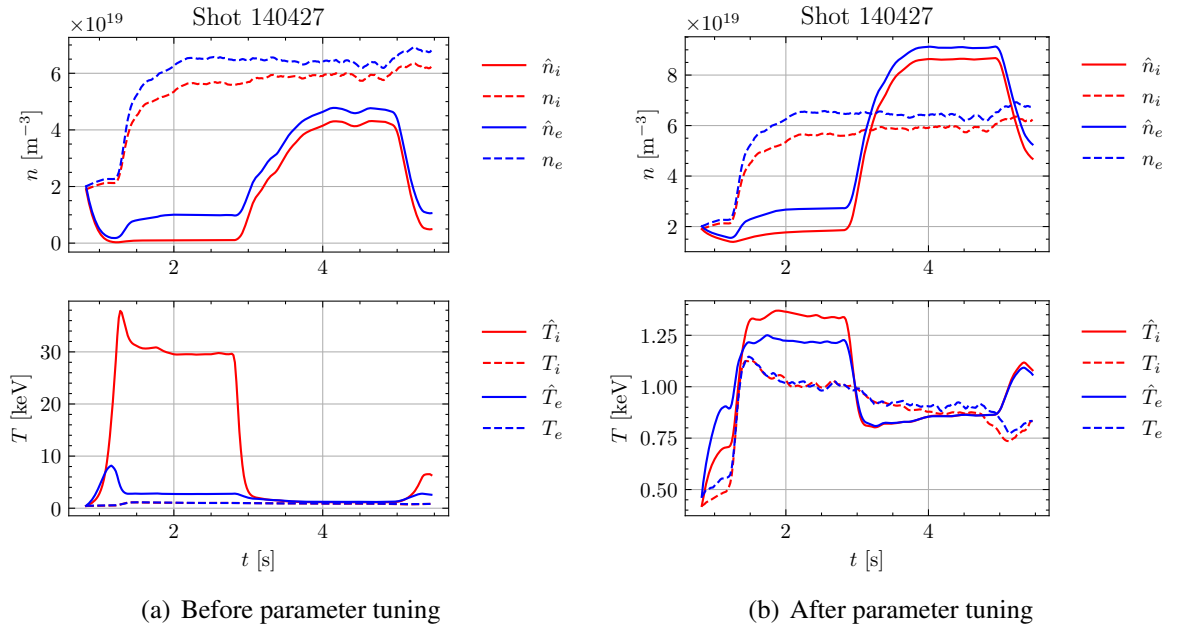


Figure A.4: Simulation results of the shot 140427, where  $\hat{n}_\sigma$  and  $\hat{T}_\sigma$  are from the one-nodal model, while  $n_\sigma$  and  $T_\sigma$  are from the experimental measurement.

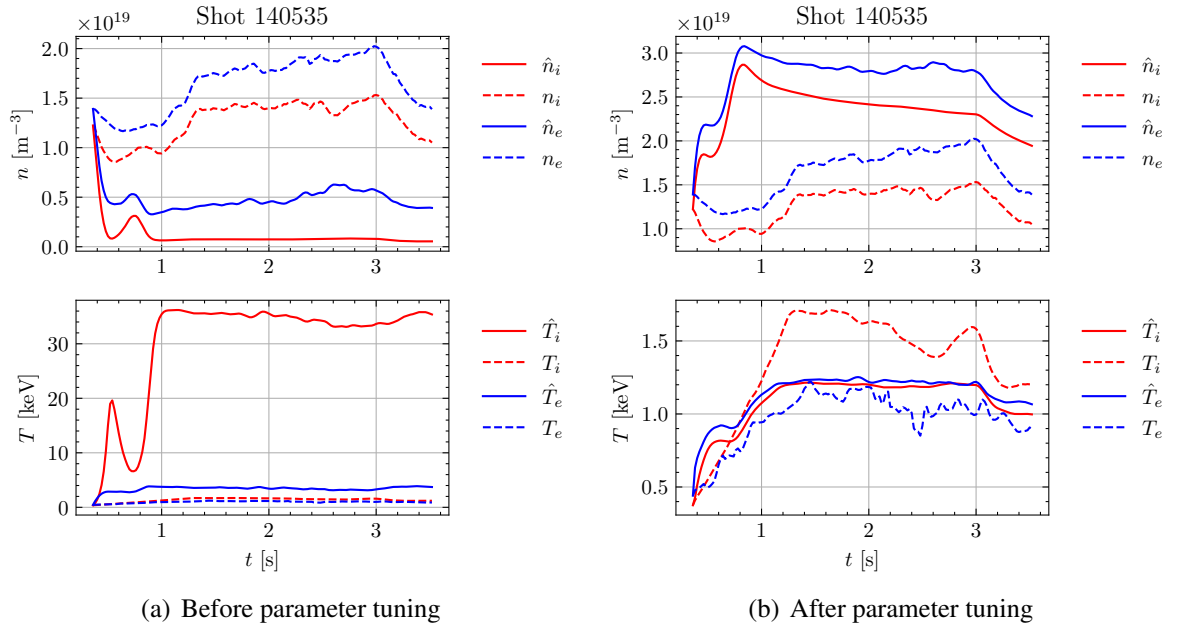


Figure A.5: Simulation results of the shot 140535, where  $\hat{n}_\sigma$  and  $\hat{T}_\sigma$  are from the one-nodal model, while  $n_\sigma$  and  $T_\sigma$  are from the experimental measurement.

## APPENDIX B

### A GENERAL MULTINODAL MODEL FOR PLASMA TRANSPORT

In this appendix, the balance equations and transport terms for a general multinodal model are derived. Unlike the multinodal model proposed in the Section 2.2, this general model does not specify the number of nodes.

#### B.1 Geometry

The geometry of the general multinodal model is illustrated in the Figure B.1, where each node is a toroidal shell and each internodal surface is a torus surface. The  $r_j$  is the minor radius of the surface  $A_j$ , and  $\Delta r_{j,j+1}$  is the radial distance between two adjacent nodes  $j$  and  $j+1$ . Still, we use some notations for the set of ion species as  $\mathcal{I} = \{D, T, \alpha, z_1, z_2, \dots\}$  and the set of species as  $\mathcal{S} = \{e\} \cup \mathcal{I}$ . The particle balance equation is derived first, then we move to the energy balance equation.

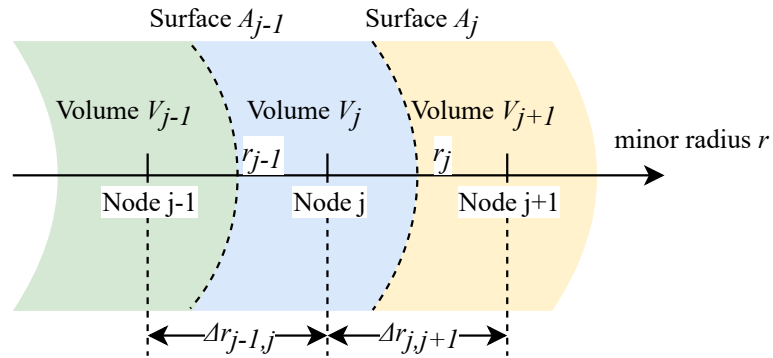


Figure B.1: A diagram for the general multinodal model, where each node is a toroidal shell and each internodal surface is a torus surface.

## B.2 Particle Balance Equations

From the continuity equation [1] of the species  $\sigma$  in the fluid theory,

$$\frac{\partial n_\sigma}{\partial t} + \nabla \cdot \mathbf{\Gamma}_\sigma = S_\sigma, \quad \sigma \in \mathcal{S}, \quad (\text{B.1})$$

where  $n_\sigma$  is the particle density,  $\mathbf{\Gamma}_\sigma = n_\sigma \mathbf{v}_\sigma$  is the particle flux, and  $S_\sigma$  is the net particle source. By averaging the continuity equation in the node  $j$ , we have

$$\frac{1}{V_j} \int_{V_j} \frac{\partial n_\sigma}{\partial t} dV = \frac{1}{V_j} \int_{V_j} S_\sigma dV - \frac{1}{V_j} \int_{V_j} \nabla \cdot \mathbf{\Gamma}_\sigma dV. \quad (\text{B.2})$$

where  $V_j$  is the volume of the node  $j$ . Define the volume-averaged particle density, net source, and transport terms:

$$\bar{n}_\sigma^{(j)} = \frac{1}{V_j} \int_{V_j} n_\sigma dV, \quad \bar{S}_\sigma^{(j)} = \frac{1}{V_j} \int_{V_j} S_\sigma dV, \quad \bar{S}_{\sigma, \text{tran}}^{(j)} = -\frac{1}{V_j} \int_{V_j} \nabla \cdot \mathbf{\Gamma}_\sigma dV. \quad (\text{B.3})$$

Then, the volume-averaged continuity equation or the nodal particle balance equation is

$$\frac{d\bar{n}_\sigma^{(j)}}{dt} = \bar{S}_\sigma^{(j)} + \bar{S}_{\sigma, \text{tran}}^{(j)}. \quad (\text{B.4})$$

Through the divergence theorem, the transport term becomes

$$\bar{S}_{\sigma, \text{tran}}^{(j)} = -\frac{1}{V_j} \int_{V_j} \nabla \cdot \mathbf{\Gamma}_\sigma dV = -\frac{1}{V_j} \left( \int_{A_j} \mathbf{\Gamma}_\sigma \cdot d\mathbf{S} - \int_{A_{j-1}} \mathbf{\Gamma}_\sigma \cdot d\mathbf{S} \right). \quad (\text{B.5})$$

From the Fick's law of diffusion,  $\mathbf{\Gamma}_\sigma = -D_\sigma \nabla n_\sigma$ , where  $D_\sigma$  is the diffusion coefficient and  $\nabla n_\sigma$  is the density gradient. In toroidal coordinates, the density gradient [1] can be written as

$$\nabla n_\sigma = \frac{\partial n_\sigma}{\partial r} \hat{\mathbf{r}} + \frac{1}{R_0 + r \cos \theta} \frac{\partial n_\sigma}{\partial \phi} \hat{\boldsymbol{\phi}} + \frac{1}{r} \frac{\partial n_\sigma}{\partial \theta} \hat{\boldsymbol{\theta}}. \quad (\text{B.6})$$

We assume that the particle gradient has toroidal and poloidal symmetries on internodal surfaces, i.e.

$$\nabla n_\sigma = \frac{dn_\sigma}{dr} \hat{\mathbf{r}}. \quad (\text{B.7})$$

Thus, the transport term becomes

$$\begin{aligned} \bar{S}_{\sigma, \text{tran}}^{(j)} &= -\frac{1}{V_j} \left( \int_{A_j} \mathbf{\Gamma}_\sigma \cdot d\mathbf{S} - \int_{A_{j-1}} \mathbf{\Gamma}_\sigma \cdot d\mathbf{S} \right) \\ &= -\frac{1}{V_j} \left[ (\Gamma_{\sigma, r})_{A_j} A_j - (\Gamma_{\sigma, r})_{A_{j-1}} A_{j-1} \right]. \end{aligned} \quad (\text{B.8})$$

The radial fluxes can be approximated by

$$(\Gamma_{\sigma, r})_{A_j} = \left( -D_\sigma \frac{dn_\sigma}{dr} \right)_{A_j} \approx -D_\sigma^{(j)} \frac{\bar{n}_\sigma^{(j+1)} - \bar{n}_\sigma^{(j)}}{\Delta r_{j, j+1}}, \quad (\text{B.9})$$

$$(\Gamma_{\sigma, r})_{A_{j-1}} = \left( -D_\sigma \frac{dn_\sigma}{dr} \right)_{A_{j-1}} \approx -D_\sigma^{(j-1)} \frac{\bar{n}_\sigma^{(j)} - \bar{n}_\sigma^{(j-1)}}{\Delta r_{j-1, j}}, \quad (\text{B.10})$$

where  $D_\sigma^{(j-1)}$  and  $D_\sigma^{(j)}$  are the diffusion coefficients at the surface  $A_{j-1}$  and  $A_j$  respectively, and  $\Delta r_{j-1, j}$  and  $\Delta r_{j, j+1}$  are the radial distances between locations of adjacent nodal centers. Let internodal particle transport times be

$$\tau_{P, \sigma}^{j \rightarrow j+1} = \frac{V_j \Delta r_{j, j+1}}{A_j D_\sigma^{(j)}} = \frac{r_j^2 - r_{j-1}^2}{2r_j} \frac{\Delta r_{j, j+1}}{D_\sigma^{(j)}}, \quad (\text{B.11})$$

$$\tau_{P, \sigma}^{j+1 \rightarrow j} = \frac{V_{j+1} \Delta r_{j, j+1}}{A_j D_\sigma^{(j)}} = \frac{r_{j+1}^2 - r_j^2}{2r_j} \frac{\Delta r_{j, j+1}}{D_\sigma^{(j)}}, \quad (\text{B.12})$$

$$\tau_{P, \sigma}^{j-1 \rightarrow j} = \frac{V_{j-1} \Delta r_{j-1, j}}{A_{j-1} D_\sigma^{(j-1)}} = \frac{r_{j-1}^2 - r_{j-2}^2}{2r_{j-1}} \frac{\Delta r_{j-1, j}}{D_\sigma^{(j-1)}}, \quad (\text{B.13})$$

$$\tau_{P, \sigma}^{j \rightarrow j-1} = \frac{V_j \Delta r_{j-1, j}}{A_{j-1} D_\sigma^{(j-1)}} = \frac{r_j^2 - r_{j-1}^2}{2r_{j-1}} \frac{\Delta r_{j-1, j}}{D_\sigma^{(j-1)}}, \quad (\text{B.14})$$

where the torus shell volume is  $V_j = 2\pi R_0 \cdot \pi(r_j^2 - r_{j-1}^2)$ , the torus surface area is  $A_j = 2\pi R_0 \cdot 2\pi r_j$ , and the  $R_0$  is the major radius. For the elongated plasma configuration,  $r_j^2$  can be replaced by the product of the semi-major radius  $a_j$  and the semi-minor radius  $b_j$  of the



poloidal cross section. Hence, the transport term becomes

$$\bar{S}_{\sigma,\text{tran}}^{(j)} = -\frac{\bar{n}_{\sigma}^{(j)} - \bar{n}_{\sigma}^{(j+1)}}{\tau_{P,\sigma}^{j \rightarrow j+1}} - \frac{\bar{n}_{\sigma}^{(j)} - \bar{n}_{\sigma}^{(j-1)}}{\tau_{P,\sigma}^{j \rightarrow j-1}}. \quad (\text{B.15})$$

Since there are relations between internodal particle transport times that

$$\tau_{P,\sigma}^{j+1 \rightarrow j} = \frac{V_{j+1} \Delta r_{j,j+1}}{A_j D_{\sigma}^{(j)}} = \frac{V_{j+1}}{V_j} \tau_{P,\sigma}^{j \rightarrow j+1}, \quad (\text{B.16})$$

$$\tau_{P,\sigma}^{j-1 \rightarrow j} = \frac{V_{j-1} \Delta r_{j-1,j}}{A_{j-1} D_{\sigma}^{(j-1)}} = \frac{V_{j-1}}{V_j} \tau_{P,\sigma}^{j \rightarrow j-1}, \quad (\text{B.17})$$

the transport term can also be written as

$$\bar{S}_{\sigma,\text{tran}}^{(j)} = -\frac{\bar{n}_{\sigma}^{(j)}}{\tau_{P,\sigma}^{j \rightarrow j+1}} + \frac{V_{j+1}}{V_j} \frac{\bar{n}_{\sigma}^{(j+1)}}{\tau_{P,\sigma}^{j+1 \rightarrow j}} - \frac{\bar{n}_{\sigma}^{(j)}}{\tau_{P,\sigma}^{j \rightarrow j-1}} + \frac{V_{j-1}}{V_j} \frac{\bar{n}_{\sigma}^{(j-1)}}{\tau_{P,\sigma}^{j-1 \rightarrow j}}. \quad (\text{B.18})$$

### B.3 Energy Balance Equations

The energy conservation equation of the species  $\sigma$  [13] in the fluid theory is

$$\frac{3}{2} n_{\sigma} \left( \frac{\partial}{\partial t} + \mathbf{v}_{\sigma} \cdot \nabla \right) T_{\sigma} + p_{\sigma} \nabla \cdot \mathbf{v}_{\sigma} + \nabla \cdot \mathbf{q}_{\sigma} = P_{\sigma}, \quad \sigma \in \mathcal{S}, \quad (\text{B.19})$$

where  $T_{\sigma}$  is the temperature (in the energy unit),  $p_{\sigma}$  is the pressure,  $\mathbf{q}_{\sigma}$  is the heat flux, and  $P_{\sigma}$  is the net energy source for the species  $\sigma$ . Let the energy density be  $U_{\sigma} = \frac{3}{2} n_{\sigma} T_{\sigma}$ .

Combining the energy conservation equation with the particle one, we can get

$$\begin{aligned} \frac{3}{2} n_{\sigma} \frac{\partial T_{\sigma}}{\partial t} + \frac{3}{2} \Gamma_{\sigma} \cdot \nabla T_{\sigma} + p_{\sigma} \nabla \cdot \mathbf{v}_{\sigma} + \nabla \cdot \mathbf{q}_{\sigma} + \frac{3}{2} T_{\sigma} \frac{\partial n_{\sigma}}{\partial t} + \frac{3}{2} T_{\sigma} \nabla \cdot \Gamma_{\sigma} &= P_{\sigma}, \\ \frac{3}{2} \frac{\partial (n_{\sigma} T_{\sigma})}{\partial t} &= P_{\sigma} - p_{\sigma} \nabla \cdot \mathbf{v}_{\sigma} - \nabla \cdot \left( \frac{3}{2} \Gamma_{\sigma} T_{\sigma} + \mathbf{q}_{\sigma} \right). \end{aligned} \quad (\text{B.20})$$

Since

$$\mathbf{\Gamma}_\sigma = -D_\sigma \nabla n_\sigma, \quad \mathbf{q}_\sigma = -k_\sigma \nabla \frac{T_\sigma}{k} = -\chi_\sigma n_\sigma c_{p,m,\sigma} \nabla \frac{T_\sigma}{k} = -\frac{5}{2} \chi_\sigma n_\sigma \nabla T_\sigma, \quad (\text{B.21})$$

where  $k_\sigma$  is the thermal conductivity,  $k$  is Boltzmann constant,  $c_{p,m,\sigma}$  is the molar heat capacity, and  $\chi_\sigma$  is the thermal diffusivity, then,

$$\frac{\partial U_\sigma}{\partial t} = (P_\sigma - p_\sigma \nabla \cdot \mathbf{v}_\sigma) + \nabla \cdot \left( \frac{3}{2} D_\sigma T_\sigma \nabla n_\sigma + \frac{5}{2} \chi_\sigma n_\sigma \nabla T_\sigma \right). \quad (\text{B.22})$$

If we assume  $D_\sigma \approx \frac{5}{3} \chi_\sigma$  [18] and let the new notations be

$$\chi_\sigma \leftarrow \frac{5}{3} \chi_\sigma \approx D_\sigma, \quad P_\sigma \leftarrow P_\sigma - p_\sigma \nabla \cdot \mathbf{v}_\sigma, \quad (\text{B.23})$$

then,

$$\frac{\partial U_\sigma}{\partial t} = P_\sigma + \nabla \cdot \left( \frac{3}{2} \chi_\sigma T_\sigma \nabla n_\sigma + \frac{3}{2} \chi_\sigma n_\sigma \nabla T_\sigma \right) = P_\sigma + \nabla \cdot (\chi_\sigma \nabla U_\sigma). \quad (\text{B.24})$$

Let the volume-averaged energy density, net power, and energy transport terms be

$$\bar{U}_\sigma^{(j)} = \frac{1}{V_j} \int_{V_j} U_\sigma \, dV, \quad \bar{P}_\sigma^{(j)} = \frac{1}{V_j} \int_{V_j} P_\sigma \, dV, \quad \bar{P}_{\sigma,\text{tran}}^{(j)} = \frac{1}{V_j} \int_{V_j} \nabla \cdot (\chi_\sigma \nabla U_\sigma) \, dV. \quad (\text{B.25})$$

The volume-averaged energy conservation equation or the nodal energy balance equation becomes

$$\frac{d\bar{U}_\sigma^{(j)}}{dt} = \bar{P}_\sigma^{(j)} + \bar{P}_{\sigma,\text{tran}}^{(j)}, \quad (\text{B.26})$$

where we assume

$$\bar{U}_\sigma^{(j)} = \frac{3}{2} \bar{n}_\sigma^{(j)} \bar{T}_\sigma^{(j)}. \quad (\text{B.27})$$

By following a similar method as the particle balance equation, we can define energy transport times as

$$\tau_{E,\sigma}^{j \rightarrow j+1} = \frac{V_j \Delta r_{j,j+1}}{A_j \chi_\sigma^{(j)}} = \frac{r_j^2 - r_{j-1}^2}{2r_j} \frac{\Delta r_{j,j+1}}{\chi_\sigma^{(j)}}, \quad (\text{B.28})$$

$$\tau_{E,\sigma}^{j+1 \rightarrow j} = \frac{V_{j+1} \Delta r_{j,j+1}}{A_j \chi_\sigma^{(j)}} = \frac{r_{j+1}^2 - r_j^2}{2r_j} \frac{\Delta r_{j,j+1}}{\chi_\sigma^{(j)}}, \quad (\text{B.29})$$

$$\tau_{E,\sigma}^{j-1 \rightarrow j} = \frac{V_{j-1} \Delta r_{j-1,j}}{A_{j-1} \chi_\sigma^{(j-1)}} = \frac{r_{j-1}^2 - r_{j-2}^2}{2r_{j-1}} \frac{\Delta r_{j-1,j}}{\chi_\sigma^{(j-1)}}, \quad (\text{B.30})$$

$$\tau_{E,\sigma}^{j \rightarrow j-1} = \frac{V_j \Delta r_{j-1,j}}{A_{j-1} \chi_\sigma^{(j-1)}} = \frac{r_j^2 - r_{j-1}^2}{2r_{j-1}} \frac{\Delta r_{j-1,j}}{\chi_\sigma^{(j-1)}}, \quad (\text{B.31})$$

where  $\chi_\sigma^{(j-1)}$  and  $\chi_\sigma^{(j)}$  are the thermal diffusivity at the surface  $A_{j-1}$  and  $A_j$  respectively.

The energy transport term is

$$\begin{aligned} \bar{P}_{\sigma,\text{tran}}^{(j)} &= -\frac{\bar{U}_\sigma^{(j)} - \bar{U}_\sigma^{(j+1)}}{\tau_{E,\sigma}^{j \rightarrow j+1}} - \frac{\bar{U}_\sigma^{(j)} - \bar{U}_\sigma^{(j-1)}}{\tau_{E,\sigma}^{j \rightarrow j-1}} \\ &= -\frac{\bar{U}_\sigma^{(j)}}{\tau_{E,\sigma}^{j \rightarrow j+1}} + \frac{V_{j+1}}{V_j} \frac{\bar{U}_\sigma^{(j+1)}}{\tau_{E,\sigma}^{j+1 \rightarrow j}} - \frac{\bar{U}_\sigma^{(j)}}{\tau_{E,\sigma}^{j \rightarrow j-1}} + \frac{V_{j-1}}{V_j} \frac{\bar{U}_\sigma^{(j-1)}}{\tau_{E,\sigma}^{j-1 \rightarrow j}}. \end{aligned} \quad (\text{B.32})$$

## APPENDIX C

### RADIAL ELECTRIC FIELD AND ELECTROSTATIC POTENTIAL PROFILES

In this appendix, we present the radial electric fields and electrostatic potentials for DIII-D and ITER with their polynomial fitting formulas. These formulas are used for ion orbit loss calculations in the Section 2.3.6

#### C.1 Radial Electric Field Profile for DIII-D

The radial electric field fitting from a profile for DIII-D-like parameters [107] is

$$E_r(\rho)(\text{kV/m}) = \begin{cases} -27\rho^3 - 54\rho^2 + 66\rho, & 0 \leq \rho < 0.85, \\ 390125\rho^4 - 1345748\rho^3 + 1734828\rho^2 - 990662\rho + 211459, & 0.85 \leq \rho \leq 1. \end{cases} \quad (\text{C.1})$$

Also, the radial electrostatic potential can be integrated from

$$\phi(r) = \int_r^a E_r(r') \, dr' \implies \phi(\rho) = a \int_\rho^1 E_r(\rho') \, d\rho', \quad (\text{C.2})$$

where  $a$  is the minor radius of DIII-D. Hence, the fitted electrostatic potential is

$$\begin{aligned} & \phi(\rho)(\text{kV}) \\ &= a \begin{cases} 6.75\rho^4 + 18\rho^3 - 33\rho^2 + 6.12, & 0 \leq \rho < 0.85, \\ -78025\rho^5 + 336437\rho^4 - 578276\rho^3 + 495331\rho^2 - 211459\rho + 35992, & 0.85 \leq \rho \leq 1. \end{cases} \end{aligned} \quad (\text{C.3})$$

## C.2 Radial Electric Field Profile for ITER

The radial electric field fitting from a predictive analysis of H-mode in ITER [108] is

$$E_r(\rho)(\text{kV/m}) = \begin{cases} -71\rho^3 - 47\rho^2 + 119\rho - 10, & 0 \leq \rho < 0.925, \\ -776\rho + 721, & 0.925 \leq \rho \leq 1. \end{cases} \quad (\text{C.4})$$

Also, the fitted electrostatic potential is

$$\phi(\rho)(\text{kV}) = a \begin{cases} 17.75\rho^4 + 15.67\rho^3 - 59.5\rho^2 + 10\rho + 14.32, & 0 \leq \rho < 0.925, \\ 388\rho^2 - 721\rho + 333, & 0.925 \leq \rho \leq 1, \end{cases} \quad (\text{C.5})$$

where  $a$  is the minor radius of ITER.

## REFERENCES

- [1] W. Stacey, *Fusion Plasma Physics*, ser. Physics textbook. Wiley, 2012, ISBN: 9783527669530.
- [2] M. Kikuchi, K. Lackner, and M. Q. Tran, *Fusion physics*. International Atomic Energy Agency, 2012, ISBN: 9789201304100.
- [3] K. Miyamoto, *Plasma physics and controlled nuclear fusion*. Springer Science & Business Media, 2005, vol. 38, ISBN: 9783540242178.
- [4] H.-S. Bosch and G. Hale, “Improved formulas for fusion cross-sections and thermal reactivities,” *Nuclear Fusion*, vol. 32, no. 4, pp. 611–631, 1992.
- [5] I. P. B. Editors, I. P. E. G. C. an Co-Chairs, I. J. C. Team, and P. Unit, “Chapter 1: Overview and summary,” *Nuclear Fusion*, vol. 39, no. 12, pp. 2137–2174, 1999.
- [6] J.-F. Wang, T. Amano, Y. Ogawa, and N. Inoue, “Simulation of burning plasma dynamics in iter,” *Fusion Technology*, vol. 32, no. 4, pp. 590–600, 1997. eprint: <https://doi.org/10.13182/FST97-A19906>.
- [7] B. J. Green, I. I. Team, and P. Teams, “ITER: Burning plasma physics experiment,” *Plasma Physics and Controlled Fusion*, vol. 45, no. 5, pp. 687–706, 2003.
- [8] J. Cordey, K. Thomsen, A. Chudnovskiy, O. Kardaun, T. Takizuka, J. Snipes, M. Greenwald, L. Sugiyama, F. Ryter, A. Kus, J. Stober, J. DeBoo, C. Petty, G. Bracco, M. Romanelli, Z. Cui, Y. Liu, D. McDonald, A. Meakins, Y. Miura, K. Shinohara, K. Tsuzuki, Y. Kamada, H. Urano, M. Valovic, R. Akers, C. Brickley, A. Sykes, M. Walsh, S. Kaye, C. Bush, D. Hogewei, Y. Martin, A. Cote, G. Pacher, J. Ongena, F. Imbeaux, G. Hoang, S. Lebedev, and V. Leonov, “Scaling of the energy confinement time with  $\beta$  and collisionality approaching ITER conditions,” *Nuclear Fusion*, vol. 45, no. 9, pp. 1078–1084, 2005.
- [9] W. M. Stacey, “A survey of thermal instabilities in tokamak plasmas: Theory, comparison with experiment, and predictions for future devices,” *Fusion Science and Technology*, vol. 52, no. 1, pp. 29–67, 2007. eprint: <https://doi.org/10.13182/FST07-A1485>.
- [10] M. D. Hill and W. M. Stacey, “Confinement tuning of a 0-d plasma dynamics model,” *Fusion Science and Technology*, vol. 72, no. 2, pp. 162–175, 2017. eprint: <https://doi.org/10.1080/15361055.2017.1320494>.

- [11] M. D. Hill, “Burn control mechanisms in tokamak fusion reactors,” Ph.D. dissertation, Georgia Institute of Technology, May 2019.
- [12] W. M. Stacey, “A nodal model for tokamak burning plasma space-time dynamics,” *Fusion Science and Technology*, vol. 77, no. 2, pp. 109–118, 2021. eprint: <https://doi.org/10.1080/15361055.2020.1851631>.
- [13] J. Freidberg, *Plasma Physics and Fusion Energy*. Cambridge University Press, 2008, ISBN: 9781139462150.
- [14] C. C. Petty, T. C. Luce, K. H. Burrell, S. C. Chiu, J. S. deGrassie, C. B. Forest, P. Gohil, C. M. Greenfield, R. J. Groebner, R. W. Harvey, R. I. Pinsker, R. Prater, R. E. Waltz, R. A. James, and D. Wròblewski, “Nondimensional transport scaling in diii-d: Bohm versus gyro-bohm resolved,” *Physics of Plasmas*, vol. 2, no. 6, pp. 2342–2348, 1995. eprint: <https://doi.org/10.1063/1.871259>.
- [15] G Becker, “Empirical scaling law for the effective heat diffusivity in ELMy h mode plasmas,” *Nuclear Fusion*, vol. 36, no. 4, pp. 527–530, 1996.
- [16] D. Baker, M. Wade, G. Jackson, R Maingi, R. Stockdale, J. deGrassie, R. Groebner, C. Forest, G. Porter, and D.-D. Team, “Measurement of electron particle transport coefficients in different operational modes of DIII-d,” vol. 38, no. 4, pp. 485–494, 1998.
- [17] G Becker, “Scaling law for effective heat diffusivity in ELMy h-mode plasmas,” *Nuclear Fusion*, vol. 44, no. 11, pp. L26–L28, 2004.
- [18] G Becker and O Kardaun, “Anomalous particle pinch and scaling of  $v_{in}/d$  based on transport analysis and multiple regression,” *Nuclear Fusion*, vol. 47, no. 1, pp. 33–43, 2006.
- [19] M. A. Mahdavi, R. Maingi, R. J. Groebner, A. W. Leonard, T. H. Osborne, and G. Porter, “Physics of pedestal density profile formation and its impact on h-mode density limit in burning plasmas,” *Physics of Plasmas*, vol. 10, no. 10, pp. 3984–3991, 2003. eprint: <https://doi.org/10.1063/1.1605101>.
- [20] W. M. Stacey, “Structure of the edge density pedestal in tokamaks,” *Physics of Plasmas*, vol. 11, no. 9, pp. 4295–4304, 2004. eprint: <https://doi.org/10.1063/1.1777590>.
- [21] C. C. Petty, T. C. Luce, D. C. McDonald, J. Mandrekas, M. R. Wade, J. Candy, J. G. Cordey, V. Drozdov, T. E. Evans, J. R. Ferron, R. J. Groebner, A. W. Hyatt, G. L. Jackson, R. J. La Haye, T. H. Osborne, and R. E. Waltz, “Beta scaling of transport on the DIII-D Tokamak: Is transport electrostatic or electromagnetic?” *Physics of Plasmas*, vol. 11, no. 5 PART 2, pp. 2514–2522, 2004.

- [22] W. M. Stacey and R. J. Groebner, “Application of a particle, momentum, and energy balance model to calculate the structure of the edge pedestal in DIII-D,” *Physics of Plasmas*, vol. 12, no. 4, pp. 1–12, 2005.
- [23] W. M. Stacey, R. W. Johnson, and J. Mandrekas, “A neoclassical calculation of toroidal rotation profiles and comparison with DIII-D measurements,” *Physics of Plasmas*, vol. 13, no. 6, 2006.
- [24] W. M. Stacey and R. J. Groebner, “Thermal transport analysis of the edge region in the low and high confinement stages of a DIII-D discharge,” *Physics of Plasmas*, vol. 14, no. 1, 2007.
- [25] G. Becker and O. Kardaun, “Anomalous particle pinch and scaling of  $v_{in}/D$  based on transport analysis and multiple regression,” *Nuclear Fusion*, vol. 47, no. 1, pp. 33–43, 2007.
- [26] W. M. Stacey, “Ion particle transport in the tokamak edge plasma,” *Contributions to Plasma Physics*, vol. 48, no. 1-3, pp. 94–98, 2008.
- [27] W. M. Stacey and R. J. Groebner, “Interpretation of particle pinches and diffusion coefficients in the edge pedestal of DIII-D H-mode plasmas,” *Physics of Plasmas*, vol. 16, no. 10, 2009.
- [28] W. Stacey, “Corrigendum: Extended fluid transport theory in the tokamak plasma edge (2017 Nucl. Fusion 57 066034),” *Nuclear Fusion*, vol. 57, no. 11, p. 119 501, 2017.
- [29] L. Baylor, T. Jernigan, R. Colchin, G. Jackson, L. Owen, and T. Petrie, “Comparison of fueling efficiency from different fueling locations on diii-d,” *Journal of Nuclear Materials*, vol. 313-316, pp. 530–533, 2003, Plasma-Surface Interactions in Controlled Fusion Devices 15.
- [30] C. Kessel, G. Giruzzi, A. Sips, R. Budny, J. Artaud, V. Basiuk, F. Imbeaux, E. Joffrin, M. Schneider, M. Murakami, T. Luce, H. S. John, T. Oikawa, N. Hayashi, T. Takizuka, T. Ozeki, Y.-S. Na, J. Park, J. Garcia, and A. Tucillo, “Simulation of the hybrid and steady state advanced operating modes in ITER,” *Nuclear Fusion*, vol. 47, no. 9, pp. 1274–1284, 2007.
- [31] *ITER Technical Basis*, ser. ITER EDA Documentation Series 24. Vienna: International Atomic Energy Agency, 2002.
- [32] M. Henderson, G. Saibene, C. Darbos, D. Farina, L. Figini, M. Gagliardi, F. Gandini, T. Gassmann, G. Hanson, A. Loarte, T. Omori, E. Poli, D. Purohit, and K. Takahashi, “The targeted heating and current drive applications for the ITER electron cyclotron system,” *Physics of Plasmas*, vol. 22, no. 2, 2015.



- [33] W. Stacey, *Fusion: An Introduction to the Physics and Technology of Magnetic Confinement Fusion*. Wiley, 2010, ISBN: 9783527629329.
- [34] J. Wesson and D. Campbell, *Tokamaks*, ser. International Series of Monographs on Physics. OUP Oxford, 2011, ISBN: 9780199592234.
- [35] C. E. Kessel, R. E. Bell, M. G. Bell, D. A. Gates, S. M. Kaye, B. P. LeBlanc, J. E. Menard, C. K. Phillips, E. J. Synakowski, G. Taylor, R. Wilson, R. W. Harvey, T. K. Mau, P. M. Ryan, and S. A. Sabbagh, “Long pulse high performance plasma scenario development for the national spherical torus experiment,” *Physics of Plasmas*, vol. 13, no. 5, p. 056 108, 2006. eprint: <https://doi.org/10.1063/1.2177645>.
- [36] G. V. Pereverzev and P. Yushmanov, “Astra. automated system for transport analysis in a tokamak,” 2002.
- [37] M Murakami, C. Greenfield, M. Wade, T. Luce, J. Ferron, H. S. John, M. Makowski, M. Austin, S. Allen, D. Brennan, K. Burrell, T. Casper, J. DeBoo, E. Doyle, A. Garofalo, P Gohil, I. Gorelov, R. Groebner, J Hobirk, A. Hyatt, R. Jayakumar, K Kajiwara, C. Kessel, J. Kinsey, R. L. Haye, J. Kim, L. Lao, J Lohr, J. Menard, C. Petty, T. Petrie, R. Pinsker, P. Politzer, R Prater, T. Rhodes, A. Sips, G. Staebler, T. Taylor, G Wang, W. West, L Zeng, and the DIII-D Team, “100% noninductive operation at high beta using off-axis ECCD in DIII-d,” *Nuclear Fusion*, vol. 45, no. 11, pp. 1419–1426, 2005.
- [38] Y. Yoshimura, A. Ejiri, R. Seki, R. Sakamoto, K. Nagaoka, T. Shimozuma, H. Igami, H. Takahashi, T. I. Tsujimura, F. Warmer, K. Yanagihara, Y. Goto, K. Ida, M. Yoshinuma, T. Kobayashi, S. Kubo, M. Osakabe, T. Morisaki, and the Lhd Experiment Group, “Effect of electron cyclotron current drive on the ion temperature in the plasma core region of the large helical device,” *Plasma and Fusion Research*, vol. 13, pp. 1 402 124–1 402 124, 2018.
- [39] J. Varela, D. A. Spong, L. Garcia, Y. Todo, J. Huang, and M. Murakami, “Study of alfven eigenmodes stability in plasma with multiple nbi driven energetic particle species,” *Physics of Plasmas*, vol. 26, no. 6, p. 062 502, 2019. eprint: <https://doi.org/10.1063/1.5098347>.
- [40] F Albajar, J Johner, and G Granata, “Improved calculation of synchrotron radiation losses in realistic tokamak plasmas,” *Nuclear Fusion*, vol. 41, no. 6, pp. 665–678, 2001.
- [41] F. Albajar, M. Bornatici, and F. Engelmann, “RAYTEC: A new code for electron cyclotron radiative transport modelling of fusion plasmas,” *Nuclear Fusion*, vol. 49, no. 11, 2009.

- [42] D. Roberts, “Total impurity radiation power losses from steady-state tokamak plasmas,” *Nuclear Fusion*, vol. 21, no. 2, pp. 215–231, 1981.
- [43] D. Morozov, E. Baronova, and I. Senichenkov, “Impurity radiation from a tokamak plasma,” *Plasma Physics Reports*, vol. 33, pp. 906–922, Jan. 2007.
- [44] J. Mandrekas and W. M. Stacey, “An impurity seeded radiative mantle for ITER,” *Nuclear Fusion*, vol. 35, no. 7, pp. 843–852, 1995.
- [45] G. Becker, “Transport simulations of ITER with broad density profiles and high radiative fraction,” *Nuclear Fusion*, vol. 35, no. 8, pp. 969–980, 1995.
- [46] T. Pütterich, E. Fable, R. Dux, M. O’Mullane, R. Neu, and M. Siccino, “Determination of the tolerable impurity concentrations in a fusion reactor using a consistent set of cooling factors,” *Nuclear Fusion*, vol. 59, no. 5, p. 056 013, 2019.
- [47] I. Hutchinson, *Lecture notes in introduction to plasma physics*, 2003.
- [48] M. Honda, “Coulomb logarithm formulae for collisions between species with different temperatures,” *Japanese Journal of Applied Physics*, vol. 52, no. 10 PART1, 2013.
- [49] W. M. Stacey, “The effect of ion orbit loss and x-loss on the interpretation of ion energy and particle transport in the diii-d edge plasma,” *Physics of Plasmas*, vol. 18, no. 10, p. 102 504, 2011. eprint: <https://doi.org/10.1063/1.3640506>.
- [50] W. Stacey, “Effect of ion orbit loss on distribution of particle, energy and momentum sources into the tokamak scrape-off layer,” vol. 53, no. 6, p. 063 011, 2013.
- [51] W. M. Stacey and M. T. Schumann, “The distribution of ion orbit loss fluxes of ions and energy from the plasma edge across the last closed flux surface into the scrape-off layer,” *Physics of Plasmas*, vol. 22, no. 4, p. 042 504, 2015. eprint: <https://doi.org/10.1063/1.4917318>.
- [52] W. M. Stacey and T. M. Wilks, “Inclusion of ion orbit loss and intrinsic rotation in plasma fluid rotation theory,” *Physics of Plasmas*, vol. 23, no. 1, p. 012 508, 2016. eprint: <https://doi.org/10.1063/1.4939884>.
- [53] W. M. Stacey, “The dependence of ion orbit loss on ion charge and mass,” *Physics of Plasmas*, vol. 25, no. 12, p. 122 506, 2018. eprint: <https://doi.org/10.1063/1.5048387>.
- [54] T. M. Wilks and W. M. Stacey, “Improvements to an ion orbit loss calculation in the tokamak edge,” *Physics of Plasmas*, vol. 23, no. 12, p. 122 505, 2016. eprint: <https://doi.org/10.1063/1.4968219>.

- [55] T. M. Wilks, “Calculation of the radial electric field in the diii-d tokamak edge plasma,” Ph.D. dissertation, Georgia Institute of Technology, May 2016.
- [56] W. M. Stacey, “A coupled plasma-neutrals model for divertor simulations,” *Physics of Plasmas*, vol. 5, no. 4, pp. 1015–1026, 1998. eprint: <https://doi.org/10.1063/1.872631>.
- [57] W. Stacey, “Modelling the neutral density in the edge of the DIII-d plasma,” vol. 40, no. 5, pp. 965–973, 2000.
- [58] R. Janev, D. Post, W. Langer, K. Evans, D. Heifetz, and J. Weisheit, “Survey of atomic processes in edge plasmas,” *Journal of Nuclear Materials*, vol. 121, pp. 10–16, 1984.
- [59] R. Janev, W. Langer, K. Evans, and D. Post, *Elementary Processes in Hydrogen-Helium Plasmas: Cross Sections and Reaction Rate Coefficients*, ser. Springer Series on Atomic, Optical, and Plasma Physics. Springer Berlin Heidelberg, 2012, ISBN: 9783642719356.
- [60] E. W. Thomas and W. M. Stacey, “Deuterium atomic cross section uncertainties and molecular recycling effects in the divertor region of tokamaks,” *Physics of Plasmas*, vol. 4, no. 3, pp. 678–689, 1997.
- [61] J. Mandrekas, “Gtneut: A code for the calculation of neutral particle transport in plasmas based on the transmission and escape probability method,” *Computer Physics Communications*, vol. 161, no. 1, pp. 36–64, 2004.
- [62] E. W. Thomas, R. K. Janev, and J. Smith, “Scaling of particle reflection coefficients,” *Nuclear Inst. and Methods in Physics Research, B*, vol. 69, no. 4, pp. 427–436, 1992.
- [63] R. J. Goldston, “A simple neutral density profile calculation for Tokamaks with  $\lambda_{mfj;a}$ ,” *Plasma Physics*, vol. 20, no. 11, pp. 1199–1203, 1978.
- [64] K. Borrass, “Disruptive tokamak density limit as scrape-off layer/divertor phenomenon,” *Nuclear Fusion*, vol. 31, no. 6, pp. 1035–1051, 1991.
- [65] W. M. Stacey, E. W. Thomas, and T. M. Evans, “Data and extended diffusion theories for neutral particle transport in tokamak divertors,” *Physics of Plasmas*, vol. 2, no. 10, pp. 3740–3756, 1995.
- [66] W. M. Stacey, J. Mandrekas, and R. Rubilar, “An improved divertor/SOL model for coupled core/SOL/divertor simulations of tokamaks,” *Contributions to Plasma Physics*, vol. 38, no. 1-2, pp. 26–30, 1998.

- [67] J. Mandrekas, R. J. Colchin, W. M. Stacey, D. Zhang, and L. W. Owen, “Neutral transport analysis of recent DIII-D neutral density experiments,” *Nuclear Fusion*, vol. 43, no. 5, pp. 314–320, 2003.
- [68] Z. W. Friis, W. M. Stacey, A. W. Leonard, and M. E. Rensink, “Analysis of neutral particle recycling and pedestal fueling in a H-mode DIII-D discharge,” *Physics of Plasmas*, vol. 17, no. 2, 2010.
- [69] T. Eich, A. W. Leonard, R. A. Pitts, W. Fundamenski, R. J. Goldston, T. K. Gray, A. Herrmann, A. Kirk, A. Kallenbach, O. Kardaun, A. S. Kukushkin, B. Labombard, R. Maingi, M. A. Makowski, A. Scarabosio, B. Sieglin, J. Terry, and A. Thornton, “Scaling of the tokamak near the scrape-off layer H-mode power width and implications for ITER,” *Nuclear Fusion*, vol. 53, no. 9, 2013.
- [70] F. D. Halpern, P. Ricci, B. Labit, I. Furno, S. Jolliet, J. Loizu, A. Masetto, G. Arnoux, J. P. Gunn, J. Horacek, M. Kočan, B. Labombard, and C. Silva, “Theory-based scaling of the SOL width in circular limited tokamak plasmas,” *Nuclear Fusion*, vol. 53, no. 12, 2013.
- [71] B. M. Covele, “2-D Magnetic Equilibrium and Transport Modeling of the X-Divertor and Super X-Divertor for Scrape-Off Layer Heat Flux Mitigation in Tokamaks,” 2014.
- [72] F. D. Halpern, P. Ricci, S. Jolliet, J. Loizu, and A. Masetto, “Theory of the scrape-off layer width in inner-wall limited tokamak plasmas,” *Nuclear Fusion*, vol. 54, no. 4, 2014.
- [73] D. Penko, L. Kos, X. Bonnin, and S. D. Pinches, “Post-processing for ITER Scrape-Off Layer Plasma Simulations (SOLPS-ITER) in IMAS Framework,” *Journal of Fusion Energy*, vol. 39, no. 5, pp. 202–211, 2020.
- [74] C. M. Bishop, P. S. Haynes, M. E. U. Smith, T. N. Todd, and D. L. Trotman, “Real-time control of a tokamak plasma using neural networks,” *Neural Computation*, vol. 7, no. 1, pp. 206–217, 1995. eprint: <https://doi.org/10.1162/neco.1995.7.1.206>.
- [75] L. Allen and C. M. Bishop, “Neural network approach to energy confinement scaling in tokamaks,” *Plasma Physics and Controlled Fusion*, vol. 34, no. 7, pp. 1291–1302, 1992.
- [76] T. Hastie, R. Tibshirani, and J. Friedman, *The Elements of Statistical Learning: Data Mining, Inference, and Prediction*, ser. Springer series in statistics. Springer, 2009, ISBN: 9780387848846.

- [77] I. Goodfellow, Y. Bengio, and A. Courville, *Deep Learning*, ser. Adaptive Computation and Machine Learning series. MIT Press, 2016, ISBN: 9780262337373.
- [78] R. T. Q. Chen, Y. Rubanova, J. Bettencourt, and D. Duvenaud, “Neural ordinary differential equations,” *Advances in Neural Information Processing Systems*, 2018.
- [79] A. Paszke, S. Gross, F. Massa, A. Lerer, J. Bradbury, G. Chanan, T. Killeen, Z. Lin, N. Gimelshein, L. Antiga, A. Desmaison, A. Kopf, E. Yang, Z. DeVito, M. Raison, A. Tejani, S. Chilamkurthy, B. Steiner, L. Fang, J. Bai, and S. Chintala, “Pytorch: An imperative style, high-performance deep learning library,” in *Advances in Neural Information Processing Systems 32*, Curran Associates, Inc., 2019, pp. 8024–8035.
- [80] O. Meneghini, S. Smith, L. Lao, O. Izacard, Q. Ren, J. Park, J. Candy, Z. Wang, C. Luna, V. Izzo, B. Grierson, P. Snyder, C. Holland, J. Penna, G. Lu, P. Raum, A. McCubbin, D. Orlov, E. Belli, N. Ferraro, R. Prater, T. Osborne, A. Turnbull, and G. Staebler, “Integrated modeling applications for tokamak experiments with omfit,” *Nuclear Fusion*, vol. 55, no. 8, p. 083 008, 2015.
- [81] C. R. Harris, K. J. Millman, S. J. van der Walt, R. Gommers, P. Virtanen, D. Cournapeau, E. Wieser, J. Taylor, S. Berg, N. J. Smith, R. Kern, M. Picus, S. Hoyer, M. H. van Kerkwijk, M. Brett, A. Haldane, J. F. del R’io, M. Wiebe, P. Peterson, P. G’erard-Marchant, K. Sheppard, T. Reddy, W. Weckesser, H. Abbasi, C. Gohlke, and T. E. Oliphant, “Array programming with NumPy,” *Nature*, vol. 585, no. 7825, pp. 357–362, Sep. 2020.
- [82] P. Virtanen, R. Gommers, T. E. Oliphant, M. Haberland, T. Reddy, D. Cournapeau, E. Burovski, P. Peterson, W. Weckesser, J. Bright, S. J. van der Walt, M. Brett, J. Wilson, K. J. Millman, N. Mayorov, A. R. J. Nelson, E. Jones, R. Kern, E. Larson, C. J. Carey, I. Polat, Y. Feng, E. W. Moore, J. VanderPlas, D. Laxalde, J. Perktold, R. Cimrman, I. Henriksen, E. A. Quintero, C. R. Harris, A. M. Archibald, A. H. Ribeiro, F. Pedregosa, P. van Mulbregt, and SciPy 1.0 Contributors, “SciPy 1.0: Fundamental Algorithms for Scientific Computing in Python,” *Nature Methods*, vol. 17, pp. 261–272, 2020.
- [83] J. D. Hunter, “Matplotlib: A 2d graphics environment,” *Computing in Science Engineering*, vol. 9, no. 3, pp. 90–95, 2007.
- [84] Q Peng, R. J. Groebner, L. L. Lao, J Schachter, D. P. Schissel, and M. R. Wade, “Between-Pulse Data Analyses At Diii – D,” no. August, 2001.
- [85] R. T. Q. Chen, B. Amos, and M. Nickel, “Learning neural event functions for ordinary differential equations,” *International Conference on Learning Representations*, 2021.

- [86] T. Sauer, *Numerical Analysis*, 2nd. USA: Addison-Wesley Publishing Company, 2011, ISBN: 0321783670.
- [87] M. Shimada, D. J. Campbell, V. Mukhovatov, M. Fujiwara, N. Kirneva, K. Lackner, M. Nagami, V. D. Pustovitov, N. Uckan, J. Wesley, N. Asakura, A. E. Costley, A. J. Donné, E. J. Doyle, A. Fasoli, C. Gormezano, Y. Gribov, O. Gruber, T. C. Hender, W. Houlberg, S. Ide, Y. Kamada, A. Leonard, B. Lipschultz, A. Loarte, K. Miyamoto, V. Mukhovatov, T. H. Osborne, A. Polevoi, and A. C. Sips, “Chapter 1: Overview and summary,” *Nuclear Fusion*, vol. 47, no. 6, 2007.
- [88] D. Bora, B. Beaumont, R. Goulding, J. Jacquinot, N. Kobayashi, D. Swain, and A. Tanga, “RF heating needs and plans for ITER,” *AIP Conference Proceedings*, vol. 933, no. October 2007, pp. 25–32, 2007.
- [89] R. Hemsworth, H. Decamps, J. Graceffa, B. Schunke, M. Tanaka, M. Dremel, A. Tanga, H. P. De Esch, F. Geli, J. Milnes, T. Inoue, D. Marcuzzi, P. Sonato, and P. Zaccaria, “Status of the ITER heating neutral beam system,” *Nuclear Fusion*, vol. 49, no. 4, 2009.
- [90] J. Jacquinot, F. Albajar, B. Beaumont, A. Becoulet, T. Bonicelli, D. Bora, D. Campbell, A. Chakraborty, C. Darbos, H. Decamps, G. Denisov, R. Goulding, J. Graceffa, T. Gassmann, R. Hemsworth, M. Henderson, G. T. Hoang, T. Inoue, N. Kobayashi, P. U. Lamalle, A. Mukherjee, M. Nightingale, D. Rasmussen, S. L. Rao, G. Saibene, K. Sakamoto, R. Sartori, B. Schunke, P. Sonato, D. Swain, K. Takahashi, M. Tanaka, A. Tanga, and K. Watanabe, “Progress on the heating and current drive systems for ITER,” *Fusion Engineering and Design*, vol. 84, no. 2-6, pp. 125–130, 2009.
- [91] F. Wagner, A. Becoulet, R. Budny, V. Erckmann, D. Farina, G. Giruzzi, Y. Kamada, A. Kaye, F. Koech, K. Lackner, N. Marushchenko, M. Murakami, T. Oikawa, V. Parail, J. M. Park, G. Ramponi, O. Sauter, D. Stork, P. R. Thomas, Q. M. Tran, D. Ward, H. Zohm, and C. Zucca, “On the heating mix of ITER,” *Plasma Physics and Controlled Fusion*, vol. 52, no. 12, 2010.
- [92] R. S. Hemsworth, D. Boilson, P. Blatchford, M. D. Palma, G. Chitarin, H. P. De Esch, F. Geli, M. Dremel, J. Graceffa, D. Marcuzzi, G. Serianni, D. Shah, M. Singh, M. Urbani, and P. Zaccaria, “Overview of the design of the ITER heating neutral beam injectors,” *New Journal of Physics*, vol. 19, no. 2, 2017.
- [93] K. Weiss, T. M. Khoshgoftaar, and D. D. Wang, *A survey of transfer learning*, 1. Springer International Publishing, 2016, vol. 3, ISBN: 4053701600.
- [94] W. M. Stacey, “A calculation model for density limits in auxiliary heated, gas fueled tokamaks and application to DIII-D model problems,” *Physics of Plasmas*, vol. 8, no. 8, pp. 3673–3688, 2001.

- [95] W. Pfeiffer, R. Davidson, R. Miller, and R. Waltz, “Onetwo: A computer code for modeling plasma transport in tokamaks,” General Atomic Co., San Diego, CA (USA), Tech. Rep., 1980.
- [96] H. John, T. Taylor, Y. Lin-Liu, and A. Turnbull, “Transport simulation of negative magnetic shear discharges,” General Atomics, San Diego, CA (United States), Tech. Rep., 1994.
- [97] T. Odstrčil, N. Howard, F. Sciortino, C. Chrystal, C. Holland, E. Hollmann, G. McKee, K. Thome, and T. Wilks, “Dependence of the impurity transport on the dominant turbulent regime in elm-y h-mode discharges on the diiii-d tokamak,” *Physics of Plasmas*, vol. 27, no. 8, p. 082 503, 2020.
- [98] H. Tsuji, M. Katsurai, T. Sekiguchi, and N. Nakano, “Time-dependent solution of fokker-planck equation for alpha-particles and its effect on alpha-particle heating characteristics in a D-T fusion reactor,” *Nuclear Fusion*, vol. 16, no. 2, pp. 287–293, 1976.
- [99] H. Saito, T. Sekiguchi, M. Katsurai, and S. Maekawa, “An approximate theory of steady-state and dynamic characteristics of alpha-particle-heated dt-fusion reactors,” *Nuclear Fusion*, vol. 17, no. 5, pp. 919–928, 1977.
- [100] J.-P. Floyd, W. M. Stacey, R. J. Groebner, and S. C. Mellard, “Evolution of edge pedestal transport between edge-localized modes in diiii-d,” *Physics of Plasmas*, vol. 22, no. 2, p. 022 508, 2015. eprint: <https://doi.org/10.1063/1.4907780>.
- [101] V. P. Lipschultz, R. La Bombard, P. Marmar, R. Pickrell, R. R. Terry, R. R. Waterson, and S. M. Wolfe, “Marfe: An edge plasma phenomenon,” *Nuclear Fusion*, vol. 24, no. 8, pp. 977–988, 1984.
- [102] W. M. Stacey, “Explanation for marfe formation and subsequent evolution into a detached symmetric plasma edge,” *Physics of Plasmas*, vol. 3, no. 7, pp. 2673–2678, 1996. eprint: <https://doi.org/10.1063/1.871524>.
- [103] F. A. Kelly, W. M. Stacey, J. Rapp, and M. Brix, “Thermal instability theory analysis of multifaceted asymmetric radiation from the edge (MARFE) in Tokamak Experiment for Technology Oriented Research (TEXTOR),” *Physics of Plasmas*, vol. 8, no. 7, pp. 3382–3390, 2001.
- [104] W. M. Stacey, R. J. Groebner, and T. Evans, “Non-diffusive transport in the tokamak edge pedestal,” *Nuclear Fusion*, vol. 52, no. 11, p. 114 020, 2012.

- [105] C. F. Curtiss and J. O. Hirschfelder, “Integration of stiff equations,” *Proceedings of the National Academy of Sciences of the United States of America*, vol. 38, no. 3, p. 235, 1952.
- [106] E. Rebhan and U. Vieth, “Burn stability and a safe operating regime of a tokamak reactor with iter scaling,” *Nuclear Fusion*, vol. 37, no. 2, pp. 251–270, 1997.
- [107] M. Becoulet, F. Orain, P. Maget, N. Mellet, X. Garbet, E. Nardon, G. Huysmans, T. Casper, A. Loarte, P. Cahyna, A. Smolyakov, F. Waelbroeck, M. Schaffer, T. Evans, Y. Liang, O. Schmitz, M. Beurskens, V. Rozhansky, and E. Kaveeva, “Screening of resonant magnetic perturbations by flows in tokamaks,” *Nuclear Fusion*, vol. 52, no. 5, p. 054 003, 2012.
- [108] R. Budny, R. Andre, G. Bateman, F. Halpern, C. Kessel, A. Kritz, and D. McCune, “Predictions of h-mode performance in ITER,” *Nuclear Fusion*, vol. 48, no. 7, p. 075 005, 2008.